

257 269



USA AVSCOM TR-92-C-01

2

# **An Investigation of Unsteady Impeller-Diffuser Interactions in a Centrifugal Compressor**

**William Barry Bryan and Sanford Fleeter**

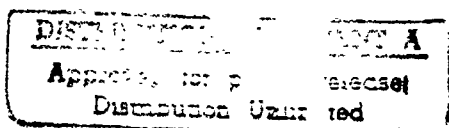
**Prepared For  
U.S. ARMY AVIATION  
SYSTEMS COMMAND**

**DTIC**  
**ELECTE**  
**NOV 4 1992**  
**S C D**

**NATIONAL AERONAUTICS AND SPACE  
ADMINISTRATION**

**NASA LEWIS RESEARCH CENTER**

**Grant NAG3-1207**



**02 109**

**92-28705**



**School of Mechanical Engineering**

**Purdue University**

**1003 Chaffee Hall**

**West Lafayette, Indiana 47907-1003**



## Report Documentation Page

1. Report No. <b>TR-92-C-017</b>		2. Government Accession No.		3. Recipient's Catalog No.	
4. Title and Subtitle <b>AN INVESTIGATION OF UNSTEADY IMPELLER-DIFFUSER INTERACTIONS IN A CENTRIFUGAL COMPRESSOR</b>				5. Report Date	
				6. Performing Organization Code	
7. Author(s) <b>WILLIAM BARRY BRYAN SANFORD FLEETER</b>				8. Performing Organization Report No.	
				10. Work Unit No.	
9. Performing Organization Name and Address <b>School of Mechanical Engineering Purdue University West Lafayette, IN 47907</b>				11. Contract or Grant No. <b>NAG3-1207</b>	
				13. Type of Report and Period Covered	
12. Sponsoring Agency Name and Address <b>US Army Propulsion Directorate Cleveland, OH 44135-3191 National Aeronautics and Space Administration Cleveland, OH 44135-3191</b> and				14. Sponsoring Agency Code	
15. Supplementary Notes <b>Project Manager, Lawrence F. Schumann, Internal Fluid Mechanics Branch, NASA Lewis Research Center</b>					
16. Abstract <b>An investigation of steady and unsteady flow phenomena in centrifugal compressors has been performed. The effect of vaned diffuser geometry on the compressor unsteady aerodynamics has been considered, with particular emphasis on the diffuser vane unsteady loading generated by the impeller circumferentially nonuniform flow field. A series of experiments was performed in the Purdue Research Centrifugal Compressor Facility to quantify the compressor performance, impeller blade and diffuser vane steady surface static pressure, vaneless diffuser steady and unsteady velocity field, diffuser vane unsteady surface static pressure, as well as surge and rotating stall occurrence. These measurements were made for various flow rates, number of diffuser vanes, diffuser vane leading edge-impeller exit radius ratios, diffuser vane stagger angles, and nonuniform circumferential vane spacing.</b>					
17. Key Words (Suggested by Author(s)) <b>Centrifugal Compressor Unsteady Aerodynamics Vaneless Diffuser Laser Anemometry Vaned Diffuser</b>			18. Distribution Statement <b>Unclassified-Unlimited</b>		
19. Security Classif. (of this report) <b>Unclassified</b>		20. Security Classif. (of this page) <b>Unclassified</b>		21. No. of pages <b>176</b>	
				22. Price	

**AN INVESTIGATION OF UNSTEADY IMPELLER-DIFFUSER  
INTERACTIONS IN A CENTRIFUGAL COMPRESSOR**

**William Barry Bryan and Sanford Fleeter**

**Prepared For**

**U.S. ARMY AVIATION SYSTEMS COMMAND**

**NATIONAL AERONAUTICS AND SPACE ADMINISTRATION  
NASA LEWIS RESEARCH CENTER  
GRANT NAG3 - 1207**

**August 1992**

**DTIC QUALITY INSPECTED 8**

**School of Mechanical Engineering  
Purdue University  
West Lafayette, Indiana 47907**

<b>Accession For</b>	
NTIS GRANT	<input checked="checked" type="checkbox"/>
DTIC TAB	<input type="checkbox"/>
Unannounced	<input type="checkbox"/>
Justification	
By _____	
Distribution/	
Availability Codes	
Dist and/or	
Dist	Special
A-1	

## ABSTRACT

An investigation of steady and unsteady flow phenomena in centrifugal compressors has been performed. The effect of vaned diffuser geometry on the compressor unsteady aerodynamics has been considered, with particular emphasis on the diffuser vane unsteady loading generated by the impeller circumferentially nonuniform flow field. A series of experiments was performed in the Purdue Research Centrifugal Compressor Facility to quantify the compressor performance, impeller blade and diffuser vane steady surface static pressure, vaneless diffuser steady and unsteady velocity field, diffuser vane unsteady surface static pressure, as well as surge and rotating stall occurrence. These measurements were made for various flow rates, number of diffuser vanes, diffuser vane leading edge-impeller exit radius ratios, diffuser vane stagger angles, and nonuniform circumferential vane spacing.

In conjunction with the above experiments, theoretical predictions of the unsteady vaneless diffuser wake velocities and the unsteady diffuser vane loading were developed. The linearized Euler equations were solved to predict the wake behavior, with a conformal transformation applied to existing axial flow cascade theory for unsteady diffuser vane loading predictions.

It was found that the compressor performance could be improved through use of a vaned diffuser, with the greatest performance improvement with zero steady loading on the vanes. The unsteady wake velocity in the radial diffuser was seen to decrease rapidly with increasing radius. The decrease was greater than predicted by the theory, with the unsteady circumferential pressure gradient and the phase angle between the radial and tangential unsteady velocities determined to be important parameters.

The diffuser vane unsteady loading was determined to be a strong function of flow rate and number of diffuser vanes, with the diffuser vane leading edge-impeller exit radius ratio important for smaller numbers of vanes. The correlation with theory was poor with a high diffuser vane row solidity, although fair correlation was seen with moderate solidity.

Finally, the vaned diffuser row had a significant impact on surge and rotating stall margins and behavior. It was found that notable improvement could be made by proper adjustment of the diffuser vane row geometry.

## TABLE OF CONTENTS

	Page
LIST OF TABLES .....	v
LIST OF FIGURES .....	vi
LIST OF SYMBOLS .....	x
 CHAPTER 1 - INTRODUCTION .....	 1
1.1 Operation of Centrifugal Impellers .....	2
1.2 Basic Theory of Radial Diffusers.....	3
1.3 Literature Review.....	5
1.4 Research Objective and Technical Approach.....	8
 CHAPTER 2 - THE PURDUE RESEARCH CENTRIFUGAL COMPRESSOR.....	 13
2.1 General .....	13
2.2 Impeller and Drive Assembly .....	13
2.3 Inlet .....	14
2.4 Diffuser.....	15
2.5 Plenum and Exhaust Piping.....	15
 CHAPTER 3 - DATA ACQUISITION AND ANALYSIS.....	 26
3.1 Steady Data Instrumentation .....	26
3.2 Unsteady Pressure Instrumentation .....	28

	Page
3.3 Laser Doppler Velocimeter .....	29
3.4 Compressor Performance Analysis .....	31
3.5 Impeller and Vaned Diffuser Steady Loading Analysis.....	32
3.6 LDV Velocity Analysis .....	33
3.7 Unsteady Pressure Data Analysis .....	34
3.8 Summary .....	35
 CHAPTER 4 - RADIAL DIFFUSER WAKE ANALYSIS.....	 42
4.1 Analysis .....	42
4.2 Results.....	49
 CHAPTER 5 - RADIAL CASCADE UNSTEADY AIRFOIL THEORY .....	 57
5.1 Transformation Analysis .....	57
5.2 Cascade Model.....	61
5.3 Boundary Condition Transformation .....	62
5.4 Model Verification.....	65
5.5 Results.....	65
 CHAPTER 6 - EXPERIMENTAL RESULTS .....	 85
6.1 Compressor Performance .....	86
6.2 Impeller Steady Loading.....	88
6.3 Diffuser Vane Steady Loading.....	89
6.4 Radial Diffuser Velocity Field .....	90
6.5 Diffuser Vane Unsteady Loading.....	94
6.6 Compressor Instabilities.....	98
 CHAPTER 7 - SUMMARY, CONCLUSIONS AND RECOMMENDATIONS .....	 170
 LIST OF REFERENCES .....	 173
 VITA.....	 177

## LIST OF TABLES

Table	Page
6.1 Research Compressor Geometric Configurations.....	85
6.2 Compressor Instabilities .....	99

## LIST OF FIGURES

Figure	Page
1.1 Typical Centrifugal Compressor Stages.....	10
1.2 Centrifugal Compressor Flow Phenomena .....	11
1.3 Jet Wake Impeller Flow .....	12
2.1 Front View of Compressor Test Facility .....	17
2.2 Cutaway of Compressor Test Facility .....	18
2.3 Inlet, Impeller, and Diffuser Flow Channel .....	19
2.4 Impeller and Drive Assembly.....	20
2.5 Impeller Pressure Tap Locations.....	21
2.6 Diffuser Vane Profile.....	22
2.7 Diffuser Wall Profile .....	23
2.8 Diffuser Vane Mounting Cams.....	24
2.9 Schematic of Centrifugal Compressor Facility .....	25
3.1 Rotating Scanivalve and LDV Final Optics .....	36
3.2 Pressure Probe Locations.....	37
3.3 Diffuser Vane Unsteady Pressure Measurement Locations .....	38
3.4 Dual Beam LDV System .....	39
3.5 LDV Table-Mounted Preliminary Optics.....	40
3.6 LDV Final Optics Assembly.....	41
4.1 Radial Turbomachine Wake .....	51
4.2 Radial Diffuser Unsteady Wake Velocity ( $\alpha_0 = 60^\circ$ , $N_b = 12$ and $\beta_0 = -45^\circ$ ).....	52
4.3 Radial Diffuser Unsteady Wake Velocity ( $\alpha_0 = 45^\circ$ , $N_b = 12$ and $\beta_0 = -45^\circ$ ).....	53
4.4 Radial Diffuser Unsteady Wake Velocity ( $\alpha_0 = 60^\circ$ , $N_b = 12$ and $\beta_0 = -30^\circ$ ).....	54
4.5 Radial Diffuser Unsteady Wake Velocity ( $\alpha_0 = 60^\circ$ , $N_b = 12$ and $\beta_0 = 0^\circ$ ) .....	55
4.6 Radial Diffuser Unsteady Wake Velocity ( $\alpha_0 = 60^\circ$ , $N_b = 20$ and $\beta_0 = -45^\circ$ ).....	56
5.1 Radial Cascade Conformal Transformation.....	68
5.2 Flat Plate Cascade Transformation.....	69
5.3 Translation and Torsion Upwash Transformation .....	70



Figure	Page
5.4 Shed Vortical Gusts in Axial and Radial Turbomachines .....	71
5.5 Baseline Axial Flow Cascade Translational Lift.....	72
5.6 Baseline Radial Flow Cascade Translational Lift .....	73
5.7 Baseline Axial Flow Cascade Torsional Moment .....	74
5.8 Baseline Radial Flow Cascade Torsional Moment .....	75
5.9 Baseline Axial Flow Cascade Convected Gust Lift.....	76
5.10 Baseline Radial Flow Cascade Convected Gust Lift .....	77
5.11 Radial Flow Cascade Translational Lift .....	78
5.12 Radial Flow Cascade Torsional Moment .....	79
5.13 Radial Flow Cascade Convected Gust Lift.....	80
5.14 Unsteady Airfoil Pressure for Translational Motion.....	81
5.15 Unsteady Airfoil Pressure for Torsional Motion.....	82
5.16 Unsteady Airfoil Pressure for Convected Gust Upwash ( $k = 2.0$ ).....	83
5.17 Unsteady Airfoil Pressure for Convected Gust Upwash ( $k = 4.0$ ).....	84
6.1 Centrifugal Compressor Performance with Vaneless Diffuser .....	102
6.2 Effect of Stagger on Compressor Performance ( $r_1/r_0 = 1.10$ , $N_v = 30$ ) .....	103
6.3 Effect of Stagger on Compressor Performance ( $r_1/r_0 = 1.10$ , $N_v = 15$ ) .....	104
6.4 Effect of Stagger on Compressor Performance ( $r_1/r_0 = 1.15$ , $N_v = 30$ ) .....	105
6.5 Effect of Vane Number on Compressor Performance ( $r_1/r_0 = 1.10$ , $\sigma = 50^\circ$ ) .....	106
6.6 Effect of Vane Number on Compressor Performance ( $r_1/r_0 = 1.10$ , $\sigma = 60^\circ$ ) .....	107
6.7 Effect of Vane Number on Compressor Performance ( $r_1/r_0 = 1.10$ , $\sigma = 70^\circ$ ) .....	108
6.8 Effect of Radius Ratio on Compressor Performance ( $\sigma = 60^\circ$ , $N_v = 30$ ).....	109
6.9 Vaned Diffuser Nonuniform Circumferential Spacing Detuning.....	110
6.10 Detuned Diffuser Compressor Performance ( $r_1/r_0 = 1.10$ , $\sigma = 60^\circ$ , $N_v = 30$ ) .....	111
6.11 Detuned Diffuser Compressor Performance ( $r_1/r_0 = 1.10$ , $\sigma = 60^\circ$ , $N_v = 10$ ) .....	112
6.12 Impeller Static Pressure ( $N_v = 0$ , $\Phi = 0.17$ ).....	113
6.13 Impeller Static Pressure ( $N_v = 0$ , $\Phi = 0.22$ ).....	114
6.14 Impeller Static Pressure ( $N_v = 0$ , $\Phi = 0.30$ ).....	115
6.15 Impeller Static Pressure ( $r_1/r_0 = 1.10$ , $\sigma = 50^\circ$ , $N_v = 30$ , $\Phi = 0.30$ ).....	116
6.16 Impeller Static Pressure ( $r_1/r_0 = 1.10$ , $\sigma = 60^\circ$ , $N_v = 30$ , $\Phi = 0.22$ ).....	117
6.17 Incidence Effects on Diffuser Vane Steady Static Pressure ( $r_1/r_0 = 1.10$ , $\sigma = 60^\circ$ , $N_v = 30$ ) .....	118

Figure	Page
6.18 Vane Number Effects on Diffuser Vane Steady Static Pressure ( $r_1/r_0 = 1.10$ , $\sigma = 60^\circ$ , $\Phi = 0.22$ ).....	119
6.19 Detuned Diffuser Vane Steady Static Pressure ( $r_1/r_0 = 1.10$ , $\sigma = 60^\circ$ , $N_v = 30$ , $\Phi = 0.30$ ) .....	120
6.20 LDV Measurement Positions .....	121
6.21 LDV Circumferential Measurement Bins .....	122
6.22 LDV Radial and Circumferential Measurement Positions .....	123
6.23 Vaneless Diffuser Time-Averaged Velocity ( $\Phi = 0.30$ ).....	124
6.24 Vaneless Diffuser Time-Averaged Velocity ( $\Phi = 0.22$ ).....	125
6.25 Vaneless Diffuser Time-Averaged Velocity ( $\Phi = 0.17$ ).....	126
6.26 Vaneless Diffuser Total Velocity (Tip Position, $\Phi = 0.30$ ).....	127
6.27 Vaneless Diffuser Total Velocity (Mean Position, $\Phi = 0.30$ ) .....	128
6.28 Vaneless Diffuser Total Velocity (Hub Position, $\Phi = 0.30$ ) .....	129
6.29 Vaneless Diffuser Total Velocity (Tip Position, $\Phi = 0.22$ ).....	130
6.30 Vaneless Diffuser Total Velocity (Mean Position, $\Phi = 0.22$ ) .....	131
6.31 Vaneless Diffuser Total Velocity (Hub Position, $\Phi = 0.22$ ) .....	132
6.32 Vaneless Diffuser Total Velocity (Tip Position, $\Phi = 0.17$ ).....	133
6.33 Vaneless Diffuser Total Velocity (Mean Position, $\Phi = 0.17$ ) .....	134
6.34 Vaneless Diffuser Total Velocity (Hub Position, $\Phi = 0.17$ ) .....	135
6.35 Vaneless Diffuser Unsteady Velocity (Tip Position, $\Phi = 0.30$ ) .....	136
6.36 Vaneless Diffuser Unsteady Velocity (Mean Position, $\Phi = 0.30$ ).....	137
6.37 Vaneless Diffuser Unsteady Velocity (Hub Position, $\Phi = 0.30$ ) .....	138
6.38 Vaneless Diffuser Unsteady Velocity (Tip Position, $\Phi = 0.22$ ) .....	139
6.39 Vaneless Diffuser Unsteady Velocity (Mean Position, $\Phi = 0.22$ ) .....	140
6.40 Vaneless Diffuser Unsteady Velocity (Hub Position, $\Phi = 0.22$ ) .....	141
6.41 Vaneless Diffuser Unsteady Velocity (Tip Position, $\Phi = 0.17$ ) .....	142
6.42 Vaneless Diffuser Unsteady Velocity (Mean Position, $\Phi = 0.17$ ).....	143
6.43 Vaneless Diffuser Unsteady Velocity (Hub Position, $\Phi = 0.17$ ) .....	144
6.44 Linear Theory Aerodynamic Gusts.....	145
6.45 Vaneless Diffuser First Harmonic Unsteady Velocity and Theory ( $\Phi = 0.30$ ).....	146
6.46 Vaneless Diffuser First Harmonic Unsteady Velocity and Theory ( $\Phi = 0.22$ ).....	147
6.47 Vaneless Diffuser First Harmonic Unsteady Velocity and Theory ( $\Phi = 0.17$ ).....	148
6.48 Vaneless Diffuser First Harmonic Unsteady Velocity and Theory (Theory $\phi_w = -160^\circ$ , $\Phi = 0.30$ ) .....	149

Figure	Page
6.49 Diffuser Vane First Harmonic Unsteady Lift ( $r_1/r_0 = 1.10$ , $N_v = 30$ ) .....	150
6.50 Diffuser Vane First Harmonic Unsteady Lift ( $r_1/r_0 = 1.15$ , $N_v = 30$ ) .....	151
6.51 Diffuser Vane First Harmonic Unsteady Lift ( $r_1/r_0 = 1.10$ , $N_v = 15$ ) .....	152
6.52 Diffuser Vane First Harmonic Unsteady Lift ( $r_1/r_0 = 1.15$ , $N_v = 15$ ) .....	153
6.53 Detuned Diffuser Vane First Harmonic Unsteady Lift ( $r_1/r_0 = 1.10$ , $N_v = 30$ ).....	154
6.54 Detuned Diffuser Vane First Harmonic Unsteady Lift ( $r_1/r_0 = 1.10$ , $N_v = 10$ ).....	155
6.55 Diffuser Vane First Harmonic Unsteady Static Pressure ( $r_1/r_0 = 1.10$ , $N_v = 30$ , $\sigma = 60^\circ$ , $\Phi = 0.30$ ) .....	156
6.56 Diffuser Vane First Harmonic Unsteady Static Pressure ( $r_1/r_0 = 1.10$ , $N_v = 30$ , $\sigma = 60^\circ$ , $\Phi = 0.22$ ) .....	157
6.57 Diffuser Vane First Harmonic Unsteady Static Pressure ( $r_1/r_0 = 1.10$ , $N_v = 30$ , $\sigma = 60^\circ$ , $\Phi = 0.17$ ) .....	158
6.58 Diffuser Vane First Harmonic Unsteady Static Pressure (Vane 1, 40% det., $r_1/r_0 = 1.10$ , $N_v = 30$ , $\sigma = 60^\circ$ , $\Phi = 0.22$ ).....	159
6.59 Diffuser Vane First Harmonic Unsteady Static Pressure (Vane 2, 40% det., $r_1/r_0 = 1.10$ , $N_v = 30$ , $\sigma = 60^\circ$ , $\Phi = 0.22$ ).....	160
6.60 Diffuser Vane First Harmonic Unsteady Static Pressure ( $r_1/r_0 = 1.10$ , $N_v = 15$ , $\sigma = 60^\circ$ , $\Phi = 0.30$ ) .....	161
6.61 Diffuser Vane First Harmonic Unsteady Static Pressure ( $r_1/r_0 = 1.10$ , $N_v = 15$ , $\sigma = 60^\circ$ , $\Phi = 0.22$ ) .....	162
6.62 Diffuser Vane First Harmonic Unsteady Static Pressure ( $r_1/r_0 = 1.15$ , $N_v = 15$ , $\sigma = 60^\circ$ , $\Phi = 0.30$ ) .....	163
6.63 Diffuser Vane First Harmonic Unsteady Static Pressure ( $r_1/r_0 = 1.15$ , $N_v = 15$ , $\sigma = 60^\circ$ , $\Phi = 0.22$ ) .....	164
6.64 Diffuser Vane First Harmonic Unsteady Static Pressure ( $r_1/r_0 = 1.10$ , $N_v = 10$ , $\sigma = 60^\circ$ , $\Phi = 0.30$ ) .....	165
6.65 Diffuser Vane First Harmonic Unsteady Static Pressure ( $r_1/r_0 = 1.10$ , $N_v = 10$ , $\sigma = 60^\circ$ , $\Phi = 0.22$ ) .....	166
6.66 Rotating Stall Unsteady Static Pressure ( $N_v = 0$ , $\Phi = 0.155$ ) .....	167
6.67 Rotating Stall Unsteady Static Pressure ( $r_1/r_0 = 1.10$ , $N_v = 30$ , $\sigma = 60^\circ$ , $\Phi = 0.148$ ).....	168
6.68 Rotating Stall Unsteady Static Pressure ( $r_1/r_0 = 1.15$ , $N_v = 30$ , $\sigma = 50^\circ$ , $\Phi = 0.160$ ).....	169

## LIST OF SYMBOLS

Symbol	Description
$c$	Airfoil Chord
$C_P$	Unsteady Pressure Coefficient
$C_{\Delta P}$	Unsteady Pressure Difference Coefficient
$C_L$	Unsteady Lift Coefficient
$C_M$	Unsteady Moment Coefficient
$\overline{C_P}$	Steady Pressure Coefficient
$\overline{C_{\Delta P}}$	Steady Pressure Difference Coefficient
$\overline{C_L}$	Steady Lift Coefficient
$h$	Translation Deflection
$\bar{i}$	Steady Flow Incidence
$k$	Reduced Frequency, $k=\omega c/U$ or $\omega r_o/U$
$N_b$	Number of Impeller Blades
$N_v$	Number of Diffuser Vanes
$p$	Pressure
$P$	Steady Pressure
$r$	Radius
$r$	Nondimensional Radius, $r/r_o$ or $r/r_1'$
$r_o$	Impeller Exit Radius
$r_1$	Diffuser Vane Leading Edge Radius
$r_1'$	Radial Diffuser Inlet Radius
$r_2$	Radial Vaned Diffuser Reference Radius
$s$	Airfoil Circumferential Spacing
$t$	Nondimensional Time, $t/(r_o/U_o)$
$u$	Streamwise Velocity
$u$	Unsteady Streamwise Axial Velocity
$U$	Steady Velocity

Symbol	Description
$U_r$	Steady Radial Velocity
$U_\theta$	Steady Tangential Velocity
$U_w$	Wheel Speed
$v$	Transverse Velocity
$v_n$	Unsteady Transverse Velocity
$v_r$	Unsteady Radial Velocity
$v_\theta$	Unsteady Tangential Velocity
$w$	Complex Potential
$W$	Rotating Reference Frame Steady Velocity
$x$	Distance Along Blade Chord
$z$	Radial Cascade Complex Coordinate
$\alpha_L$	Logarithmic Spiral Angle
$\alpha_o$	Impeller Exit Absolute Flow Angle
$\alpha$	Pitching Deflection
$\beta_o$	Impeller Exit Relative Flow Angle
$\beta_w$	Wake Velocity Vector Phase Angle
$\gamma$	LDV Half Angle
$\zeta$	Axial Flow Cascade Complex Coordinate
$\eta$	Axial Flow Cascade Axial Coordinate
$\theta$	Scaled Tangential Coordinate, $\theta/(U/U_w)$
$\xi$	Axial Flow Cascade Tangential Coordinate
$\rho$	Density
$\sigma$	Diffuser Vane Stagger Angle
$\phi_b$	Interblade Phase Angle
$\phi_w$	Wake Velocity Component Phase Angle
$\Phi$	Velocity Potential
$\Psi$	Stream Function
$\Psi$	Pressure Rise Coefficient
$\omega$	Frequency
$\Omega$	Unsteady Vorticity
$\Omega_b$	Blade Passing Frequency
$\Omega_r$	Rotational Frequency
$\Omega_s$	Steady Vorticity

## CHAPTER 1

### INTRODUCTION

Centrifugal compressors have found wide use in industrial, aerospace and ground based transportation applications. Important systems include small gas turbine engine compressors, piston engine turbochargers, compressed air and refrigeration systems, and turbopumps for liquid fueled rocket engines. The earliest jet engines employed centrifugal compressors. However, axial compressors became favored due to their smaller cross sectional area which facilitated use in high-thrust jet engines. Centrifugal compressors do have several distinct advantages, including their relative ease of manufacture and much higher pressure rise per stage as compared with axial machines. These advantages have begun to be exploited in the past two decades, prompting the need for research to improve centrifugal compressor performance.

A centrifugal compressor is a rotating machine which increases the stagnation enthalpy of a flowing fluid, with the throughflow mainly in a radial direction. It is this radial throughflow which allows a centrifugal compressor to attain a very high pressure rise per stage. The impeller and radial diffuser comprise a centrifugal compressor stage, with inlet guide vanes sometimes utilized to impart prewhirl to the incoming flow. The radial diffuser is generally vaneless. However, many modern compressor stages employ vaned diffusers to increase efficiency.

Two typical centrifugal compressor stages are depicted in Figure 1.1. The fluid enters the impeller axially at the eye or inlet. Ideally, the forward portion of the impeller, termed the inducer, allows the flow to enter the impeller smoothly and directs the flow radially. The fluid static pressure is continuously increased throughout the radial portion of the impeller due to centripetal acceleration. A static pressure gradient exists across the impeller channel resulting from the coriolis acceleration of the fluid. This gradient produces a pressure difference across each impeller blade which exerts torque on the impeller. The flow leaving the impeller attains a greater velocity than the inlet flow due to the added wheel speed. The radial diffuser is designed to receive this flow and to attain the largest possible pressure recovery.

The actual flow through a centrifugal compressor stage is highly complex, as depicted schematically in Figure 1.2 (Wood, et al., 1983). The flow through the impeller passages is complicated by several interacting phenomena. The static pressure and velocity are circumferentially nonuniform at the impeller exit due to the potential effects of flow through the impeller passage and viscous effects manifested in trailing edge wakes and flow separation. This circumferentially nonuniform flow is unsteady to the stationary diffuser, which is expected to attain the largest possible pressure recovery. The potential disturbance of the diffuser vanes is also felt upstream, imposing an unsteady backpressure on the rotating impeller. In addition to these periodic disturbances with the rotational or blade passing frequency, instabilities can develop in centrifugal compression systems in the form of rotating stall and surge. All of these unsteady interactions and disturbances can significantly impact the compressor performance and produce aerodynamically induced stress and vibration which may result in structural failure.

It has therefore become necessary to attain a greater understanding of the unsteady flow phenomena in centrifugal compressors. Since many modern centrifugal compressors employ vaned diffusers, experimental investigations in conjunction with analyses are needed to produce the most efficient designs and minimize undesirable unsteady flow phenomena.

### 1.1 Operation of Centrifugal Impellers

The flow enters the forward portion of the impeller, which is termed the inducer. It is designed to allow the flow to enter the impeller smoothly and to turn the flow to a radial direction with minimal loss. The inducer inlet blades are typically given some angle with respect to axial to match the relative angle of the inlet flow over a certain range of operation. Most of the energy transfer to the air occurs in the radial portion of the impeller. The blades at the impeller exit typically are radially oriented or given some angle from radial opposite the impeller rotation. The motivation for radially oriented blades includes ease of manufacture and reduced stress in high speed machines. Backswept blades are used to stabilize the impeller flow and reduce the velocity into the diffuser which aids in pressure recovery. This lowers the power output of the stage but can increase the efficiency. Forward swept blades are rarely used.

In a centrifugal impeller, as previously mentioned, the flow in the impeller channel will be nonuniform, producing a temporal variation in both the pressure and velocity at the impeller exit. This causes the flow in the radial diffuser to be unsteady. In fact, Dean

(1959) shows that it is impossible for a turbomachine to work on a flowing fluid by other than viscous forces without time variation in the flow. It is therefore impossible for a turbomachine to operate without unsteady flow phenomena, with these phenomena generally increasing in magnitude as the work output of the machine increases.

### 1.2 Basic Theory of Radial Diffusers

The radial diffuser is a critical component in the centrifugal compressor stage. Its purpose is to reduce the velocity from the impeller exit and to increase the pressure as efficiently as possible. Vaned diffusers are typically employed to increase efficiency.

It is helpful both in the study of vaneless and vaned diffusers to develop a basic analysis for flow in a vaneless diffuser. The continuity equation and the radial and angular momentum equations for axisymmetric incompressible frictionless flow in a radial parallel wall diffuser are

$$\frac{1}{r} \frac{\partial}{\partial r} (\rho_0 r U_r) = 0 \quad 1.10$$

$$U_r \frac{\partial U_r}{\partial r} - \frac{U_\theta^2}{r} = - \frac{1}{\rho_0} \frac{\partial p}{\partial r} \quad 1.11$$

and

$$U_r \frac{\partial U_\theta}{\partial r} + \frac{U_r U_\theta}{r} = 0 \quad 1.12$$

where the flow is assumed to be steady for the simplified analysis and the tangential pressure gradient is assumed to be zero.

Integrating Equations 1.10 and 1.12 yields

$$r U_r = r_1 U_{r1} \quad 1.13$$

$$r U_\theta = r_1 U_{\theta 1} \quad 1.14$$

where the subscript 1 refers to the diffuser inlet.

Combining Equations 1.11, 1.13 and 1.14 and integrating yields



$$\frac{P - P_1}{1/2 \rho_0 U_1^2} = (1 - (\frac{r_1}{r})^2) \quad 1.15$$

where  $U_1^2 = U_{\theta 1}^2 + U_{r1}^2$ . Thus, the pressure decreases with the inverse of the radius squared.

In an incompressible flow, both the radial and the tangential velocity components decrease as  $1/r$ . Thus, from continuity and conservation of angular momentum, both velocity components are reduced in the vaneless diffuser due to the increase in radius.

It is useful in the understanding of diffuser flows to obtain the equation for a streamline. The equation of a streamline for an incompressible flow is given by

$$\frac{1}{r} \frac{dr}{d\theta} = \frac{U_r}{U_\theta} \quad 1.16$$

Assuming steady, frictionless, axisymmetric flow, Equations 1.13 and 1.14 can be used along with Equation 1.16 yielding

$$\frac{1}{r} \frac{dr}{d\theta} = \frac{U_{r1}}{U_{\theta 1}} \quad 1.17$$

where the subscript 1 again refers to the diffuser inlet.

Integrating Equation 1.17 from diffuser inlet yields

$$\ln \frac{r}{r_1} = (\theta - \theta_1) / \tan \alpha_L \quad 1.18$$

where the angle, measured from the radial direction,  $\alpha_L = \tan^{-1}(U_{\theta 1}/U_{r1})$  and the subscript 1 refers to the diffuser inlet.

Equation 1.18 is the equation of a logarithmic spiral, which forms an angle  $\alpha_L$  with any radial line, where  $\alpha_L$  is termed the logarithmic spiral angle. Thus, the incompressible flow in a parallel wall radial diffuser follows logarithmic spiral streamlines whereas the flow in an axial machine tends to follow a line with a constant angle from axial. This fact must be considered in the analysis and design of radial turbomachine components.

### 1.3 Literature Review

Much attention in the literature has been given to centrifugal impeller and diffuser flowfields. The impeller exit flow, depicted in Figure 1.3, has typically been described as a jet-wake type of flowfield. Because of boundary layer growth and flow separation in the impeller, the exit velocity profile is circumferentially nonuniform. This type of circumferentially nonuniform flow has been discussed by several authors. Dean and Senoo (1960) formulated a mathematical model of this jet-wake impeller flow. They concluded that a reversible work interaction in circumferentially nonuniform flows between the jet and wake causes the velocity deficit to decrease rapidly within a small radial distance from the impeller exit. They also discovered that the unsteady tangential velocity component in the radial diffuser can increase before its eventual decay. Eckardt (1975) performed measurements with high frequency instrumentation in the jet-wake flow of a low pressure ratio centrifugal impeller. He found a significant jet-wake pattern existed and that the radial extension of the nonuniform circumferential velocity profile decayed more slowly than predicted by mathematical models such as the one formulated by Dean and Senoo.

Krain (1987) measured the velocity field within a newly designed impeller using an L2F system. Velocity profile nonuniformities were found within the impeller passages but a relatively uniform velocity profile at the impeller exit which differed significantly from the typical jet wake pattern. Fagan and Fleeter (1989) measured the flowfield in the passages of a mixed-flow, low pressure ratio centrifugal impeller. The traditional jet-wake exit flowfield pattern was observed at the design point and near stall. From these investigations, it appears that although the typical impeller exit flow is nonuniform circumferentially, the actual flow pattern is dependent on the impeller design, with even near uniform profiles possible if separation in the impeller is controlled. The many interacting phenomena in impeller flows are not well understood, however, and it does not seem reasonable to expect either complete elimination of separation or circumferentially nonuniform flows in radial impellers.

Vaned diffusers serve as flow guides and also incorporate turning of the flow so as to reduce the tangential velocity component at a greater rate than in a vaneless diffuser, thus reducing the size of the diffuser. Vaned diffusers have typically been of two configurations: cambered vane diffusers and wedge or channel diffusers. Representative examples of these diffusers are shown in Figure 1.1. The cambered vane diffuser has developed from analogy to airfoil or turning vane cascades. Cambered vane diffusers with logarithmic spiral profiles and little or no flow turning have been found to increase stage

efficiency (Smith, 1970). This is attributed to their ability to inhibit secondary flows and separation. Thus, use of vaned diffusers simply as flow guides can increase performance.

The second major type of vaned diffuser is the wedge or channel diffuser. The purpose of the channel diffuser is to remove the tangential velocity component and to limit the area increase of the diffuser. Channel diffusers are generally designed using some divergence angle obtained from two-dimensional straight diffuser theory. Channel diffusers have been given much attention in the literature and have shown good performance.

Clements and Artt (1986) and Rodgers (1982) investigated the performance of channel type diffusers considering the diffusion capabilities of different geometries. Clements and Artt conclude that the performance of channel diffusers is superior to that of cambered vane diffusers. Bammert, Jansen and Rautenberg (1983) considered both types of diffusers along with a twisted vane diffuser. Their data does not support the conclusion of Clements and Artt, with cambered vane diffuser stages having somewhat higher efficiency. Yoshinaga et al. (1980) investigated the performance of sixteen cambered vane diffusers with moderate to high diffusion ratio. They compared their experimental results with potential flow solutions using conformal mapping and found fair to good correlation with the theory.

The effect of the radius ratio of the vaneless space in vaned radial diffusers has been discussed by several authors. Optimum values given range from 1.1 to 1.15 (Rodgers, 1982; Bammert et al., 1983; Fisher and Inoue, 1981; Inoue and Cumpsty, 1984). It is generally concluded in the literature that vaned diffusers become less effective at larger radius ratios. Therefore, it is desired to position the diffuser vanes as close as possible to the impeller while avoiding large unsteady interactions and reduced performance caused by these interactions.

Very few investigations have considered the unsteady flow phenomena such as the interactions between the impeller and the vaned diffuser or unsteady diffuser vane performance. Fisher and Inoue (1981) made instantaneous measurements in the vaneless space of a low speed compressor stage. However, only time averaged data were compared to steady flow predictions from conformal mapping and Martensen singularity theory (Gostelow, 1984), with good correlation obtained. Although several authors have concluded that the vaned diffuser had little effect on the overall impeller performance, Fisher and Inoue concluded that the vaned diffuser significantly affects the impeller discharge and vaneless space flowfield. Inoue and Cumpsty (1984) investigated impeller discharge flow in vaneless and vaned diffusers. The vaned diffusers employed 10, 20 and 30 blades and were operated at diffuser entrance/impeller tip radius ratios of 1.04, 1.1 and

1.2. They found circumferentially nonuniform velocity profiles in the vaneless diffuser at large radii, but these nonuniformities did not propagate very far into the vaned diffuser. Arndt et al. (1988) investigated the interaction between impeller blade and diffuser vanes in a diffuser pump. Their measurements were made at various flow rates, impeller speeds, and diffuser vane leading edge/impeller exit radius ratios. They found increasing the radius ratio strongly decreased the unsteady vane loading.

In the above unsteady diffuser flow investigations, only Arndt measured the unsteady vane loading, with no comparison with theory. In fact, no general theory for unsteady vane loading due to impeller-diffuser interactions is known. Therefore, it is important to extend the experimental data base of unsteady impeller-diffuser interactions, with detailed flowfield measurements, as well as developing a theory to predict these interactions.

Greitzer (1981) discussed the types of instabilities that arise in pumping and compression systems. He showed analytically that system dynamic instabilities in the form of surge can develop in compression systems when the slope of the pressure characteristic becomes positive. He also considered rotating stall in centrifugal compressors and showed that rotating stall inception can occur before surge, although the mechanisms for rotating stall inception are not well understood. Van den Braembussche (1984) considered rotating stall and surge in centrifugal compressors. He believes that rotating stall occurs as a self-sustaining oscillation in which the inviscid flow field reacts to a viscous perturbation, typically stalling of the impeller or vaned diffuser.

Very little of the literature concerning rotating stall and surge in centrifugal compressors considers diffuser geometry. It is believed that diffuser geometry can have an important effect on this behavior. Therefore, it is desirable to investigate the effect of diffuser geometry on surge and rotating stall.

Although the literature concerning centrifugal compressor diffusers is quite extensive, the emphasis has been on steady flow performance, with very few comparisons between predictions and data. Examples of these comparisons include Yoshinaga (1980), and Fisher and Inoue (1981). Faulders (1956) discusses the application of potential flow theory and conformal mapping to existing steady cascade data to predict diffuser performance. Smith (1970) calls for a diffuser technology based on conformal transformation without regard to channel or cambered vane types. That a coherent technology and method of presentation of data is lacking is evident from the various and sometimes contradictory conclusions drawn by different authors. Although Faulders paper was published in 1956, very few authors have attempted to correlate data using his work.

Much of the variation in the published data is probably due to the dependence of the data on the particular research facility.

Bryan and Fleeter (1987) experimentally investigated the effects of inlet prewhirl on the impeller flowfield and overall performance of the Purdue Research Centrifugal Compressor. This is a large scale, low speed machine which was originally designed and operated by Vavra (1955). The facility was established at Purdue by Bryan and Fleeter and is used in the current investigation. It was shown that inlet prewhirl significantly affected the impeller flow, especially in the inducer region and that performance could be optimized by varying inlet prewhirl. It was also discovered that very little effect of the prewhirl propagated into the impeller discharge/diffuser region where the flowfield was almost solely determined by flow rate.

Thus in summary, considerable effort has been made to determine the performance of centrifugal compressor stages with emphasis on the radial diffuser. Investigations of unsteady phenomena and the effect of diffuser geometry on such phenomena, however, have been given relatively little attention, with few or no theoretical predictions. Therefore, it is imperative that these unsteady phenomena be investigated and the important machine parameters affecting them be determined.

#### 1.4 Research Objective and Technical Approach

The overall objective of this investigation is to quantify the dependence of significant steady and unsteady flow phenomena inherent in centrifugal compressors on vaned diffuser geometry, with emphasis on the radial vaned diffuser unsteady aerodynamics generated by the impeller-diffuser interaction. Specific objectives include:

- Determination of Centrifugal Compressor Performance
- Impeller and Diffuser Vane Steady Loading Measurement
- Diffuser Unsteady Flowfield Measurement
- Diffuser Vane Unsteady Loading Measurement
- Determination of Surge and Rotating Stall Occurrence and Characteristics
- Development of Theory to Determine Radial Vaneless Diffuser Wake Behavior and Unsteady Diffuser Vane Loading

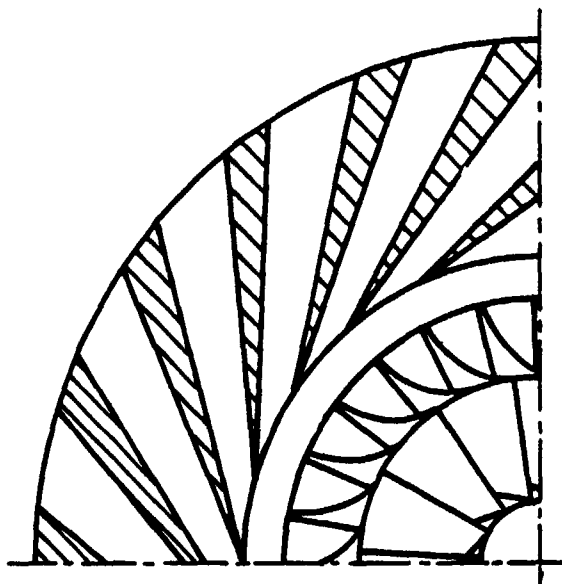
The above experimental objectives were accomplished by performing a series of experiments in the Purdue Centrifugal Compressor Facility. Steady flowfield measurements were made using pressure probes throughout the machine to determine

performance. Steady surface static pressure measurements were made on the rotating impeller and vaned diffuser to determine loading. The time-variant flowfield in the radial diffuser were measured using an LDV system. High response pressure transducers were utilized to measure the unsteady diffuser vane surface static pressure as well as static pressure variations at the impeller exit for determination of surge and rotating stall.

The above experiments were performed for various diffuser geometries and flow rates. In particular, the number of diffuser vanes, the diffuser vane stagger, the diffuser vane leading edge/impeller exit radius ratio and the circumferential spacing were varied independently along with the mass flow rate through the machine. The compressor performance and detailed flowfield were determined at each machine operating condition.

Analyses were developed using linearized theory to predict the unsteady wake behavior in the radial vaneless diffuser. This was incorporated into existing unsteady cascade theory using conformal mapping to predict the unsteady loading on the vaned diffuser due to wakes shed from the rotating impeller.

WEDGE OR  
CHANNEL  
DIFFUSER



CAMBERED VANE  
DIFFUSER

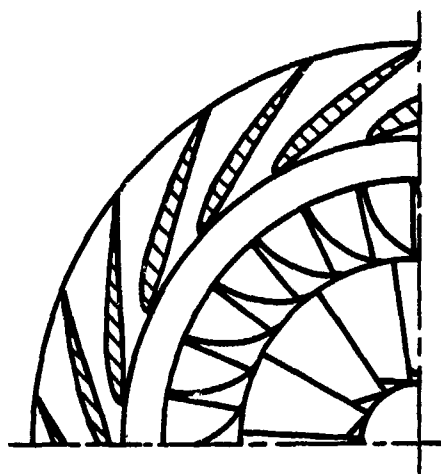


Figure 1.1 Typical Centrifugal Compressor Stages

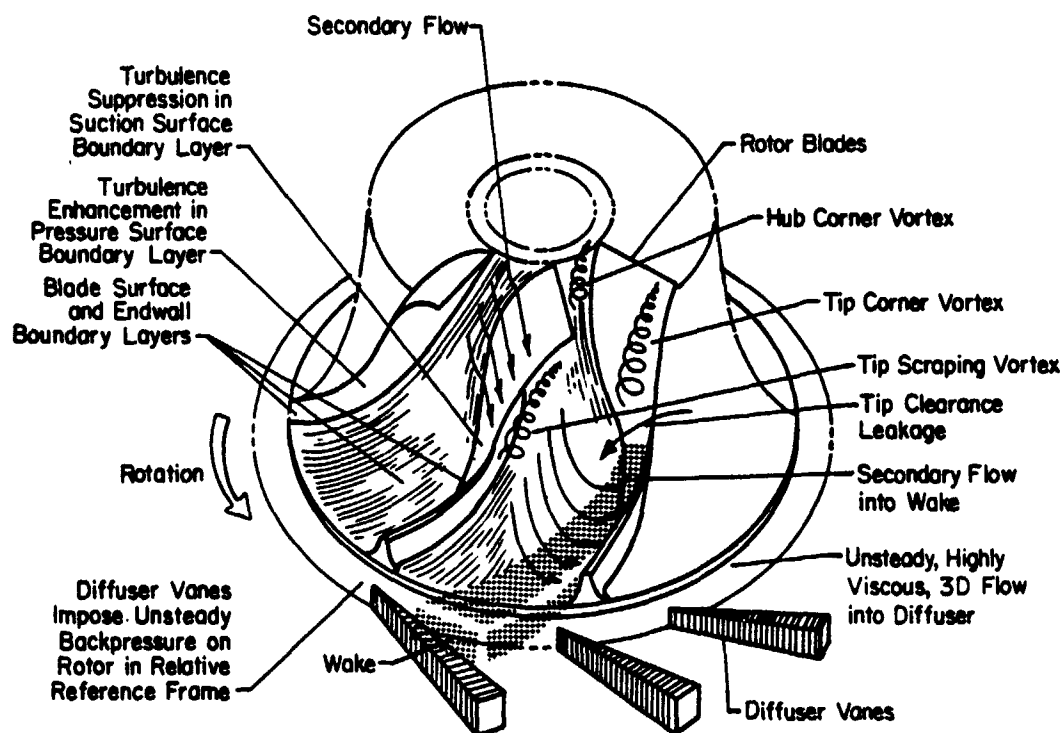


Figure 1.2 Centrifugal Compressor Flow Phenomena



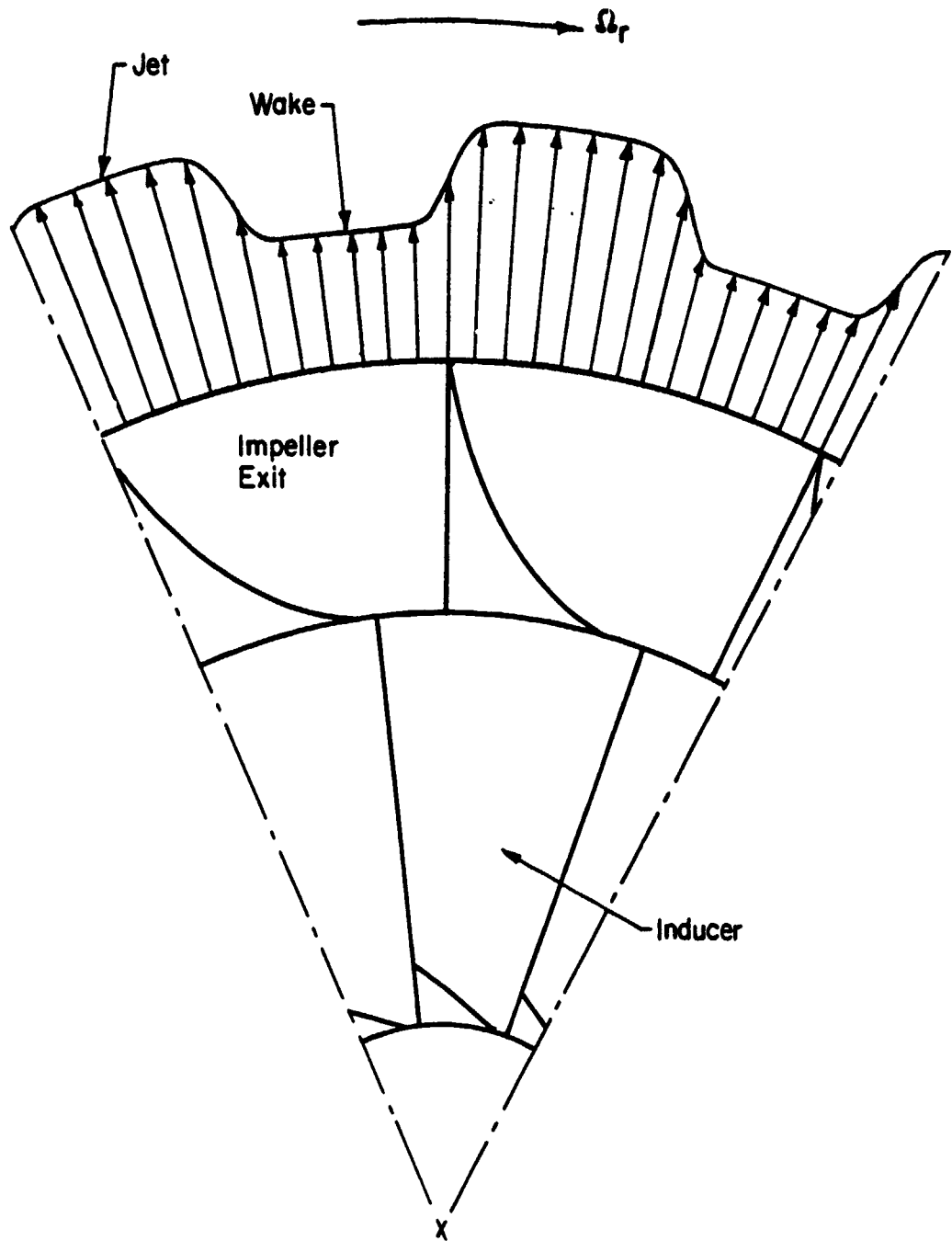


Figure 1.3 Jet Wake Impeller Flow

## CHAPTER 2

### THE PURDUE RESEARCH CENTRIFUGAL COMPRESSOR

#### 2.1 General

The Purdue Research Centrifugal Compressor experimentally models the fundamental aerodynamic phenomena inherent in centrifugal compressor stages including the circumferentially nonuniform impeller exit flow, diffuser vane incidence and radius ratio, and unsteady impeller diffuser interactions. The compressor is belt driven using a jackshaft and pulley arrangement by a 29.8 kW (40 hp) induction motor and is operated at 1790 rpm. The facility is shown in Figure 2.1 and depicted schematically in Figure 2.2.

The general operation of the machine can be described by considering the flow path shown in Figure 2.3. Air is drawn into the machine through the bellmouth inlet section which converges to an axial direction at the impeller eye. The air enters the mixed flow impeller which changes the axial inlet flow to a nearly radial flow at the outlet and also imparts a tangential component of velocity to the air. The center of the rotor is hollow, permitting the installation of instrumentation to transmit pressure data from the surfaces of the rotating blades to the data acquisition and analysis system located outside of the machine in the stationary frame of reference.

On leaving the impeller, the air enters the radial diffuser whose walls curve smoothly to a parallel configuration. The air then passes through a row of stationary diffuser vanes which are located at the upstream portion of the parallel wall diffuser and is discharged into a large annular plenum chamber. From this plenum, the air passes into a straight discharge pipe which contains a sharp edged orifice for flow rate measurement and a throttle valve to regulate the flow rate.

#### 2.2 Impeller and Drive Assembly

The impeller and drive assembly are shown in Figure 2.4. The impeller consists of 23 aluminum blades cast integrally with the hub. The tip is covered with a plexiglass shroud for aerodynamic purposes and optical access. A mixed-flow impeller configuration is used

with a deloaded blade profile. In a mixed-flow impeller, the flow channels never turn to a completely radial direction. Therefore, the flow maintains an appreciable component of velocity in the axial direction during its entire passage through the impeller. With an impeller of this type, the blade need not lie in a purely meridional plane, but may follow a spiral path along the hub from inlet to exit. The use of a spiral type of flow path introduces a great deal of flexibility into the aerodynamic design and permits use of a deloaded blade design. In a general way, this is an impeller blade on which the pressure side is concave over the first part of its length and essentially convex over the last part. This reversal of curvature tends to reduce the aerodynamic loading near the blade exit and increase the loading over the central portion of the blade.

The steady pressure distributions in the impeller blade passages are measured with static pressure taps on the blade surfaces. There are 32 such taps, with two redundant pairs, located along three streamlines at five normal locations. These are shown in Figure 2.5. The steady pressures on the impeller are measured using a rotating pressure multiplexer.

The shaft and motor are track mounted on a steel base. The entire impeller-drive assembly can be retracted to perform necessary service. The impeller assembly utilizes four cam mounted wheels which are lowered onto the track upon retracting the impeller. When the impeller is in place, the wheels are raised allowing the base to rest in a v-groove in the track. The base and impeller drive assembly are then bolted to the track. The impeller is fixed in the stationary passages by a metal seal which bolts onto the rear passage of the diffuser section downstream of the impeller. The inner part of this seal contains the rear labyrinth seal.

### 2.3 Inlet

The facility inlet allows air to flow smoothly from the atmosphere into the impeller. The inlet tip wall consists of a plexiglass bellmouth of identical profile to the impeller blade tip. The inlet hub or centerbody consists of a conical section smoothly tapered to a cylinder with a diameter equal to that of the impeller hub. The inlet has been developed using wall tufts to detect separation points or flow nonuniformities. Pressure probe data show the flow to be very uniform at the impeller face.

## 2.4 Diffuser

The radial diffuser consists of a smoothly curved vaneless space followed by a parallel wall vaned radial diffuser. The diffuser vanes have a chord length of 16.5 cm (6.5 in.), with a NACA 4312 airfoil profile, Figure 2.6. The wall profile, Figure 2.7, facilitates the close spacing of the diffuser vane leading edge and impeller trailing edge. This profile was obtained by fitting a cubic spline from the impeller trailing edge to the parallel wall radial diffuser. The performance of the diffuser flow path was evaluated by computing the axisymmetric potential flow and applying the boundary layer code CBTSL with a Mangler transformation, utilizing impeller exit flowfield data obtained by Fagan (1989) as a boundary condition. The flow in the diffuser was smooth and nonseparated over the design operating range, as indicated through flow visualization using wall tufts. The diffuser tip wall contains 30 eccentric blade mounting cams, Figure 2.8, which allow the diffuser vane leading edge radius and stagger angle to be varied and also permit nonuniform circumferential vane spacing.

The diffuser walls are instrumented with a field of static pressure taps as well as static taps along the diffuser vane chord at mid-span. A three head cobra probe is situated at the impeller exit to measure total and static pressure as well as flow angle. Two similar probes are located downstream of the diffuser vane row.

## 2.5 Plenum and Exhaust Piping

An overhead schematic of the complete facility is shown in Figure 2.9. The diffuser section is attached to the plenum into which the flow is discharged. The plenum is toroidal with a square cross section. The inner diameter is 1.69 m (66.4 in.), the outer diameter is 3.15 m (123.9 in.), and the width is 74.2 cm (29.2 in.). The plenum has a circular outlet with a 70.0 cm (24 in.) i.d. The exhaust piping system is attached to the plenum exit. As air leaves the plenum, it enters a 90° elbow with an inner diameter of 70.0 cm (24.0 in.). The elbow is followed by a reducer which reduces the inner diameter to 40.6 cm (16 in.). A straight section of 40.6 cm (16 in.) inner diameter and 18 pipe diameters in length follows the reducer. A flow straightener of 7.6 cm (3 in.) diameter tubing and 55.9 cm (22 in.) length is located 2 pipe diameters downstream of the reducer to remove any swirling or radial nonuniformities in the flow. A sharp edged orifice plate of 30.48 cm (12.0 in.) orifice diameter in conjunction with 1-diameter and 1/2-diameter pressure taps is located at the end of the straight section for mass flow measurement. A straight section 8 pipe diameters in length is located behind the orifice plate and contains a thermocouple 6 pipe

diameters downstream of the orifice. A butterfly type throttle valve, driven by a gear motor, is located at the exit of the 90° elbow to control the compressor flow rate. The motor is actuated through a set of relays under control of the data acquisition system.

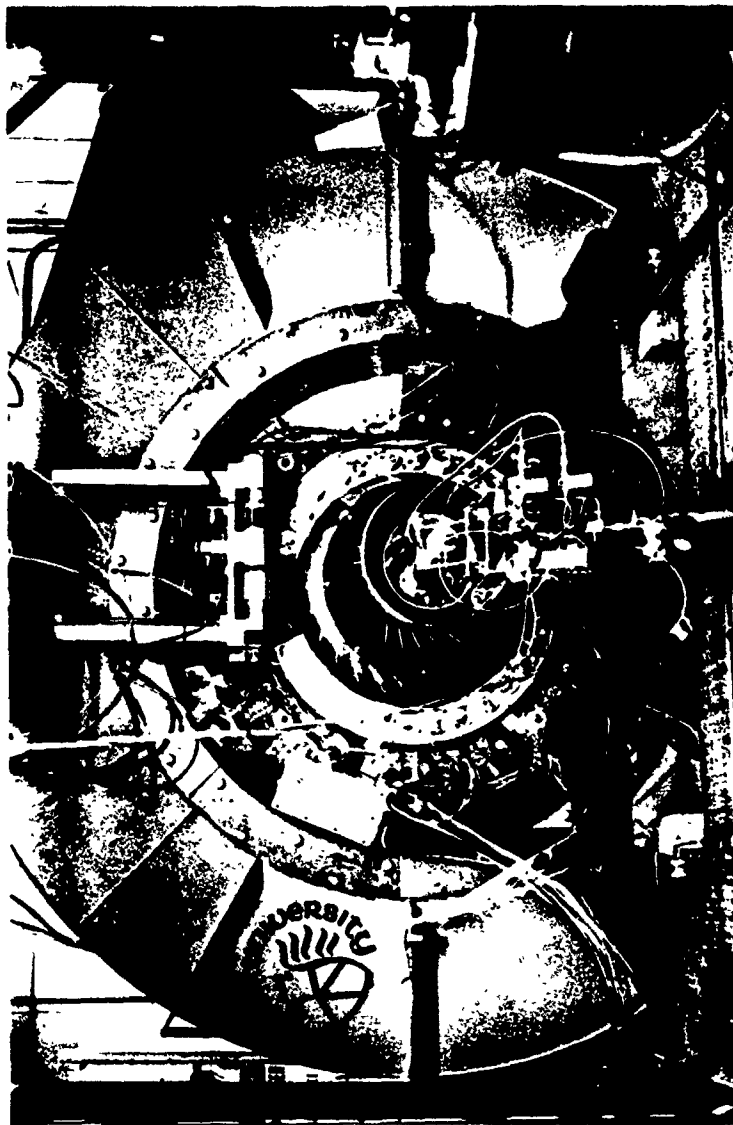


Figure 2.1 Front View of Compressor Test Facility

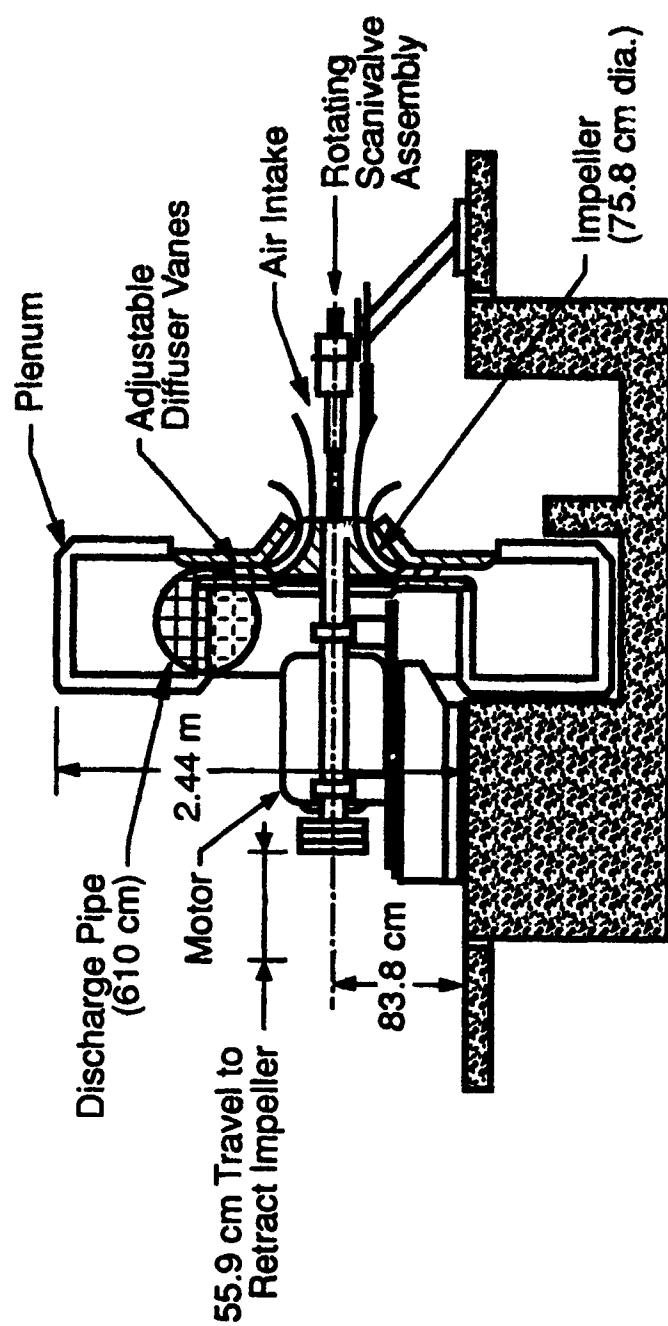


Figure 2.2 Cutaway of Compressor Test Facility

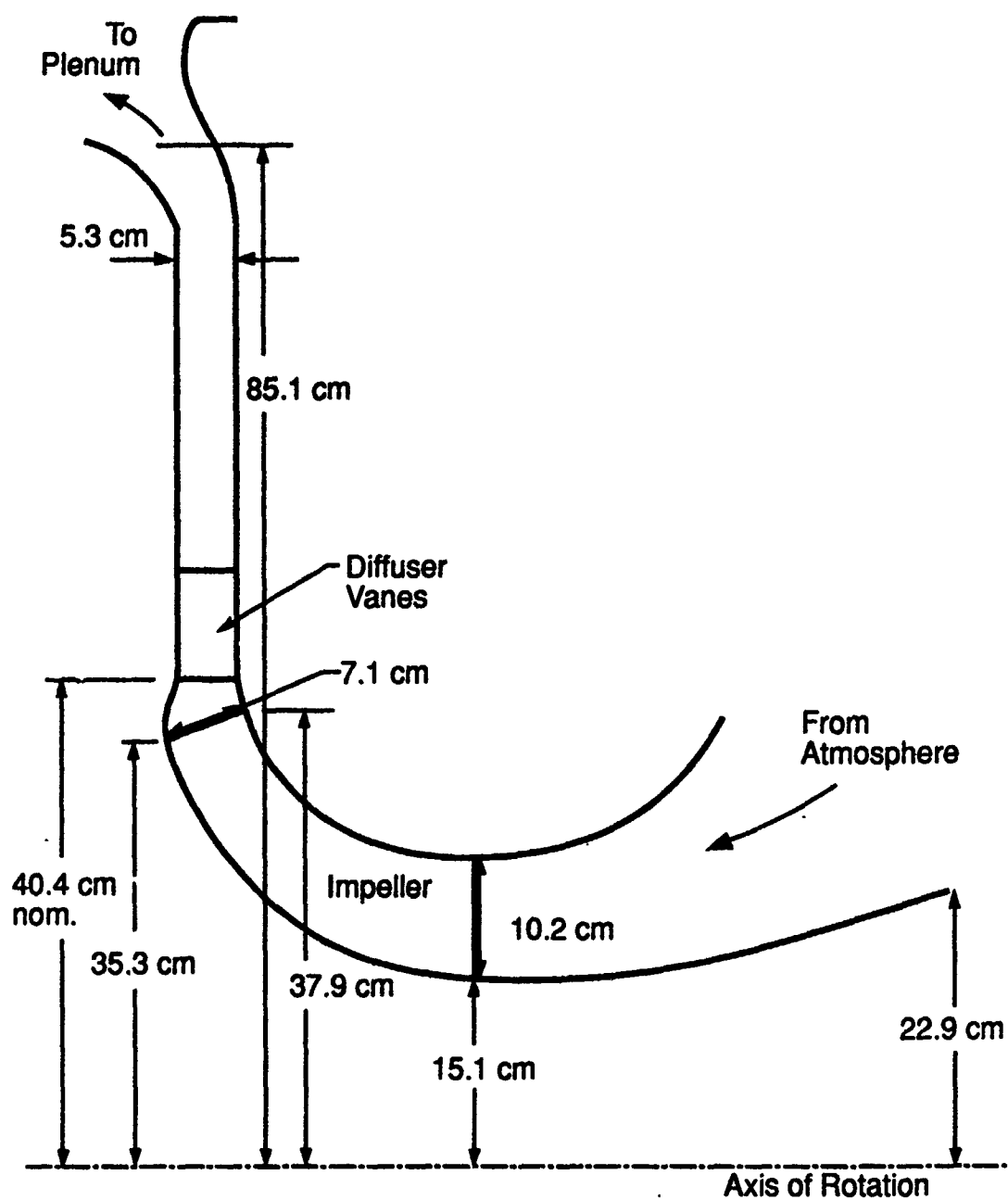


Figure 2.3 Inlet, Impeller, and Diffuser Flow Channel



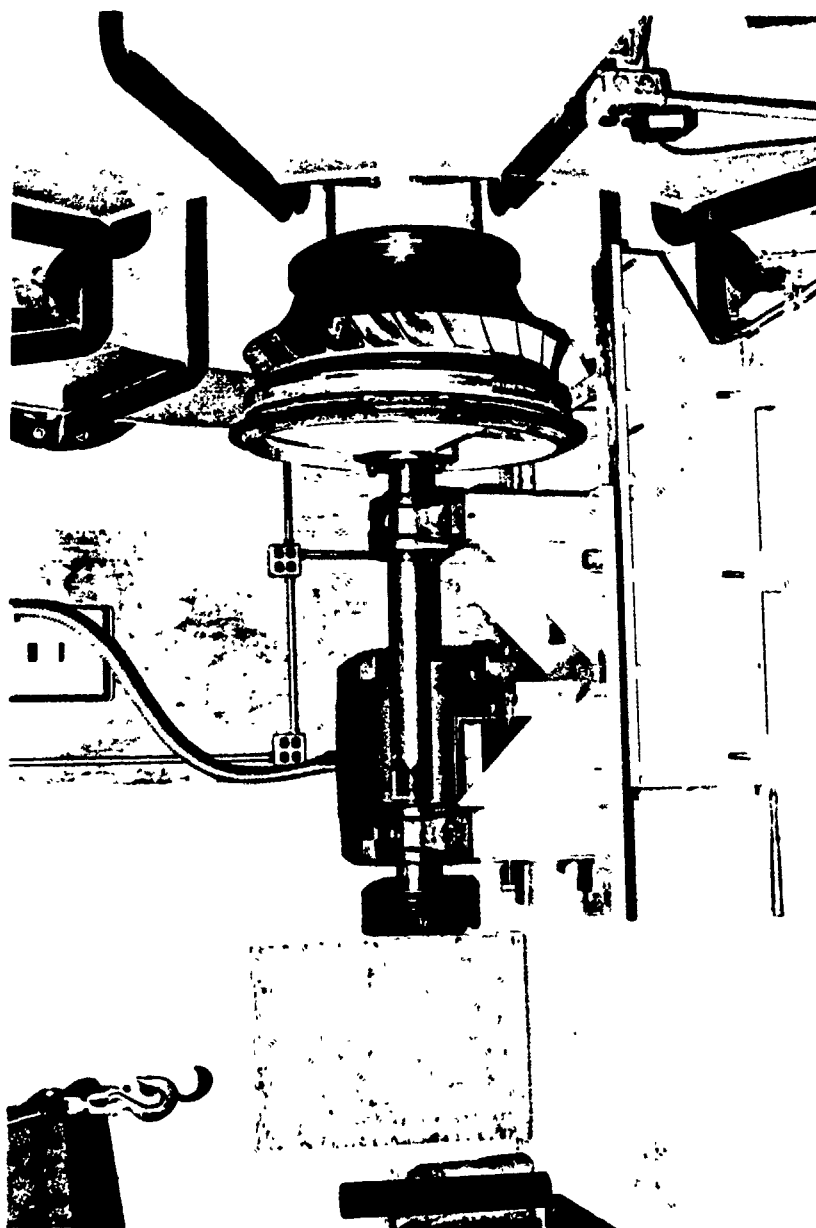


Figure 2.4 Impeller and Drive Assembly

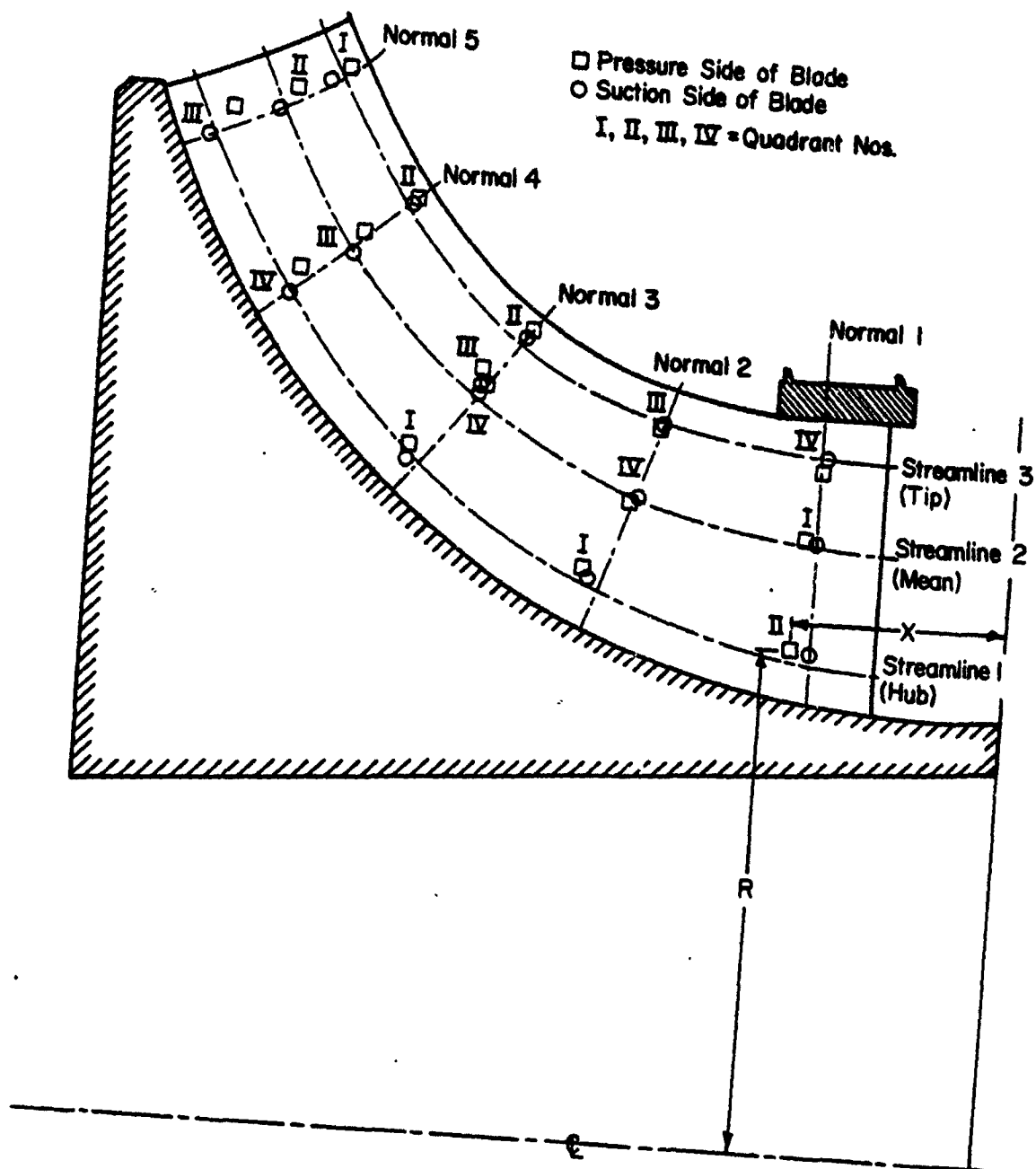
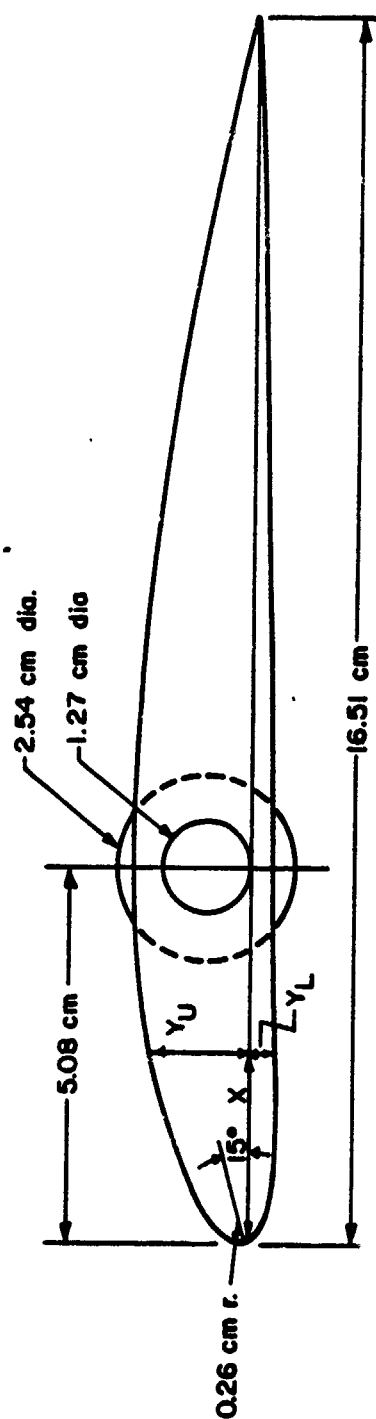


Figure 2.5 Impeller Pressure Tap Locations



NACA 4312 AIRFOIL SECTION

Figure 2.6 Diffuser Vane Profile

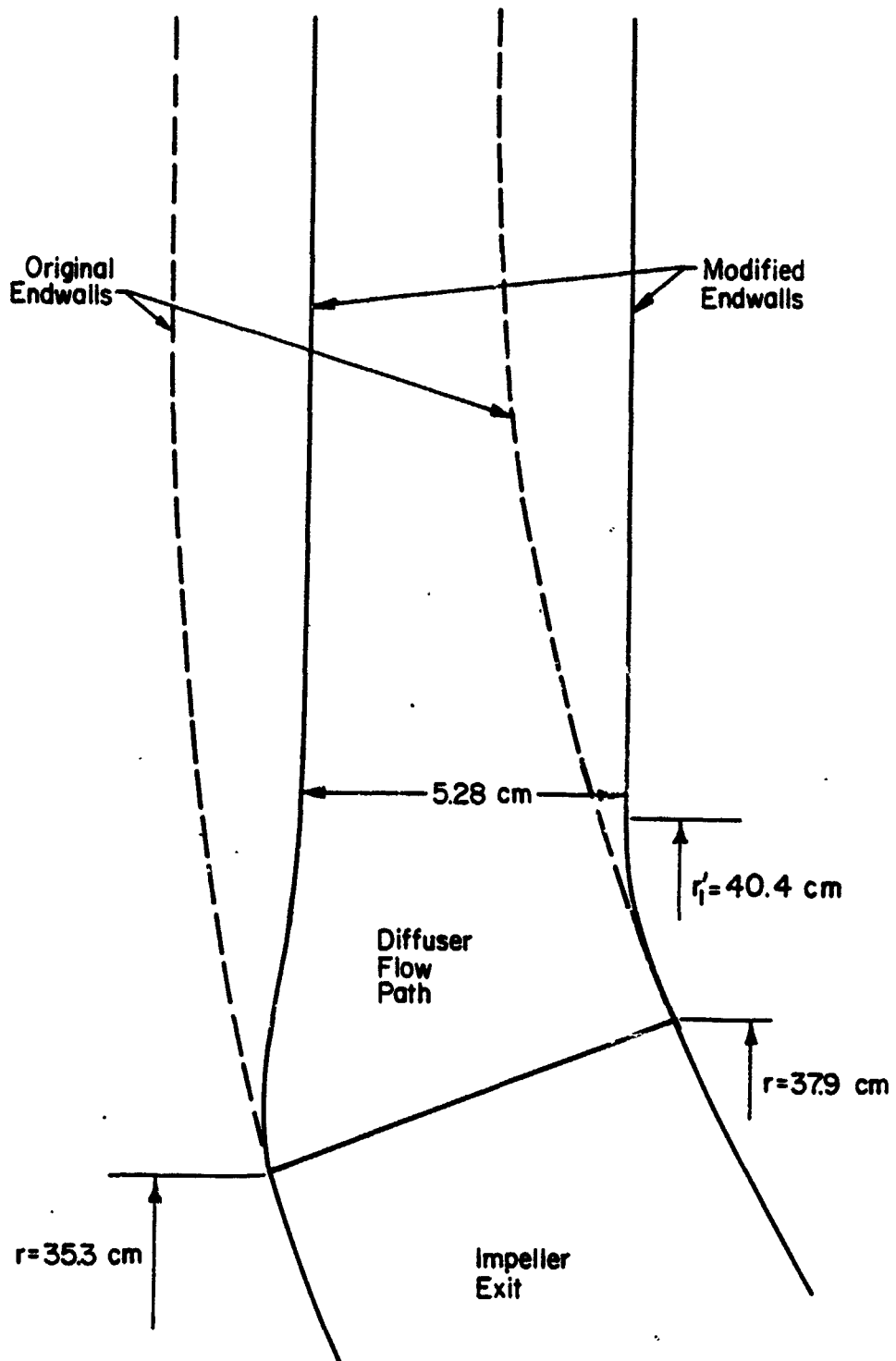


Figure 2.7 Diffuser Wall Profile

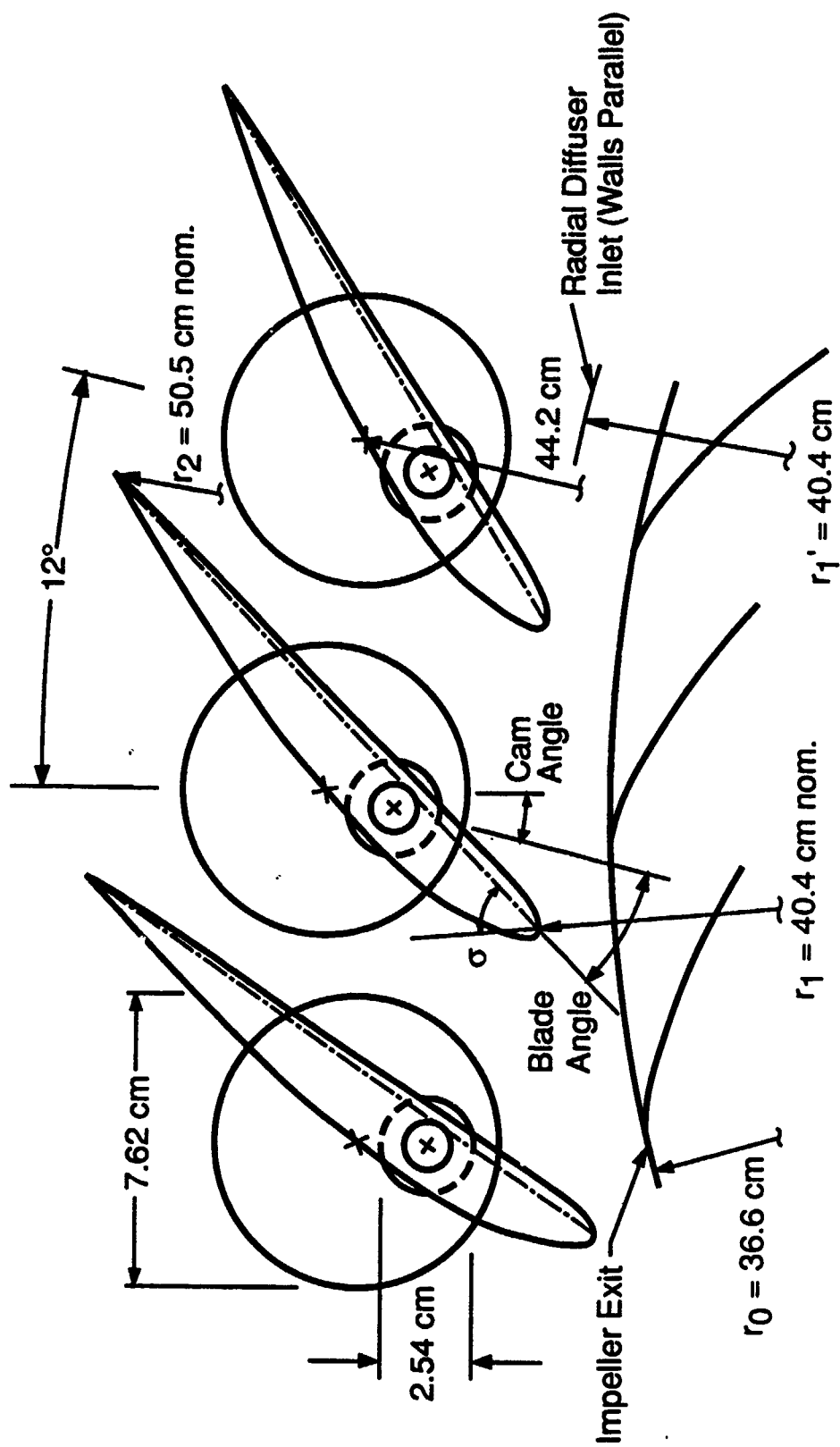


Figure 2.8 Diffuser Vane Mounting Cams

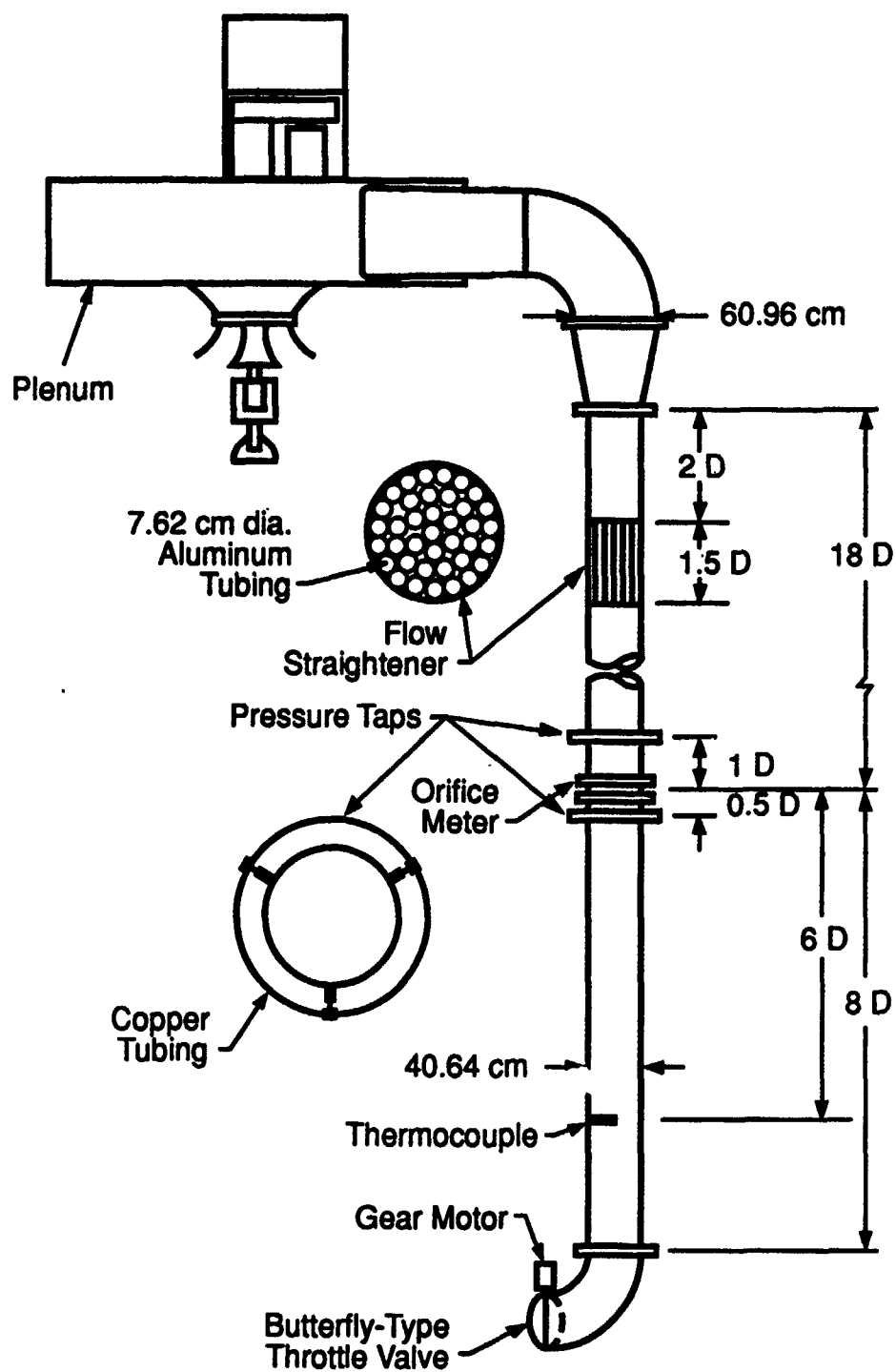


Figure 2.9 Schematic of Centrifugal Compressor Facility

## CHAPTER 3

### DATA ACQUISITION AND ANALYSIS

In the current investigation, the data of fundamental interest are: 1) the compressor steady operating conditions, including the aerodynamic performance of the impeller and diffuser; 2) the detailed impeller blade and diffuser vane steady aerodynamic loading distributions, defined by the surface static pressure distributions; 3) the diffuser mean flow field; 4) the impeller exit-diffuser vane inlet mean and periodic flow field; 5) the unsteady pressure distributions on the diffuser vane surfaces; and 6) the unsteady static pressure at the impeller exit/diffuser entrance.

In this chapter, the instrumentation, data acquisition system and analysis techniques to acquire these data are discussed. Static pressure taps on the impeller blades and diffuser vanes and high response miniature pressure transducers embedded in the diffuser vanes were used to determine the detailed steady and unsteady aerodynamic data. The diffuser steady and time-variant flow field information was acquired with direction sensitive pressure probes and laser Doppler velocimetry (LDV).

#### 3.1 Steady Data Instrumentation

The centrifugal compressor steady data acquisition system is described in detail by Bryan and Fleeter (1987). The time-averaged pressures on the stationary components are measured using 6.9 kPa (1 psi) strain-gage pressure transducers in conjunction with a Scanivalve pressure multiplexing system. The transducers are calibrated using a water manometer with reference pressure and vacuum sources. The transducer output voltage is measured via computer using a Hewlett Packard HP3497 Data Acquisition Unit.

The impeller is instrumented with 32 static pressure taps on the rotating blade surfaces. The static pressures are measured using a rotating Scanivalve pressure multiplexer and strain gage pressure transducer. The rotating Scanivalve multiplexer is capable of measuring 36 static pressures on a rotating impeller. The Scanivalve employs a pneumatic stepping motor and optical encoder for positioning. The pressure from the rotating

multiplexer assembly is exposed to a stationary pressure transducer by way of a rotating o-ring gland seal. The Scanivalve is connected to the impeller through a manifold and flexible coupling. The entire assembly is shown in Figure 3.1.

The rotating Scanivalve transducer is mounted on the compressor axis while the pressure taps are at off-axis radii. The impeller centripetal acceleration imposes a pressure gradient in the tube connecting the pressure tap to the transducer yielding a lower measured pressure than the static tap pressure. A correction for this difference is given in Equation 3.1 (Bryan and Fleeter, 1987)

$$P_{tap} = P_{axis} \exp \left( \frac{\Omega_r^2 r^2}{2RT} \right) \quad 3.1$$

where  $\Omega_r$  and  $r$  are the rotational speed and static pressure tap radius, and  $R$  and  $T$  are the gas constant and temperature, which is assumed to be constant along the tube.

The centrifugal compressor facility is instrumented with pressure probes for measuring total and static pressure as well as flow velocity and direction, Figure 3.2. The design of these probes is described by Bryer and Pankhurst (1971). A five port total pressure rake with one cobra head is located at the impeller inlet. A three head cobra probe is located at the impeller exit and two such probes are located downstream of the diffuser vane row. The inlet probe allows the total pressure and velocity to be measured at five locations across the inlet annulus as well as the flow angle at the mean radius. The three diffuser probes allow measurement of the total pressure, velocity and angle at three positions across the radial diffuser.

The fluid temperature is measured at the impeller inlet, the diffuser exit and downstream of the orifice plate. This is accomplished using type T thermocouples in conjunction with an HP3497 Type T Thermocouple Interface Card with electronic ice point. The thermocouple voltage is measured using the HP3497 voltmeter and the temperature is calculated by a ninth-order polynomial specified by Omega Engineering.

For the above steady data acquisition, the data is sampled 30 times for each pressure and temperature. The mean and standard deviation is calculated and an uncertainty is found using the t-distribution with a 95% confidence interval. The uncertainties in the pressure and temperature measurements are typically less than 1%.



### 3.2 Unsteady Pressure Instrumentation

Time varying pressures on the diffuser vanes are measured using reverse mounted, high natural frequency miniature pressure transducers. Two diffuser vanes are each instrumented with eight Kulite LQ-125-5 G strain gage pressure transducers, the pressure surface of one vane and the suction surface of the other. The transducers have 2.18 mv/kPa (15 mV/psi) sensitivity with a 70 kHz natural frequency. The diameter and thickness are 0.3175 cm and 0.0889 cm (0.125 and 0.035 in.) respectively, with a sensing element diameter of 0.0965 cm (0.038 in.). Two additional vanes are instrumented with static pressure taps at the same chordwise locations as the Kulite transducers for time averaged static pressure measurement. These measurement locations are shown in Figure 3.3.

The transducers are reverse mounted in a cavity-pressure tap arrangement that can be modeled as a Helmholtz resonator. The volume is sufficiently small to insure no phase shift or attenuation within the frequency range of interest, with accurate unsteady pressure transmission at three times the impeller blade pass frequency. The signals from the diffuser vane mounted transducers are preamplified using Analog Devices' AD624 precision instrumentation amplifiers with a gain of 200. The signals are then conditioned using adjustable gain Ithaco Model 455 amplifiers. The blade mounted transducers are statically calibrated to determine sensitivity and to insure linearity. A dynamic calibration (Capece and Fleeter, 1987) showed negligible phase shift and attenuation to 2100 Hz, three times the impeller blade pass frequency.

The unsteady static pressure at the impeller exit/diffuser entrance is measured using PCB Piezotronics 103A piezoelectric transducers. These transducers incorporate self-contained amplifiers and have a sensitivity of 217.5 mv/kPa (1500 mV/psi) with a natural frequency of 13 kHz. The diameter and thickness are 0.9525 cm and 0.5588 cm (0.375 and 0.22 in.) respectively, with a sensing element diameter of 0.254 cm (0.10 in.). Two such transducers are mounted through pressure taps to the diffuser tip wall at 40.39 cm (15.9 in.) radius and 33° angular spacing.

The unsteady pressure measurement signals are recorded using a Gould Biomation 2805 Waveform Digitizer. The Biomations are triggered by an impeller mounted photodetector and simultaneously store 2048 readings on four separate channels with a user adjustable timebase. The raw buffer data is transferred to the computer through a parallel interface. The impeller synchronous pressure traces are phase averaged over 200 ensembles to eliminate random unsteadiness and isolate the periodic pressure fluctuations which are of primary interest.

### 3.3 Laser Doppler Velocimeter

The installation of the Laser Doppler Velocimeter (LDV) optics assembly is described by Fagan (1989). A dual-beam LDV system operating in backscatter mode is utilized, schematically shown in Figure 3.4. In a dual-beam system, the beam emitted by the laser is split into two equal strength beams. The beams symmetrically enter the focusing lens and cross at the lens focal plane, forming the probe volume. The light scattered from small particles passing through the probe volume is collimated by the focusing lens and reflected into the receiving lens by a mirror. This backscattered light is focused on the photodetector by the receiving lens.

A custom assembly has been constructed with bench mounted preliminary optics, Figure 3.5, connected via fiber optic link to the final optics assembly, Figures 3.1 and 3.6. The beam from a 4 watt argon-ion laser operating at 514.4 nm wavelength is turned 180° by two first surface mirrors. A beamsplitter divides the beams into two equal power beams. The beams are acousto-optically frequency shifted 40 MHz and 30 MHz respectively using twin bragg cells, with an effective shift of 10 MHz. Frequency shifting is utilized to minimize fringe bias and eliminate directional ambiguity. The beams are then directed into a translator module for proper positioning into the fiber optic input coupler. The beams are transmitted to the final optics assembly through two polarization preserving fibers.

The final optics assembly contains the fiber optic output coupler, the focusing lens, the probe volume positioning mirror and the receiving optics. The fiber optic output coupler collimates and positions the beams leaving the fiber optic cables. It can be rotated 360° by a stepping motor for beam orientation. The beams emitted from the fiber optic output coupler are directed into the focusing lens. The beams are then reflected into the test section through a plexiglass window by the probe volume positioning mirror, which can be rotated in two planes about the beam axis by stepping motors. The LDV system operates in backscatter mode in which the scattered light is collected through the transmitting mirror and lens. The scattered light is reflected by the positioning mirror and collimated by the focusing lens. It is turned by a second mirror and focused on the photodetector aperture by the receiving optics focusing lens. The entire final optics assembly can be translated along x, y and z axes using stepping motors, yielding a total of six positioning axes.

A 250 mm focal length focusing lens is utilized in the current investigation, yielding probe volume dimensions of  $d_m=126.6 \mu\text{m}$  (0.005 in.),  $h_m=127.2 \mu\text{m}$  (0.005 in.) and  $l_m=1266 \mu\text{m}$  (0.05 in.), with a volume of  $0.0106 \text{ mm}^3$  ( $6.47 \times 10^{-7} \text{ in.}^3$ ). The flow is seeded using a 50/50 mixture of propylene glycol and ethanol with particle diameters

between 0.5 and 1.5  $\mu\text{m}$ . The velocity ratio for these particles at the impeller wheel speed,  $U_w=80\text{m/s}$ , is greater than 98%.

To determine the probe volume position and orientation, an inverse ray tracing algorithm is used which performs an exact ray trace from the probe volume, through the access window to the focusing lens. Prior to data acquisition, the six-axis positioning system is manually positioned on a reference mark with proper orientation. The HP1000 computer initializes the stepper motor positioners, then the axis settings for the desired measurement location and direction are used by the computer to move the six-axis positioner to the desired location.

A TSI Model 1990 Counter Processor is utilized for photodetector signal processing. The Doppler burst frequency is determined from the time required for a seed particle to cross 16 probe volume fringes. Measurements with less than 16 fringe crossings are invalidated. Along with the Doppler burst frequency time measurement, a 1 MHz clock circuit is utilized to latch a timing word at the data ready signal from the counter processor and is reset at each revolution. This timing word is transferred to the computer along with the LDV word and used to determine the impeller angular position at the instant of the measurement. The 23 bladed impeller is divided into 460 circumferential bins, 20 per blade passage, and the data is stored in the bin corresponding to the proper impeller position. Data is collected at a given location until a requisite number of samples are in each bin. In this scheme, the time varying velocity signal around the impeller circumference can be determined.

The particle velocity can be determined from Equation 3.2 (Fagan and Fleeter, 1989), which is an expression for the photodetector output frequency,  $\omega$ . The first term on the right hand side of Equation 3.2 is the frequency difference of the two illuminating beams, which have been frequency shifted in the current investigation. The second term is proportional to the particle velocity,  $u$ , and is a function of the beam half angle,  $\gamma$ , which is determined by the ray tracing algorithm using the focusing lens focal length, and the beam wavelength,  $\lambda$ , which is known.

$$\omega = (\omega_{01} - \omega_{02}) + \frac{2 \sin \gamma}{\lambda} u \quad 3.2$$

The particle velocity measurement is independent of the photodetector position.

Velocity bias can occur in LDV systems since a measurement can only be made when a particle crosses the probe volume. The occurrence of a measurement is related to its

instantaneous velocity, since more particles will cross the probe volume in a given time increment at greater velocities. Roesler, Stevenson and Thompson (1980) discovered that constant frequency (equal time) sampling at lower frequency than the data realization rate eliminates the correlation between instantaneous velocity and sampling rate. Since the data in the current investigation are stored in bins according to impeller position, the data in each bin is effectively equal time sampled and velocity bias is eliminated.

### 3.4 Compressor Performance Analysis

The compressor performance is determined from the steady pressure and temperature data and the mass flow rate measured from the orifice plate static pressure taps. The total and static pressures as well as the flow velocities at the impeller inlet, impeller exit, and diffuser exit are determined from the pressure probe data. If the density changes through the machine are small (< 5%), which is a good approximation in the current investigation, the machine performance can be expressed as the pressure rise coefficient,  $\Psi$ , and the efficiency,  $\eta$ , as a function of the flow coefficient,  $\Phi$  (Dixon, 1978).

The pressure rise coefficients for the impeller and the impeller/diffuser stage are defined in Equation 3.3

$$\Psi_i = \frac{P_{o1} - P_{oi}}{1/2\rho U_w^2} \quad 3.3a$$

$$\Psi_s = \frac{P_{o2} - P_{oi}}{1/2\rho U_w^2} \quad 3.3b$$

where  $P_{oi}$ ,  $P_{o1}$ , and  $P_{o2}$  are the total pressures at the impeller inlet, impeller exit and diffuser exit respectively, and  $\rho$  and  $U_w$  are the density and wheel speed at the mean impeller exit radius.

The efficiencies are defined as the ratio of the useful energy imparted to the fluid to the work done by the machine, Equation 3.4.

$$\eta_i = \frac{(P_{o1} - P_{oi})/\rho}{U_w U_{\theta 1} - U_{wi} U_{\theta i}} \quad 3.4a$$

$$\eta_s = \frac{(P_{o2} - P_{oi})/\rho}{U_w U_{\theta 1} - U_{wi} U_{\theta i}} \quad 3.4b$$

where  $U_{\theta i}$  and  $U_{\theta 1}$  are the absolute tangential velocities at the impeller inlet and impeller exit and  $U_{wi}$  is the wheel speed at the impeller inlet. The flow coefficient is defined in Equation 3.5,

$$\Phi = \frac{U_{r0}}{U_w} \quad 3.5$$

where  $U_{r0}$  is the absolute radial velocity at the impeller exit.

The pressure rise coefficients and efficiencies are measured for the impeller and the impeller/diffuser stage in a vaneless configuration. For vaned diffuser configurations, only the stage performance is determined due to interference effects on the impeller exit probe by the diffuser vanes. The denominator of Equation 3.4 is determined for all cases from the vaneless data since the vaned diffuser had little effect on the impeller loading.

### 3.5 Impeller and Vaned Diffuser Steady Loading Analysis

The static pressure distributions on the rotating impeller blades and the diffuser vanes were measured. A pressure and pressure difference coefficient for the impeller are defined in Equations 3.6 and 3.7.

$$\overline{C_p} = \frac{P}{1/2\rho U_w^2} \quad 3.6$$

$$\overline{C_{\Delta P}} = \frac{P_{pres} - P_{suct}}{1/2\rho U_w^2} \quad 3.7$$

This steady pressure coefficients are presented as a function of the nondimensional radius along the blade,  $r/r_0$ , where  $r_0$  is the impeller exit radius.

The pressure coefficient and the pressure difference coefficient for the diffuser vanes is given in Equations 3.8 and 3.9.

$$\overline{C_p} = \frac{P}{1/2\rho U_1^2} \quad 3.8$$

$$\overline{C_{\Delta P}} = \frac{P_L - P_U}{1/2 \rho U_1^2} \quad 3.9$$

where  $U_1$  is the steady absolute velocity at the diffuser entrance.

The pressure coefficients are presented as a function of the nondimensional distance along the blade chord,  $x/c$ . The steady lift coefficient is

$$\overline{C_L} = \int_0^1 \overline{C_{\Delta P}} dx/c \quad 3.10$$

where  $c$  is the vane chord.

The diffuser vane mean incidence angle is,  $\bar{i} = \sigma - \alpha_1$ , where  $\sigma$  is the diffuser vane row stagger and  $\alpha_1$  is the vane leading edge absolute flow angle.

The uncertainties can be calculated for the performance and loading parameters from the uncertainties of the raw data. Typically, the uncertainties in the above coefficients are less than 2%.

### 3.6 LDV Velocity Analysis

The LDV data are sampled at each measurement location until approximately 2000 samples are taken for each blade passage. As previously mentioned, the data are stored in 460 bins spaced circumferentially around the impeller, 20 per blade passage. The mean and standard deviation are calculated for the data in each bin, and the total unsteady velocity distribution around the impeller is constructed from the mean velocity in each bin. Fagan (1989) has shown that the uncertainty of the mean in each bin is approximately 0.15%.

The time averaged radial and tangential velocity components,  $U_r$  and  $U_\theta$ , are evaluated by taking the average of the radial and tangential velocity. A Fast Fourier Transform (FFT) is performed on the velocity data to determine the harmonic content of the unsteady portion of the data. The first harmonic unsteady radial and tangential velocities,  $v_r$  and  $v_\theta$ , are determined from the FFT.

### 3.7 Unsteady Pressure Data Analysis

The impeller synchronous ensemble averaged unsteady airfoil static pressure and impeller exit static pressure are measured using the high-response transducers mentioned previously. The ensemble average eliminates random unsteadiness and preserves the pressure variations which are synchronous with the impeller rotation. The measured voltage signals are converted to pressure through the transducer calibration and an FFT is performed on the pressure signals to determine the first harmonic amplitude and phase. The first harmonic unsteady pressures can then be expressed in complex form,  $p = \bar{p} \exp(-i\omega t)$ , where  $\bar{p}$  is the complex amplitude of the first harmonic unsteady pressure.

An airfoil surface unsteady pressure coefficient is defined by

$$C_p = \frac{p}{\rho v_{n1} U_1} \quad 3.11$$

where  $U_1$  is the steady absolute velocity at the diffuser entrance and  $v_{n1}$  is the transverse velocity which is the unsteady first harmonic velocity at the airfoil leading edge normal to the mean flow

$$v_{n1} = v_{r1} \sin \alpha_1 - v_{\theta 1} \cos \alpha_1 \quad 3.12$$

where  $\alpha_1$  is steady absolute flow angle at the diffuser entrance.

A pressure difference coefficient is defined as

$$C_{\Delta p} = \frac{p_U - p_L}{\rho v_{n1} U_1} \quad 3.13$$

where  $p_U$  and  $p_L$  are the upper and lower surface unsteady pressures.

The complex unsteady lift coefficient is given in Equation 3.14

$$C_L = \int_0^1 C_{\Delta p} dx/c \quad 3.14$$

This lift coefficient expresses the unsteady lift based on the leading edge steady and unsteady normal velocities. A second lift coefficient based on the unsteady pressure amplitude and steady velocity is given in Equation 3.15

$$C_{Ls} = \int_0^1 \frac{|p_u - p_l|}{1/2 \rho U_w^2} dx/c \quad 3.15$$

This coefficient indicates the vane loading level as a function of the machine operating point.

The reduced frequency and interblade phase angle are defined as

$$k = \frac{\Omega_b c}{U_1} \quad 3.16$$

$$\phi_b = -2\pi \frac{N_b}{N_v} \quad 3.17$$

where  $\Omega_b$  is the impeller blade pass frequency, and  $N_b$  and  $N_v$  are the number of impeller blades and number of diffuser vanes respectively.

### 3.8 Summary

The Purdue Research Centrifugal Compressor instrumentation allows extensive steady and time-varying measurements to be made in the inlet, impeller and diffuser. The steady static and total pressure along with flow direction and velocity at the impeller inlet, exit and diffuser exit are measured along with static pressures on the channel walls, diffuser vanes and impeller blades. The time varying static pressures are measured on the diffuser vanes and diffuser endwalls at the impeller exit. The detailed two-dimensional time-varying diffuser velocity field is measured, with the capability of three-dimensional measurements throughout the axial inlet, impeller passages and vaned diffuser.



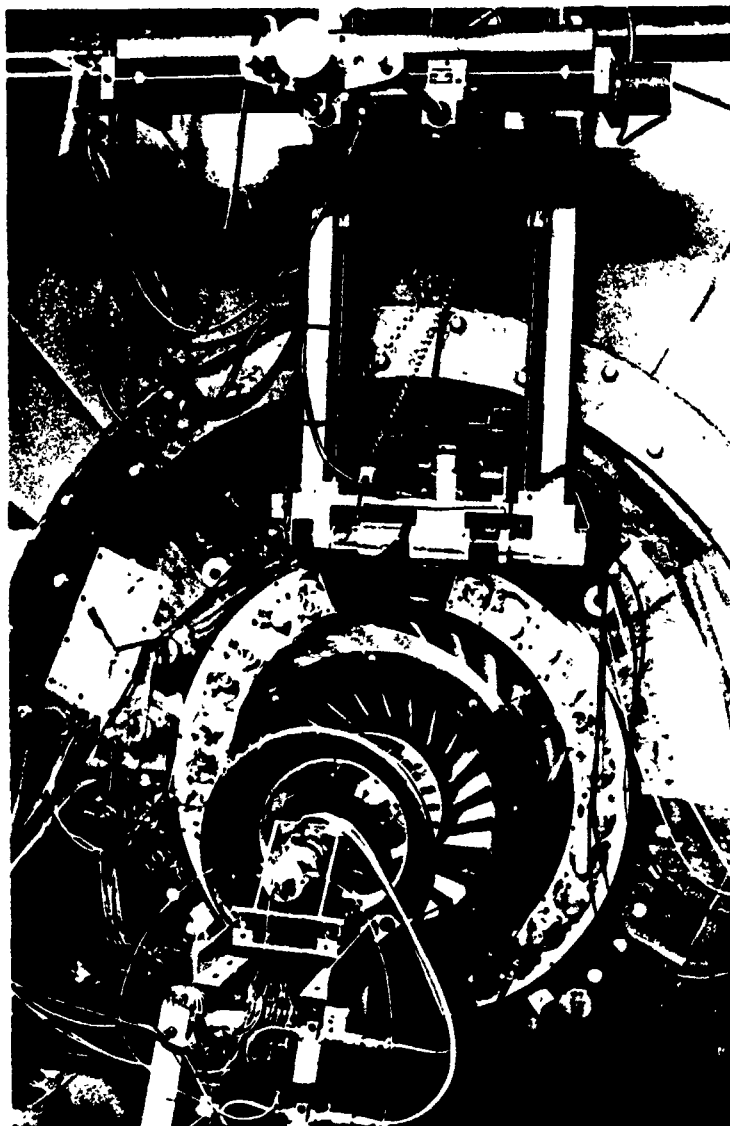


Figure 3.1 Rotating Scanivalve and LDV Final Optics

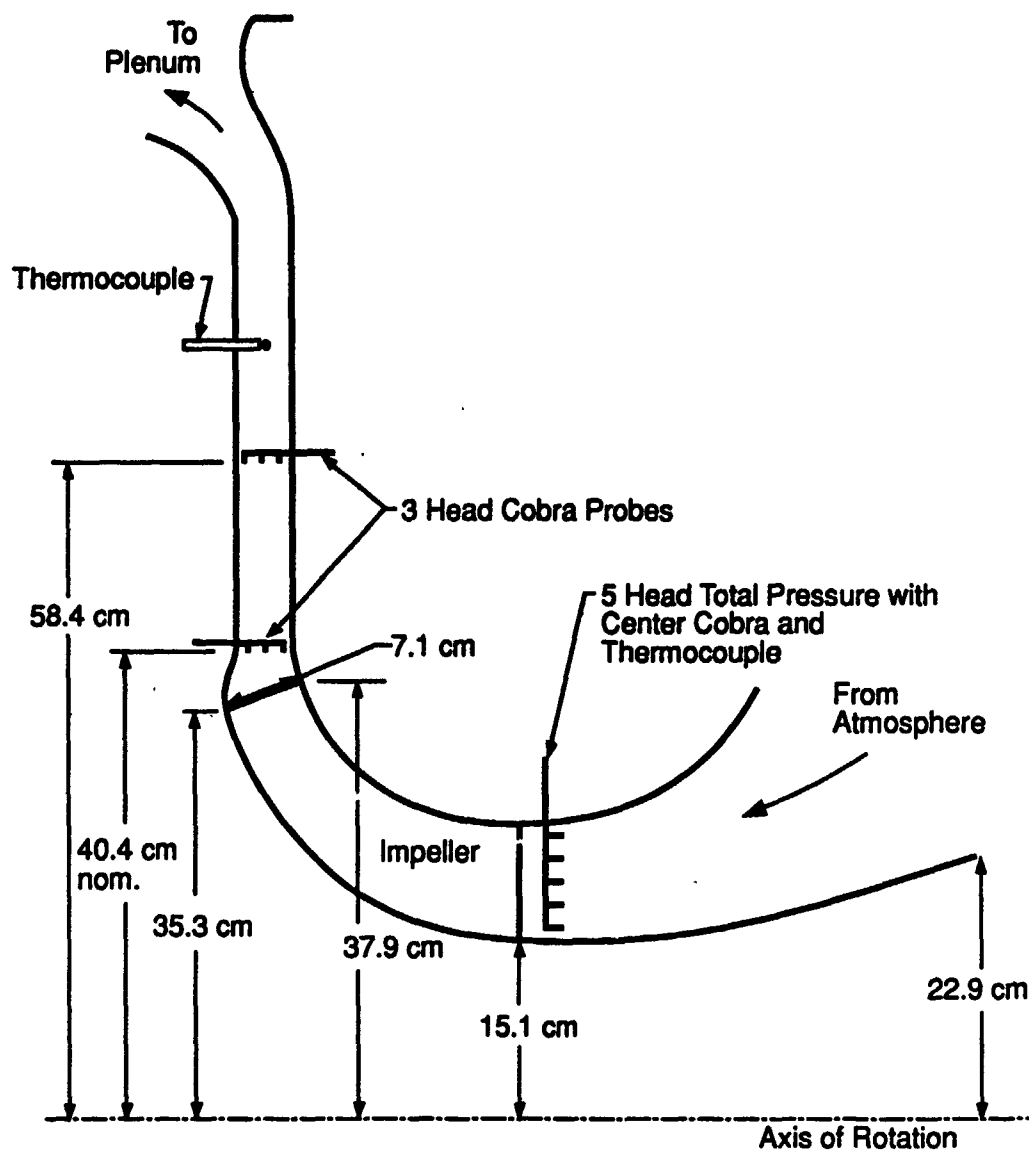


Figure 3.2 Pressure Probe Locations

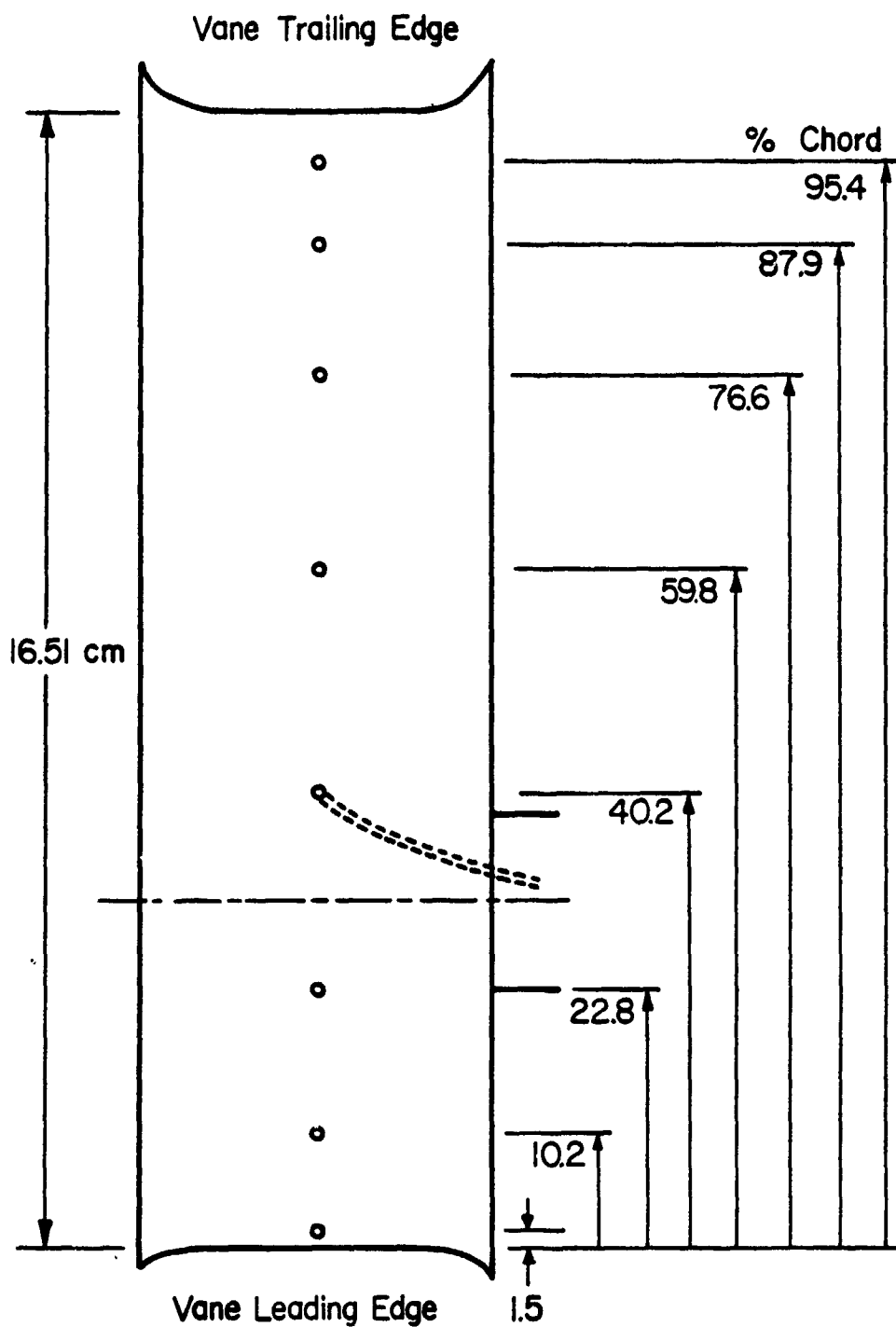


Figure 3.3 Diffuser Vane Unsteady Pressure Measurement Locations

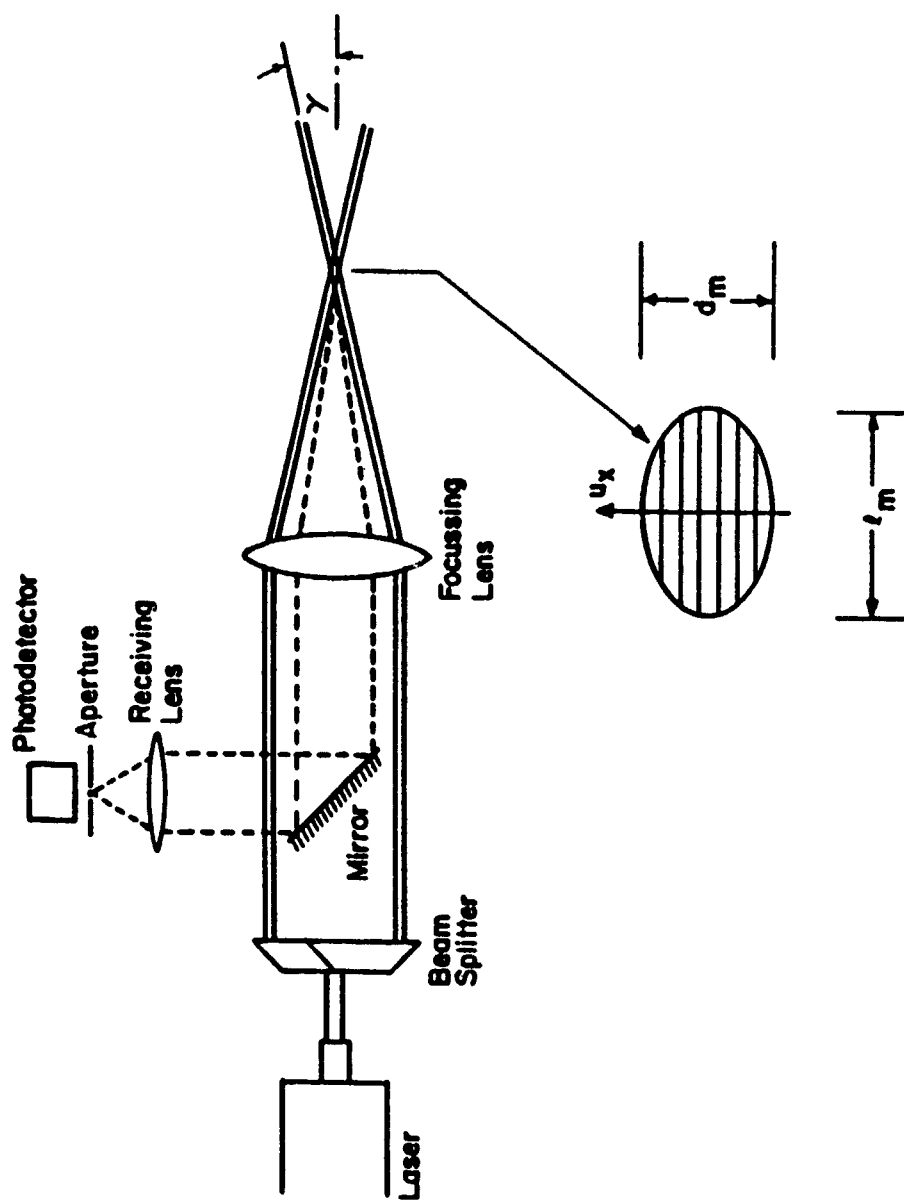


Figure 3.4 Dual Beam LDV System

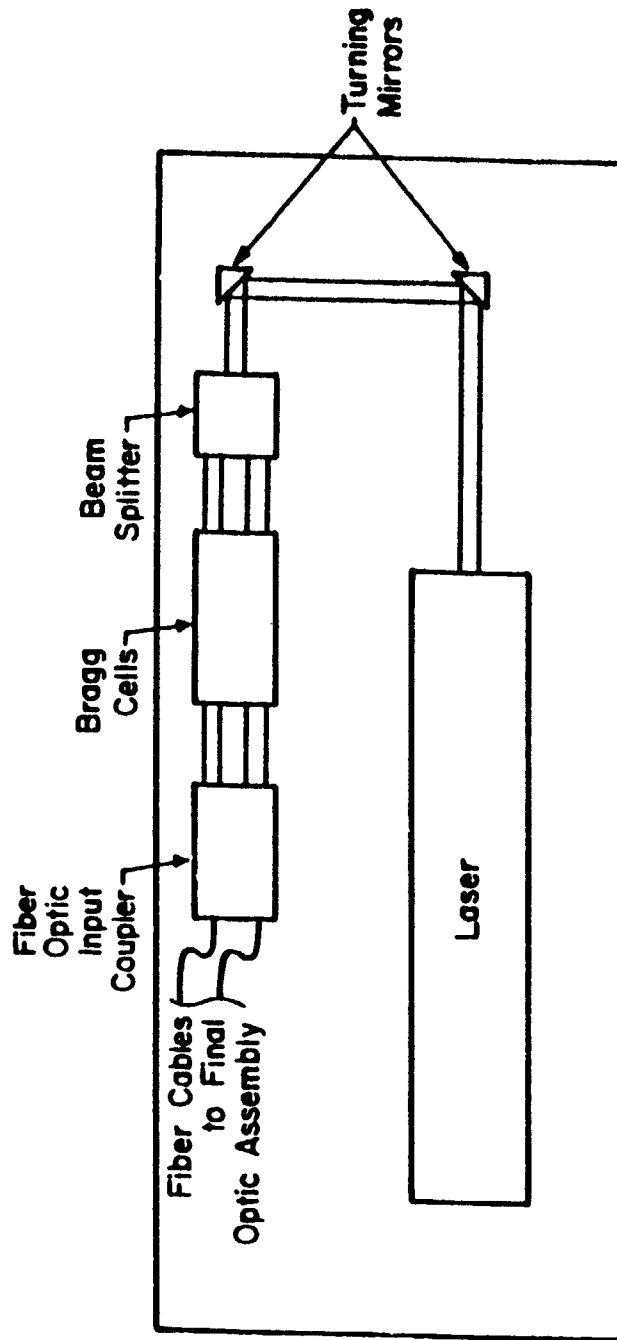


Figure 3.5 LDV Table-Mounted Preliminary Optics

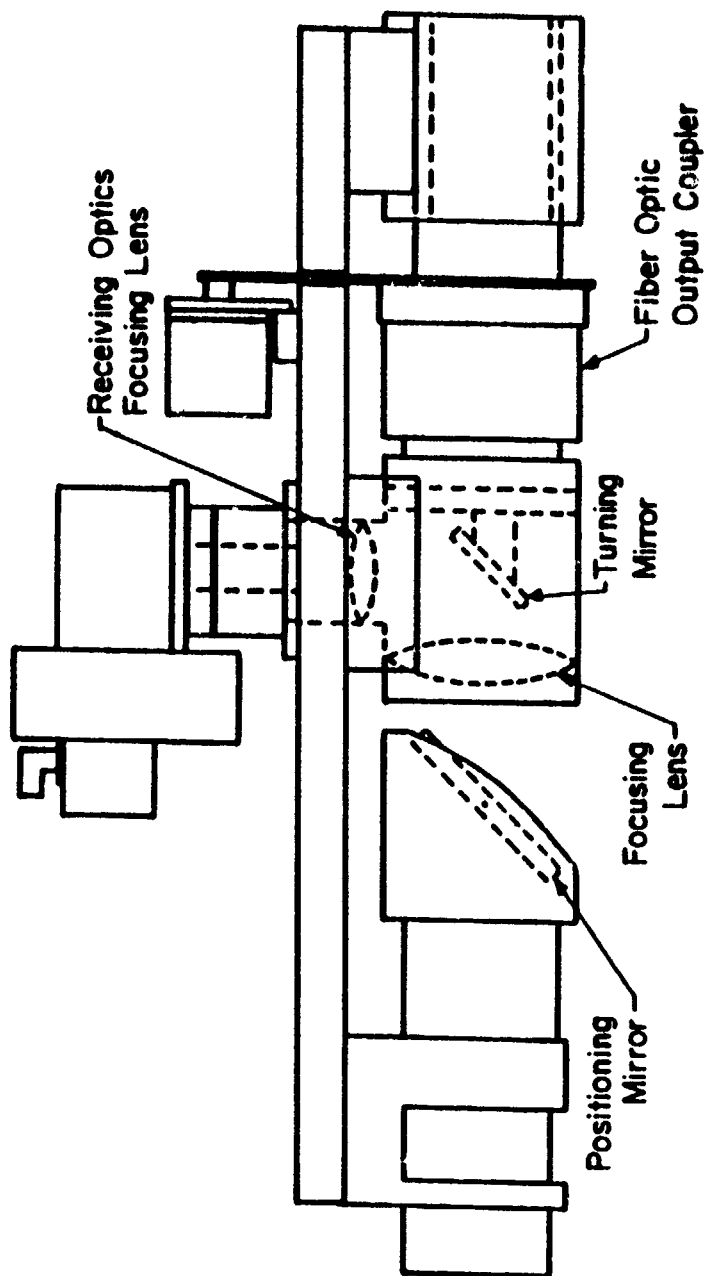


Figure 3.6 LDV Final Optics Assembly

## CHAPTER 4

### RADIAL DIFFUSER WAKE ANALYSIS

Several analyses have been developed to predict the unsteady pressure distribution on axial flow cascades (Whitehead, 1960; Whitehead 1978; Chiang and Fleeter, 1988) and recently in radial flow cascades (Bryan and Fleeter, 1990). Typically, these unsteady aerodynamic models are linearized, i.e., the unsteady velocities and pressures are considered small perturbations superimposed on a steady mean flow, with second order and higher terms neglected. The unsteady velocity field is predicted by solving for the unsteady velocity potential, with boundary conditions given far from the blade row and also on the blade surface. When solving for the unsteady pressure distribution generated by an upstream wake, the velocity induced by the wake on the airfoil surface is specified as a boundary condition. In most models, the wake is assumed to be convected through the cascade, undisturbed by the airfoils. Only the effect of the wake on the airfoil unsteady pressure distribution is considered.

In this chapter, a mathematical model is developed to determine the behavior of vortical wakes in a radial vaneless diffuser for use in unsteady aerodynamic models for radial flow blade rows. Several investigations have considered both steady and time-variant radial diffuser flows, including unsteady wake behavior (Dean and Senoo, 1960; Senoo and Ishida, 1975). These unsteady wake models are control volume solutions and are not directly applicable for use as boundary conditions in unsteady airfoil models. Therefore, a model is developed which describes the behavior of small amplitude vortical impeller wakes convected through the radial diffuser by the mean flow.

#### 4.1 Analysis

The flowfield in a parallel wall radial vaneless diffuser is considered. The flow in the radial diffuser is assumed to be incompressible and inviscid. The imposed boundary conditions are derived from the flow behind a radial impeller, with these boundary

conditions assumed to be equal to the radial diffuser inlet boundary conditions where velocity measurements are made.

The radial and tangential velocities are considered to consist of a small amplitude unsteady velocity superimposed on the mean steady velocity.

$$v_r = U_r + v_r \quad 4.1a$$

$$v_\theta = U_\theta + v_\theta \quad 4.1b$$

The nonuniform circumferential flow leaving the relative reference frame of the centrifugal impeller is unsteady in the absolute reference frame of the radial diffuser, Figure 4.1. Since the flow is inviscid, the flowfield can be described using the unsteady Euler equations. Assuming the unsteady flow to be a small disturbance superimposed on the steady mean flow, Equations 4.1, the steady and unsteady velocities can be described by separate equations, where second order terms in the unsteady velocities are neglected.

$$(\vec{V} \cdot \nabla) \Omega_s = 0 \quad 4.2a$$

$$\nabla^2 \psi_s = -\Omega_s \quad 4.2b$$

$$\left( \frac{\partial}{\partial t} + \vec{V} \cdot \nabla \right) \Omega = 0 \quad 4.3a$$

$$\nabla^2 \psi = -\Omega \quad 4.3b$$

where  $\vec{V}$  is the steady velocity vector,  $\Omega$  and  $\Omega_s$  are the unsteady and steady vorticity and  $\psi$  and  $\psi_s$  are the unsteady and steady stream functions. The steady flow, Equations 4.2, is independent of the unsteady flow, however, the unsteady flow, Equations 4.3, is dependent on the steady flow.

The boundary conditions for Equations 4.2 and 4.3 in the relative reference frame of the impeller are depicted in Figure 4.1 and given by Equations 4.4.

$$v_r = W_o \cos \beta_o + v_{r0} \exp(i N_b \theta_r) @ r=r_o \quad 4.4a$$



$$v_\theta = W_0 \sin \beta_0 + v_{\theta 0} \exp(i N_b \theta_r) \quad @ \quad r=r_0 \quad 4.4b$$

$$v_r = v_\theta = 0 \quad \text{as } r \rightarrow \infty \quad 4.4c$$

where  $W_0$  is the mean velocity in rotating frame,  $N_b$  is the number of impeller blades,  $\beta_0$  is the mean relative flow angle,  $r_0$  is the impeller exit radius and  $v_{r0}$  and  $v_{\theta 0}$  are the complex amplitudes of the wake velocities at the impeller exit.

The boundary conditions specified in Equations 4.4 can be transformed to the stationary reference frame by adding the wheel speed  $U_w$  to the tangential velocity and expressing the relative tangential coordinate,  $\theta_r$ , in terms of the absolute tangential coordinate  $\theta$ , and time,  $t$ . The absolute coordinate  $\theta$ , is related to the relative coordinate  $\theta_r$ , by  $\theta = \theta_r + \omega t$ . Substituting this into Equations 4.4 and adding the wheel speed yields the radial and tangential velocity boundary conditions at the impeller exit.

$$v_r = W_0 \cos \beta_0 + v_{r0} \exp(ik(\theta - t)) \quad @ \quad r = r_0 \quad 4.5a$$

$$v_\theta = W_0 \sin \beta_0 + v_{\theta 0} \exp(ik(\theta - t)) + U_w \quad @ \quad r = r_0 \quad 4.5b$$

where  $\theta = \theta/(U/U_w)$  and  $t$  is scaled by  $r_0/U_0$ , where  $U_0$  is the steady absolute velocity at the impeller exit.

The solution to Equations 4.2, assuming no variation in the steady velocity with  $\theta$ , are

$$U_r = U_{r0} / r \quad 4.6a$$

$$U_\theta = U_{\theta 0} / r \quad 4.6b$$

where  $U_{r0}$  and  $U_{\theta 0}$  are the steady mean absolute velocities at the impeller exit radius,  $r_0$ , and  $r$  is the nondimensional radius,  $r/r_0$ .

The unsteady vorticity equation, Equation 4.2a, in radial coordinates is

$$\left( \frac{\partial}{\partial t} + U_r \frac{\partial}{\partial r} + \frac{U_\theta}{r} \frac{\partial}{\partial \theta} \right) \Omega = 0 \quad 4.7$$

With  $U_r$  and  $U_\theta$  determined, Equation 4.7 can be solved for the unsteady vorticity,  $\Omega$ . The unsteady vorticity is considered an harmonic function of time,

$$\Omega = \bar{\Omega} \exp(-i \omega t) \quad 4.8$$

where  $\bar{\Omega}$  is the complex unsteady vorticity amplitude which is a function of  $r$  and  $\theta$ .

Substituting Equations 4.4 and 4.8 into Equation 4.7 yields the following equation for the unsteady vorticity amplitude,  $\bar{\Omega}$ .

$$\left( -ik + \frac{U_{r0}}{r} \frac{\partial}{\partial r} + \frac{U_{\theta 0}}{r^2} \frac{\partial}{\partial \theta} \right) \bar{\Omega} = 0 \quad 4.9$$

where  $U_{r0}$  and  $U_{\theta 0}$  are nondimensionalized by the absolute velocity leaving the impeller,  $U_0$ , and  $k$  is the reduced frequency,  $\omega r_0 / U_0$ .

Equation 4.9 is a first order, linear partial differential equation with the following solution (Zachmanoglou and Thoe, 1986)

$$\bar{\Omega} = \Omega_0 \exp\left(\frac{-ik}{2 U_{r0}} r^2\right) f\left(r \exp\left(-\frac{U_{r0}}{U_{\theta 0}} \theta\right)\right) \quad 4.10$$

where  $\Omega_0$  is the complex amplitude of the unsteady vorticity and  $f$  is a functional form to be determined.

The functional form,  $f$ , can be determined from the boundary conditions, Equations 4.5. The vorticity is defined as

$$\Omega = \frac{1}{r} \frac{\partial(rv_\theta)}{\partial r} - \frac{1}{r} \frac{\partial v_r}{\partial \theta} \quad 4.11$$

Since  $\Omega$  is determined from partial derivatives of the velocity, the dependence of  $\Omega$  on  $\theta$  must be the same as the dependence of the velocity derivatives, which is an exponential. Therefore, the functional form,  $f$ , must be

$$f(x) = x^{(-iN_b(U_{\theta 0}/U_{r0}))} \quad 4.12$$

The unsteady vorticity, determined from Equation 4.8, becomes,

$$\bar{\Omega} = \Omega_0 \exp(A \ln r + B r^2) \exp(ik\theta) \quad 4.13$$

where

$$A = -ik \frac{U_0 U_{\theta 0}}{U_w U_{r0}} = -ik \frac{\tan \alpha_0}{(\tan \alpha_0 - \tan \beta_0) \cos \alpha_0} \quad \text{and} \quad B = \frac{ik}{2 U_{r0}} = \frac{ik}{2 \cos \alpha_0}$$

and  $\alpha_0$  is the steady mean flow angle in the absolute coordinate system.

To determine the unsteady stream function,  $\psi$ , the expression for the unsteady vorticity, Equation 4.13, is substituted into Equation 4.3b.

$$\frac{\partial^2 \bar{\psi}}{\partial r^2} + \frac{1}{r} \frac{\partial \bar{\psi}}{\partial r} + \frac{1}{r^2} \left( \frac{U}{U_w} \right)^2 \frac{\partial^2 \bar{\psi}}{\partial \theta^2} = -r_0^2 \Omega_0 \exp(A \ln r + B r^2) \exp(ik\theta) \quad 4.14$$

The solution to Equation 4.14 is determined as a complex Fourier series by a finite Fourier transform, Equation 4.15, taking advantage of the fact that the solution is periodic in  $\theta$ .

$$\bar{\psi}(r, \theta) = \sum_{n=-\infty}^{\infty} c_n(r) e^{in\theta} \quad 4.15$$

The left hand side coefficients are defined by

$$c_n(r) = \frac{n}{2\pi} \int_{-\pi/n}^{\pi/n} \bar{\psi}(r, \theta) e^{-in\theta} d\theta \quad 4.16$$

and the source term coefficients are

$$C_n(r) = \frac{n}{2\pi} \int_{-\pi/n}^{\pi/n} \bar{\Omega}(r, \theta) e^{-in\theta} d\theta \quad 4.17$$

Substituting Equations 4.16 and 4.17 into Equation 4.14 yields

$$\frac{d^2 c_n}{dr^2} + \frac{1}{r} \frac{dc_n}{dr} - \frac{k^2}{r^2} \left( \frac{U}{U_w} \right)^2 c_n = -r_0^2 \Omega_0 \exp(A \ln r + B r^2) \quad 4.18$$

Equation 4.18 is a Cauchy-Euler differential equation. The complementary solution is given in Equation 4.19 (Ross, 1980).

$$c_n = a_1 r^{k_2} + a_2 r^{-k_2} \quad 4.19$$

where  $k_2 = k(U_0/U_w)$ .

The particular solution to Equation 4.19 is found by variation of parameters. The complete solution for  $c_n$  is given in Equations 4.20 and 4.21.

$$c_n = a_1 r^{k_2} + a_2 r^{-k_2} + \frac{r_0^2 \Omega_0}{2 k_2} r^{k_2} \int_1^r \exp(A \ln r + B r^2) r^{1-k_2} dr - \frac{r_0^2 \Omega_0}{2 k_2} r^{-k_2} \int_1^r \exp(A \ln r + B r^2) r^{1+k_2} dr \quad 4.20$$

$$\text{and} \quad c_{-n} = b_1 r^{k_2} + b_2 r^{-k_2} \quad 4.21$$

The stream function can be constructed from the Fourier series, Equation 4.15.

$$\begin{aligned} \psi = & \frac{r_0^2 \Omega_0}{2 k_2} \left( r^{k_2} \int_1^r \exp(A \ln r + B r^2) r^{1-k_2} dr - \right. \\ & \left. r^{-k_2} \int_1^r \exp(A \ln r + B r^2) r^{1+k_2} dr \right) \exp(ik(\theta - t)) + \\ & (a_1 r^{k_2} + a_2 r^{-k_2}) \exp(ik(\theta - t)) + (b_1 r^{k_2} + b_2 r^{-k_2}) \exp(ik(-\theta - t)) \end{aligned} \quad 4.22$$

Since the solution is not a function of  $e^{-ik\theta}$ ,  $b_1$  and  $b_2$  are zero. The unsteady radial and tangential velocities are evaluated from the stream function.

$$v_r = \frac{1}{r} \frac{\partial \psi}{\partial \theta} = \frac{i r_0 \Omega_0}{2} \left( r^{k_2-1} \int_1^r \exp(A \ln r + B r^2) r^{1-k_2} dr - \right. \\ \left. r^{-k_2-1} \int_1^r \exp(A \ln r + B r^2) r^{1+k_2} dr \right) \exp(ik(\theta - t)) + \\ \left( \frac{ik_2 a_1}{r_0} r^{k_2-1} + \frac{ik_2 a_2}{r_0} r^{-k_2-1} \right) \exp(ik(\theta - t)) \quad 4.23$$

and

$$v_\theta = -\frac{\partial \psi}{\partial r} = -\frac{r_0 \Omega_0}{2} \left( r^{k_2-1} \int_1^r \exp(A \ln r + B r^2) r^{1-k_2} dr + \right. \\ \left. r^{-k_2-1} \int_1^r \exp(A \ln r + B r^2) r^{1+k_2} dr \right) \exp(ik(\theta - t)) + \\ \left( -\frac{k_2 a_1}{r_0} r^{k_2-1} + \frac{k_2 a_2}{r_0} r^{-k_2-1} \right) \exp(ik(\theta - t)) \quad 4.24$$

The unsteady wake velocities, Equations 4.23 and 4.24, are composed of a vortical velocity component and an irrotational velocity component. The irrotational component corresponds to the homogeneous solution of Equation 4.14, with the rotational component corresponding to the particular solution, which contains the  $\Omega_0$  term in Equations 4.23 and 4.24.

The unsteady wake velocity solution, Equations 4.23 and 4.24, is determined by specifying  $\alpha_0$ ,  $\beta_0$  and  $k$ . The integrals are evaluated numerically using Simpson's 1/3 rule. The constants  $a_1$  and  $a_2$  are evaluated from the boundary conditions, Equations 4.5a and 4.5b. The vorticity magnitude,  $\Omega_0$ , is evaluated from the third boundary condition, Equation 4.4c.

The unsteady wake velocities,  $v_r$  and  $v_\theta$ , are for a vaneless, parallel wall, radial diffuser. The steady flowfield is determined by the absolute flow angle,  $\alpha_0$ . The wake

propagation is determined by the relative flow angle,  $\beta_0$ , the reduced frequency,  $k$ , and the boundary conditions of the wake,  $v_{r0}$  and  $v_{\theta 0}$ . In principle, the wave number,  $k_2$ , can assume any value for given  $\alpha_0$ ,  $\beta_0$  and  $k$ . In practice,  $k_2$  is equal to the number of impeller blades,  $N_b$ , and will always be an integer. Thus, given the number of impeller blades,  $N_b$ , the relative flow angle,  $\beta_0$ , and the absolute flow angle,  $\alpha_0$ , the unsteady wake velocities can be determined from Equations 4.23 and 4.24.

## 4.2 Results

The unsteady wake model developed herein is utilized to demonstrate the effect of steady centrifugal compressor parameters, including the absolute flow angle,  $\alpha_0$ , the relative flow angle,  $\beta_0$ , and the number of impeller blades,  $N_b$ . The unsteady wake velocities,  $v_r$  and  $v_\theta$ , are constant amplitude harmonic functions of the tangential coordinate  $\theta$ , and time  $t$ , at a particular value of  $r$ . However, the velocity varies in amplitude with  $r$  due to the radial geometry and thus variation in steady velocity with radius. In the following figures, the radial dependence of  $v_r$  and  $v_\theta$  is presented as a function of the nondimensional radius, assuming no variation of the relative flow angle,  $\beta_0$ , with the tangential direction,  $\theta$ . A parametric study is performed by varying  $\alpha_0$ ,  $\beta_0$  and  $N_b$ . The baseline values are  $\alpha_0 = 60^\circ$ ,  $N_b = 12$  and  $\beta_0 = -45^\circ$ . Negative  $\beta_0$  values indicate impeller blades leaning in the opposite direction of rotation.

Figures 4.2 and 4.3 show the results for the baseline case with  $\alpha_0 = 60^\circ$  and for  $\alpha_0 = 45^\circ$ . The radial velocity monotonically approaches zero whereas the circumferential velocity increases to a maximum before approaching zero. This behavior is typical for  $\beta_0 < -45^\circ$ . The radial velocity decreases more rapidly than the tangential velocity, with both components decreasing more rapidly as the absolute flow angle,  $\alpha_0$  is increased.

Figures 4.4 and 4.5 show the wake velocities for  $\beta_0 = -30^\circ$  and  $\beta_0 = 0^\circ$ . Changing  $\beta_0$ , the relative flow angle, changes the boundary conditions for  $v_{r0}$  and  $v_{\theta 0}$ , under the assumption of circumferentially constant  $\beta_0$ . For various values of  $\beta_0$ , the radial velocity component demonstrates behavior similar to the baseline, with only a magnitude variation. The tangential velocity again increases before its eventual decay, but the maximum occurs at larger values of  $r$  for  $\beta_0$  closer to zero.

Figure 4.6 presents the wake velocities with  $N_b = 20$ . Variation in the number of impeller blades,  $N_b$ , has a minimal affect on the amplitude of the wake velocities, with only the phase changing more rapidly with increasing  $N_b$ .

The predicted wake velocities,  $v_r$  and  $v_\theta$ , will be compared to the measured wake velocities in the vaneless radial diffuser configuration of the Purdue Research Centrifugal Compressor. As mentioned previously, these velocity expressions will also be utilized as a boundary condition in the unsteady radial airfoil cascade analysis in Chapter 5.

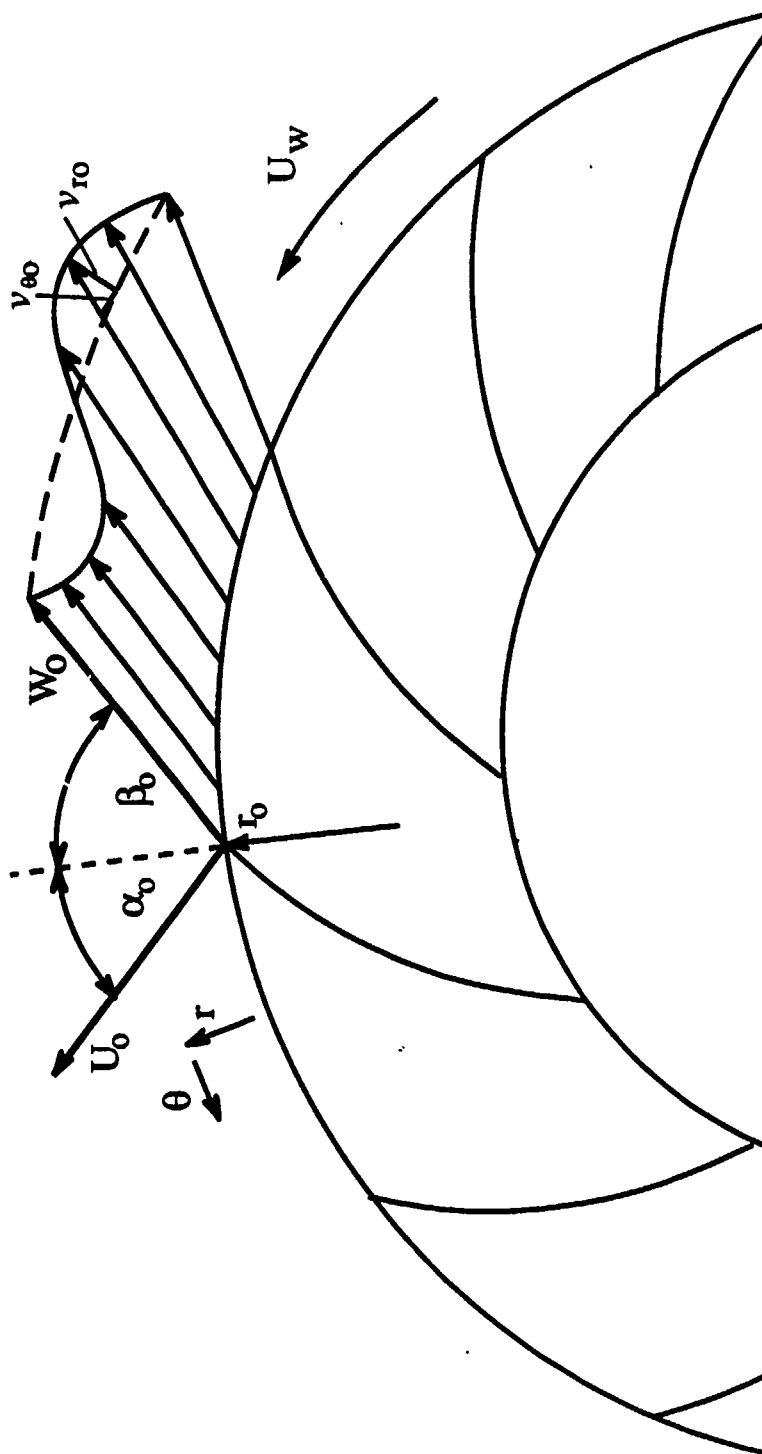


Figure 4.1 Radial Turbomachine Wake



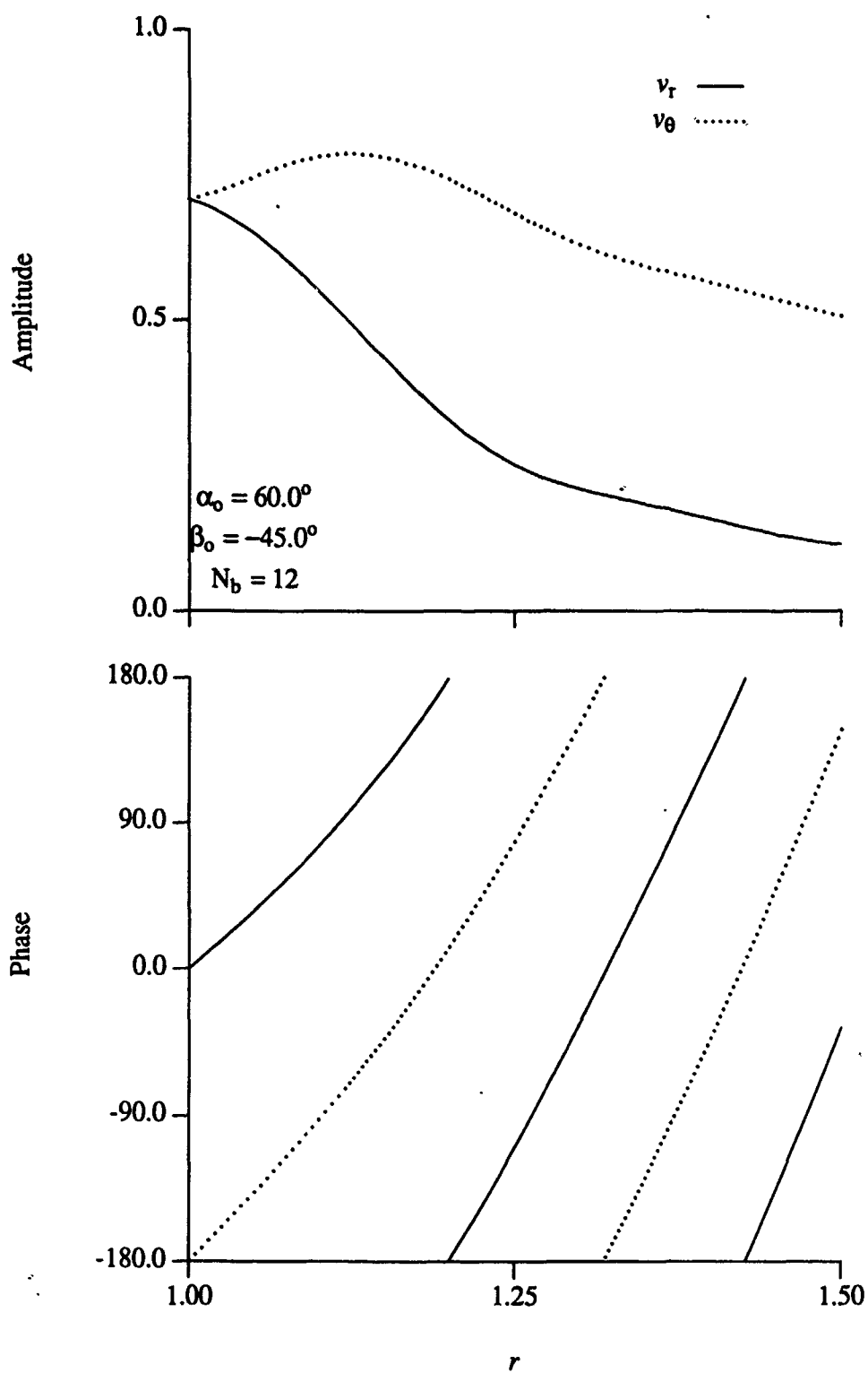


Figure 4.2 Radial Diffuser Unsteady Wake Velocity ( $\alpha_o = 60^\circ$ ,  $N_b = 12$  and  $\beta_o = -45^\circ$ )

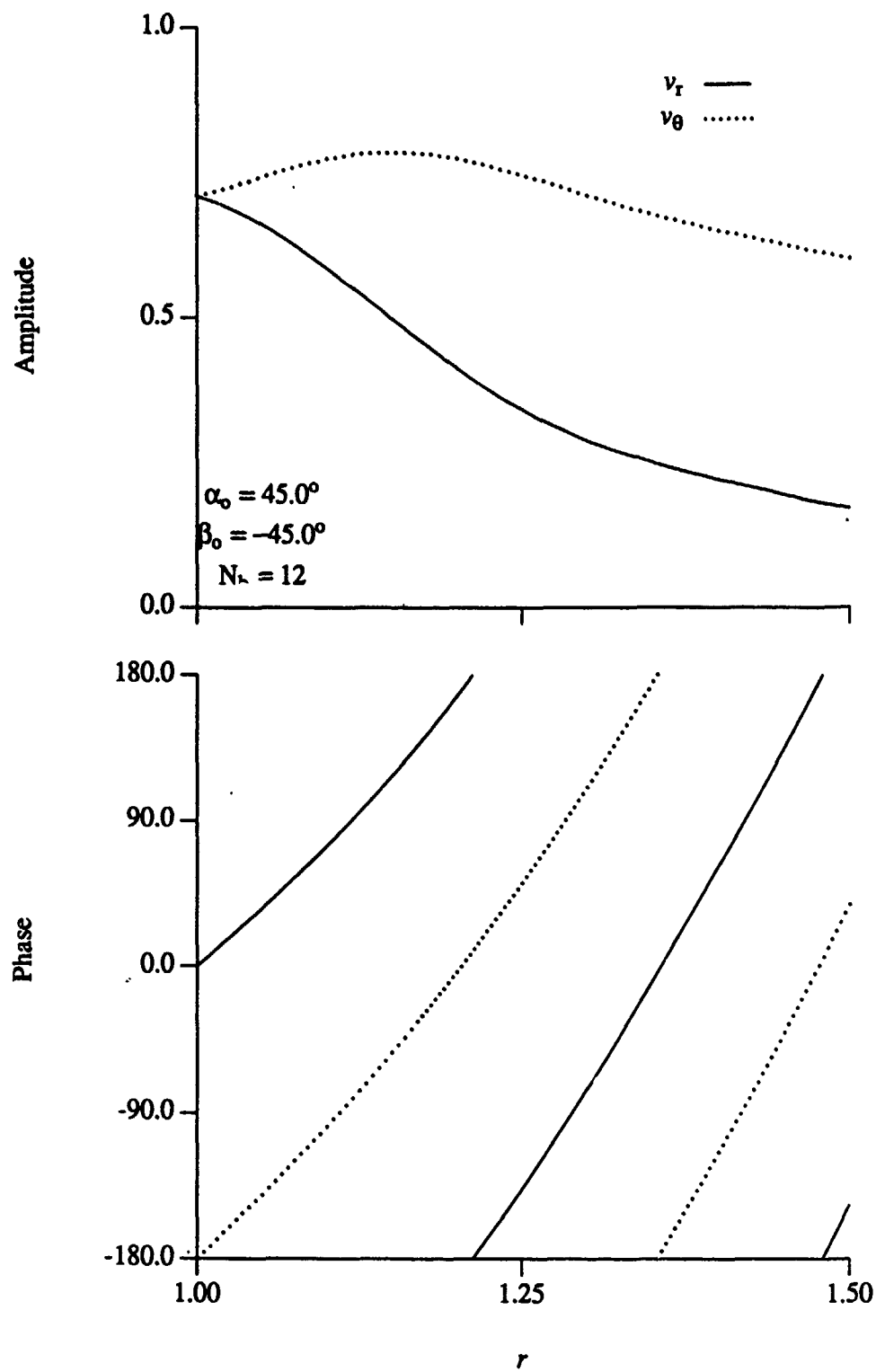


Figure 4.3 Radial Diffuser Unsteady Wake Velocity ( $\alpha_0 = 45^\circ$ ,  $N_b = 12$  and  $\beta_0 = -45^\circ$ )

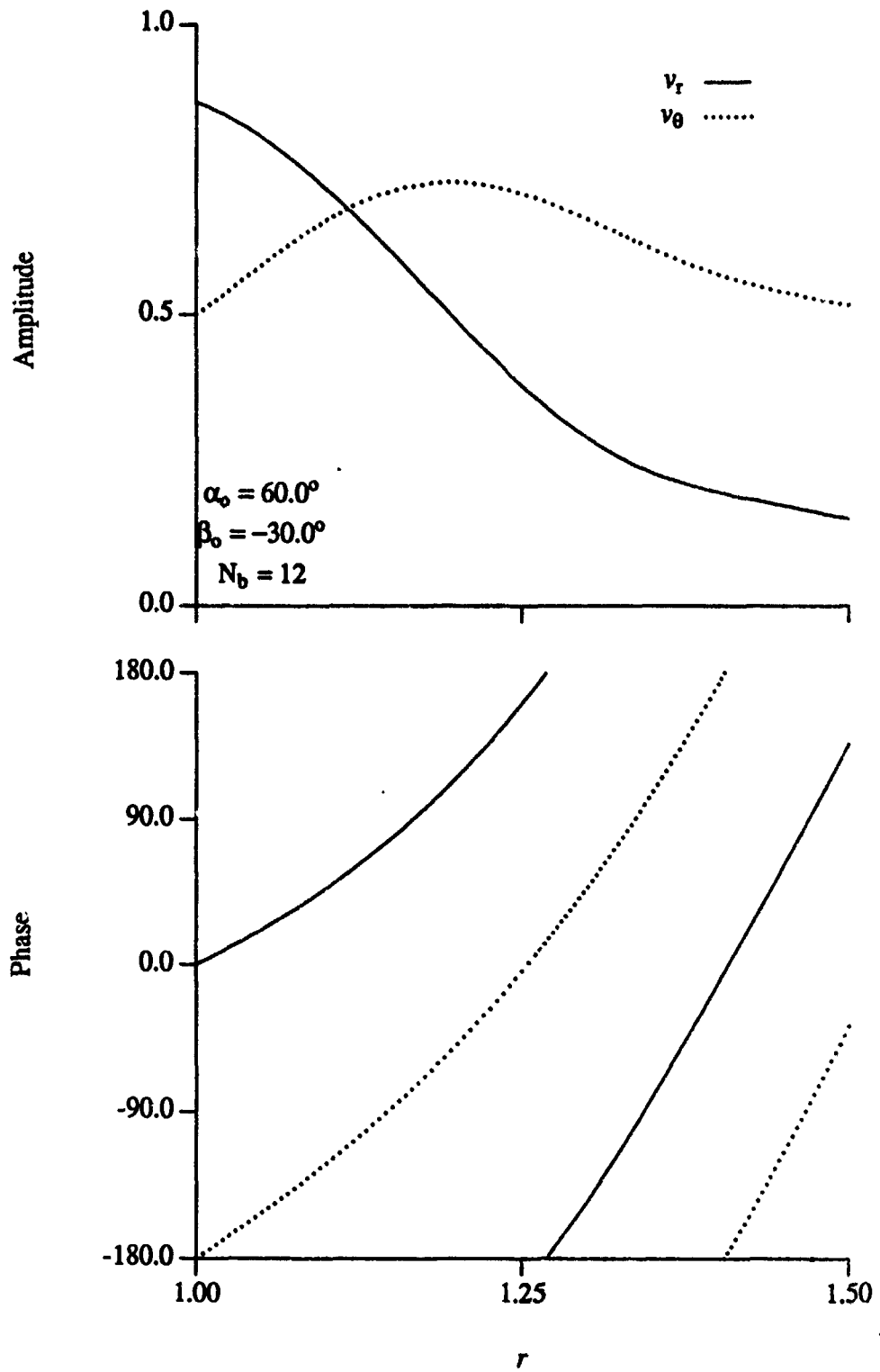


Figure 4.4 Radial Diffuser Unsteady Wake Velocity ( $\alpha_0 = 60^\circ$ ,  $N_b = 12$  and  $\beta_0 = -30^\circ$ )

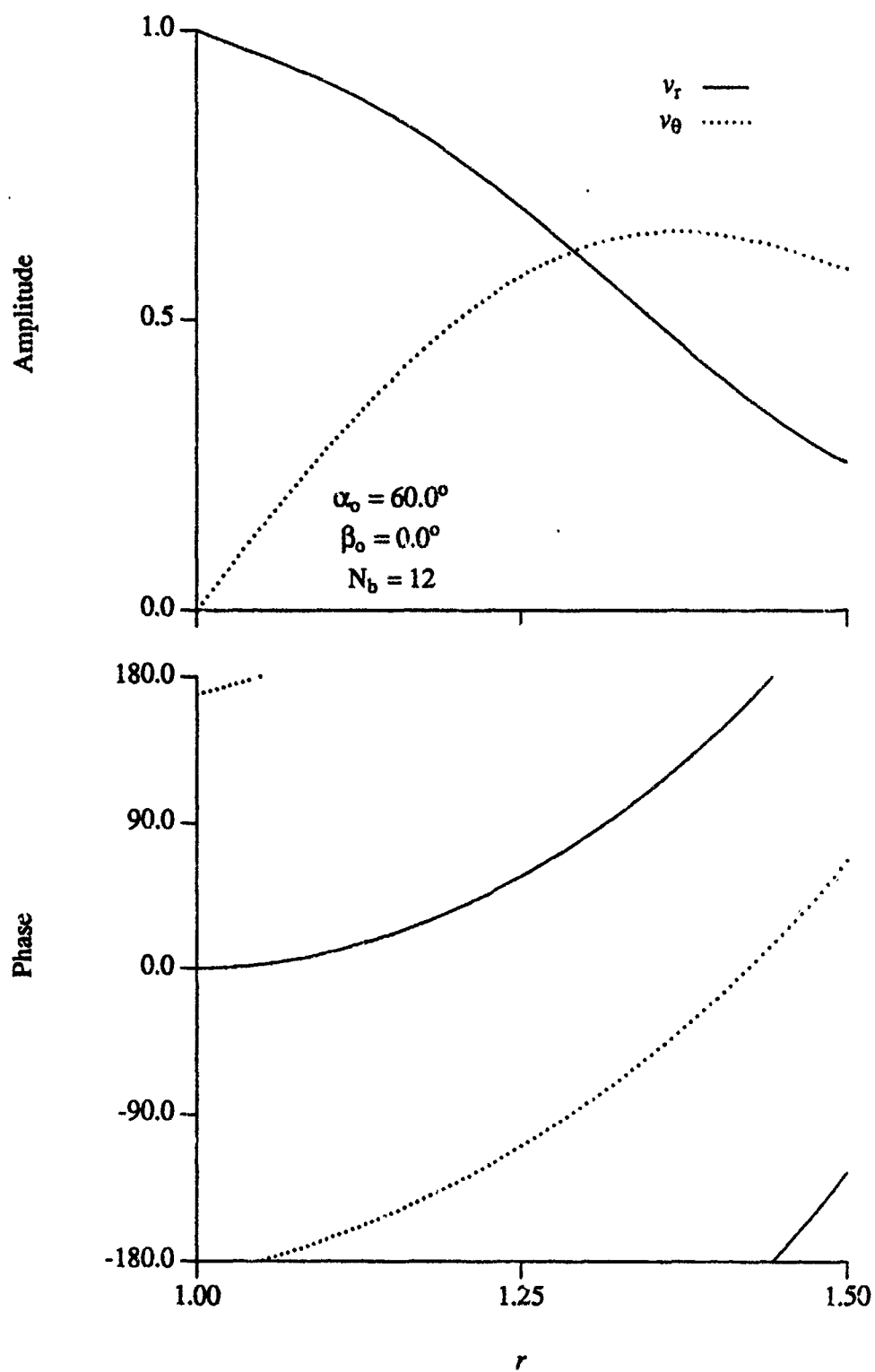


Figure 4.5 Radial Diffuser Unsteady Wake Velocity ( $\alpha_0 = 60^\circ$ ,  $N_b = 12$  and  $\beta_0 = 0^\circ$ )

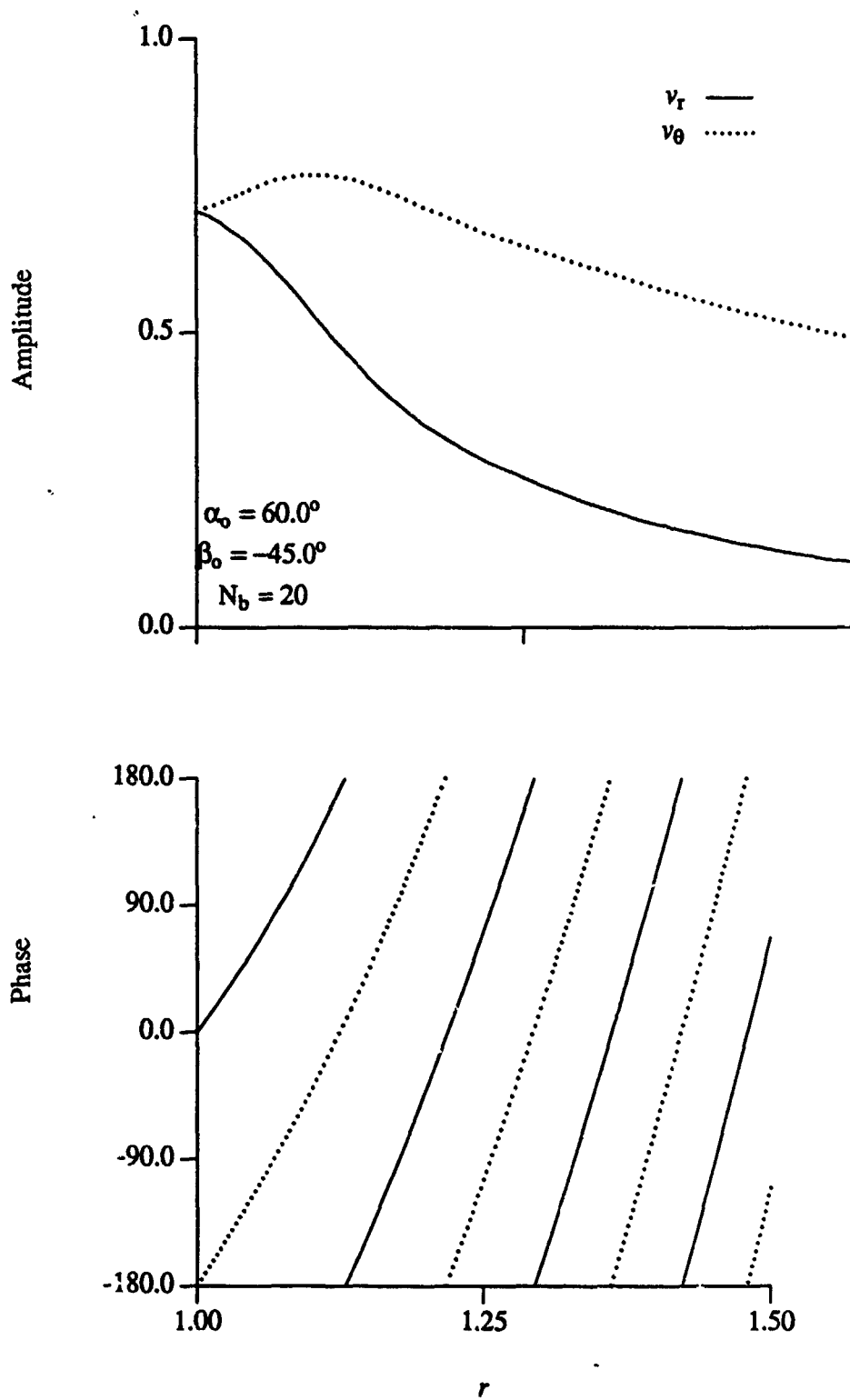


Figure 4.6 Radial Diffuser Unsteady Wake Velocity ( $\alpha_o = 60^\circ$ ,  $N_b = 20$  and  $\beta_o = -45^\circ$ )

## CHAPTER 5

### RADIAL CASCADE UNSTEADY AIRFOIL THEORY

Much attention has been devoted in the literature to the unsteady aerodynamics of isolated airfoils and axial flow cascades. In contrast, relatively little attention has been directed at unsteady flow in radial cascades, with the experimental investigations of Inoue and Cumpsty (1984) and Arndt et al. (1988) two of the few examples. Radial turbomachine cascade flow fields and geometries are different than those for axial flow machines. Due to these differences, axial flow cascade unsteady aerodynamic models are not directly applicable to radial flow cascades. Thus, unsteady aerodynamic models applicable to radial flow airfoil cascades are needed.

An analysis is developed to predict the unsteady fluid dynamics of radial flow cascades while taking advantage of the existing research for axial flow turbomachines. This is accomplished by developing a conformal transformation which allows a potential flow solution for a given axial flow cascade to be applied to a radial cascade (Smith, 1970; Faulders, 1956). Thus, this transformation mathematically unwraps the steady and unsteady flowfields in a radial cascade into a corresponding axial cascade flow. This transformation is then coupled to an incompressible flat plate cascade analysis (Whitehead, 1960; 1978). The effects of the cascade geometry on the unsteady fluid dynamics of radial cascades are then demonstrated by applying this model to a series of radial flow cascade geometries.

#### 5.1 Transformation Analysis

For a two-dimensional, incompressible and irrotational flow, the velocity potential  $\phi$  is described by the Laplace equation.

$$\frac{\partial^2 \phi}{\partial x^2} + \frac{\partial^2 \phi}{\partial y^2} = 0$$

5.1

From the theory of complex variables, any function  $\phi$  of the cartesian variables  $x$  and  $y$  which satisfies the Laplace equation can be expressed solely in terms of the complex variable  $z = x + iy$ . Also, a conjugate function  $\psi$  exists such that the complex potential,  $w = \phi + i\psi$  is a function only of the complex variable  $z$ , with  $\phi$  and  $\psi$  individually satisfying the Laplace equation (Churchill, 1984).

The converse is also true. Given any function of a complex variable  $\zeta = \eta + i\xi = f(z)$ , the real and imaginary components of  $\zeta$  individually satisfy the Laplace equation provided  $\zeta$  is an analytic function of  $z$ . Any complex function of a complex variable,  $\zeta = \eta(x,y) + i\xi(x,y) = f(x+iy)$  can also be considered a transformation from the variables  $x$  and  $y$  to the variables  $\eta$  and  $\xi$ . In this case, the transformation is termed a conformal transformation.

If a solution to the Laplace equation can be found for a given geometry, the solution in any other geometry can be found by applying an appropriate conformal transformation. For a radial cascade, the simple transformation given in Equation 5.2 transforms the solution to a two-dimensional, infinite, axial flow cascade, as depicted in Figure 5.1.

$$\zeta = \ln z \quad 5.2$$

where  $z$  is the coordinate in the radial diffuser and  $\zeta$  is the coordinate in the transformed plane. Thus, this transformation unwraps the steady and unsteady radial cascade flow fields into those of a corresponding axial cascade. This allows a potential flow solution for a given axial cascade to be applied to a corresponding radial cascade.

Steady potential flow streamlines in a parallel wall radial diffuser follow logarithmic spirals as shown in Chapter 1 and given in Equation 5.3.

$$\ln \left( \frac{r}{r_2} \right) = \frac{\theta}{\tan \alpha_L} \quad 5.3$$

where  $\alpha_L$  is the angle between the streamline and a radial line, i.e.,  $\alpha_L$  is the logarithmic spiral angle,  $r$  denotes the radius,  $r_2$  is a reference radius and  $\theta$  is the angular coordinate. These streamlines are transformed into parallel straight streamlines by Equation 5.2. Thus, the flat plate airfoils in axial flow unsteady aerodynamic models are transformed into logarithmic spiral airfoils in the radial cascade.

A modified form of the transformation specified by Equation 5.2 is used for the actual conformal transformation. Namely, the transformation given in Equation 5.4 is utilized to maintain the Kutta condition through the transformation in the unsteady flow.

$$\zeta = r_2 (\ln z - \ln r_2) \quad 5.4$$

where  $z$  is the coordinate for the radial geometry and  $\zeta$  is the coordinate for the transformed axial geometry. Equation 5.4 expressed in radial coordinates is,

$$\eta + i\xi = r_2 (\ln \frac{r}{r_2} + i\theta) \quad 5.5$$

The velocities in the two coordinate systems are related by Equation 5.6.

$$\frac{U_\eta - iU_\xi}{r_2} = U_r - iU_\theta \quad 5.6$$

where  $U_\eta$  and  $U_\xi$  are the axial cascade velocity components in the axial and tangential directions respectively, with  $U_r$  and  $U_\theta$  denoting the radial cascade velocity components in the radial and tangential directions.

The Kutta condition, applied to both the steady and unsteady flow fields, is maintained through the transformation. In a steady incompressible, inviscid flow, the pressure at any point in the flowfield is given by the following Bernoulli equation.

$$\frac{P}{\rho} + \frac{U^2}{2} = \frac{P_\infty}{\rho} + \frac{U_\infty^2}{2} \quad 5.7$$

Since the right hand side of Equation 5.7 is constant, the steady pressure is proportional to the square of the steady velocity. Kutta's hypothesis requires that the pressure be continuous at the airfoil trailing edge and that the trailing edge velocity is finite. Therefore the velocities on the upper and lower airfoil surfaces must approach a common value at the trailing edge. Since the upper and lower velocities are scaled by the same  $r/r_2$  as appears in the radial coordinate form of the transformation, Equation 5.5, the Kutta condition requirement of no steady pressure discontinuity at the airfoil trailing edge is satisfied automatically independent of the value of  $r_2$ .



The unsteady pressure is described by the following incompressible unsteady Bernoulli equation.

$$\frac{p}{\rho} + \frac{u^2}{2} + \frac{\partial \phi}{\partial t} = \frac{P_{\infty}}{\rho} + \frac{U_{\infty}^2}{2} \quad 5.8$$

In axial flow cascade linearized aerodynamic models, the unsteady flow is considered to be an harmonic small perturbation to a steady uniform mean flow in the chordwise direction. In the chordwise direction, the pressure, velocity components, and velocity potential are thus given by Equation 5.9.

$$p = P + \bar{p} \exp(-i \omega t) \quad 5.9a$$

$$u = U + \bar{u} \exp(-i \omega t) \quad 5.9b$$

$$v = \bar{v} \exp(-i \omega t) \quad 5.9c$$

$$\phi = \Phi + \bar{\phi} \exp(-i \omega t) \quad 5.9d$$

where  $P$ ,  $\Phi$ , and  $U$  are the steady values of the pressure, velocity potential and freestream chordwise velocity, with  $\bar{p}$ ,  $\bar{\phi}$ ,  $\bar{u}$  and  $\bar{v}$  the complex amplitudes of the unsteady pressure, velocity potential, and chordwise and normal velocity components which are functions only of the spatial coordinates. Note that in the axial flow cascade,  $U$  and  $P$  are constant. In the radial cascade,  $U$  is proportional to  $1/r$  and  $P$  is proportional to  $1/r^2$ .

The linearized unsteady Bernoulli equation, Equation 5.10, is determined by substituting Equation 5.9 into Equation 5.8 and retaining only first order terms in the perturbation quantities.

$$\frac{\bar{p}}{\rho} + \bar{u}U - i\omega\bar{\phi} = F(t) \quad 5.10$$

Applying the linearized unsteady Bernoulli equation to the upper and lower surfaces of a reference airfoil in either the axial or radial cascade results in the following equation for the complex unsteady pressure difference across the reference airfoil chordline.

$$\frac{\bar{p}_U - \bar{p}_L}{\rho} = -U(\bar{u}_U - \bar{u}_L) + i\omega(\bar{\phi}_U - \bar{\phi}_L) \quad 5.11$$

The value of the velocity potential  $\phi$  at each point in the axial cascade is the same as at its image point in the corresponding radial cascade. However, the axial cascade velocity and velocity components must be multiplied by the metric of the transformation,  $1/(r/r_2)$ . Thus, the first term on the right hand side of Equation 5.11 must be multiplied by  $1/(r/r_2)^2$ . For the pressure to be continuous and therefore the pressure difference across the airfoil to vanish at the trailing edge,  $r/r_2$  must be equal to unity at the trailing edge, i.e., the radial cascade airfoil trailing edge is defined by  $r = r_2$ .

### 5.2 Cascade Model

For a flat plate axial flow cascade at zero incidence in an incompressible flow, the parameters necessary to specify the problem are the solidity,  $c/s$ , the reduced frequency,  $k = \omega c/U$ , the stagger angle,  $\sigma$ , and the interblade phase angle,  $\phi_b$ . For the radial cascade, the important parameters are the number of radial airfoils,  $N_v$ , the airfoil radial extent divided by the trailing edge radius,  $\Delta r/r_2$ , the reduced frequency based on the airfoil leading edge velocity,  $k = \omega c/U_1$ , the stagger angle,  $\sigma$ , which is equal to the logarithmic spiral angle,  $\alpha_L$ , and the interblade phase angle,  $\phi_b$ .

Figure 5.2 shows the flat plate axial flow cascade transformation of a radial cascade. To apply existing axial flow cascade unsteady aerodynamic analyses to radial cascades, it is necessary to determine the axial cascade parameters which correspond to a specified radial cascade geometry. Given the parameters defining the radial cascade, the appropriate corresponding parameters for the axial cascade unsteady aerodynamic models are calculated through the transformation specified in Equation 5.5. In the following equations, unsubscripted values refer to the radial cascade and values with the A subscript refer to the axial cascade transformation of the radial cascade.

The chord in the transformed axial cascade is given by Equation 5.12

$$c_A = \frac{-r_2 \ln (1 - \Delta r/r_2)}{\cos \sigma} \quad 5.12$$

The transformed axial cascade solidity,  $c_A/s_A$  is

$$\frac{c_A}{s_A} = - \frac{N_v}{2\pi} \left( \frac{\ln (1 - \Delta r/r_2)}{\cos \sigma} \right) \quad 5.13$$

The relationship between the reduced frequencies for the axial and radial cascades is given by

$$k_A = -k \frac{\ln(1 - \Delta r/r_2)}{(\Delta r/r_2)(1 - \Delta r/r_2)} \quad 5.14$$

where  $k$  is the radial cascade reduced frequency.

The state-of-the-art axial flow cascade unsteady aerodynamic models predict the unsteady aerodynamic lift and moment as well as the pressure distribution for airfoils executing translational and torsional motions and subjected to convected harmonic vortical gusts. The unsteady pressure difference, and unsteady lift and moment coefficients for translation, torsion and gust are defined as

$$C_{\Delta P} = \frac{\Delta p}{\rho U h}, \frac{\Delta p}{\rho U^2 \alpha}, \frac{\Delta p}{\rho U v} \quad 5.15a$$

$$C_L = \frac{\text{Lift}}{\rho U h c}, \frac{\text{Lift}}{\rho U^2 \alpha c}, \frac{\text{Lift}}{\rho U v c} \quad 5.15b$$

$$C_M = \frac{\text{Moment}}{\rho U h c^2}, \frac{\text{Moment}}{\rho U^2 \alpha c^2}, \frac{\text{Moment}}{\rho U v c^2} \quad 5.15c$$

where  $h$  and  $\alpha$  are the translation and torsion airfoil motions  $h = h_0 \exp(-i k t)$ ,  $\alpha = \alpha_0 \exp(-i k t)$  and  $v$  is the wake or gust velocity at the airfoil leading edge,  $v = v_0 \exp(-i k t)$ . In the previous expressions,  $h_0$ ,  $\alpha_0$  and  $v_0$  are the motion and velocity amplitudes. In the radial cascade,  $U$  and  $v$  are the values at the airfoil leading edge.

The unsteady pressure distribution for the radial cascade is calculated from the unsteady velocities in the axial cascade through the transformation defined by Equations 5.5 and 5.6, with the unsteady aerodynamic lift and moment coefficients calculated from this by integration.

### 5.3 Boundary Condition Transformation

The radial cascade logarithmic spiral airfoils undergoing translation and torsion motions do not transform exactly to flat plates in the axial cascade undergoing the same motions.

To correct for this, the airfoils in the radial cascade are assumed to undergo small amplitude torsional and translation motions, Figure 5.3, with the corresponding motions in the axial cascade calculated through the transformation, Equation 5.5. The translation and torsion boundary conditions in the form of upwash velocities for the radial cascade are given in Equations 5.16 and 5.17.

$$v_h = \frac{dh}{dt} \quad 5.16$$

$$v_\alpha = U\alpha + \frac{d\alpha}{dt}(x - x_{ea}) \quad 5.17$$

where  $x$  is the distance along the vane nondimensionalized by the chord and  $x_{ea}$  is the nondimensional elastic axis location defined in Figure 5.2.

In classical isolated airfoil and axial flow cascade unsteady aerodynamic models, upstream airfoil wakes are modeled by convected harmonic gusts, Figure 5.4. The behavior of these convected gusts was discussed in Chapter 4, with the radial and tangential unsteady velocity components shown again in Equations 5.18 and 5.19.

$$\begin{aligned} v_r = \frac{1}{r} \frac{\partial \psi}{\partial \theta} = & \frac{i r_0 \Omega_0}{2} \left( r^{k_2 - 1} \int_1^r \exp(A \ln r + B r^2) r^{1 - k_2} dr - \right. \\ & \left. r^{-k_2 - 1} \int_1^r \exp(A \ln r + B r^2) r^{1 + k_2} dr \right) \exp(ik(\theta - t)) + \\ & \left( \frac{ik_2 a_1}{r_0} r^{k_2 - 1} + \frac{ik_2 a_2}{r_0} r^{-k_2 - 1} \right) \exp(ik(\theta - t)) \end{aligned} \quad 5.18$$

and

$$\begin{aligned} v_\theta = -\frac{\partial \psi}{\partial r} = & -\frac{r_0 \Omega_0}{2} \left( r^{k_2 - 1} \int_1^r \exp(A \ln r + B r^2) r^{1 - k_2} dr + \right. \\ & \left. r^{-k_2 - 1} \int_1^r \exp(A \ln r + B r^2) r^{1 + k_2} dr \right) \exp(ik(\theta - t)) + \\ & \left( -\frac{k_2 a_1}{r_0} r^{k_2 - 1} + \frac{k_2 a_2}{r_0} r^{-k_2 - 1} \right) \exp(ik(\theta - t)) \end{aligned} \quad 5.19$$

From these velocity components, the normal velocity induced by the wakes on the airfoil surfaces is computed, Equation 5.20.

$$v_n = v_r \sin \alpha_0 - v_\theta \cos \alpha_0 \quad 5.20$$

The translation, torsion and wake boundary conditions in the radial cascade, Equations 5.16, 5.17 and 5.20, are transformed to the axial flow cascade using the velocity transformation, Equation 5.6. The results are presented in Equations 5.21 through 5.23.

$$v_{hA} = \frac{dh}{dt} (r/r_2) \quad 5.21$$

$$v_{\alpha A} = \frac{U\alpha + \frac{d\alpha}{dt}(x - x_{ea})}{r/r_2} \quad 5.22$$

$$v_{nA} = \frac{v_r \sin \alpha_0 - v_\theta \cos \alpha_0}{r/r_2} \quad 5.23$$

The expressions for the radial cascade wake behavior, Equations 5.18 and 5.19, cannot be evaluated for  $k_2 < 2$ , due to the fact that  $\Omega_0$  cannot be chosen so that the wake velocities will remain bounded as  $r \rightarrow \infty$ . Because of this, the standard axial cascade upwash, Equation 5.24, is used in the transformed axial cascade at low reduced frequency.

$$v = v_0 \exp(ik'_A x - ik_A t) \quad 5.24$$

where the reduced frequency,  $k_A$ , is equal to the transformed reduced frequency in Equation 5.14, and  $k'_A$  is a transformed boundary condition reduced frequency. This separate reduced frequency occurs due to the deceleration of the steady flow with radius, thus decreasing the wavelength of the wake.

The transformation reduced frequency, Equation 5.14, is necessary due to the chord length change through the transformation and also the change in velocity at the leading edge. The reduced frequency in the boundary condition, Equation 5.24, is the ratio of the chord,  $c$ , to the gust wavelength,  $U/\omega$ , thus determining the number of wake wavelengths on the vane. Due to the velocity decrease with radius in the radial cascade, the gust

wavelength becomes smaller toward the trailing edge. The transformed boundary condition reduced frequency is then

$$k'_A = k \frac{(2 - \Delta r/r_2)}{2(1 - \Delta r/r_2)} \quad 5.25$$

The boundary condition, Equation 5.20, is only necessary at low  $k$ , with the more physically realistic wake velocities in Equations 5.18 and 5.19 used at higher values of  $k$  which would be encountered in real machines.

#### 5.4 Model Verification

To validate the transformation technique and radial cascade modeling, the radial cascade unsteady aerodynamic lift and moment are predicted for the special case of  $\Delta r/r_2 \rightarrow 0$ . In this case, the radial cascade flowfield approaches that of an axial flow cascade. The radial cascade parameters are  $N_v = 300$ ,  $\sigma = 60^\circ$ ,  $\Delta r/r_2 = 0.01$  and  $r_{ea} = 0$ , as defined in Figure 5.2. For the axial cascade,  $s/c = 1.0$ ,  $\sigma = 60^\circ$ , and  $x_{ea} = 0$ . The number of airfoils in the radial cascade was chosen to give a transformed axial cascade solidity of 1.0.

Figures 5.5 through 5.10 show the unsteady lift due to translation, the unsteady moment due to torsion and the unsteady lift due to a transverse gust for both the baseline axial and radial flow cascades over a range of reduced frequencies and interblade phase angles. The predicted unsteady aerodynamics of the baseline radial cascade approach that of the axial cascade, thereby verifying the transformation and the radial cascade unsteady aerodynamic modeling.

#### 5.5 Results

The fundamental differences between radial and axial cascade unsteady aerodynamics are considered by utilizing this model to predict radial and corresponding axial cascade unsteady aerodynamics. In particular, the unsteady aerodynamic translational lift, torsional moment, and convected gust lift as well as the corresponding unsteady pressure distributions are analyzed. The baseline radial cascade parameters are  $N_v = 12$ ,  $\sigma = 60^\circ$ ,  $\Delta r/r_2 = 0.25$  and  $r_{ea} = 0$ . The baseline geometry differs from the previous cases only in

that the vane radial extent,  $\Delta r/r_2$ , is greater, thereby demonstrating the effects of the radial geometry.

Figure 5.11 shows the unsteady aerodynamic translational lift,  $C_L$ , for the baseline radial cascade as a function of the reduced frequency and interblade phase angle. For this translational response, the unsteady lift will amplify the motion when the real part of  $C_L$  is positive, indicating a possible flutter condition. For both the axial and radial cascades, all points shown have negative real values and thus are stable. Also, the stability margins for both cascades are similar. The unsteady lift amplitude for the radial cascade is slightly higher in general than the axial flow cascade.

Figure 5.12 presents the unsteady aerodynamic torsional moment,  $C_M$ , for the baseline radial cascade as a function of the reduced frequency and interblade phase angle. In this case, the imaginary part of  $C_M$  determines stability, with a stable cascade for  $C_M < 0$ . The stability is similar for both the axial and radial cascades, with the zero reduced frequency results unstable for both cascades, but all other reduced frequency configurations stable. As for the translational response, the interblade phase angle has a lesser effect on the unsteady moment for the radial cascade than for the axial. The unsteady moment amplitudes are greater for the axial cascade at low reduced frequency and become roughly equal at higher reduced frequency.

The unsteady aerodynamic response of the baseline cascade to a convected transverse gust as a function of the reduced frequency and interblade phase angle is shown in Figure 5.13. Since the reduced frequency is low ( $k < 2$ ), the standard axial cascade upwash, Equation 4.2, is used in the transformed axial cascade. As with the translational and torsional responses, Figure 5.10 shows that the interblade phase angle has a lesser effect in the radial cascade than the axial cascade. The unsteady lift amplitude is smaller for the radial cascade than the axial.

Figures 5.14 and 5.15 show the unsteady airfoil pressure difference  $C_{\Delta P}$  due to translation and torsion for a single reduced frequency/interblade phase angle combination from each of Figures 5.11 through 5.13. The unsteady pressure difference is presented for the radial cascade and for the axial cascade conditions of Figures 5.5, 5.7 and 5.9. The unsteady pressure is greater for the radial cascade undergoing plunging motions which is consistent with Figure 5.11. The unsteady pressure due to pitching is greater at the airfoil leading edge for the radial cascade and greater at the trailing edge for the axial cascade.

Figure 5.16 shows the unsteady airfoil pressure difference due to a convected gust upwash for radial and axial flow cascades. In this figure,  $k = 2$  and  $\phi_b = 0^\circ$ , with the transformed cascade upwash given by Equation 5.20. In Figure 5.17,  $k = 4$  and the radial

cascade airfoil pressure difference with the wake model upwash, Equations 5.18 and 5.19, is shown. The axial cascade unsteady pressure is greater than the radial cascade, consistent with Figure 5.13. In Figure 5.17, the axial cascade unsteady pressure is greater than the radial cascade with the standard upwash, Equation 5.20, but is less than the radial cascade with the wake model upwash, Equations 5.18 and 5.19. Using these more physically realistic wake expressions increases the predicted radial cascade lift.

In Chapter 6, the unsteady diffuser vane pressure distribution measured in the Purdue Centrifugal Compressor Facility will be presented. The preceding analysis will be compared with the measured data.



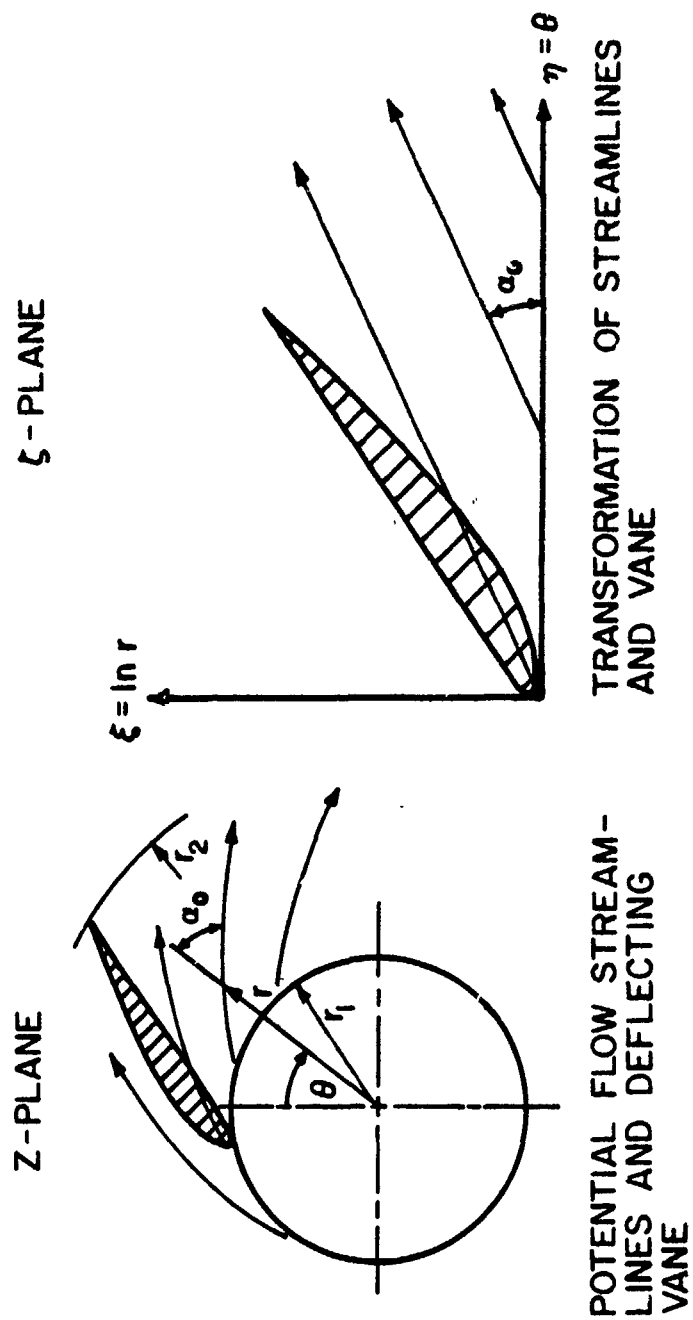


Figure 5.1 Radial Cascade Conformal Transformation

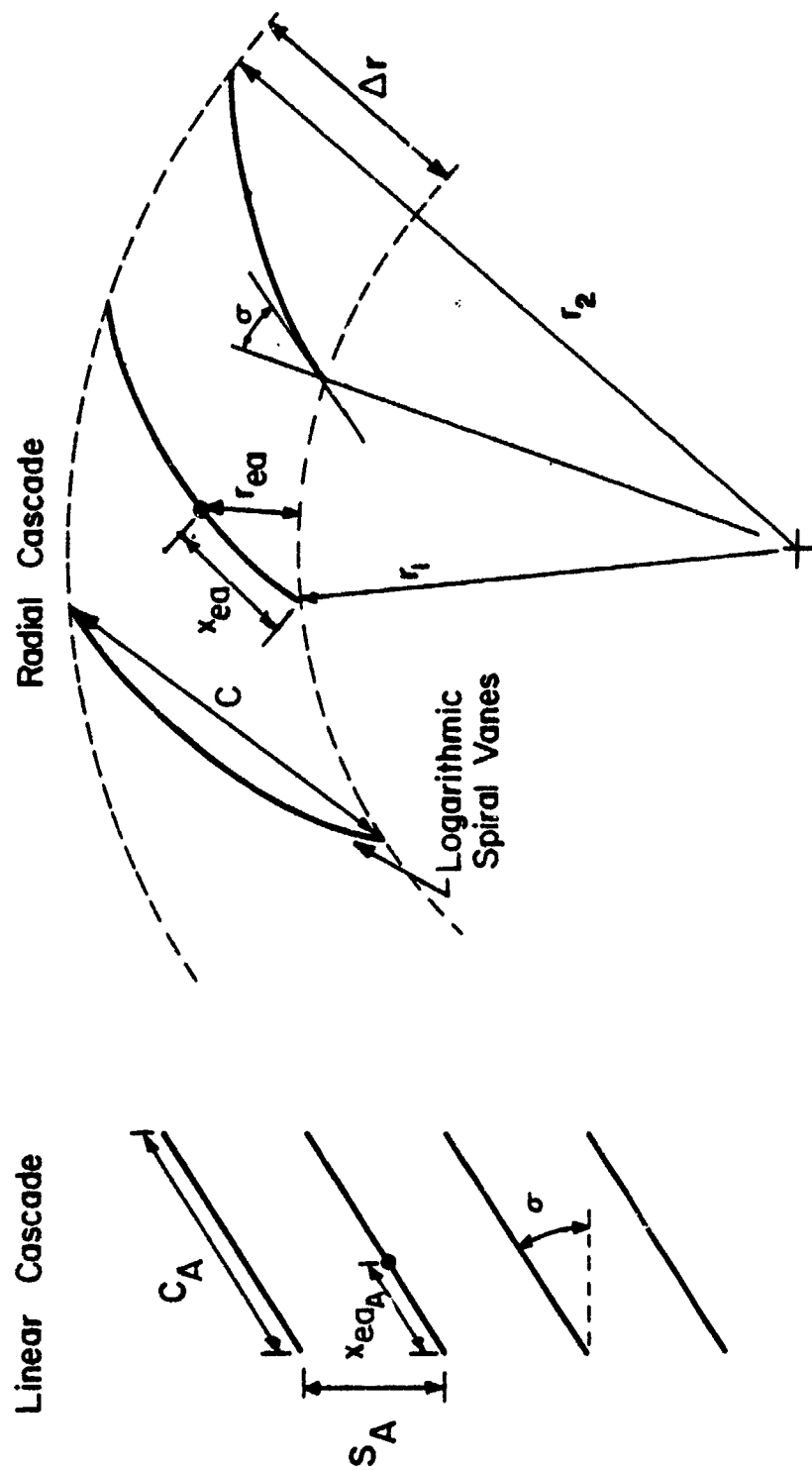


Figure 5.2 Flat Plate Cascade Transformation

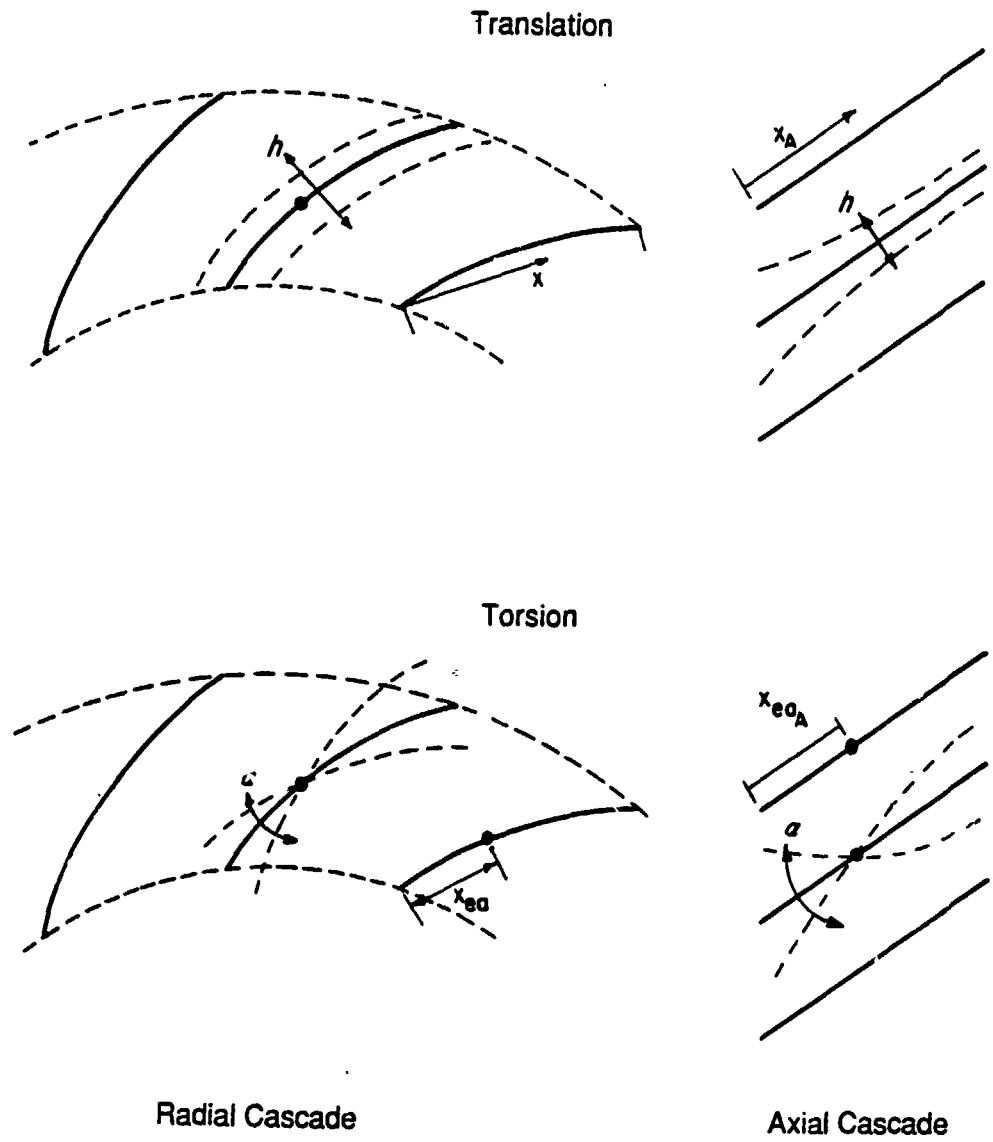
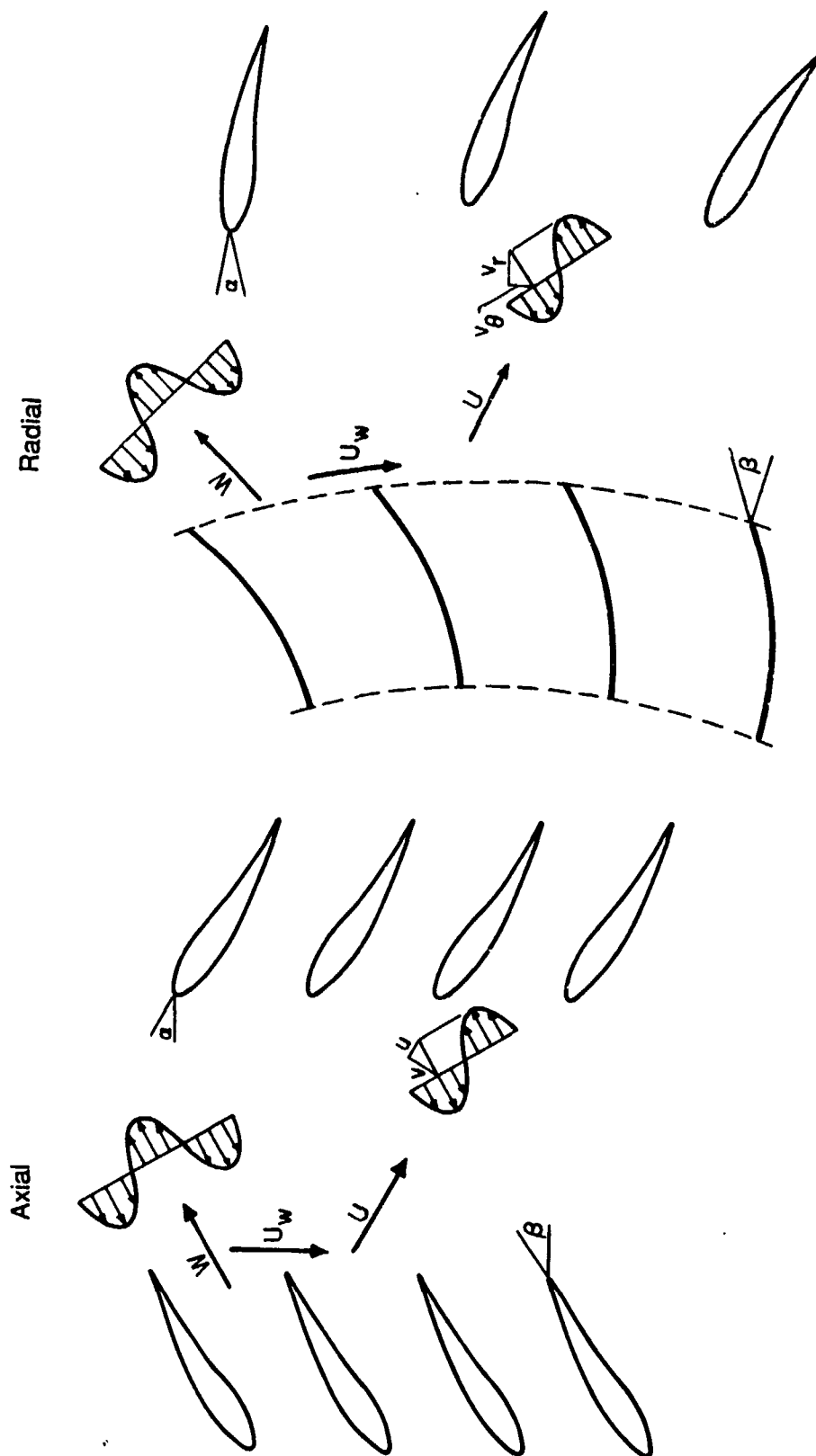


Figure 5.3 Translation and Torsion Upwash Transformation



### Figure 5.4 Shed Vortical Gusts in Axial and Radial Turbomachines

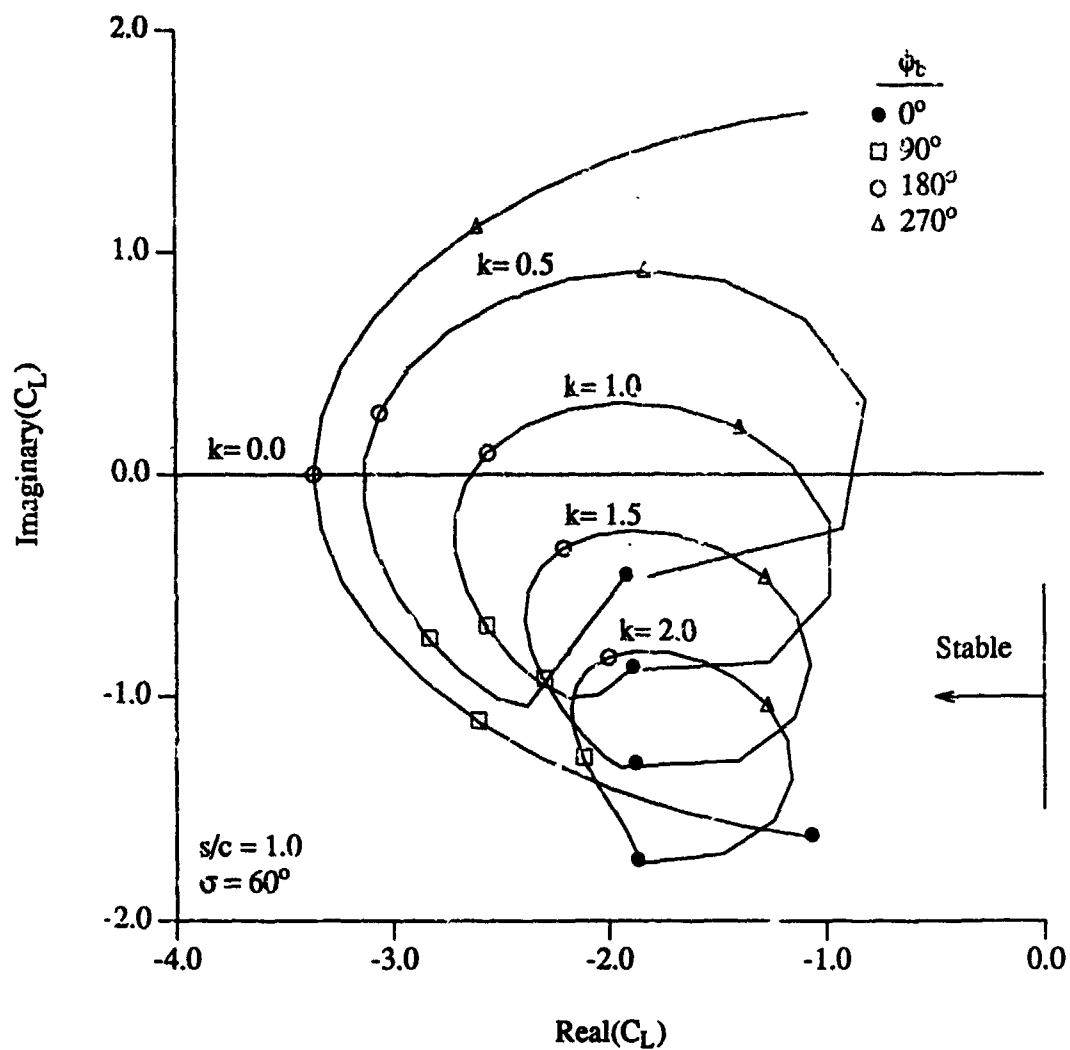


Figure 5.5 Baseline Axial Flow Cascade Translational Lift

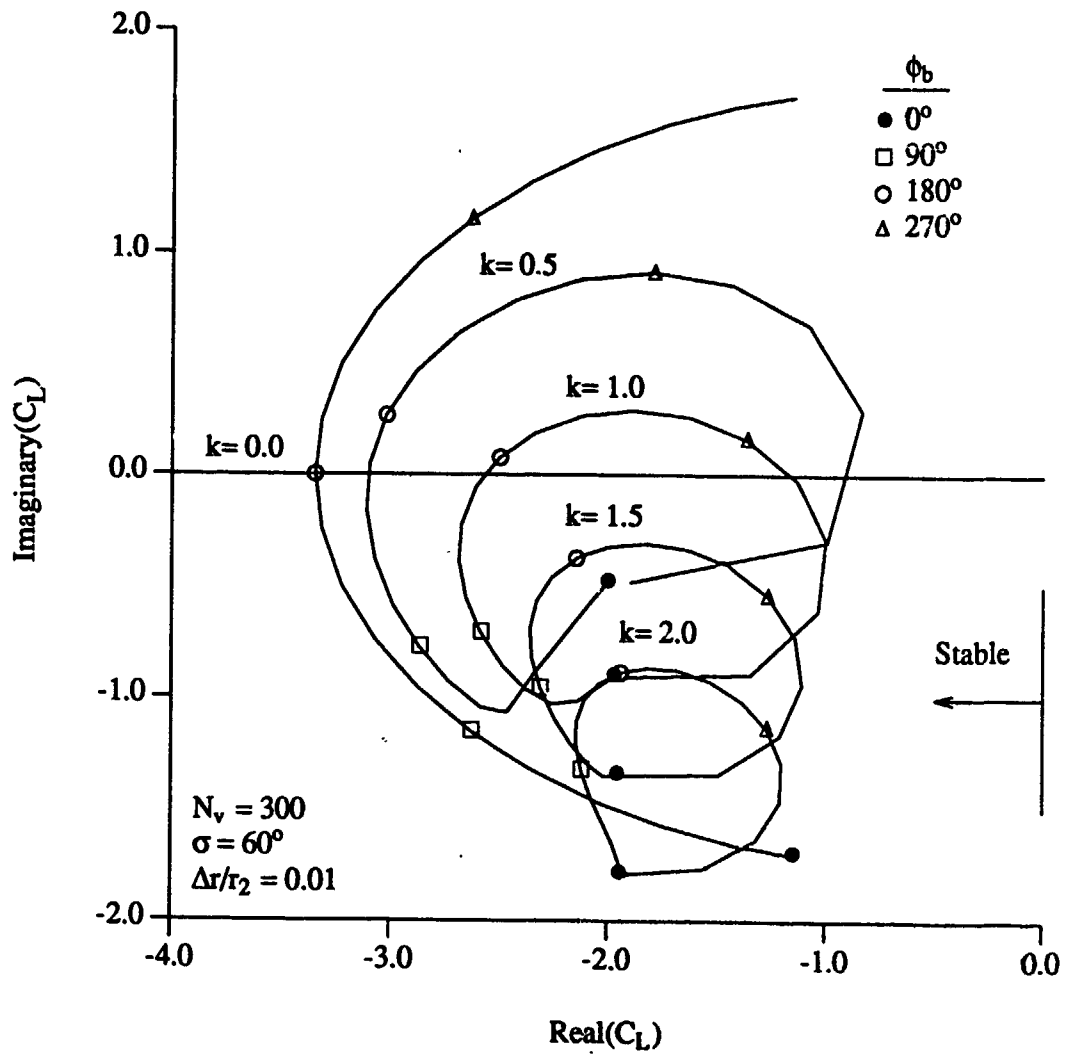


Figure 5.6 Baseline Radial Flow Cascade Translational Lift

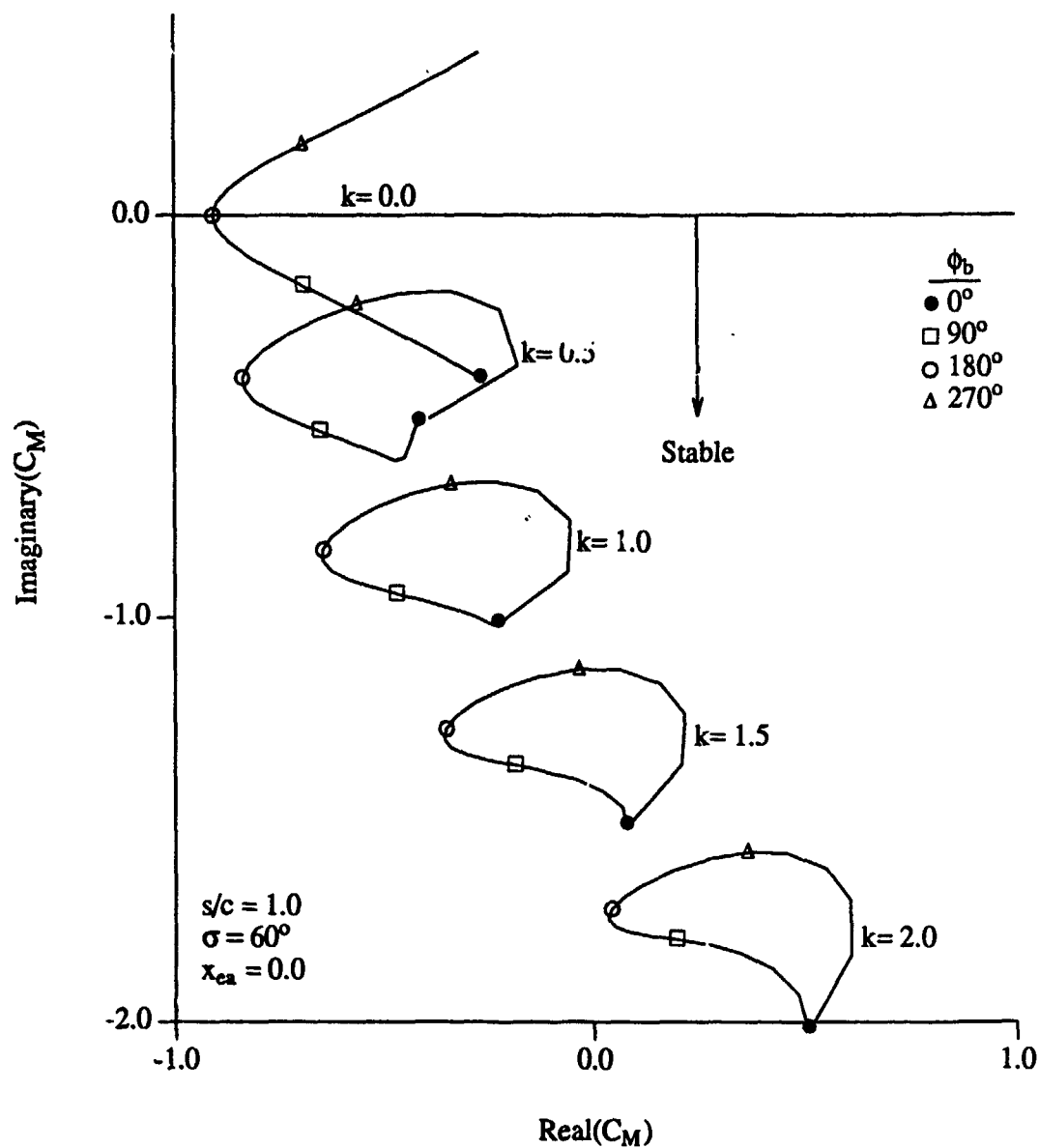


Figure 5.7 Baseline Axial Flow Cascade Torsional Moment

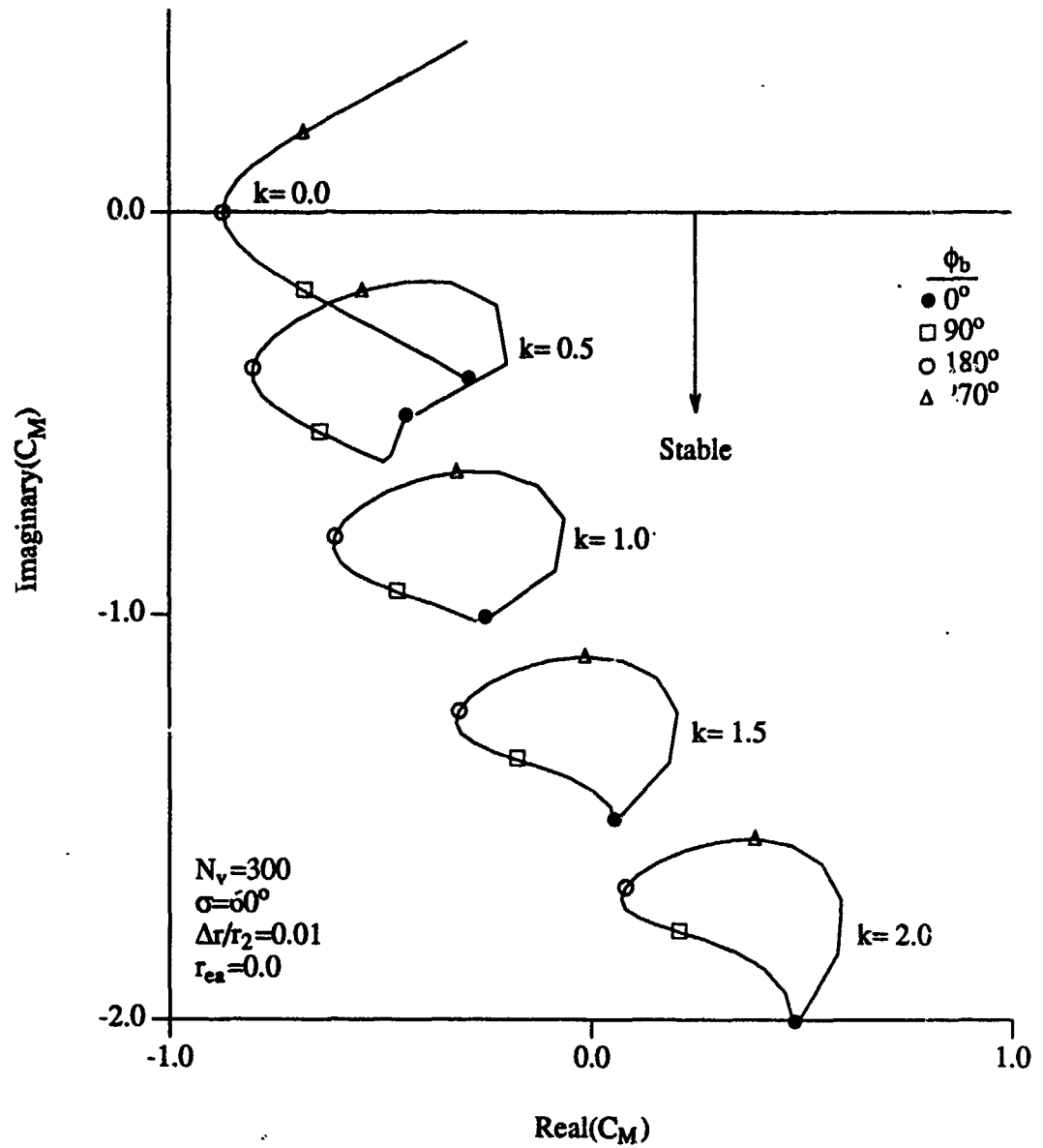


Figure 5.8 Baseline Radial Flow Cascade Torsional Moment



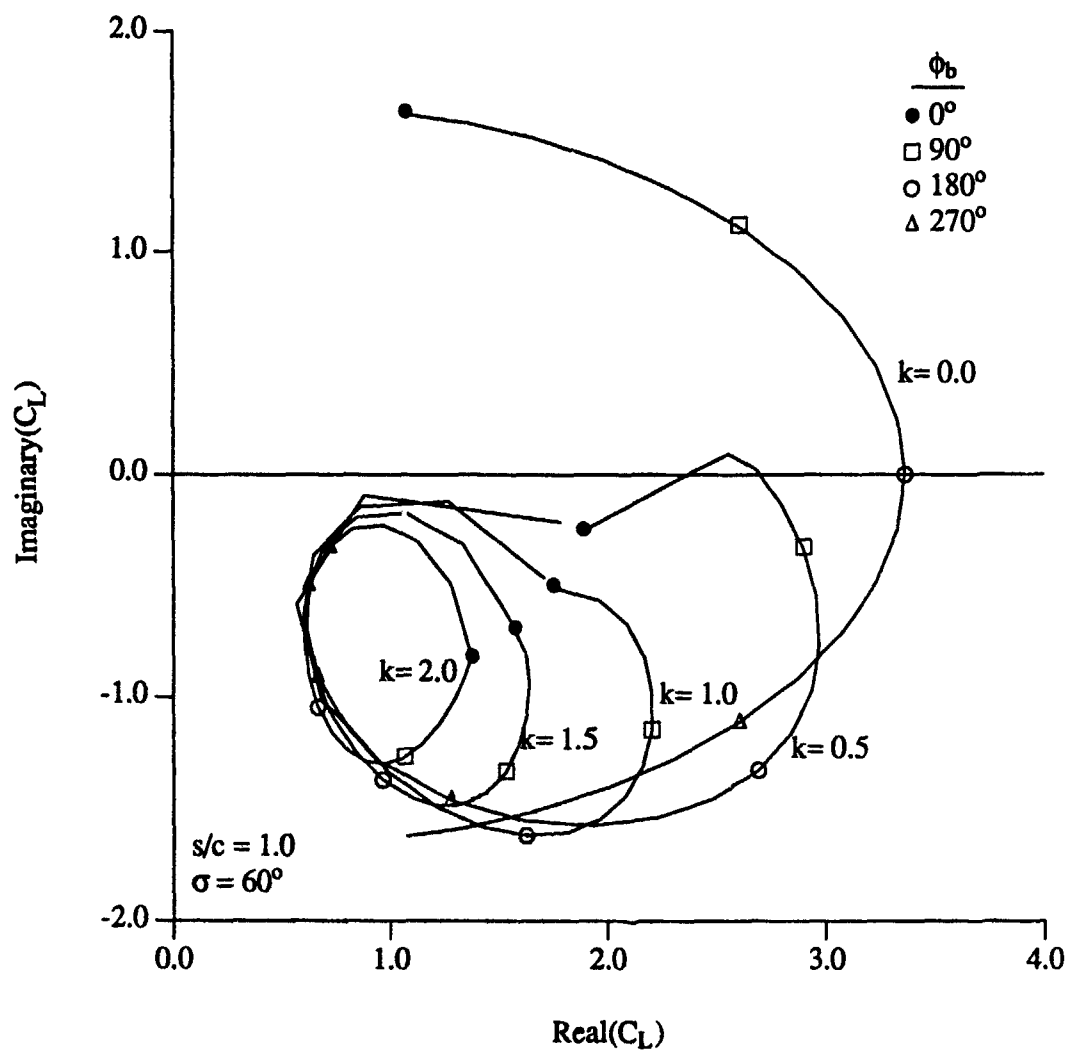


Figure 5.9 Baseline Axial Flow Cascade Convected Gust Lift

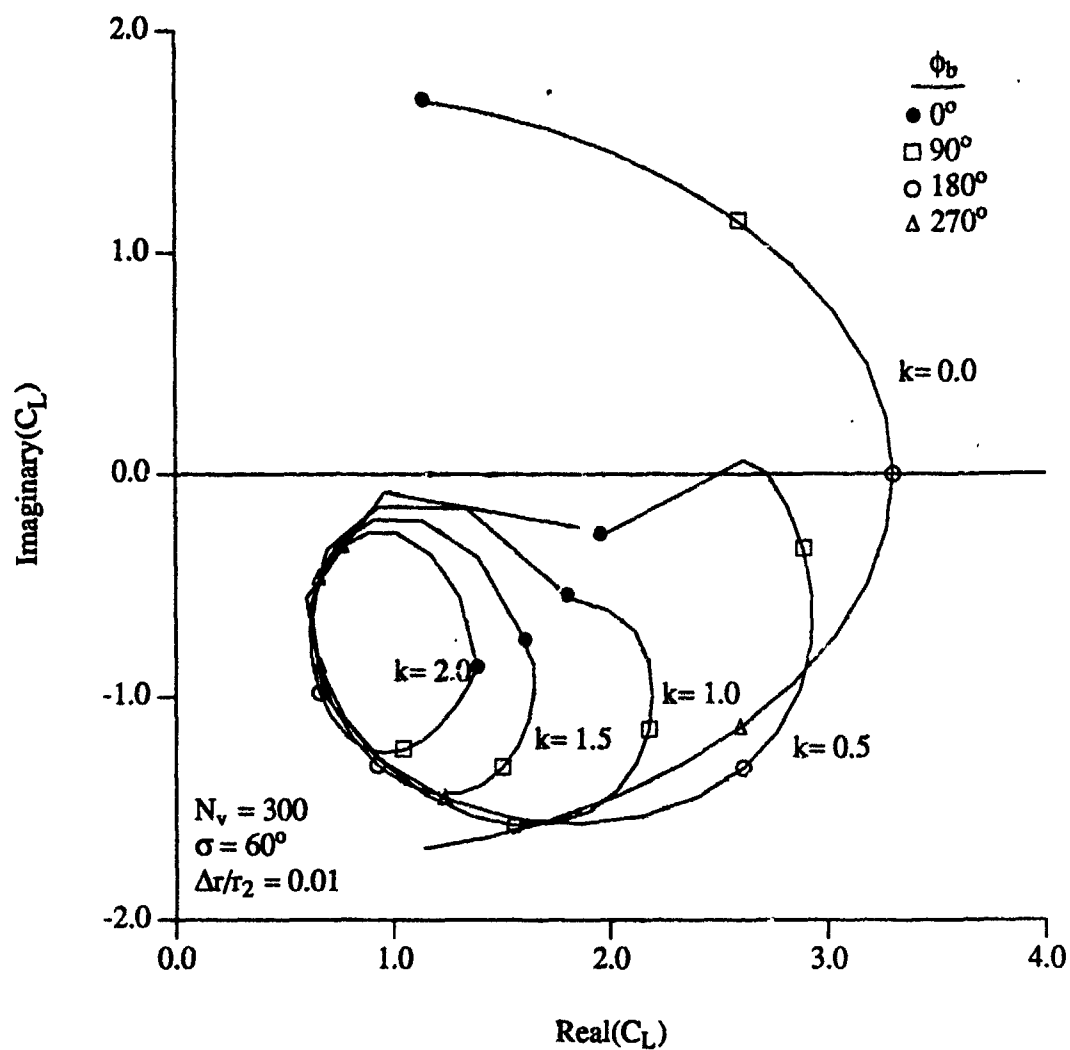


Figure 5.10 Baseline Radial Flow Cascade Convected Gust Lift

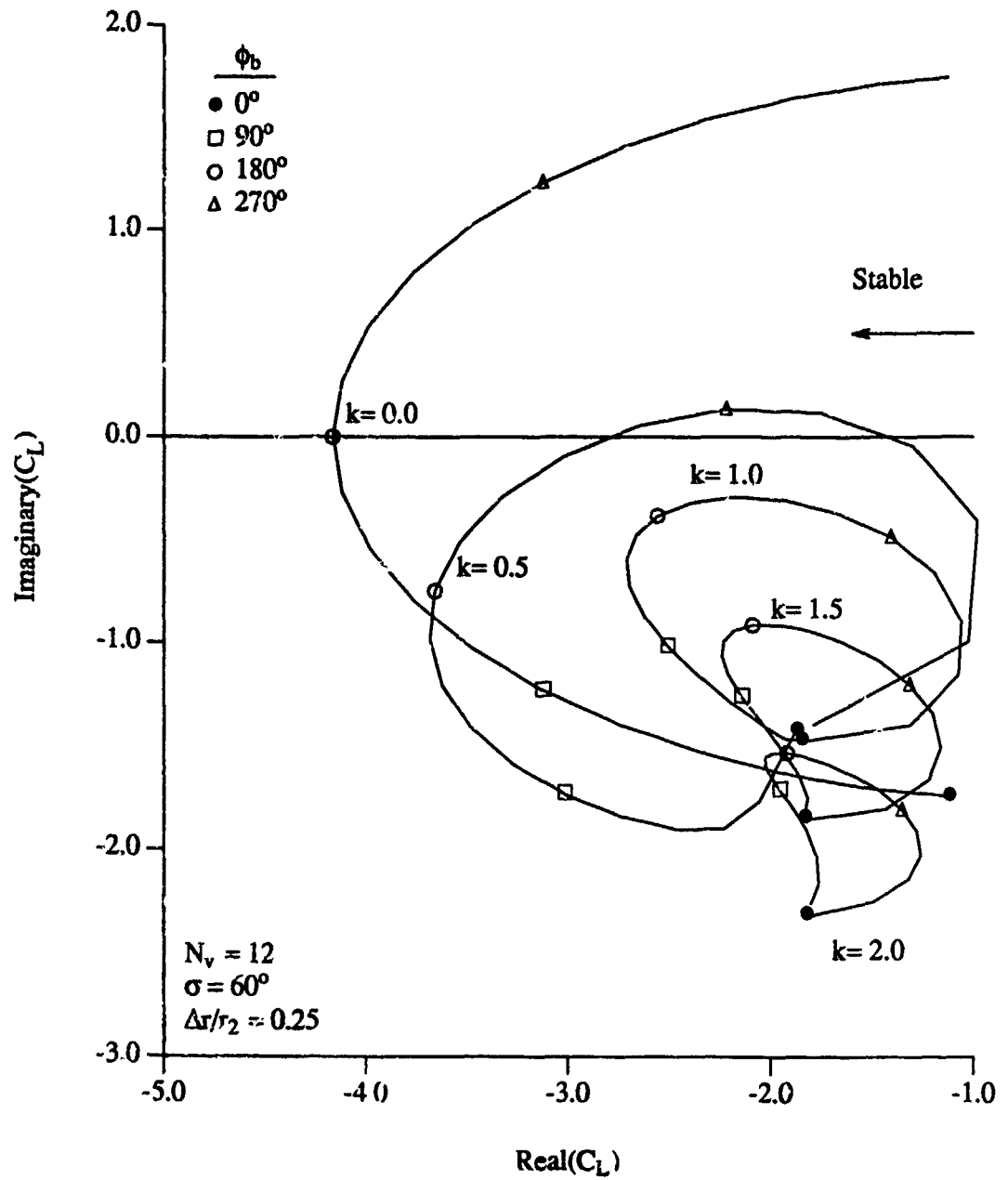


Figure 5.11 Radial Flow Cascade Translational Lift

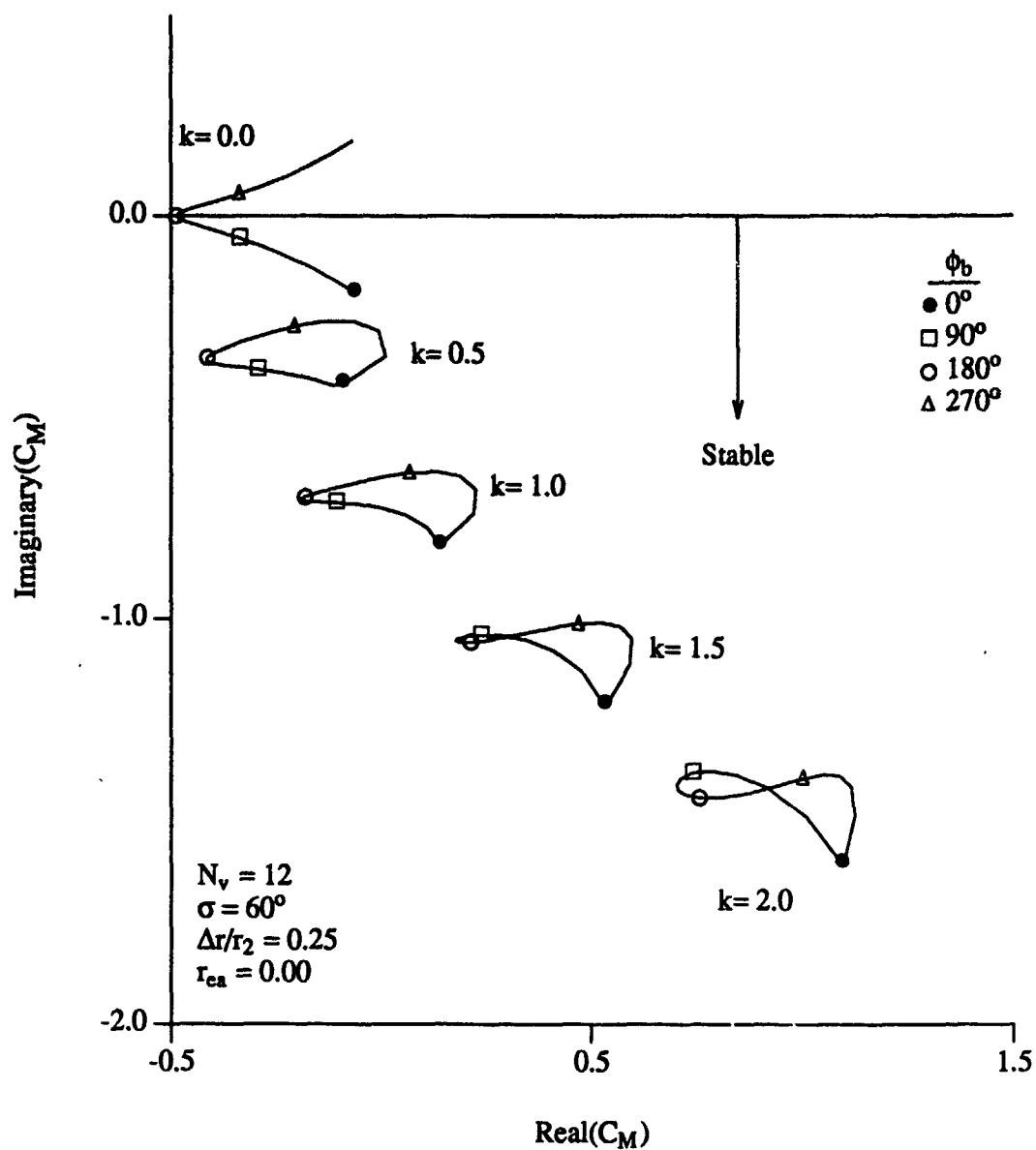


Figure 5.12 Radial Flow Cascade Torsional Moment

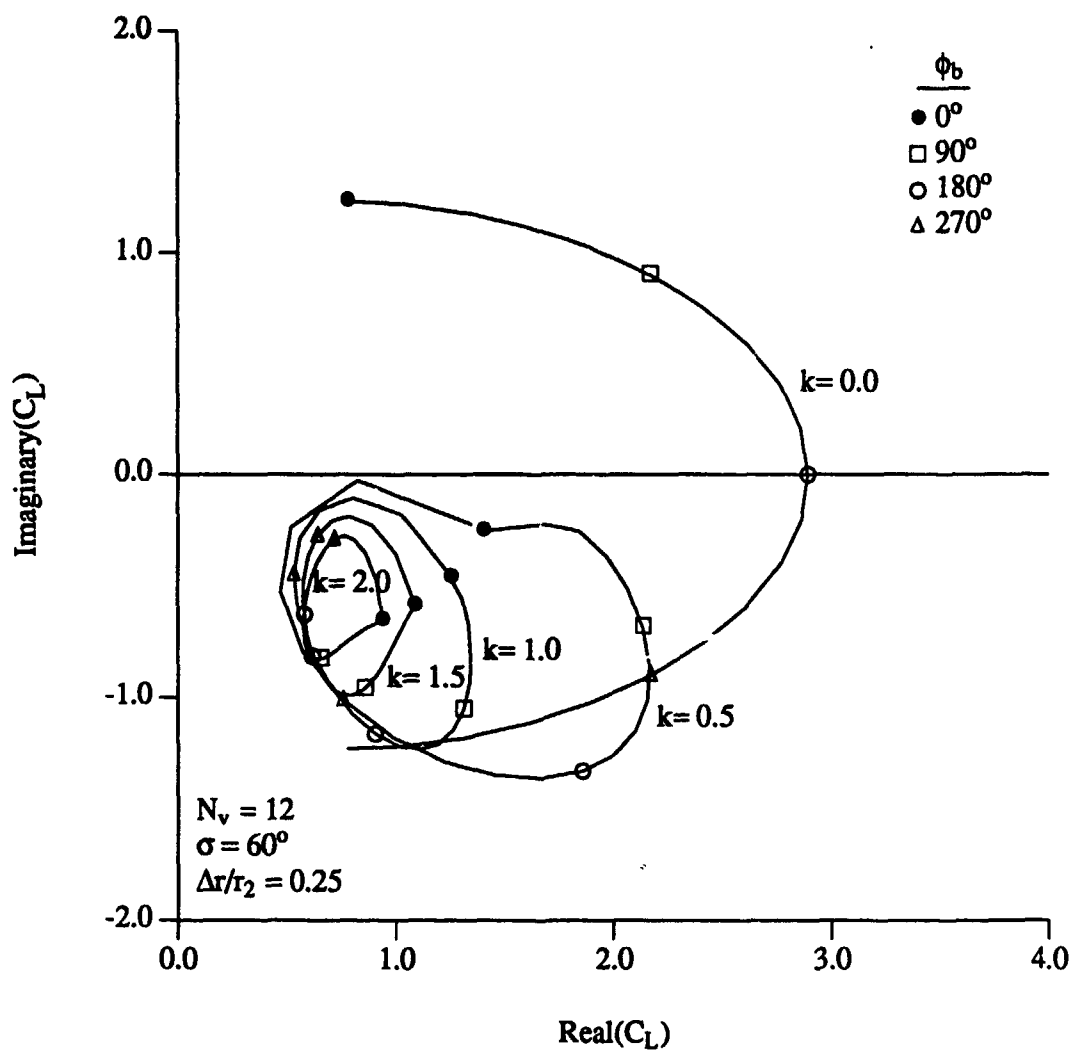


Figure 5.13 Radial Flow Cascade Convected Gust Lift

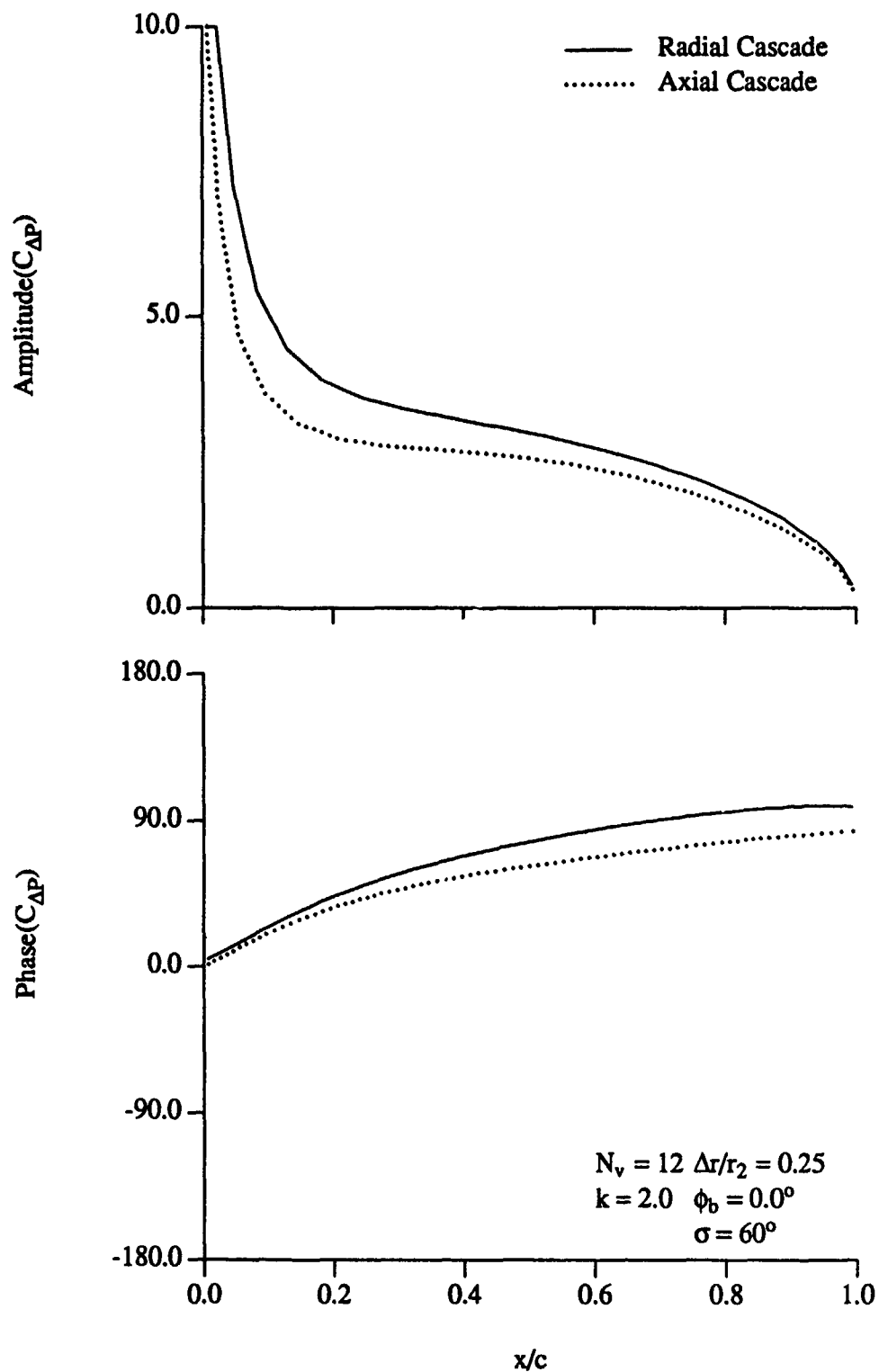


Figure 5.14 Unsteady Airfoil Pressure for Translational Motion

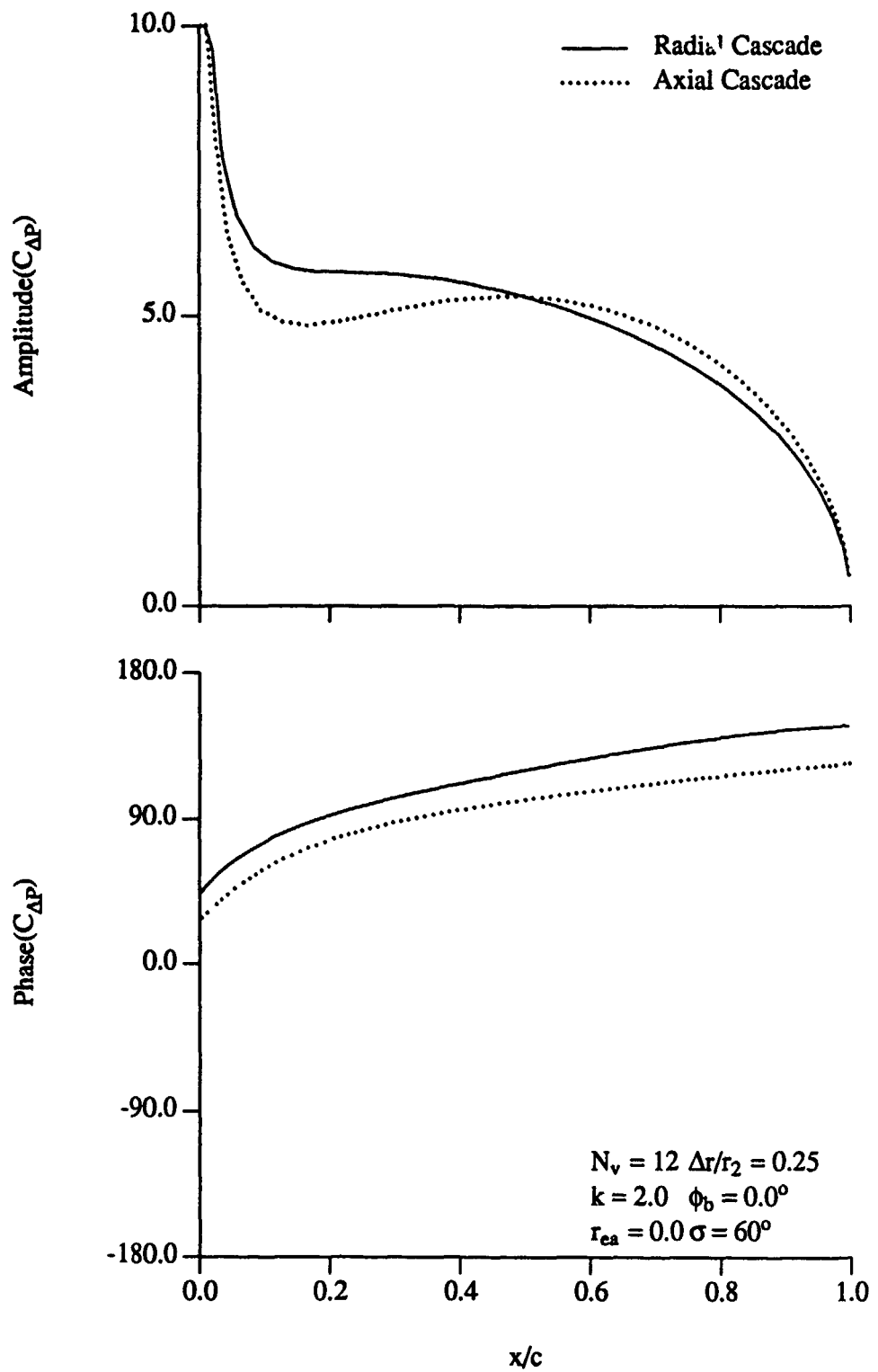


Figure 5.15 Unsteady Airfoil Pressure for Torsional Motion

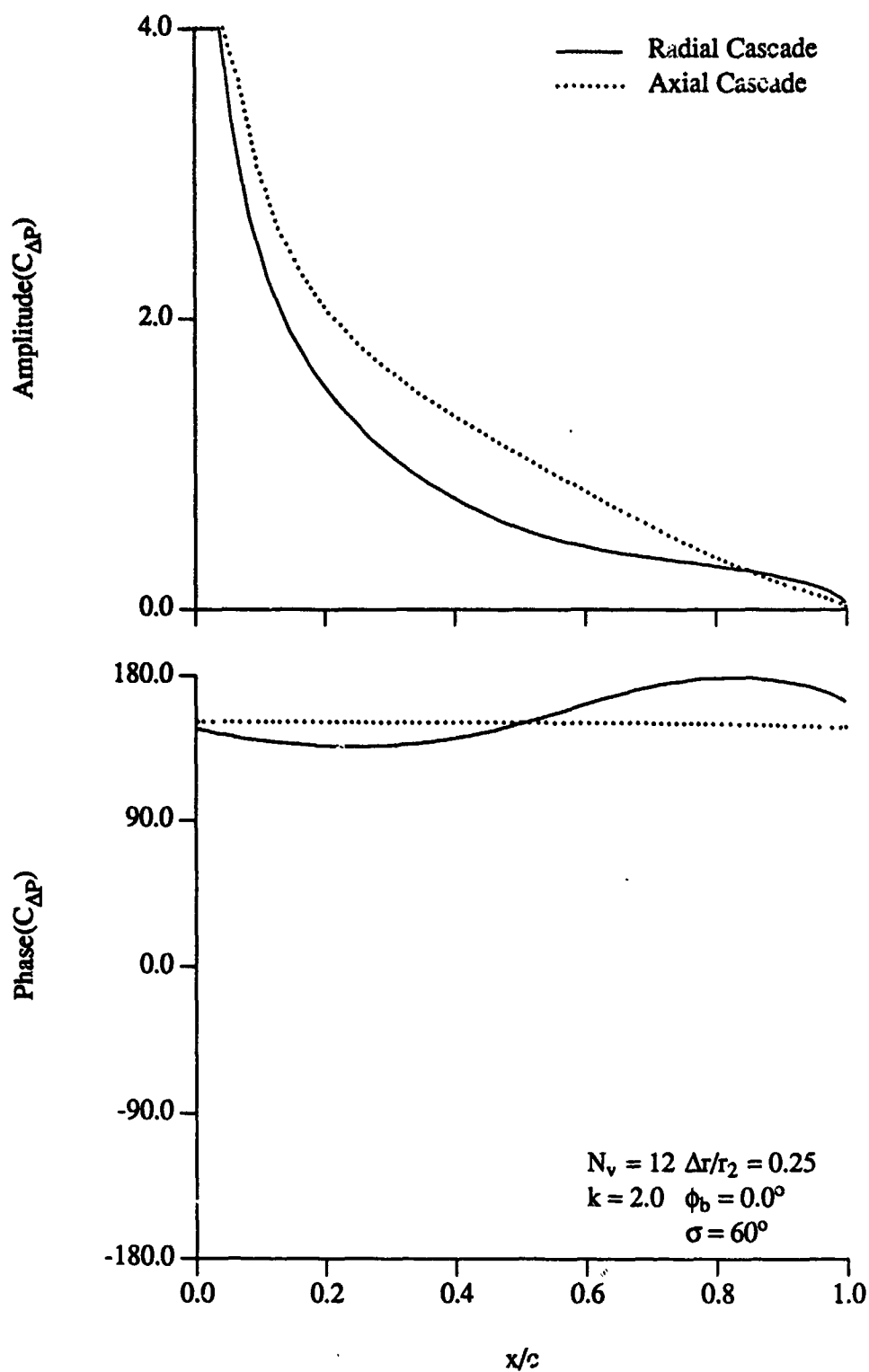


Figure 5.16 Unsteady Airfoil Pressure for Convected Gust Upwash ( $k = 2.0$ )



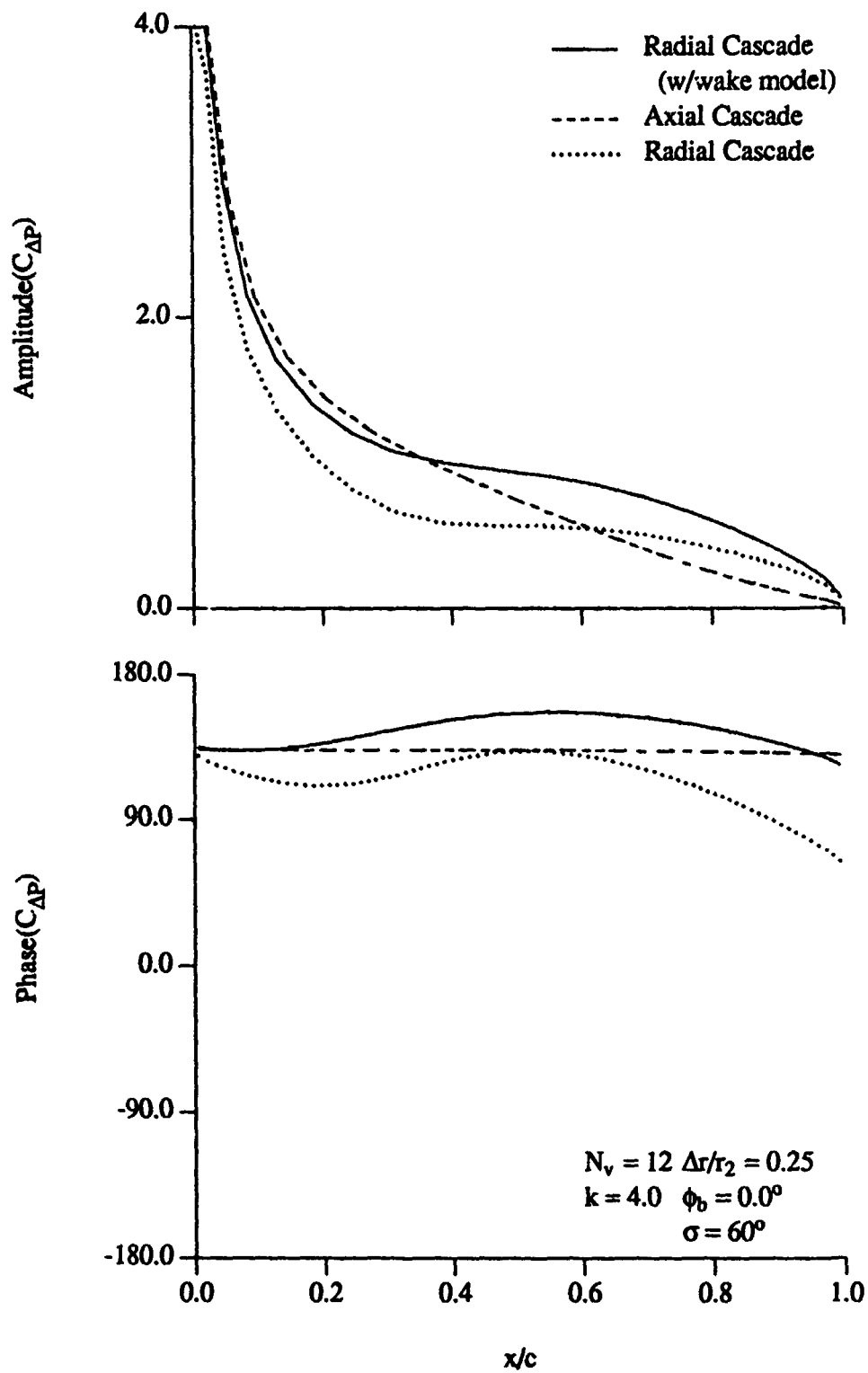


Figure 5.17 Unsteady Airfoil Pressure for Convected Gust Upwash ( $k = 4.0$ )

## CHAPTER 6

### EXPERIMENTAL RESULTS

A set of experiments was performed in the Purdue Research Centrifugal Compressor to investigate the overall impeller and diffuser performance, impeller and diffuser steady flowfield, unsteady radial diffuser wake behavior, unsteady diffuser vane surface static pressure and the occurrence of rotating stall and surge. These quantities are measured for varying flow rate,  $\Phi$ , number of diffuser vanes,  $N_v$ , diffuser vane stagger,  $\sigma$ , diffuser vane leading edge/impeller exit radius ratio,  $r_1/r_0$ , and diffuser vane row detuning using nonuniform circumferential spacing. The various machine geometric conditions are shown in the following table.

Table 6.1 Research Compressor Geometric Configurations

	$N_v = 30$	$N_v = 15$	$N_v = 10$	$N_v = 0$
$\sigma = 50^\circ$	$r_1/r_0 = 1.10$ $r_1/r_0 = 1.15$	$r_1/r_0 = 1.10$		
$\sigma = 60^\circ$	$r_1/r_0 = 1.10$ $r_1/r_0 = 1.10$ (40% detuned) $r_1/r_0 = 1.15$	$r_1/r_0 = 1.10$ $r_1/r_0 = 1.15$	$r_1/r_0 = 1.10$ $r_1/r_0 = 1.10$ (13% detuned)	Vaneless
$\sigma = 70^\circ$	$r_1/r_0 = 1.10$ $r_1/r_0 = 1.15$	$r_1/r_0 = 1.10$		

At each of the diffuser geometric configurations listed in Table 6.1, steady data are acquired over a range of flow coefficients, typically from  $\Phi = 0.16$  to 0.33. Additionally, unsteady airfoil surface pressure data are acquired at  $\Phi = 0.17$ , 0.22 and 0.30. Laser velocimeter measurements are made for the vaneless configuration at  $\Phi = 0.17$ , 0.22 and 0.30.

### 6.1 Compressor Performance

The compressor performance was determined for each of the geometric conditions in Table 6.1. The performance is presented as the pressure rise coefficient,  $\Psi$ , and efficiency,  $\eta$ , versus the flow coefficient,  $\Phi$ . For the vaneless diffuser, the results are presented for the impeller and also for the impeller/diffuser stage. For the vaned diffuser, only the stage results are presented. The high flow coefficient on the performance plots corresponds to the completely open throttle valve, whereas the low flow coefficients correspond to stall or surge (typically  $\Phi \approx 0.16$ ). The stall and surge points will be discussed more fully in Section 6.6.

Generally, vaned diffusers are utilized to improve the stage performance. The vaned diffuser itself imposes a performance loss and can adversely affect the overall operating range as well as the stall and surge margins. The benefits are due to its ability to favorably affect the aft impeller and vaneless space flowfields, thereby improving overall stage performance and sometimes extending the machine operating range into either lower or higher flow rates.

The vaneless diffuser machine performance is presented in Figure 6.1. The maximum pressure rise occurs at  $\Phi = 0.19$ , with the maximum efficiency at  $\Phi = 0.22$ . These values are also typical of the vaned diffuser performance. There is typically a 5% loss in both the total pressure and efficiency through the vaneless diffuser at each operating point.

Figures 6.2 and 6.3 present the stage performance for various values of the diffuser vane stagger angle,  $\sigma$ . In these figures,  $r_1/r_0 = 1.10$ , and  $N_v = 30$  and 15 respectively. For  $N_v = 30$ , the stage performance with the vaneless diffuser is typically similar or better than that with the vaned diffuser. The stage performance at  $\sigma = 70^\circ$  is particularly worse due to the large blockage (vane row open area/total area). For the vaned diffuser with  $N_v = 15$ , the stage performance is greater than for the vaneless stage. For all values of  $\sigma$ , the vaned diffuser yields a stage performance improvement over that with the vaneless diffuser for  $\Phi > 0.27$ . At the maximum efficiency point, there is a 3% efficiency gain for  $\sigma = 70^\circ$  over the vaneless case. The performance is greater at higher  $\Phi$  for smaller values of  $\sigma$  and greater at lower  $\Phi$  for larger  $\sigma$ . This is due in part to the incidence angle variation on the diffuser vane row with flow rate. Since the impeller is backswept, the absolute flow angle,  $\alpha_0$ , decreases with increasing flow rate, increasing the incidence on the diffuser vanes. Therefore, smaller values of  $\sigma$  yield improved performance at higher flow rates with higher  $\sigma$  better at low flow. In Figure 6.4,  $r_1/r_0 = 1.15$  and  $N_v = 30$ . The performance is similar to  $r_1/r_0 = 1.10$  except for  $\sigma = 60^\circ$  where the performance is significantly improved. This behavior is not understood since the performance at  $\sigma = 50^\circ$

and  $70^\circ$  is slightly greater at  $r_1/r_0 = 1.10$  and typically, the performance is improved for closer vane/impeller spacing.

Figures 6.5 through 6.7 present the stage performance for various numbers of diffuser vanes,  $N_v$ . In Figure 6.5, the performance is slightly greater for  $N_v = 15$ , except for  $\Phi > 0.30$ , where presumably the greater number of vanes delays separation at negative incidence angles. In Figure 6.6, the performance is similar for  $N_v = 30$  and 15 but improved at higher flow rates for  $N_v = 10$ . In Figure 6.7, the performance improves for  $N_v = 15$ .

As the vane stagger angle,  $\sigma$ , is increased, the area blocked by the diffuser vane row increases with the flow area between the vanes decreasing. This reduces the flow area with respect to the surface area, thus increasing the relative effects of skin friction. Therefore, at lower values of  $\sigma$ , the number of diffuser vanes has a lesser effect but for higher  $\sigma$ , the blocked area increases with more vanes yielding a performance penalty. If the number of vanes is small, the skin friction is less but the ability of the vane row to favorably affect the flow and to avoid separation is diminished. Therefore, competing effects due to the number of vanes and vane stagger angle exist which must be determined from the desired performance and operating range.

In Figure 6.8, the effect of radius ratio,  $r_1/r_0$ , is shown for  $\sigma = 60^\circ$ . A significant gain in total pressure and efficiency is seen for  $r_1/r_0 = 1.15$  as compared to  $r_1/r_0 = 1.10$  or the vaneless case, with a maximum efficiency gain of 3%. For  $\sigma = 50^\circ$  and  $\sigma = 70^\circ$ , the change in performance due to radius ratio is minimal.

The performance for the detuned diffuser vane row using nonuniform circumferential spacing is also determined. To accomplish this, every other blade mounting cam is rotated in the opposite direction of its neighbor, yielding a nonuniform circumferential airfoil spacing, Figure 6.9. An even number of blades must be used and only one detuning ratio is possible for each  $\sigma$  and  $r_1/r_0$ , due to the cam geometry. Figures 6.10 and 6.11 show the effect of detuning for  $\sigma = 60^\circ$  and  $r_1/r_0 = 1.10$ . For Figure 6.10,  $N_v = 30$  with 40% detuning, indicating every other airfoil has been angularly displaced 40% of the uniformly spaced cascade angle. For this case, the performance change is minimal, with all differences within the experimental uncertainty. For Figure 6.11,  $N_v = 10$  with 13% detuning. A slight increase in the efficiency and pressure rise coefficient is seen for lower flow rates. For the tuned vane row with  $\sigma = 60^\circ$  and  $r_1/r_0 = 1.10$ , the performance with  $N_v = 10$  is decreased compared to that for higher numbers of vanes at lower flow rates. Perhaps the detuning yields an effect similar to increasing  $N_v$ , since every other blade is more closely spaced.

In summary, the vaned diffuser can improve the stage performance over that of a vaneless diffuser. The performance improvement is greatest when the diffuser vane incidence is low and the blockage is small. The diffuser vane stagger angle and the number of vanes were the most important parameters.

## 6.2 Impeller Steady Loading

Impeller blade static pressure measurements are made to determine the steady loading on the rotating impeller. This is accomplished using the rotating Scanivalve described in Chapter 3. Measurement locations are shown in Figure 2.5. The pressure and suction surface static pressure coefficient,  $\overline{C_p}$ , and the pressure difference coefficient,  $\overline{C_{\Delta p}}$  are plotted versus the nondimensional impeller radius,  $r/r_0$  along three streamlines.

Figures 6.12 through 6.14 show the impeller blade surface static pressure distributions for  $\Phi = 0.17, 0.22$  and  $0.30$  for the vaneless diffuser. At  $\Phi = 0.17$ , the blade loading indicated by the pressure difference coefficient,  $\overline{C_{\Delta p}}$ , is uniform at the hub and mean with the tip having higher loading at impeller inlet and exit. The higher loading at the impeller inlet tip is likely due to positive blade incidence caused by the low axial velocity. The blade loading at the maximum efficiency point,  $\Phi = 0.22$ , is uniform for each streamline with the loading slightly less than that at  $\Phi = 0.17$  along the mean and tip streamline. The impeller blade loading at  $\Phi = 0.30$  is less uniform than the previous cases, although higher in magnitude. At the impeller inlet, a low pressure on the pressure surface and higher pressure on the suction surface occurs, especially toward the blade tip, indicating a slight negative incidence separation. Generally, the blade loading increases with flow rate, due to the increased coriolis acceleration.

In Figure 6.15, the impeller blade surface static pressure and pressure difference for  $r_1/r_0 = 1.10$ ,  $\sigma = 50^\circ$ ,  $N_v = 30$  and  $\Phi = 0.30$  are presented along with the vaneless data at  $\Phi = 0.30$ . The impeller blade loading indicated by  $\overline{C_{\Delta p}}$  is greater for the vaneless diffuser over the entire blade except at the impeller inlet tip, where the loading with the vaned diffuser is slightly greater. Although the loading is higher with the vaneless diffuser, the overall static pressure,  $\overline{C_p}$ , is generally greater for the vaned diffuser. In Figure 6.16, the impeller blade surface static pressure and loading for  $r_1/r_0 = 1.10$ ,  $\sigma = 60^\circ$ ,  $N_v = 30$  and  $\Phi = 0.22$  is presented along with the vaneless data. The vaned diffuser has caused a slight increase in impeller loading at the tip and mean blade positions. The results for  $\sigma = 70^\circ$  are similar.

For Figures 6.15 and 6.16, the diffuser vane incidence angle is low and therefore the diffuser vane loading indicated by the steady pressure difference is small. For  $\Phi = 0.30$  in Figure 6.15, the performance indicated by the efficiency and pressure rise coefficients is higher for the vaned diffuser. For Figure 6.15 with  $\Phi = 0.22$ , the performance is the same for the vaned and vaneless diffusers. At all other flow rates and diffuser geometries, no effect of diffuser geometry is seen on the impeller blade static pressure or loading.

Therefore, the impeller loading indicated by the blade surface static pressure differential generally increases with increased flow rate. The impeller blade loading is only affected when 30 diffuser vanes are used and the diffuser vane incidence is low producing low vane loading.

### 6.3 Diffuser Vane Steady Loading

Diffuser vane surface static pressure measurements are made at the vane mean axial position and chordwise locations indicated in Figure 3.2. The pressure and suction surface steady pressure coefficients,  $\overline{C_p}$ , and the pressure difference coefficient,  $\overline{C_{\Delta p}}$  are presented as a function of nondimensional chordwise distance.

In Figure 6.17, the diffuser vane static pressure is presented for  $r_1/r_0 = 1.10$ ,  $\sigma = 60^\circ$  and  $N_v = 15$ . Three curves are shown on each plot, each for a separate value of  $\Phi$  and therefore different diffuser vane mean incidence angles,  $\bar{i}$ . At  $\Phi = 0.30$ , the incidence is slightly positive,  $\bar{i} = 4.5^\circ$ , and the vane loading is small,  $\overline{C_L} = -0.146$ . As is expected, decreasing the incidence to greater negative angles cause the loading to increase negatively. The vane loading for a given  $N_v$  is independent of  $\sigma$  and therefore not shown in the figures.

In Figure 6.18,  $r_1/r_0 = 1.10$ ,  $\sigma = 60^\circ$ ,  $\Phi = 0.22$  and  $\bar{i} = -5.8^\circ$ . Three curves are presented per plot for  $N_v = 30, 15$  and  $10$  vanes. Decreasing the vane number causes the loading to be more negative. This behavior is typical for other diffuser geometries investigated.

The effect of detuning on the diffuser vane row is shown in Figure 6.19, with a 40% detuned vane row as defined in Figure 6.9. In this figure,  $r_1/r_0 = 1.10$ ,  $\sigma = 60^\circ$ ,  $N_v = 30$ ,  $\Phi = 0.30$  and  $\bar{i} = 4.5^\circ$ . The loading on the detuned vanes is changed slightly, with the leading edge pressure surface pressure affected most significantly. The loading on vane 1 has increased above the tuned vaned while the loading on vane 2 has decreased. At lower flow rates, the pressure change due to detuning is less significant. The case with 13% detuning and  $N_v = 10$  is not shown, since no change in loading due to detuning occurs.

It is interesting to note that in cases where the greatest performance increase is realized utilizing the vaned diffuser, the vanes are typically lightly loaded. This lends credibility to the belief that the vaned diffuser increases performance by affecting the aft impeller and vaneless space flowfields (Fisher and Inoue, 1981), thereby reducing secondary flows and separation. Thus, if a vaned diffuser is utilized to increase efficiency, the vane stagger should be equal to the absolute flow angle at the operating point, minimizing the loading.

In summary, the diffuser vane loading indicated by the surface static pressure and steady lift coefficient, is mainly dependent on the vane incidence and number of vanes. Changing the stagger angle has a minimal effect on the loading if the incidence is held constant.

#### 6.4 Radial Diffuser Velocity Field

LDV velocity measurements are made at each of the axial and radial positions shown in Figure 6.20 for the vaneless diffuser at  $\Phi = 0.17, 0.22$  and  $0.30$ . The instantaneous velocity is measured and the mean radial and tangential velocity in each measurement bin around the impeller circumference is determined, as described in Section 3.3 and depicted in Figures 6.21 and 6.22.

Figures 6.23 through 6.25 show the steady time-averaged radial and tangential velocities,  $U_r$  and  $U_\theta$ , nondimensionalized by the diffuser inlet velocities,  $U_{r1}$  and  $U_{\theta1}$ . These are presented at each axial position as a function of nondimensional radius,  $r = r/r_1'$ , where  $r_1'$  is the vaneless diffuser inlet depicted in Figure 6.22. Each figure represents a separate flow coefficient and the incompressible, inviscid, ideal solution,  $U_r/U_{r1} = 1/r$  and  $U_\theta/U_{\theta1} = 1/r$  are also shown.

For  $\Phi = 0.22$  and  $0.30$ , the tangential velocities follow the ideal solution, whereas the radial velocities tend to remain constant, except at the tip for  $\Phi = 0.30$ , where a decrease is seen. This behavior is presumably due to boundary layer formation on the diffuser walls, decreasing the velocity near the wall and increasing the core velocity to satisfy continuity. Viscous effects and mixing appear to have little effect on the tangential velocity since it tends to follow the ideal behavior. Therefore, viscous effects in the diffuser appear to be confined to the wall region and have not penetrated to the measurement locations.

For  $\Phi = 0.17$  in Figure 6.25, the flow shows increased departure from the ideal solution. This operating point is at incipient stall which is discussed in Section 6.6 ( $\Phi = 0.16$  for the vaneless diffuser). Therefore, turbulent mixing and separation are more likely. A slight decrease in the tangential velocity from the ideal solution is observed. The

radial velocity shows a significant departure with an increase at the tip and mean positions and a decrease at the hub. At the two largest measurement radii, a more pronounced departure from the theory is seen in the radial and tangential velocities indicating a possible diffuser wall separation.

In Figures 6.26 through 6.34, a vector plot of the vaneless diffuser total velocity, ensemble averaged using the data from the individual impeller passages, is shown for each flow coefficient and axial position. This geometry of these figures is depicted in Figure 6.22. The wheel speed magnitude and direction is shown for comparison and the scale is the same for each figure. In Figures 6.26 through 6.28, the results for  $\Phi = 0.30$  are presented. The circumferential nonuniformity of the flow can be observed, especially at  $r = 1.0$  and  $1.06$  at the tip and mean positions. The impeller exit flow angle,  $\alpha_0$ , is greatest at the tip due to the greater impeller tip radius and thus greater wheel speed. This behavior is consistent at each radius. The velocity magnitude shows the opposite behavior with the hub velocities being the greatest. Similar behavior is observed in Figures 6.29 through 6.31 for  $\Phi = 0.22$ , although the velocity magnitude is more uniform from tip to hub. In Figures 6.32 through 6.34 for  $\Phi = 0.17$ , the circumferentially nonuniform flow is less pronounced than in the previous figures. The flow angle is greatest at the tip for  $r = 1.0$  and  $1.06$ , but this behavior is reversed at larger radii. At the hub position, a sharp velocity decrease is seen at  $r = 1.32$  and  $1.45$ , which is also observed in Figure 6.25. It appears that a thick boundary layer has developed or that separation is occurring on the diffuser hub wall.

In Figures 6.35 through 6.43, the vaneless diffuser unsteady, circumferentially nonuniform velocity is presented by subtracting the steady time averaged velocity from each vector in the previous figures. These figures more clearly show the effect of flow rate and radius on the unsteady radial diffuser wake behavior. In each figure, the steady radial velocity magnitude and direction at the same axial location is shown for comparison. At the mean axial position and  $r = 1.0$  for each  $\Phi$ , Figures 6.36, 6.39 and 6.42, the first harmonic circumferential impeller exit/diffuser entrance unsteady static pressure is shown scaled by  $\rho U_1$ . Since the unsteady vaned diffuser airfoil surface static pressures are nondimensionalized by  $\rho U_1 v_n$ , the relative effect of the unsteady impeller exit/diffuser entrance static pressure on the vaned diffuser can be estimated. The plot scales for  $\Phi = 0.22$  and  $\Phi = 0.17$  are  $2x$  and  $4x$  respectively that of  $\Phi = 0.30$ .

In Figures 6.35 through 6.37 for  $\Phi = 0.30$ , the wake is mainly confined to the tip and mean positions. It can be seen that the wake has nearly disappeared at  $r = 1.45$ , which is typical for all of the measurements made. For  $\Phi = 0.22$  in Figures 6.38 through 6.40, the



wake is also confined mainly to the tip and mean. The wake velocity vectors are less parallel at  $r = 1.0$  than for  $\Phi = 0.30$ . At  $\Phi = 0.17$  in Figures 6.41 through 6.43, the wake velocity vectors tend to be more aligned with the absolute flow whereas the vectors at  $\Phi = 0.30$  and 0.22 are more aligned with the flow relative to the impeller.

A comparison of the vaneless radial diffuser unsteady velocities shown in Figures 6.35 through 6.43 is made with the theory developed in Chapter 4. This is accomplished by taking the first harmonic unsteady radial and tangential velocities, scaled by the magnitude at the vaneless diffuser inlet,  $|v| = (v_r^2 + v_\theta^2)^{1/2}$ , and plotting the magnitude and phase along with theory. Because measurements were not made immediately at the impeller exit, the vaneless radial diffuser inlet,  $r_1'$ , will be considered the impeller exit. Before these results are presented, it is useful to consider the parameters which describe wakes in classical linear airfoil theory for axial flow cascades.

Typically, wakes shed from turbomachine blade rows are considered small amplitude sinusoidal gusts superimposed on the steady relative flow leaving the rotor, Figures 4.1 and 6.44. The upper example in Figure 6.44 depicts the classical linear theory gust where the velocity vectors are parallel and aligned with the relative flow angle,  $\beta_0$ . In this type of gust, the gust phase angle or phase angle between  $v_r$  and  $v_\theta$  is  $\phi_w = 180^\circ$ , and the ratio,  $v_r/v_\theta = \tan \beta_0$ . In the bottom left example,  $\phi_w = 180^\circ$  but  $v_r/v_\theta \neq \tan \beta_0$ . Here, the velocity vectors are parallel but not aligned with the relative flow angle,  $\beta_0$ . In the bottom right example,  $v_r/v_\theta = \tan \beta_0$ , but  $\phi_w \neq 180^\circ$ . In this example, the velocity vectors are no longer parallel.

Figures 6.45 through 6.47 show the mean axial position first harmonic unsteady radial and tangential velocity components compared with the theory from Chapter 4. In the theory as mentioned previously,  $\phi_w = 180^\circ$  and  $v_r/v_\theta = \tan \beta_0$ , although the theory can accommodate  $\phi_w \neq 180^\circ$  and  $v_r/v_\theta \neq \tan \beta_0$ . For the experimental data, the velocity ratio and gust phase angle as well as the absolute and relative flow angles,  $\alpha_0$  and  $\beta_0$ , are calculated at the diffuser inlet,  $r_1' = 40.4$  cm (15.9 in.). In Figure 6.45,  $\Phi = 0.30$ , the gust phase angle,  $\phi_w$ , is  $160^\circ$  and  $v_r/v_\theta \approx \tan \beta_0$ . In a general sense, the magnitude of  $v_r$  follows the theory. However, the magnitude of  $v_\theta$  decreases more rapidly with  $r$  than the theory. The phase of both  $v_r$  and  $v_\theta$  vary less rapidly with  $r$  than in the theory. In Figure 6.46,  $\Phi = 0.22$ , the gust phase angle,  $\phi_w$ , is  $148^\circ$  and again,  $v_r/v_\theta \approx \tan \beta_0$ . As in the previous figure, the radial velocity magnitude generally follows the theory with the tangential velocity decreasing more rapidly with  $r$ . The phase varies less rapidly with  $r$  for

the data than for the theory. In Figure 6.47,  $\Phi = 0.17$ , the gust phase angle,  $\phi_w$ , is  $60^\circ$  and  $v_r/v_\theta \approx \tan \beta_0$ . The radial and tangential velocity magnitudes decrease more rapidly with  $r$  than the theory with poor phase correlation.

It can be seen in Figures 6.45 through 6.47 that the correlation of the data with the theory deteriorates as  $\Phi$  decreases and the gust phase angle,  $\phi_w$ , departs from  $180^\circ$ . Therefore, as the wake velocity departs from the linear theory profile in Figure 6.44, the correlation with the theory becomes worse.

In Figure 6.48,  $\beta_0 = -55^\circ$  and the theoretical  $\phi_w$  is  $-160^\circ$ , equal to the data phase angle. This is accomplished by introducing a phase angle between  $v_{r0}$  and  $v_{\theta 0}$  in the boundary condition, Equations 4.5. The phase correlation is somewhat improved due to the fact that the impeller exit relative flow angle is probably closer to the backsweep angle of  $51^\circ$ . However the amplitude correlation is unimproved, with an oscillation in the theory amplitude at lower  $r$ .

It is hypothesized that the presence of the circumferential unsteady static pressure gradient plays an important role in wake behavior. Because an unsteady circumferential static pressure gradient is generated by potential effects due to impeller rotation, Section 1.2, with the velocity nonuniformity generated by viscous effects, the wake analysis does not directly account for it. Henderson (1991) has shown unsteady circumferential pressure gradients to exist in axial machines significant distances downstream of the rotor, and that wake behavior and downstream airfoil forced response are significantly different than in classical linear theory. In their experiment, linear theory type gusts are only generated with perforated plates which have minimal lift and no large areas of separation. Therefore, surfaces producing lift such as exist in any turbomachine will produce circumferential pressure gradients that affect wake behavior and downstream airfoil response.

In summary, it is seen that the steady circumferential velocity generally follows the ideal theory whereas an acceleration of the steady radial velocity due to boundary layer thickening causes departure from theory. The unsteady wake velocities decrease rapidly with radius, with the wake velocities disappearing at a nondimensional radius of 1.45. The measured unsteady wake velocities generally decrease more rapidly with increasing radius than predicted by the theory. The phase angle between the unsteady radial and tangential velocities and the unsteady circumferential pressure gradient are hypothesized to be important factors in the departure from theory.

### 6.5 Diffuser Vane Unsteady Loading

Unsteady diffuser vane static pressure measurements are made at each of the geometric configurations listed in Table 6.1 at  $\Phi = 0.17, 0.22$  and  $0.30$ . The unsteady lift coefficients  $C_L$  and  $C_{Ls}$ , defined in Equations 3.14 and 3.15, are presented along with the steady lift coefficient,  $\overline{C_L}$ , to evaluate the diffuser vane loading as a function of diffuser geometry and flow rate. The diffuser vane surface static pressure coefficients and pressure difference coefficients are presented along with the theory developed in Chapter 5.

Figures 6.49 through 6.54 present the unsteady and steady lift coefficients,  $C_{Ls}$  and  $\overline{C_L}$ , as a function of flow rate for the various diffuser geometries. The unsteady lift coefficient  $C_{Ls}$  is the first harmonic unsteady lift amplitude nondimensionalized by the dynamic pressure based on wheel speed, Equation 3.15. This yields an absolute measure of the vane loading as a function of the machine operating point.

In Figure 6.49, the unsteady and steady lift for  $r_1/r_0 = 1.10$  and  $N_v = 30$  is presented for the various stagger angles. The unsteady lift increases markedly with  $\Phi$  and with increasing stagger,  $\sigma$ . The steady lift changes more rapidly with  $\Phi$  as  $\sigma$  is increased, with  $\overline{C_L}$  becoming more positive with increasing  $\Phi$  and  $\sigma$ .

In Figure 6.50, the radius ratio has been increased to  $r_1/r_0 = 1.15$ . The unsteady lift changes less rapidly with  $\Phi$  and  $\sigma$ , although the lift at  $\Phi = 0.30$  is greater for  $\sigma = 60^\circ$  and  $70^\circ$  in Figure 6.50 than for Figure 6.49. For  $\sigma = 60^\circ$ , the unsteady lift is greater in Figure 6.50 with  $r_1/r_0 = 1.15$  for all  $\Phi$ . The increased lift at higher  $r_1/r_0$  is surprising since the wake velocities are decreasing with increased radius. The steady lift behavior is similar in both cases. It is interesting to note that the steady lift for  $\sigma = 50^\circ$  attains a minimum at  $\Phi = 0.22$  and further decrease in  $\Phi$  and thus the negative incidence has minimal effect on the lift. It is likely that the vaned diffuser begins to stall at this point. This behavior is observed for all diffuser geometries.

Figure 6.51 is similar to Figure 6.49 but with  $N_v = 15$ . The reduction in vane number has a significant effect on the unsteady lift behavior. The unsteady lift is typically greater than for  $N_v = 30$ , however the effect of  $\Phi$  on the lift is different at each value of  $\sigma$ . For  $\sigma = 50^\circ$ , the unsteady lift is greatest at high  $\Phi$ , for  $\sigma = 60^\circ$ , the unsteady lift is greatest at moderate  $\Phi$ , and for  $\sigma = 70^\circ$ , the unsteady lift is greatest at low  $\Phi$ . Each of these stagger and flow rate combinations corresponds closely to the point of minimum steady incidence. The steady lift is shifted in the negative direction but shows similar behavior to the previous figures. In Figure 6.52, the unsteady and steady lift is shown for  $r_1/r_0 = 1.15$  and  $N_v = 15$ . Only measurements for  $\sigma = 60^\circ$  are made. The unsteady lift is significantly

reduced by increasing  $r_1/r_0$  to 1.15. At this radius ratio, the unsteady lift is a minimum for minimum incidence, as opposed to a maximum as in the previous figure.

In Figures 6.53 and 6.54, the effect of detuning on the unsteady lift is presented for  $N_v = 30$  with 40% detuning, and  $N_v = 10$  with 13% detuning respectively. For all measurement points, the unsteady lift is increased on one or both of the vanes. It cannot be concluded from these cases that detuning will always produce an adverse effect on the lift, although in general it is not always beneficial. The detuning affects the steady lift less significantly than does the incidence.

A comparison of the unsteady airfoil surface pressure data is made with the unsteady radial cascade airfoil theory developed in Chapter 5. The experimental diffuser vane unsteady static pressure coefficients,  $C_p$ , are presented for both the suction and pressure surfaces, along with the experimental and theoretical pressure difference coefficient,  $C_{\Delta p}$ , as defined in Chapter 3. Pressure coefficients for  $r_1/r_0 = 1.15$  have been nondimensionalized by the transverse velocity at  $r_1/r_0 = 1.10$  in order to evaluate the radius ratio effect and since no velocity measurements are made at  $r_1/r_0 = 1.15$ . Since the phase is different at the blade leading edge than at the velocity measurement location, a phase correction is made. The time taken for the wave to be convected from the measurement point to the vane leading edge is computed using the steady velocity corrected for phase.

Before making a comparison with the theory, it is useful to consider the wake velocity profiles given in the vector plots of Figures 6.36, 6.39 and 6.42 along with the data/theory comparison in Figures 6.45 through 6.47. In Figures 6.36 and 6.39 for  $\Phi = 0.30$  and 0.22, the wake velocity vectors are nearly parallel with the steady relative flow, and therefore nearly transverse to the airfoils in the radial diffuser. In Figure 6.42 for  $\Phi = 0.17$ , the wake velocity vectors are nearly parallel with the absolute steady flow, and therefore nearly parallel to the airfoil chord, with the transverse unsteady velocity component very small. It is observed in the data/theory comparison of Figures 6.45 through 6.47 that the tangential velocity component decreases with radius more rapidly than predicted by the theory. However, the radial component showed reasonable magnitude correlation in a general sense for  $\Phi = 0.30$  and 0.22. Since the radial velocity is the major component in the airfoil transverse velocity, especially at higher  $\sigma$ , the deficiencies in the radial diffuser wake theory will not necessarily be a major source of error in the unsteady airfoil theory.

Figures 6.55 through 6.65 present the unsteady first harmonic airfoil surface static pressure distributions. On the lefthand axes of each figure, the amplitude and phase of the unsteady static pressure coefficient,  $C_p$ , is plotted versus nondimensional vane chord for

pressure and suction surfaces. On the righthand axes, the amplitude and phase of the unsteady pressure difference coefficient,  $C_{\Delta P}$ , is presented along with the theory versus nondimensional chord. The legend presents the experimental and theoretical lift coefficients,  $C_L$  and  $C_{Lt}$ , as defined in Equation 3.14, along with the lift coefficient,  $C_{Ls}$ , defined in Equation 3.15.

Figures 6.55 through 6.57 show the first harmonic unsteady static pressure distribution for  $\Phi = 0.30, 0.22$  and  $0.17$ , respectively, with  $N_v = 30$ ,  $r_1/r_0 = 1.10$  and  $\sigma = 60^\circ$ . For  $\Phi = 0.30$ , the amplitude of  $C_p$  is high at the leading edge for pressure and suction surfaces as is typical in steady and unsteady cascade flows. The pressure surface phase is nearly constant along the airfoil chord with some variation in the suction surface phase. Good correlation is seen in the phase of  $C_{\Delta P}$  with the theory. However, the theory generally overpredicts the amplitude of  $C_{\Delta P}$  by a factor of 2 or more.

In Figure 6.56 for  $\Phi = 0.22$ , the amplitude of  $C_p$  is somewhat higher than in the previous figure but the behavior is similar. The phase behavior of  $C_p$  is similar for the suction surface but the pressure surface shows more variation. The phase correlation of  $C_{\Delta P}$  has deteriorated with a greater phase decrease in the data toward the trailing edge. The steady flow incidence,  $\bar{i}$ , is negative for this case and positive for the previous case. Greater phase decrease at negative incidence is seen for all measurements made with  $N_v = 30$ . The amplitude is closer to the theory at the airfoil trailing edge than in the previous case. However, the theory still generally overpredicts the amplitude by a factor of 2 or more.

Figure 6.57 presents the unsteady pressure for  $\Phi = 0.17$ . The amplitude and phase behavior of  $C_p$  is similar to the previous figure but the amplitude is much greater. The phase decrease in the data for  $C_{\Delta P}$  occurs due to negative incidence. The amplitude of  $C_{\Delta P}$  is now underpredicted by the theory. This behavior is generally seen for all geometries at  $\Phi = 0.17$ , with the data greater than the theory over most of the airfoil chord. This is attributed to the small transverse wake component at  $\Phi = 0.17$  which was mentioned previously. Since the unsteady pressure coefficients  $C_p$  and  $C_{\Delta P}$  are nondimensionalized using this transverse wake component, other effects such as incidence, airfoil geometry and impeller circumferential pressure gradients, which are not considered in the theory, will have a greater relative effect on the pressure distribution.

Figures 6.58 and 6.59 show the detuned cascade results for  $N_v = 30$ ,  $r_1/r_0 = 1.10$ ,  $\sigma = 60^\circ$  and  $\Phi = 0.22$ . The surface pressure distributions show smoother behavior than for the tuned cascade, although the theory does not consider detuning. The correlation of

$C_{\Delta P}$  with the theory is good for both vanes, with the phase slightly higher for the data than the theory for vane 2.

The correlation of the data with the theory is generally poor for the tuned cascade with  $N_v = 30$ . This is believed to be due to the close spacing of the airfoils, thus greatly affecting the steady flowfield, and distorting the wake which the theory does not consider. It is hypothesized that the detuning of the cascade lessens the effect of the steady flowfield and correlation with the theory is improved.

Figures 6.60 and 6.61 present the unsteady airfoil static pressure distribution for  $\Phi = 0.30$  and  $0.22$  respectively, with  $N_v = 15$ ,  $r_1/r_0 = 1.10$  and  $\sigma = 60^\circ$ . The correlation with theory in these cases is reasonable with some deviation in the phase correlation. The theory generally appears to overpredict the pressure amplitude from 10 to 25% chord for all diffuser geometries, with this especially evident in the present figures. This is possibly attributable to vane camber and thickness which affect the steady flow around the airfoil. The phase decrease with negative incidence no longer occurs with  $N_v = 15$ . In Figures 6.62 and 6.63, the same configuration with  $r_1/r_0 = 1.15$  is shown. The phase correlation is good, with the theoretical amplitude somewhat greater than the data. This is attributable to the unsteady pressure being non-dimensionalized by the wake transverse velocity at  $r_1/r_0 = 1.10$  instead of  $r_1/r_0 = 1.15$ , where velocity data are not available.

Finally, unsteady pressure data are presented for  $N_v = 10$  in Figures 6.64 and 6.65 for  $\Phi = 0.30$  and  $0.22$  respectively. The correlation with the theory is poor in both of these figures. This behavior is not expected since the correlation appeared to improve with decreasing vane number. The suction surface data for  $N_v = 10$  matches closely the suction surface data for  $N_v = 15$ , however the pressure surface data is considerably different. No explanation is evident for this behavior.

In summary, the unsteady lift increases with flow rate  $\Phi$ , for  $N_v = 30$ , with this behavior particularly noticed at higher vane stagger angles. Increasing  $r_1/r_0$  decreased the unsteady lift at higher  $\Phi$  and  $\sigma$ , although at lower  $\Phi$ , the effect is less evident. With  $N_v = 15$ , the unsteady lift is generally greater than for  $N_v = 30$ , with less variation due to flow rate,  $\Phi$ . Increasing  $r_1/r_0$  decreased the unsteady lift significantly. Nonuniform circumferential spacing detuning increased the lift on one or both of the vanes in all cases.

Poor correlation of the unsteady pressure data with the theory was seen for  $N_v = 30$ , with the very close vane spacing a probable cause. Reasonable correlation between data and theory was seen with  $N_v = 15$  at points of low vane steady loading. An unexplainable poor correlation with theory was seen with  $N_v = 10$ .

### 6.6 Compressor Instabilities

In all types of pumping and compression systems, various forms of local and system instabilities occur. Of primary relevance to gas compressors are surge and rotating stall. Surge is defined as a global instability of large mass flow oscillation through the machine at low frequency. This can occur, as shown by Greitzer (1981), when the slope of the compressor operating characteristic (pressure versus mass flow, as in Figures 6.1 through 6.11) becomes positive. At this point, a small perturbation in system mass flow can increase in amplitude until the flow is completely reversed in some systems, often causing catastrophic failure.

Rotating stall is a more localized instability, in which stalling of one or more blade passages propagates around the machine circumference at some fraction of the wheel speed, typically 20 to 70% according to Greitzer (1981). Stability analyses for rotating stall are generally more complicated and less exact than for surge, with precise a priori prediction of a compressor stall point difficult to obtain. However, rotating stall is generally observed around the zero slope portion of the compressor operating characteristic, with stalling more severe as the flow rate is decreased. Rotating stall is sometimes observed on the negatively sloped portion of the compressor operating characteristic, especially in high speed, multi-stage axial compressors. Non-stalled operation on the positive portion of the characteristic is rare.

The classic explanation of rotating stall onset is given by Emmons, et al. (1955). When a turbomachine blade row is operating at high incidence angle, a disturbance in the flow can locally increase this angle, stalling one of the blades. As this blade stalls, the flow through the stalled passage is diverted into the adjacent passages, decreasing the incidence on one, while increasing the incidence on the other, thus causing it to stall. This sequence repeats itself, causing the stall cell to rotate around the machine. More recent studies have shown stall to develop from small amplitude rotating waves which can increase in amplitude at certain machine operating points. It has been observed in the literature (Van den Braembussche, 1984) and also in the present investigation, that localized or global blade stalling is not always a sufficient condition for rotating stall.

Surge and rotating stall are distinct phenomena. However, they are not unrelated. Occurrence of rotating stall can often trigger the global instability of surge in axial compressors. Although much effort has been made to predict and reduce these phenomena in turbomachines, their occurrence and behavior is still not well understood, especially in centrifugal compressors. In this regard, occurrence of system instabilities in the Purdue

Research Centrifugal Compressor is investigated, with the effects of vaned diffuser geometry on this behavior presented.

A summary of the various flow instabilities is given in Table 6.2 for the vaned diffuser. For detection of surge and rotating stall, flow visualization in conjunction with the diffuser wall high response pressure transducers are utilized. Flow visualizing tufts are located at the impeller inlet as well as in the radial diffuser. Along with a strobe light, these tufts and the transducer signals allow determination of stall or surge occurrence, location of stall (impeller or diffuser), relative amplitude and number of stall cells.

Table 6.2 Compressor Instabilities

$N_v = 30$			
	$\sigma = 50^\circ$	$\sigma = 60^\circ$	$\sigma = 70^\circ$
$r_1/r_0 = 1.10$	Stall: $\omega = 5.8$ Hz (2 lobes) $\omega = 12.3$ Hz (5 lobes) $\Phi = 0.155$	Surge: $\omega = 5.2$ Hz $\Phi = 0.148$	Stall: $\omega = 25$ Hz (1 lobe) $\Phi = 0.148$
$r_1/r_0 = 1.15$	Stall: $\omega = 6$ Hz (2 lobes) $\omega = 15$ Hz (5 lobes) $\omega = 21$ Hz (3 lobes) $\Phi = 0.160$	Surge: $\omega = 5.2$ Hz $\Phi = 0.148$	No Stall $\Phi = 0.100$

$N_v = 15$			
	$\sigma = 50^\circ$	$\sigma = 60^\circ$	$\sigma = 70^\circ$
$r_1/r_0 = 1.10$	Stall: $\omega = 26$ Hz (1 lobe) $\Phi = 0.160$	Surge: $\omega = 5.2$ Hz $\Phi = 0.148$	Stall: $\omega = 25$ Hz (1 lobe) $\Phi = 0.145$
$r_1/r_0 = 1.15$		Surge: $\omega = 5.2$ Hz $\Phi = 0.150$	

During compressor operation with the vaneless diffuser ( $N_v = 0$ ), rotating stall occurs at  $\Phi = 0.16$ . Figure 6.66 shows the unsteady pressure signal from one of the diffuser wall mounted transducers as a function of time. In the bottom graph, the Fast Fourier Transform (FFT) of the signal is shown. In the figure, one distinct frequency attributable



to rotating stall is seen at  $\omega = 26$  Hz. This frequency decreases slightly as  $\Phi$  is reduced. The tufts at the impeller inlet and exit respond to the stall cell, which appears to originate in the impeller. At all times during stall, only one stall cell is observed (inferred from the phase angle between the transducer signals). The machine is operated to  $\Phi = 0.12$ , with the single cell impeller stall the only instability observed.

For vaned diffuser operation, several types of instability are observed. The frequency given in Table 2 is the cell passing frequency. Therefore, a stall pattern at  $\omega = 5.8$  Hz with 2 cells is a 2-celled pattern rotating at 2.9 Hz. The impeller rotational speed is 29.8 Hz, therefore the stall frequency is approximately 20% of the impeller frequency. When several frequencies are present, some of the harmonics can add or subtract to yield other harmonics.

The first half of Table 6.2 show results with  $N_v = 30$ . In the first row, flow instabilities with  $r_1/r_0 = 1.10$  are listed. For  $\sigma = 50^\circ$ , the diffuser stall contains two distinct frequencies and number of cells. The stall at  $\omega = 5.8$  Hz appears to be surge during operation. However, the transducer phase content suggests that it is stall. Since rotating stall can trigger surge, it is likely that this stall frequency will produce surge at lower flow rates. For  $\sigma = 60^\circ$ , surge occurs at  $\Phi = 0.148$ . The transducer signal is shown in Figure 6.67. The single surge frequency around  $\omega = 5$  Hz is seen. The phase difference between the transducers is close to zero, indicating the global mass flow oscillation. No rotating stall patterns are observed before surge. For  $\sigma = 70^\circ$ , a stall develops which is similar to the vaneless diffuser impeller stall. However, minimal tuft movement is observed at the impeller inlet as opposed to the vaneless case thus the location of this stall is uncertain.

The behavior for  $r_1/r_0 = 1.15$  is given in the second row of Table 6.2. Figure 6.68 presents the transducer signal and FFT for  $\sigma = 50^\circ$ . Three distinct frequencies are evident at  $\omega = 6, 15$  and  $21$  Hz, with the apparent number of stall cells being 2, 5 and 3 respectively. It is possible that 2 patterns exist and that their sum or difference produces the third frequency. For  $\sigma = 60^\circ$ , the behavior is similar to  $r_1/r_0 = 1.10$ , with surge occurring. For  $\sigma = 70^\circ$ , no instabilities are observed operating the machine to  $\Phi = 0.10$ . For  $N_v = 15$ , impeller stall occurs at  $\sigma = 50^\circ$  and  $70^\circ$ . The flow coefficient for  $\sigma = 70^\circ$  is lower,  $\Phi = 0.145$ , than for the vaneless impeller stall where  $\Phi = 0.160$ . For  $\sigma = 60^\circ$ , surge occurs as in the previous cases.

The vaned diffuser is seen to have a significant influence on the occurrence of compressor instabilities. The flow coefficient for stall can be reduced by proper geometry selection. For  $N_v = 30$ ,  $\sigma = 70^\circ$  and  $r_1/r_0 = 1.15$ , stall and surge behavior are completely eliminated, thus giving support to the belief that rotating disturbances will only be amplified

under certain conditions, with static stalling of individual blades or vanes not always sufficient.

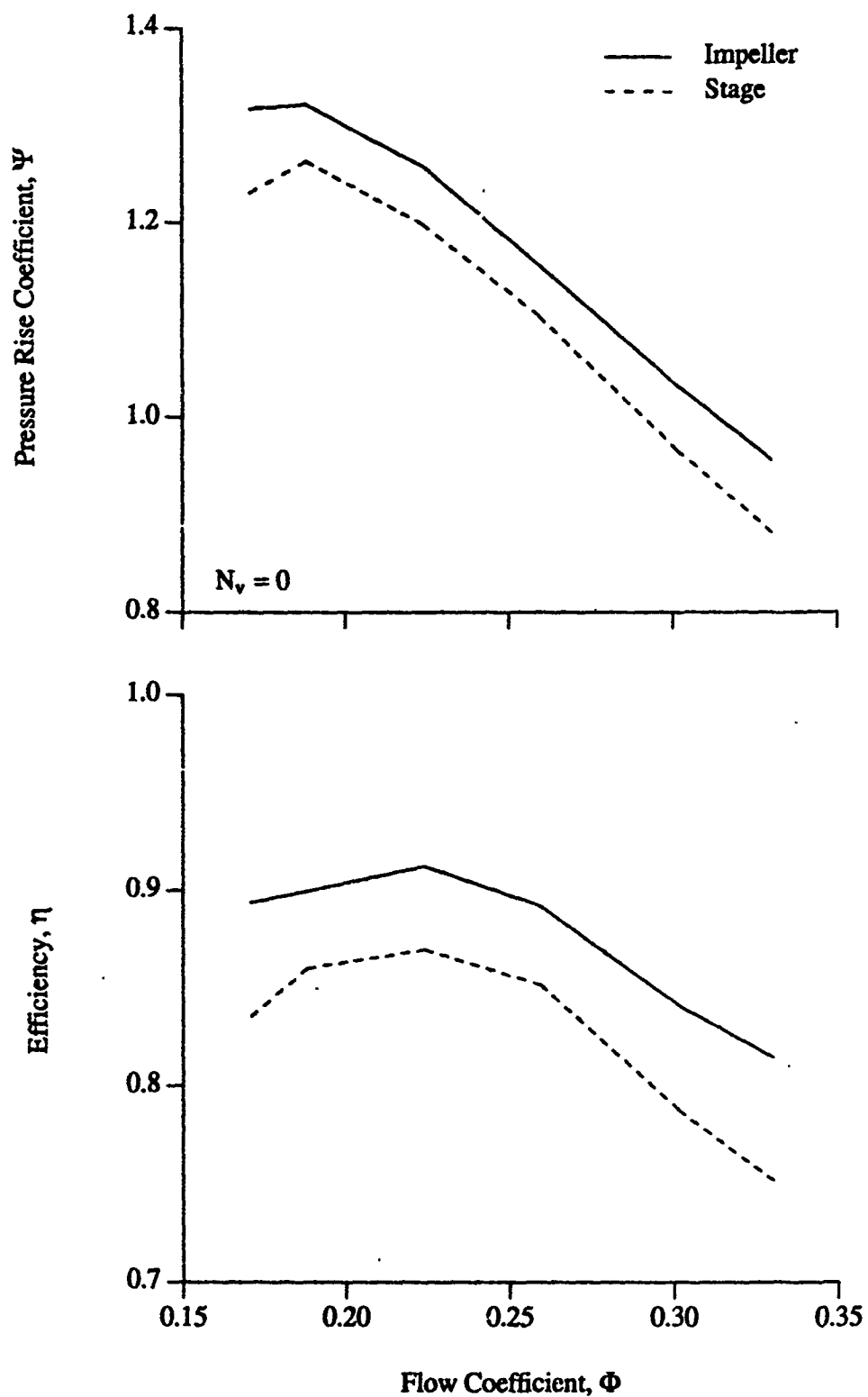


Figure 6.1 Centrifugal Compressor Performance with Vaneless Diffuser

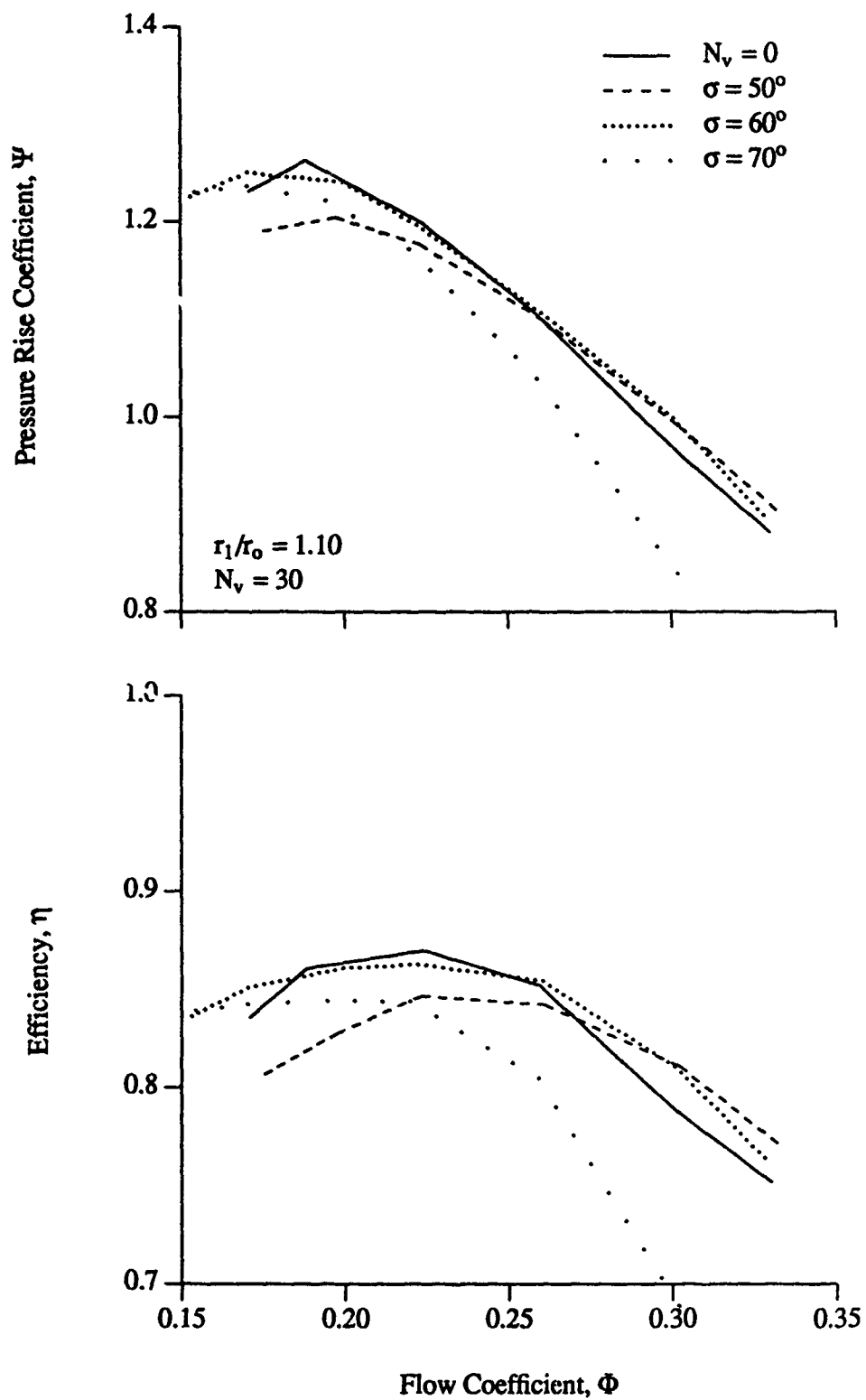


Figure 6.2 Effect of Stagger on Compressor Performance ( $r_1/r_0 = 1.10$ ,  $N_v = 30$ )

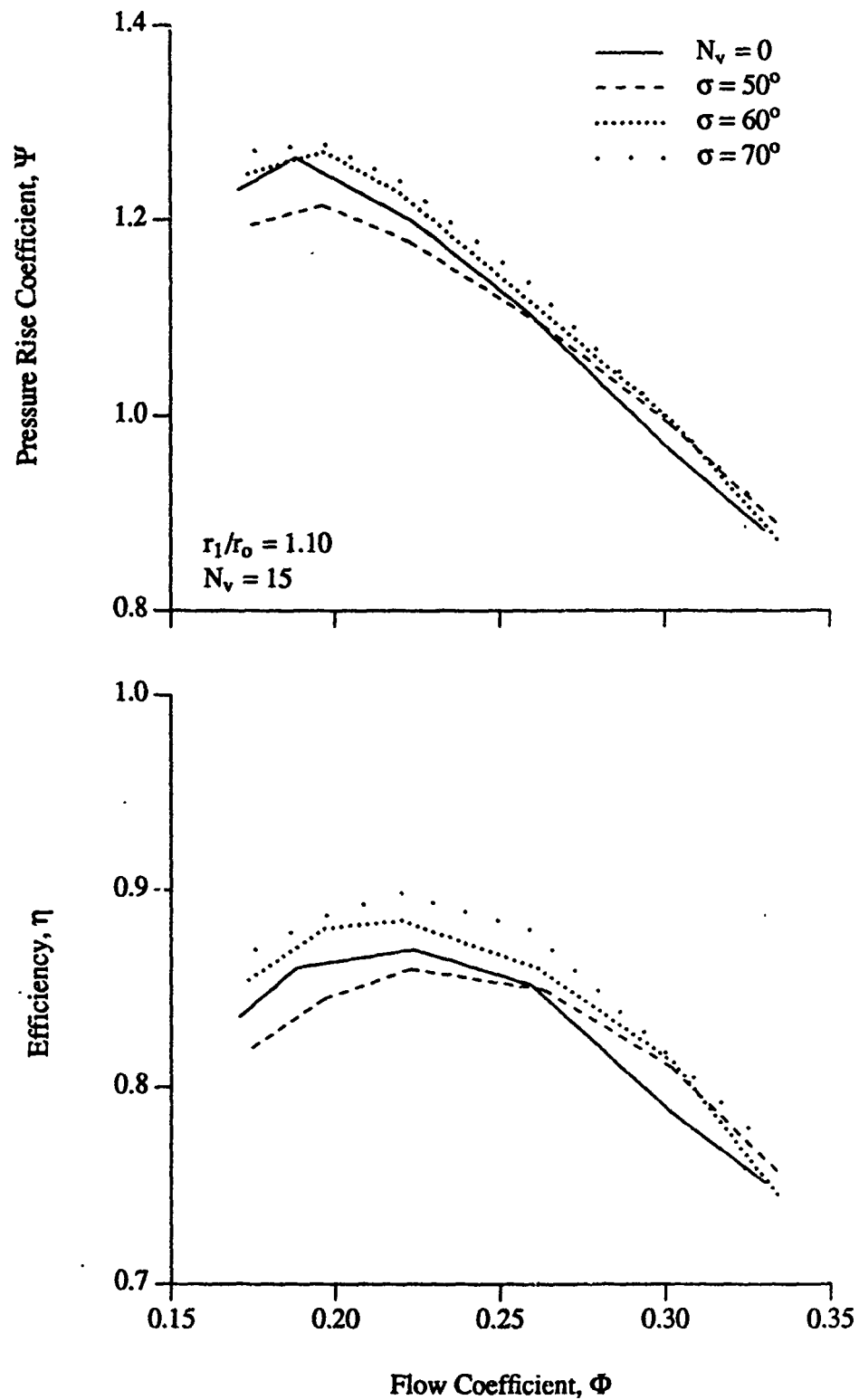


Figure 6.3 Effect of Stagger on Compressor Performance ( $r_1/r_0 = 1.10$ ,  $N_v = 15$ )

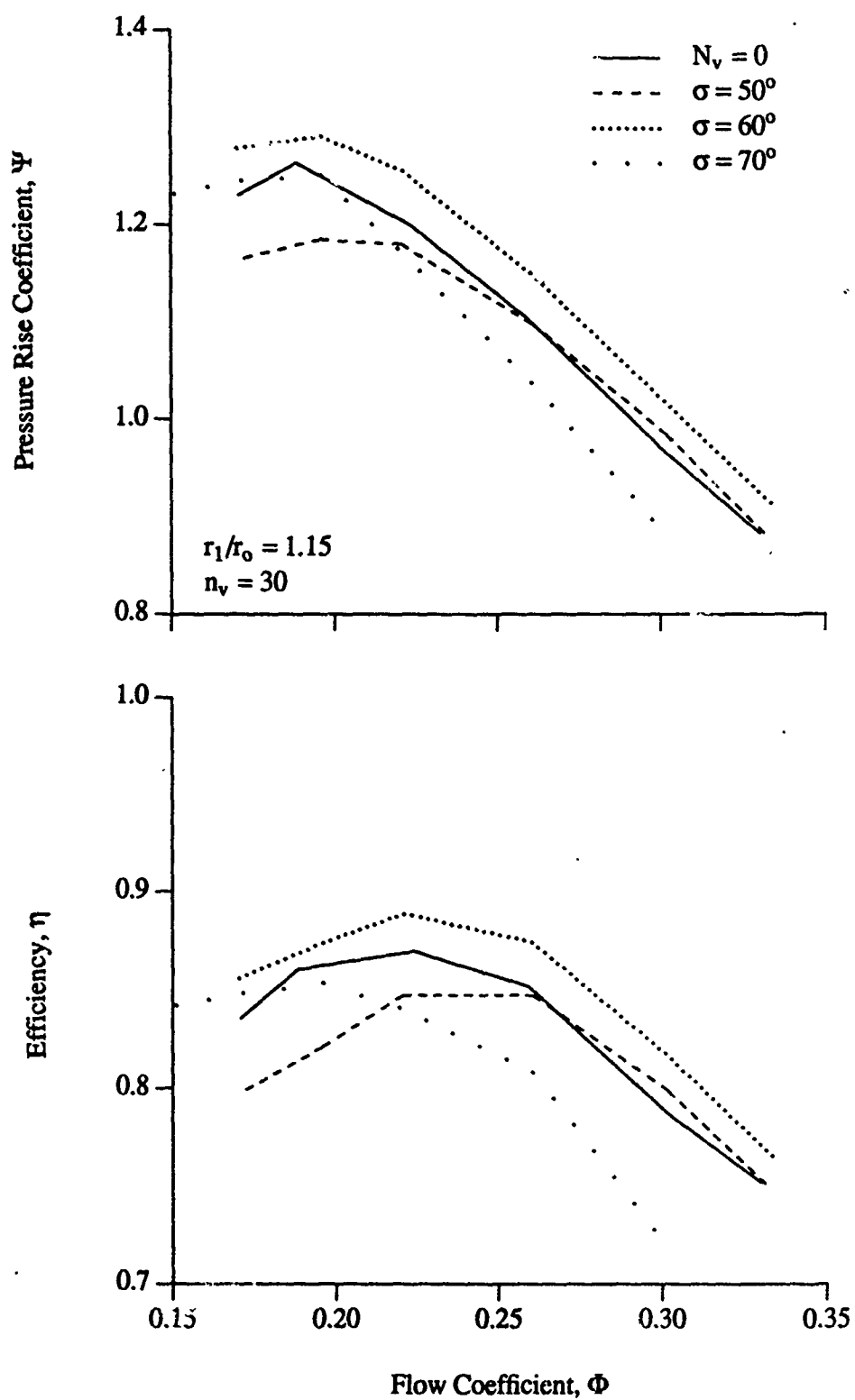


Figure 6.4 Effect of Stagger on Compressor Performance ( $r_1/r_0 = 1.15$ ,  $N_v = 30$ )

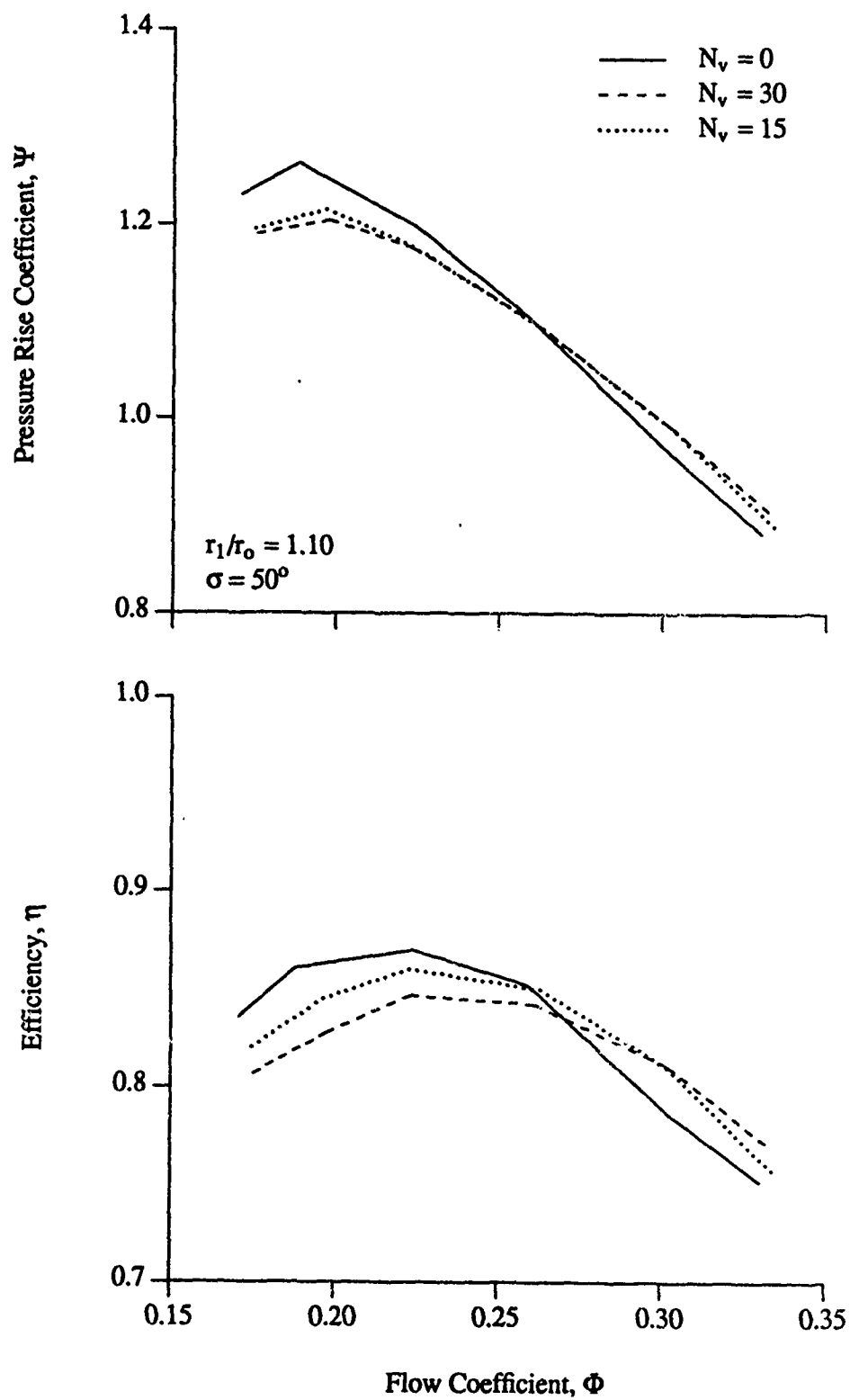


Figure 6.5 Effect of Vane Number on Compressor Performance ( $r_1/r_0 = 1.10$ ,  $\sigma = 50^\circ$ )

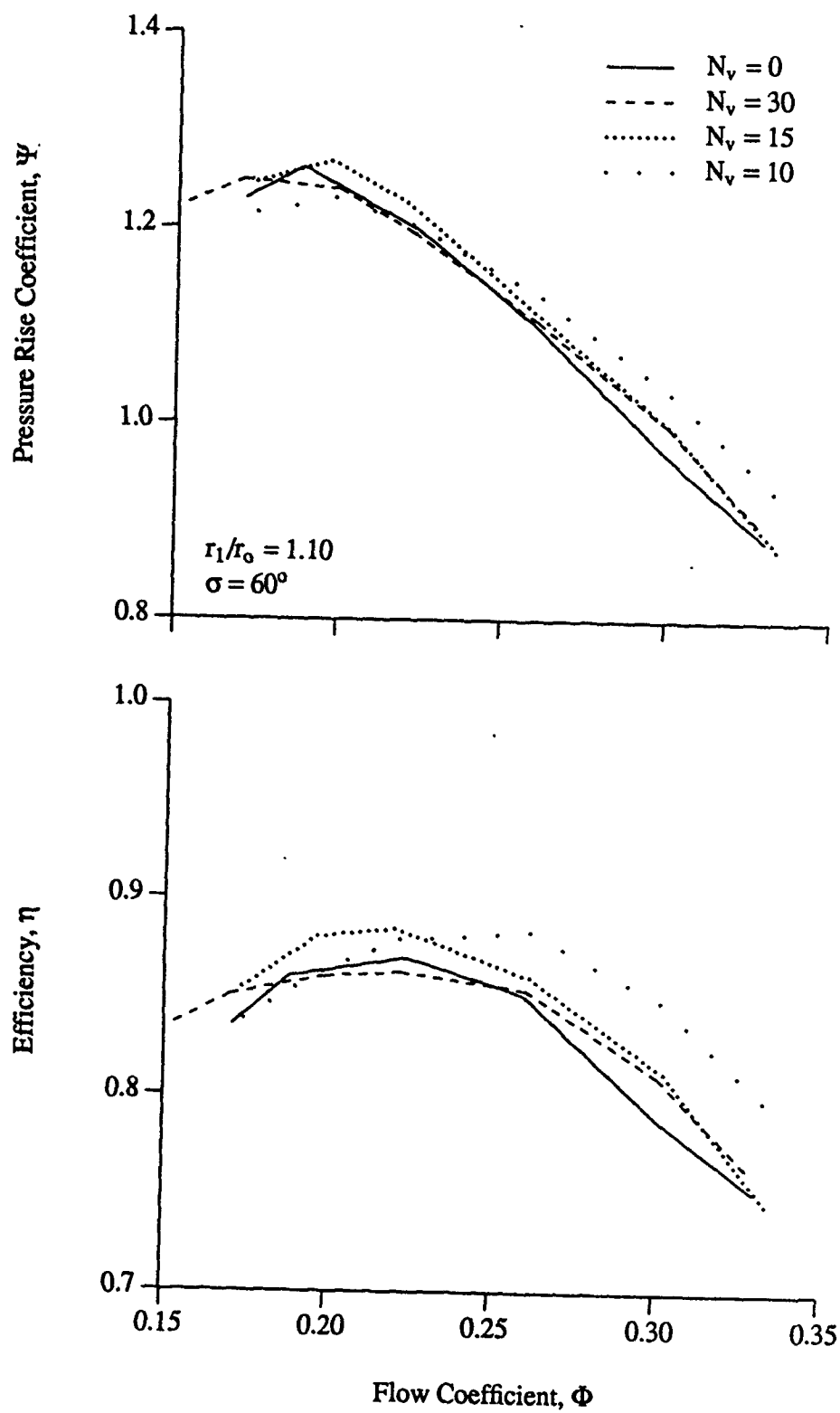


Figure 6.6 Effect of Vane Number on Compressor Performance ( $r_1/r_0 = 1.10$ ,  $\sigma = 60^\circ$ )



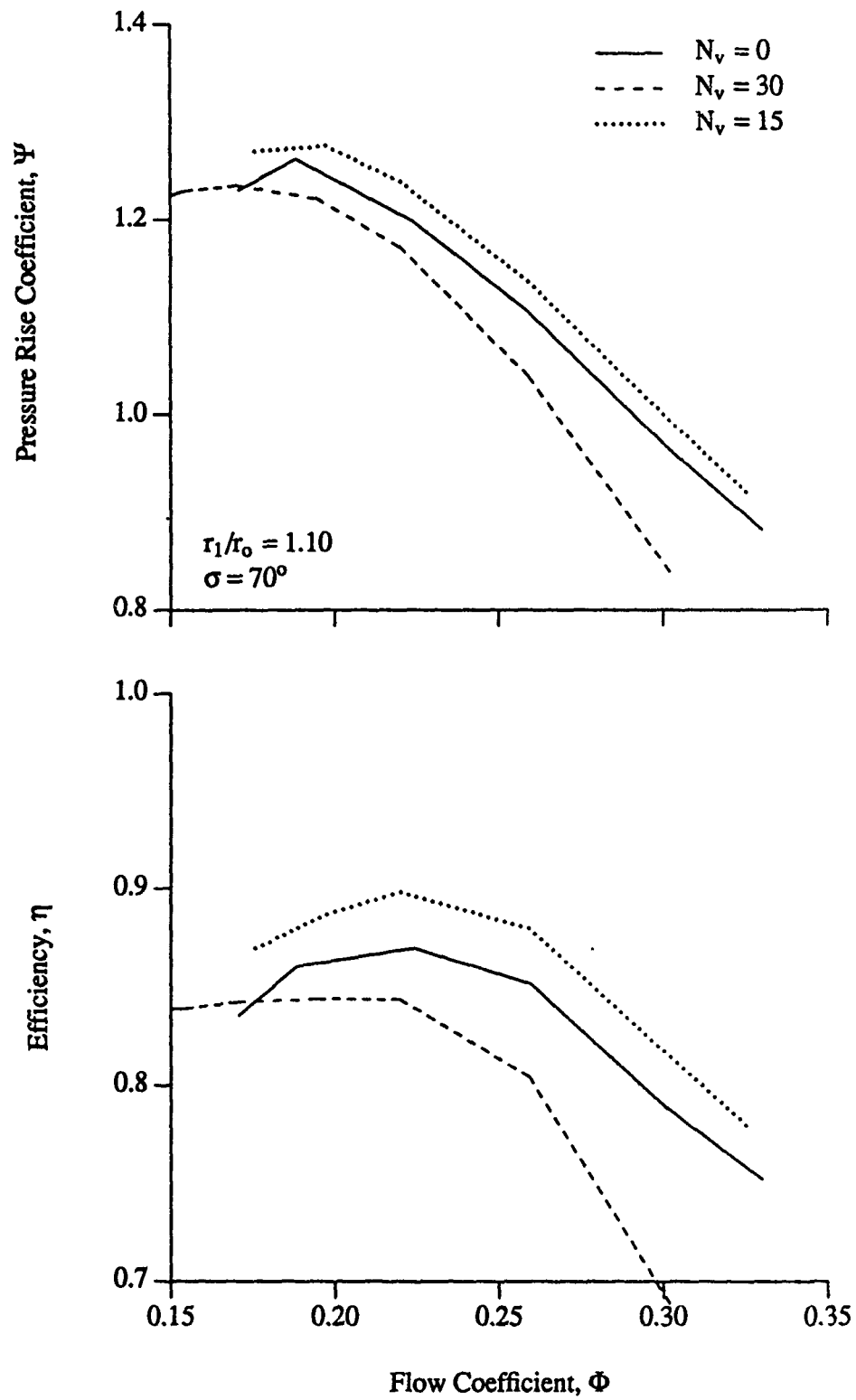


Figure 6.7 Effect of Vane Number on Compressor Performance ( $r_1/r_0 = 1.10$ ,  $\sigma = 70^\circ$ )

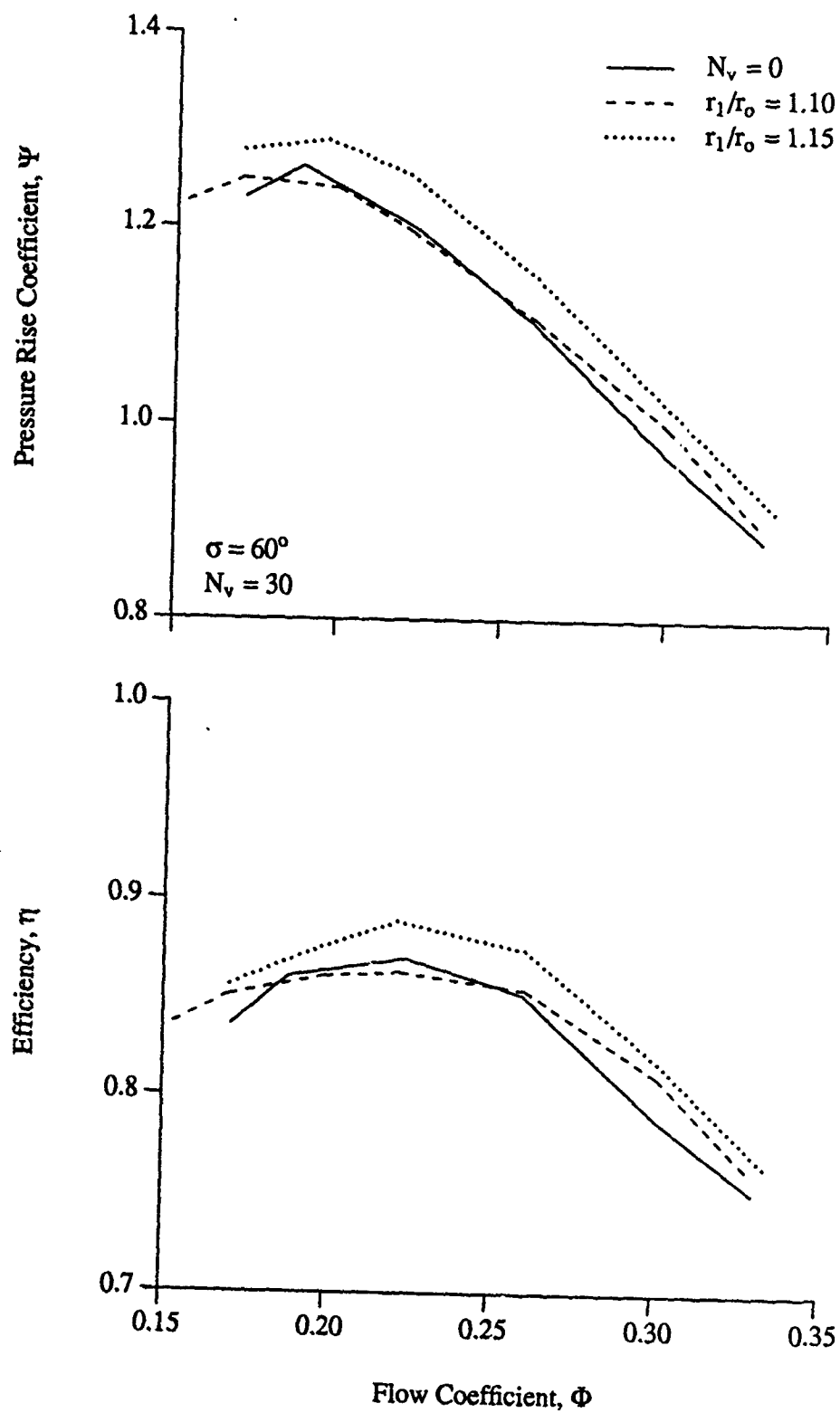


Figure 6.8 Effect of Radius Ratio on Compressor Performance ( $\sigma = 60^\circ$ ,  $N_v = 30$ )

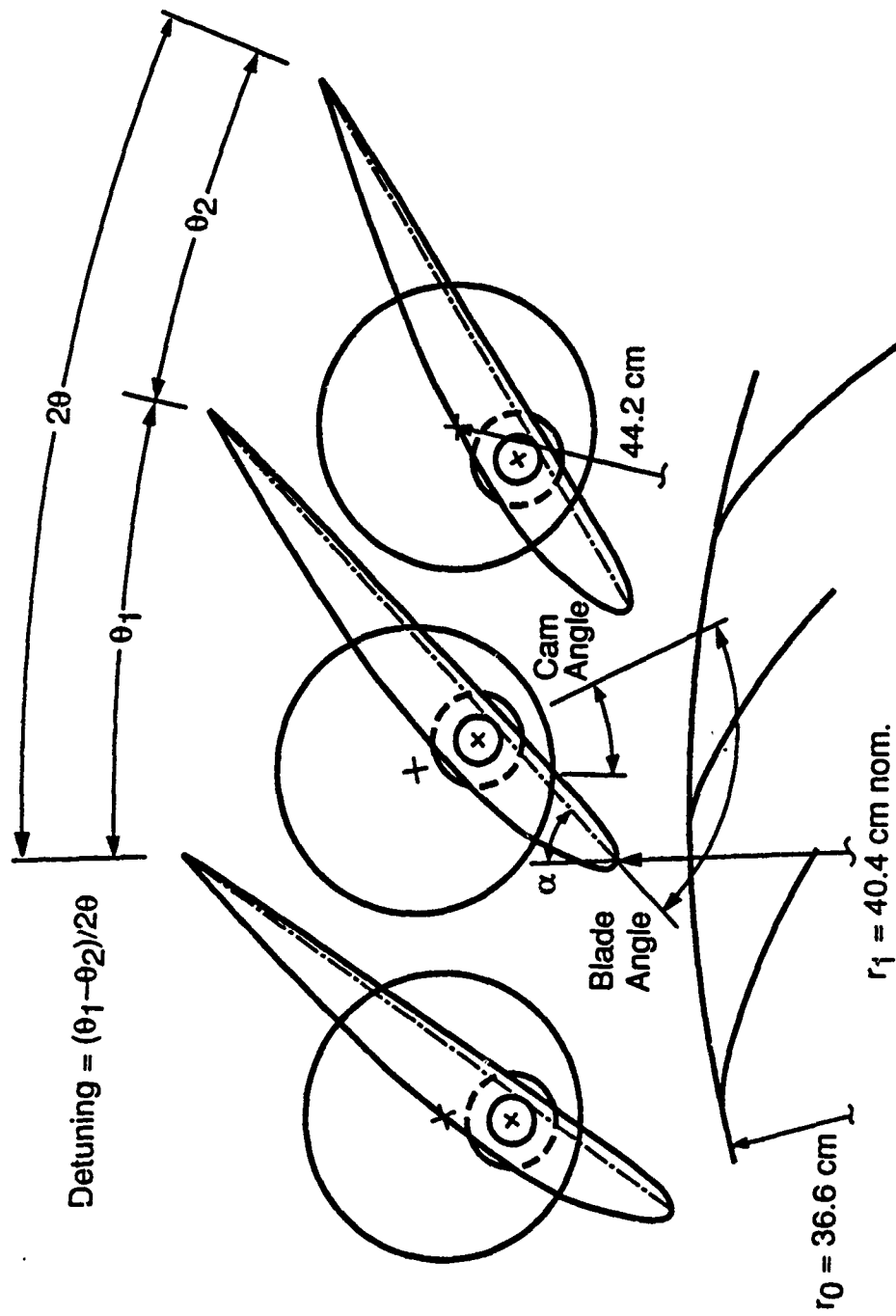


Figure 6.9 Vaned Diffuser Nonuniform Circumferential Spacing Detuning

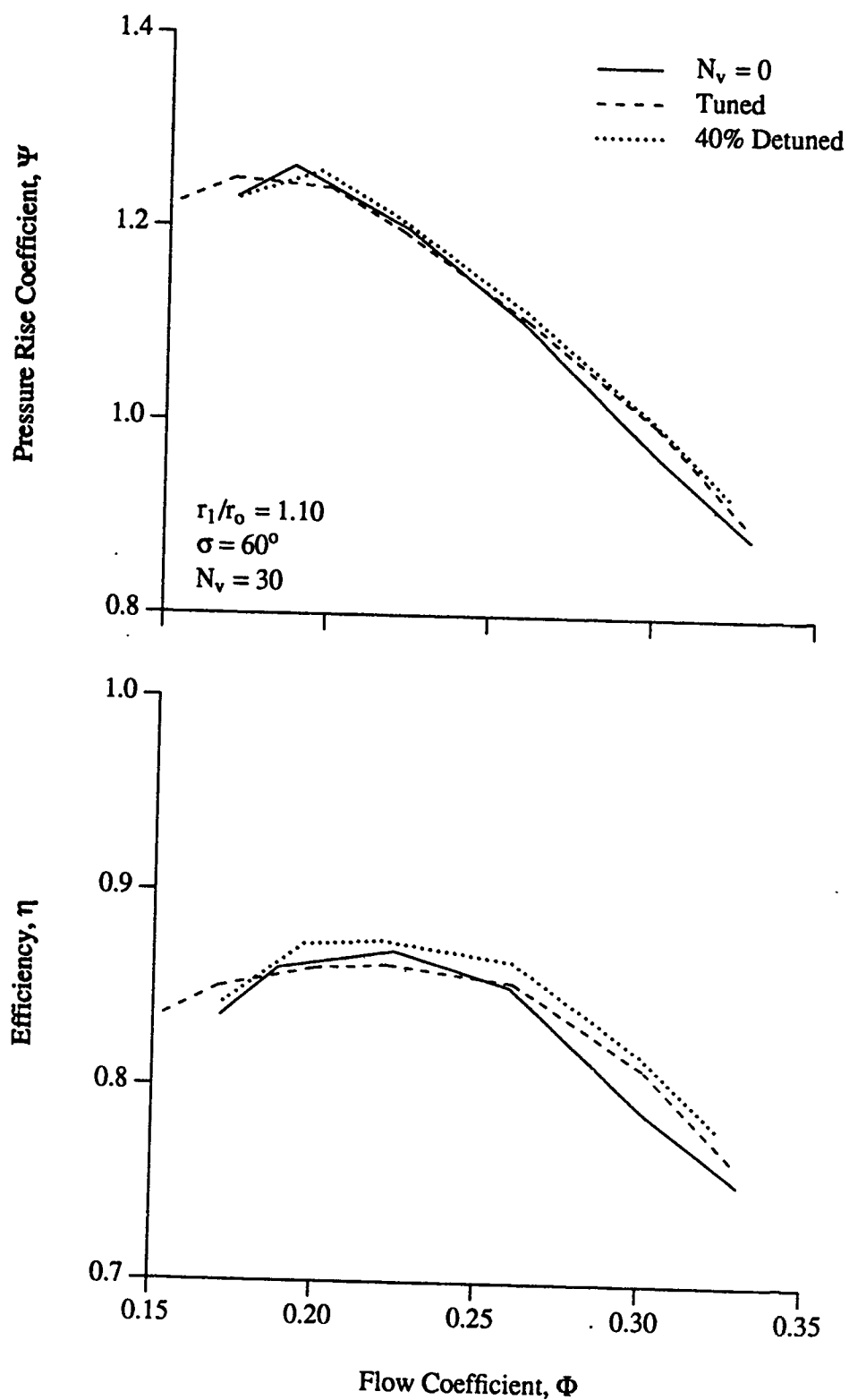


Figure 6.10 Detuned Diffuser Compressor Performance ( $r_1/r_0 = 1.10$ ,  $\sigma = 60^\circ$ ,  $N_v = 30$ )

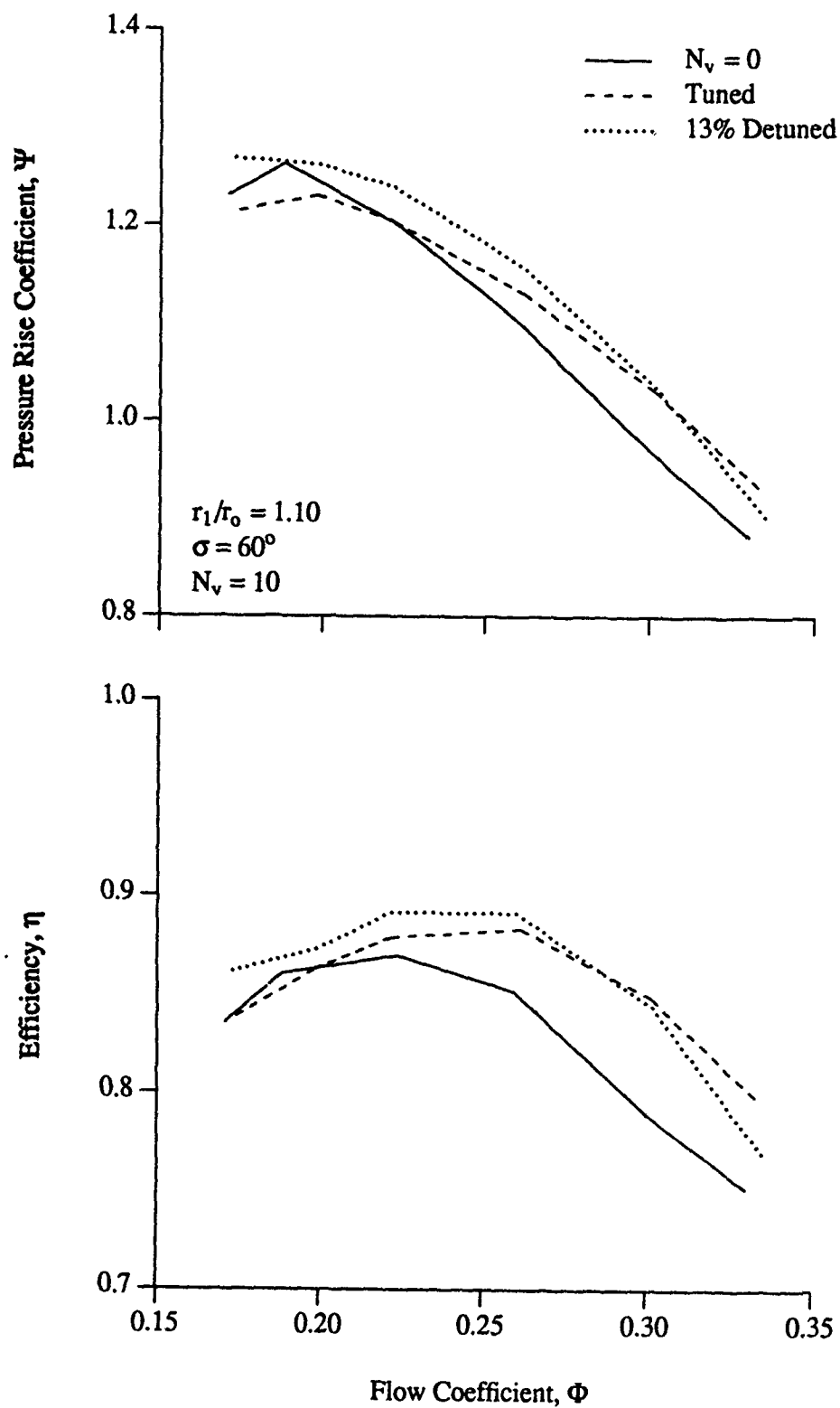
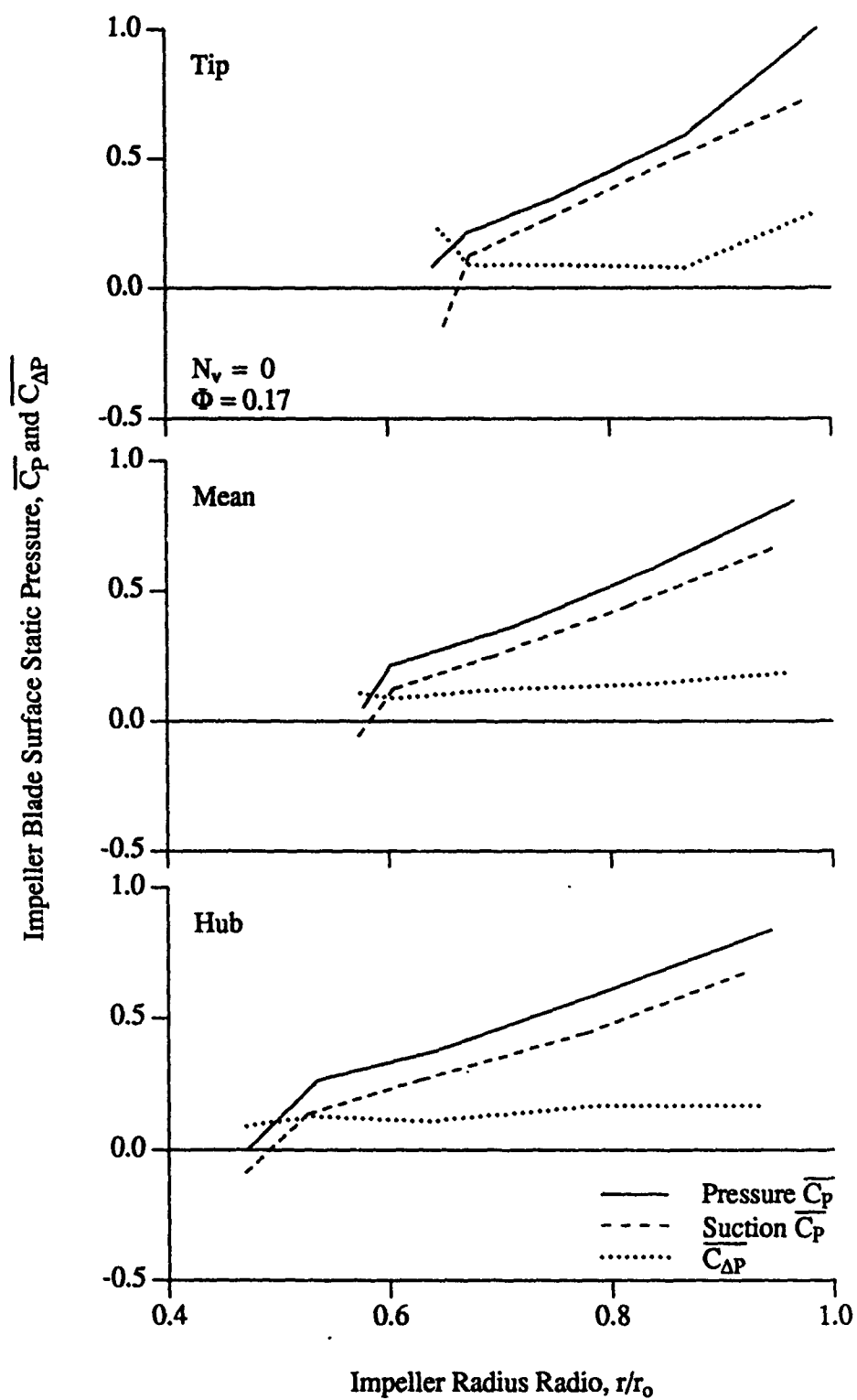
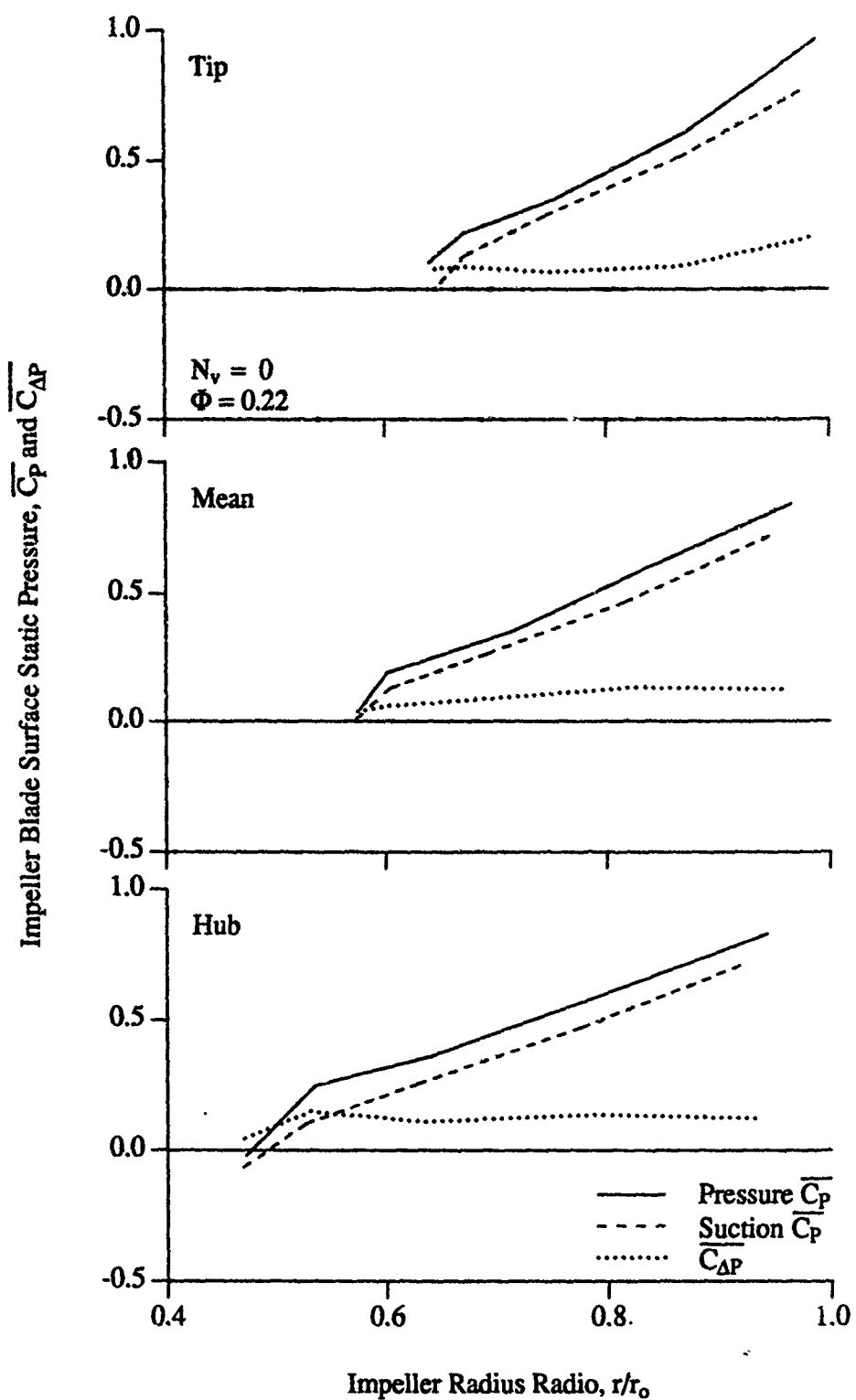
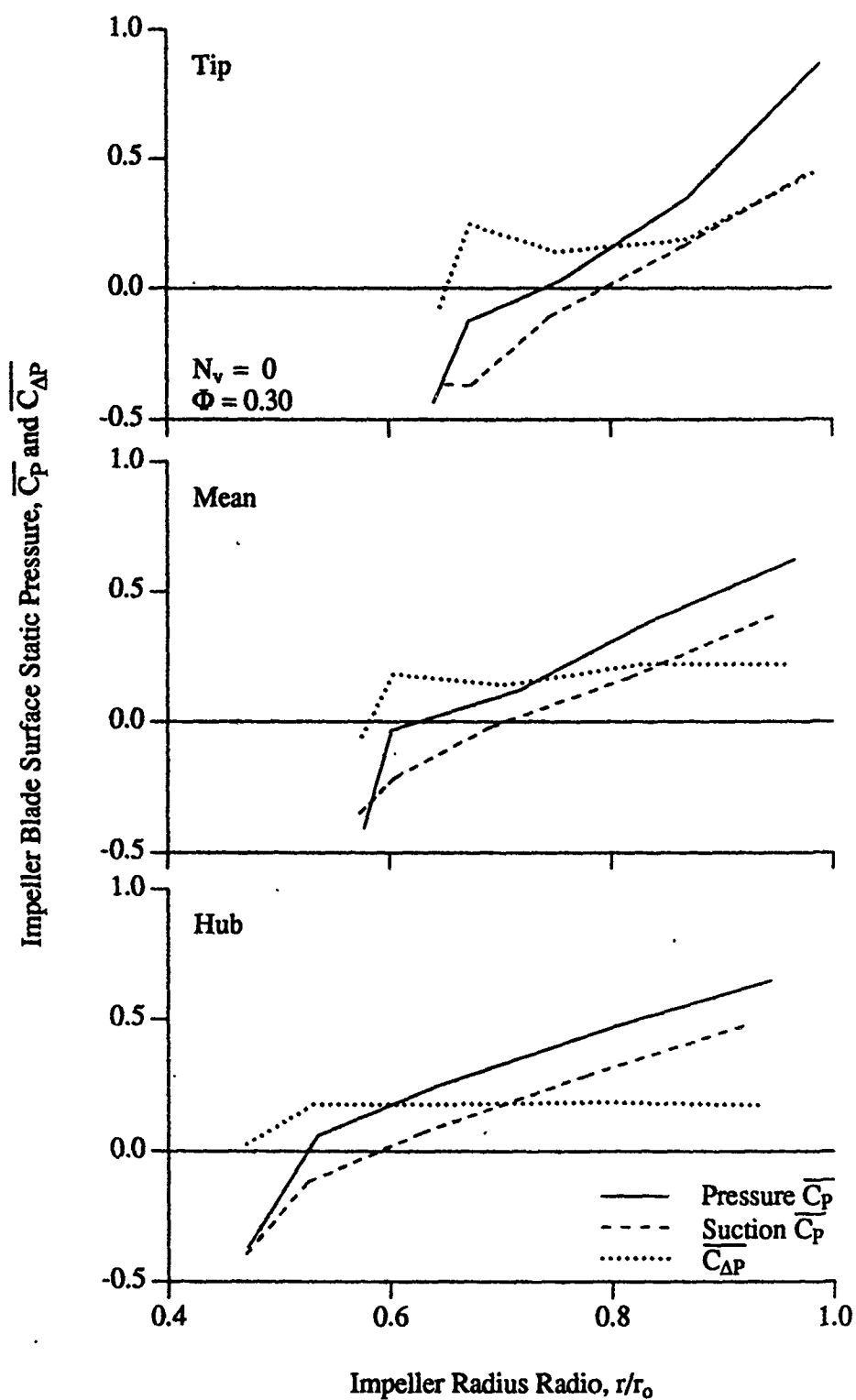


Figure 6.11 Detuned Diffuser Compressor Performance ( $r_1/r_0 = 1.10$ ,  $\sigma = 60^\circ$ ,  $N_v = 10$ )

Figure 6.12 Impeller Static Pressure ( $N_v = 0$ ,  $\Phi = 0.17$ )

Figure 6.13 Impeller Static Pressure ( $N_v = 0$ ,  $\Phi = 0.22$ )

Figure 6.14 Impeller Static Pressure ( $N_v = 0$ ,  $\Phi = 0.30$ )



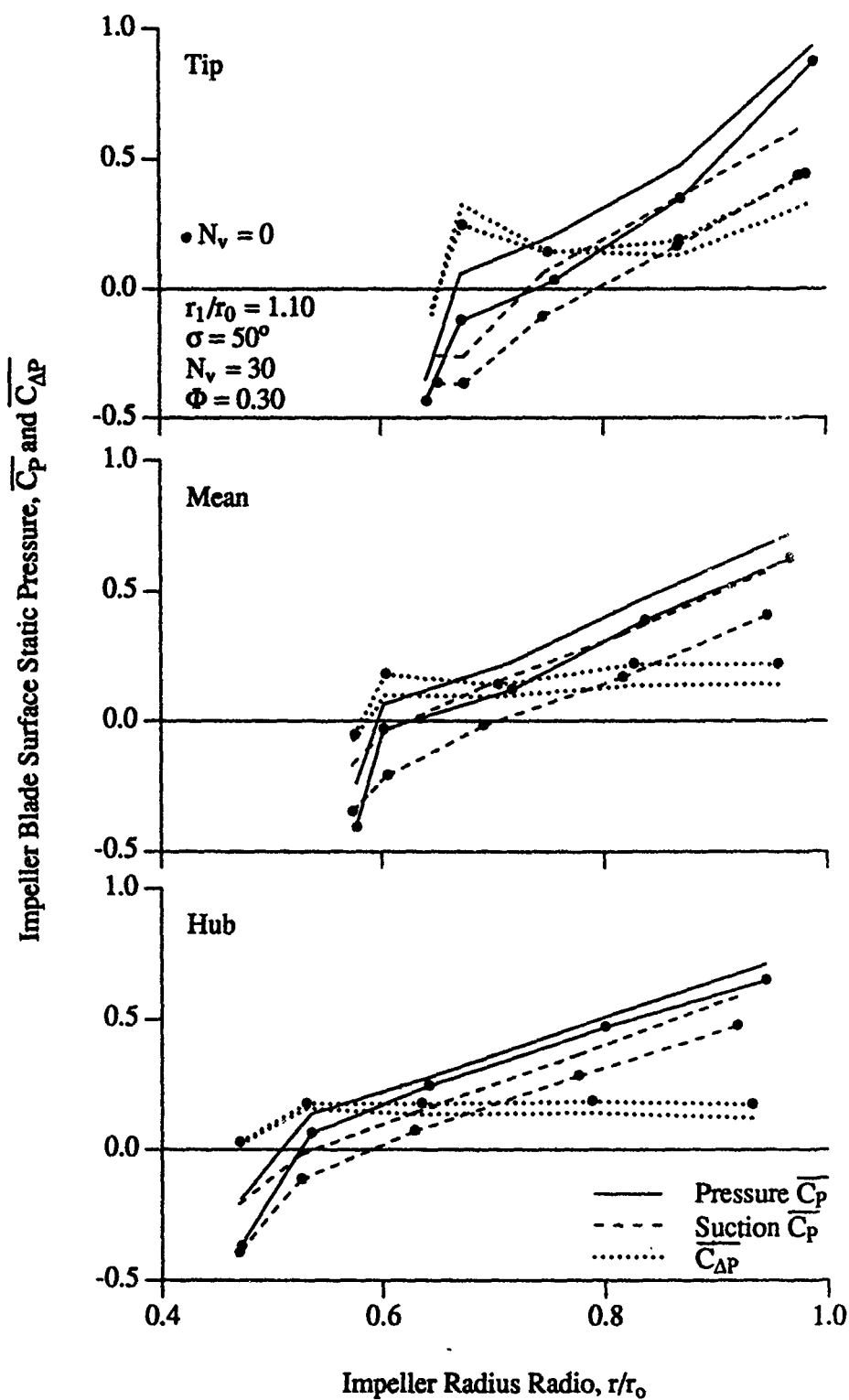


Figure 6.15 Impeller Static Pressure ( $r_1/r_0 = 1.10$ ,  $\sigma = 50^\circ$ ,  $N_v = 30$ ,  $\Phi = 0.30$ )

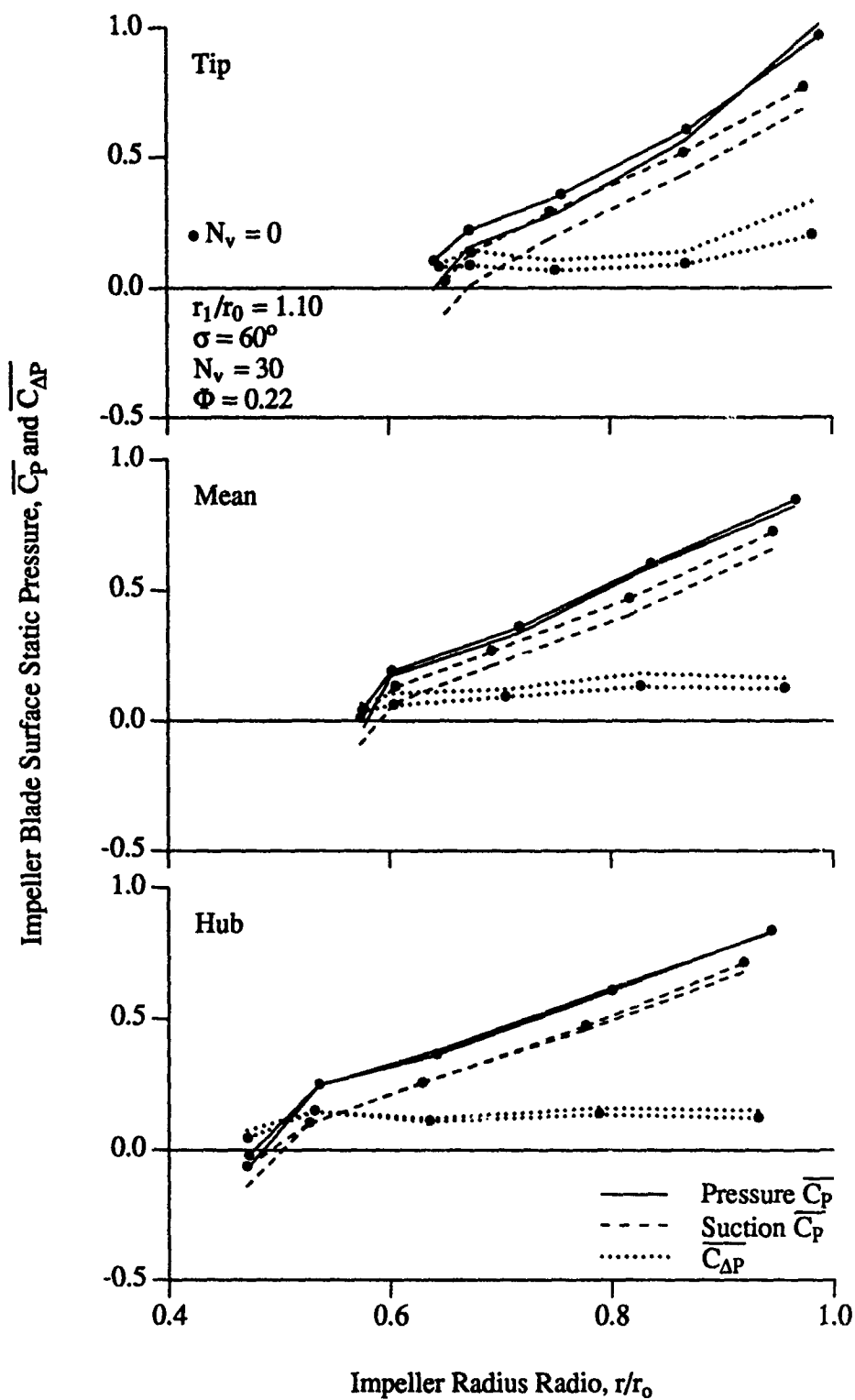


Figure 6.16 Impeller Static Pressure ( $r_1/r_0 = 1.10$ ,  $\sigma = 60^\circ$ ,  $N_v = 30$ ,  $\Phi = 0.22$ )

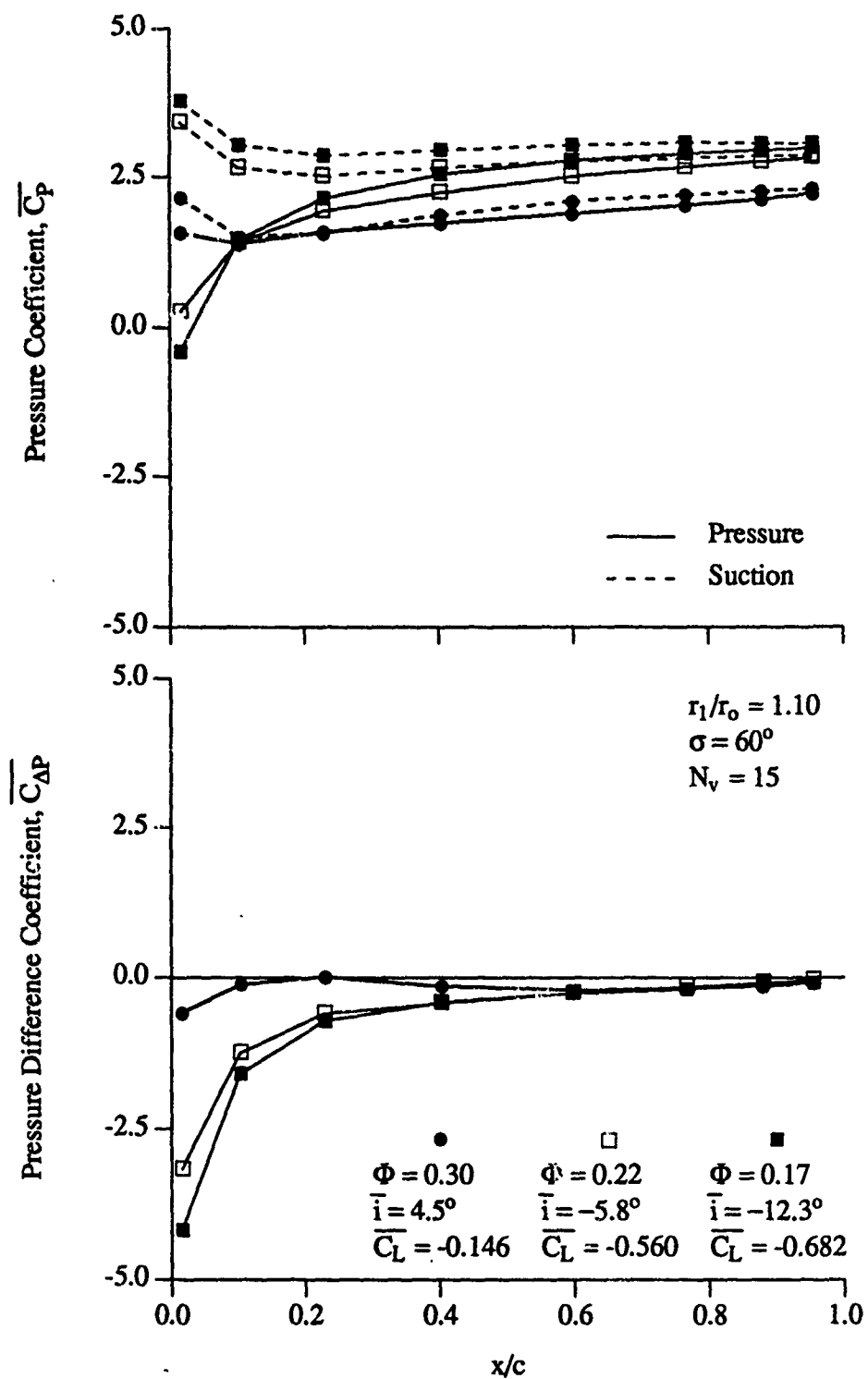


Figure 6.17 Incidence Effects on Diffuser Vane Steady Static Pressure  
( $r_1/r_0 = 1.10$ ,  $\sigma = 60^\circ$ ,  $N_v = 15$ )

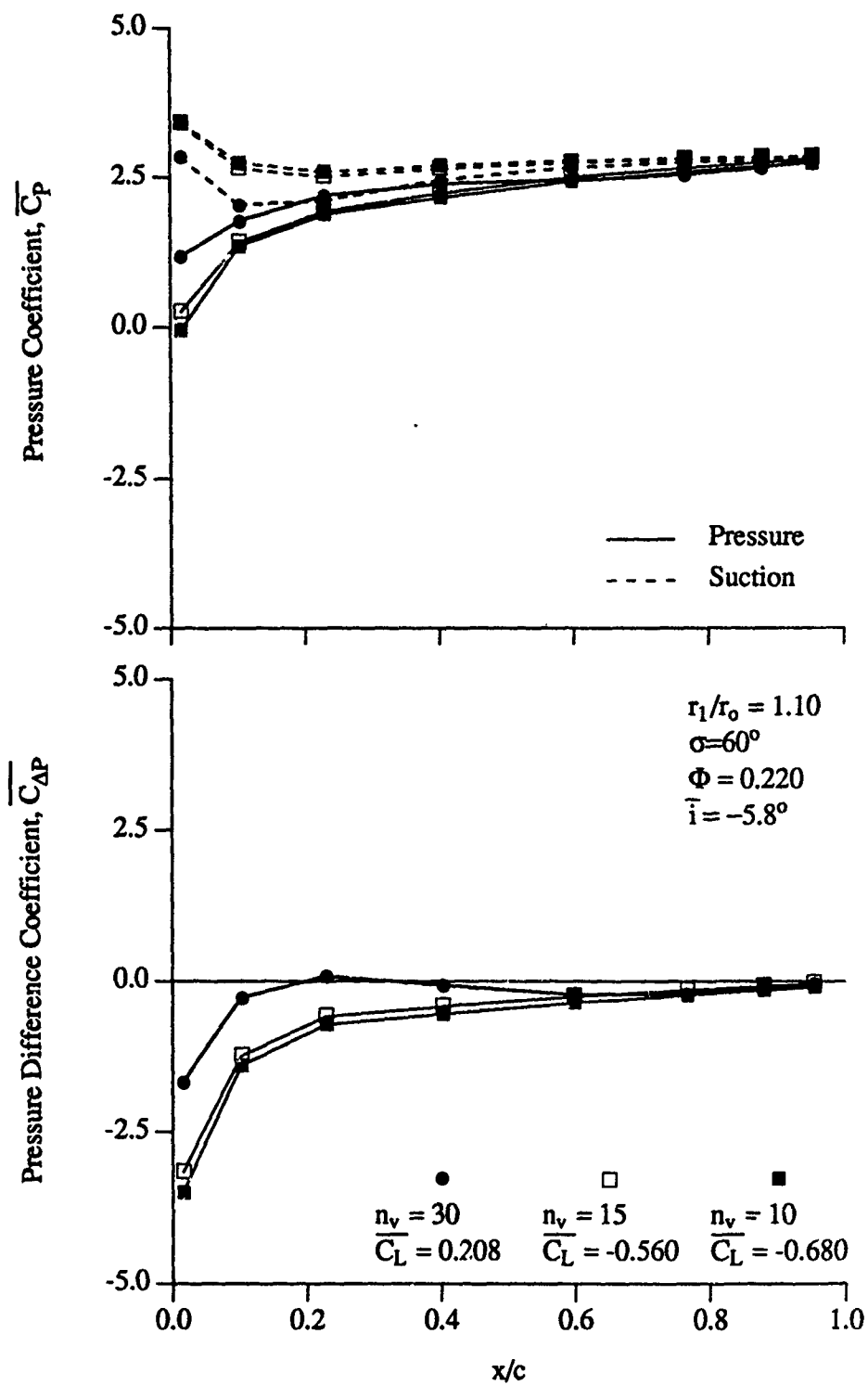


Figure 6.18 Vane Number Effects on Diffuser Vane Steady Static Pressure  
 $(r_1/r_o = 1.10, \sigma = 60^\circ, \Phi = 0.22)$

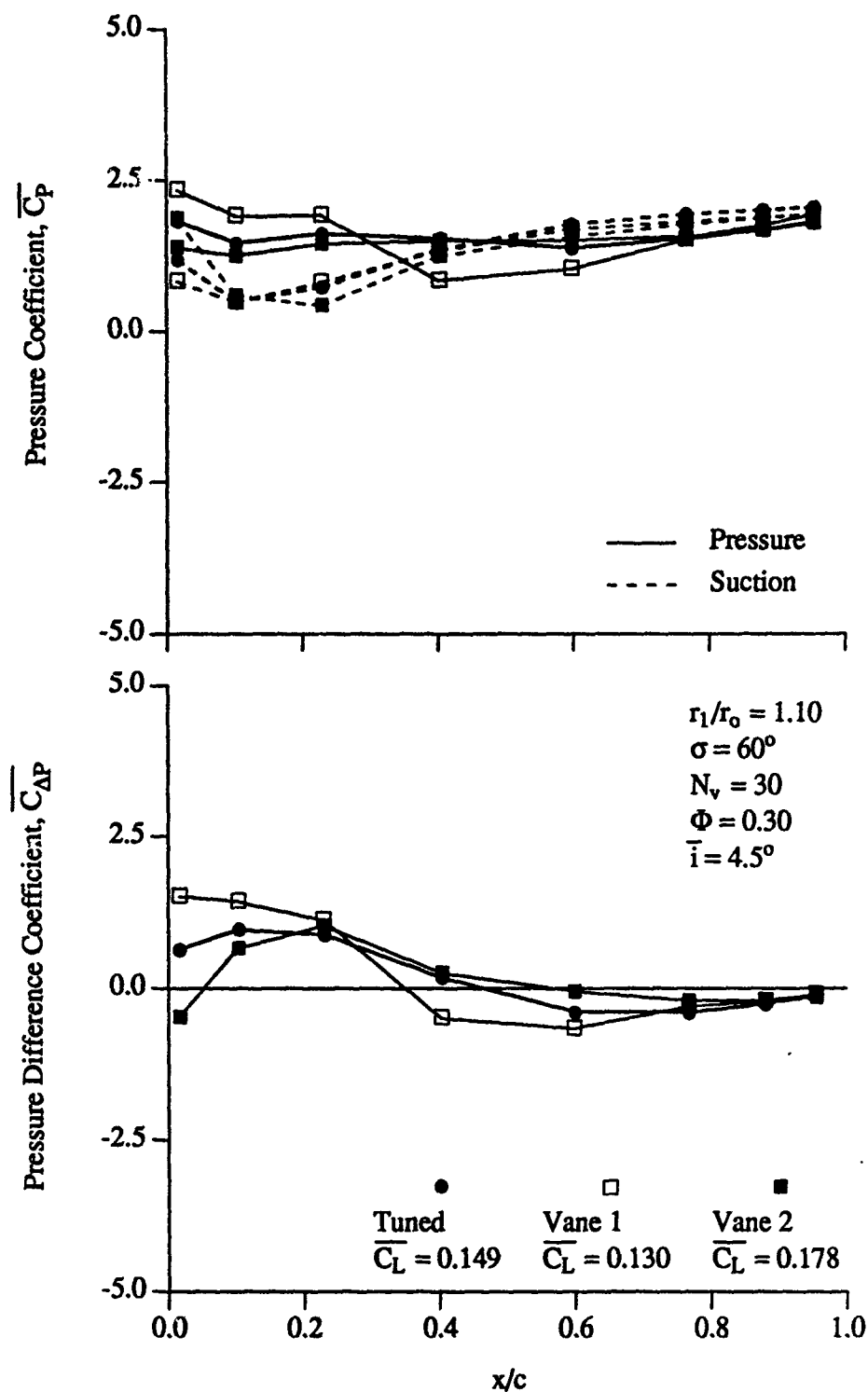


Figure 6.19 Detuned Diffuser Vane Steady Static Pressure  
 $(r_1/r_0 = 1.10, \sigma = 60^\circ, N_v = 30, \Phi = 0.30)$

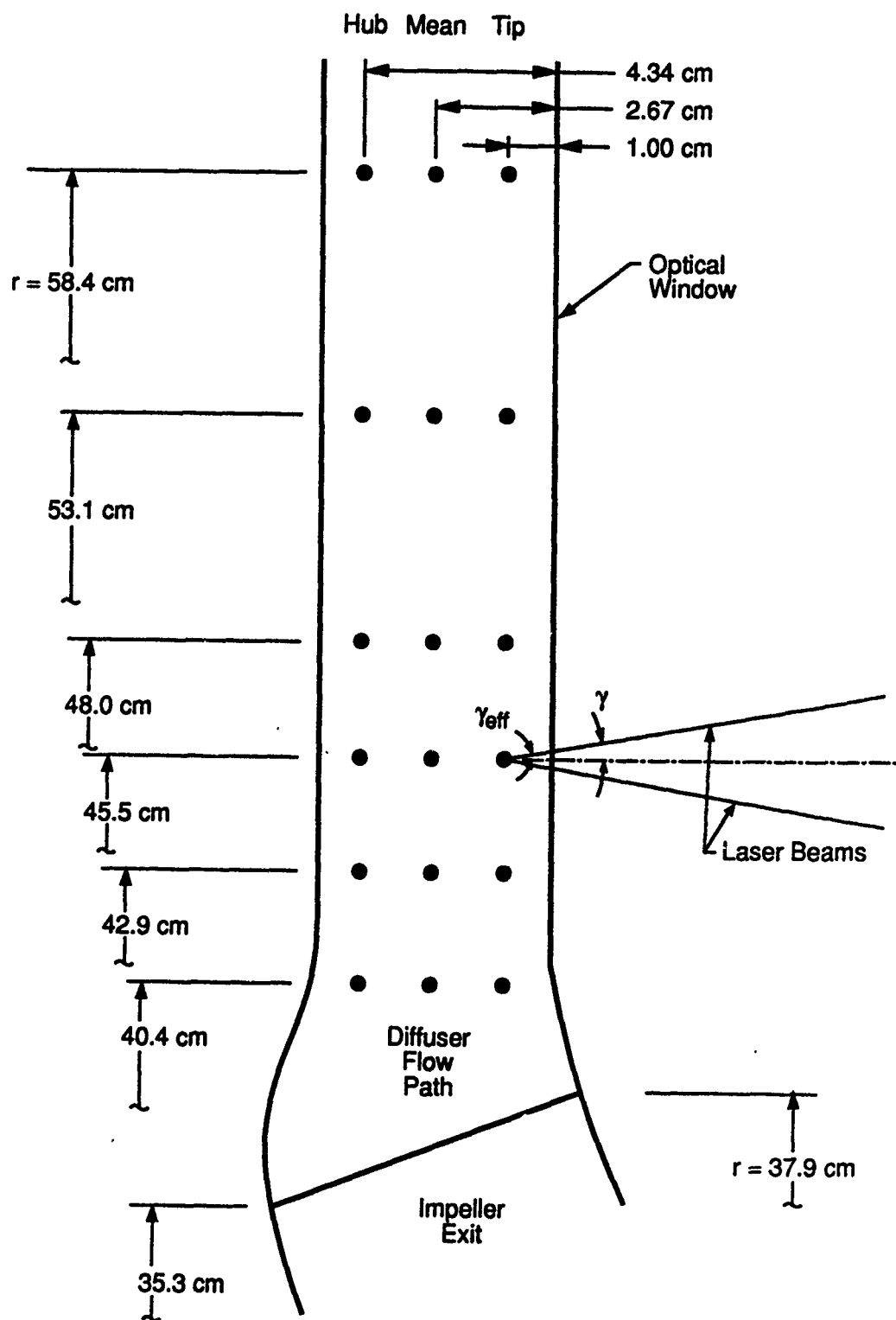


Figure 6.20 LDV Measurement Positions

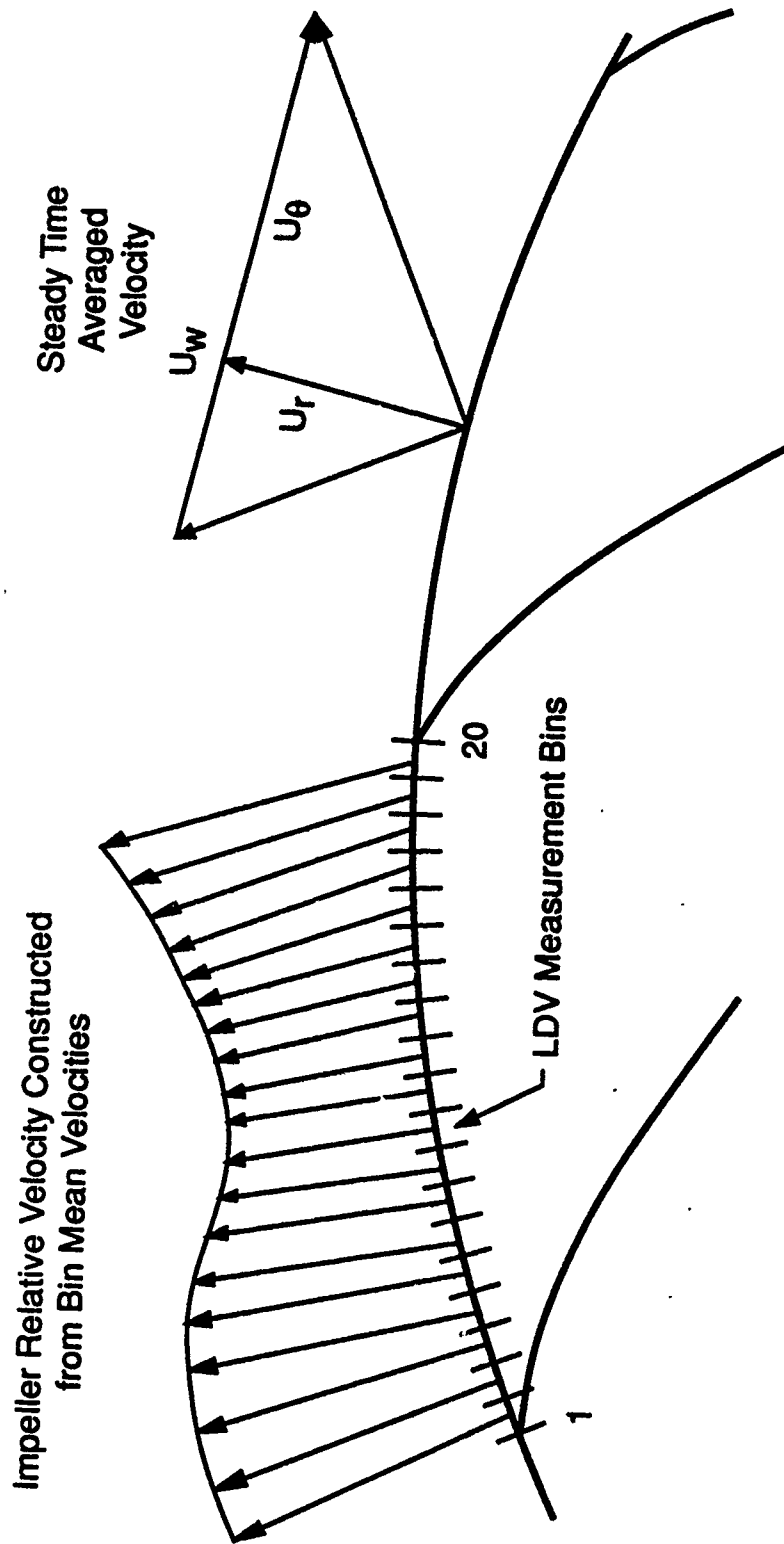


Figure 6.21 LDV Circumferential Measurement Bins

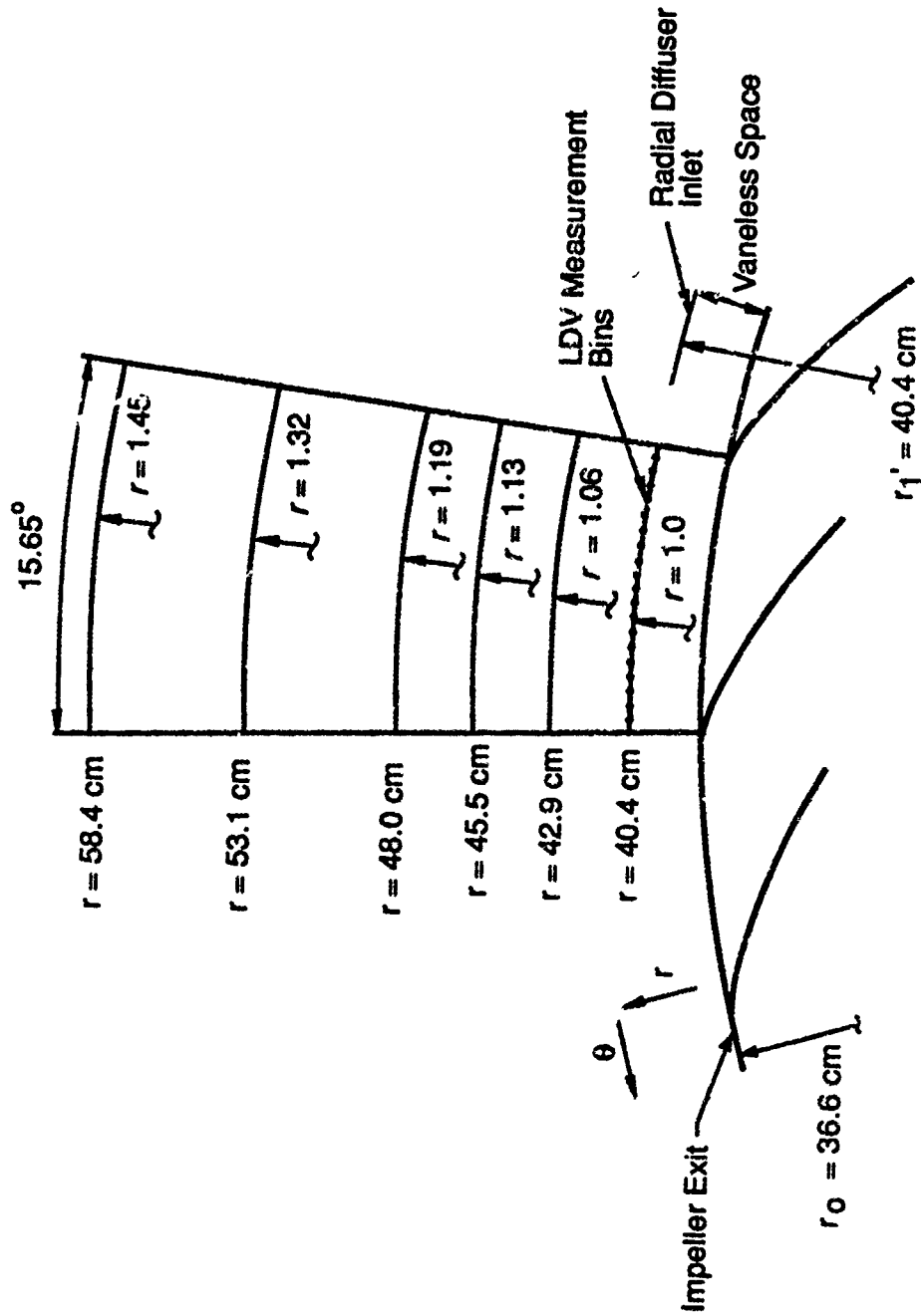


Figure 6.22 LDV Radial and Circumferential Measurement Positions



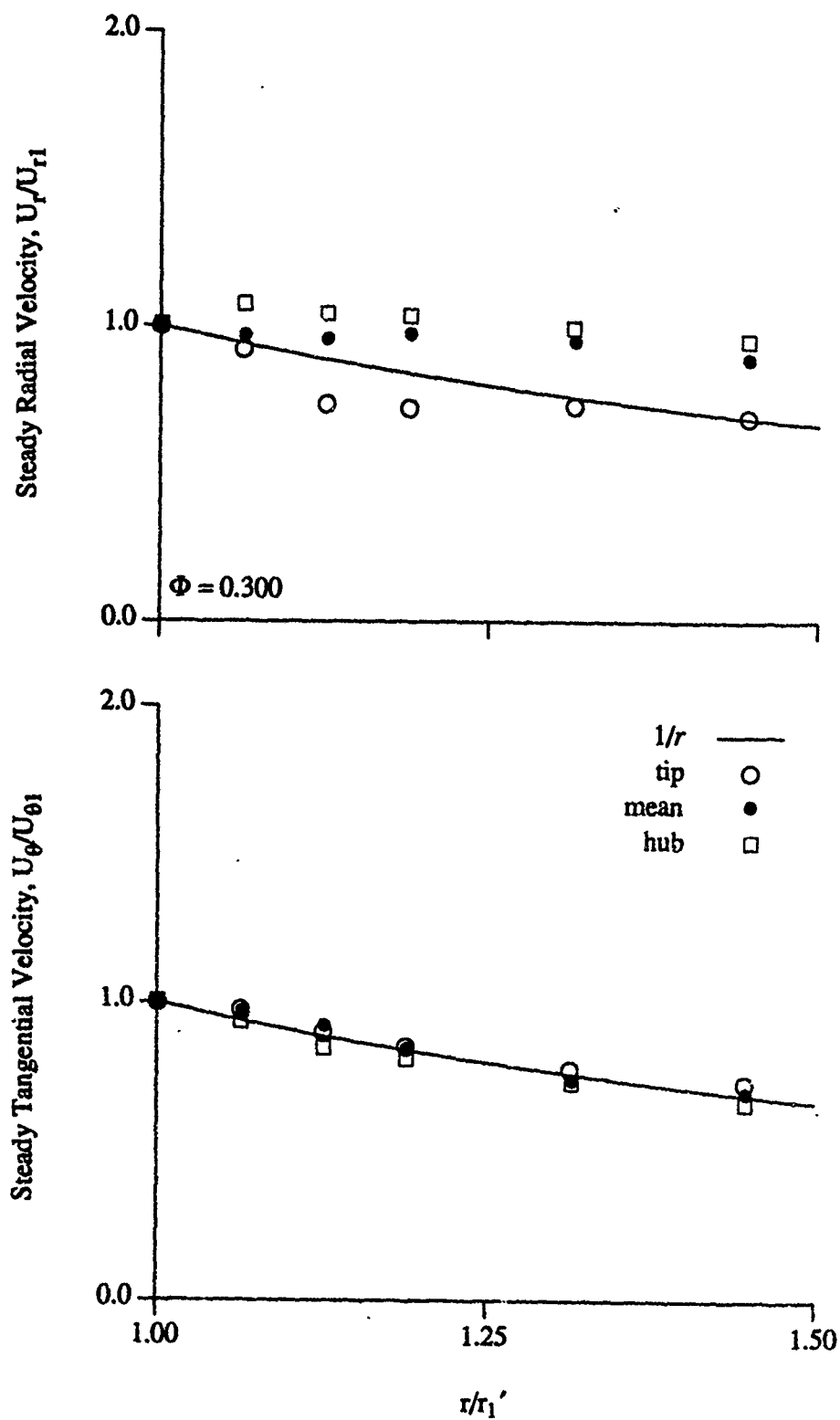


Figure 6.23 Vaneless Diffuser Time-Averaged Velocity ( $\Phi = 0.30$ )

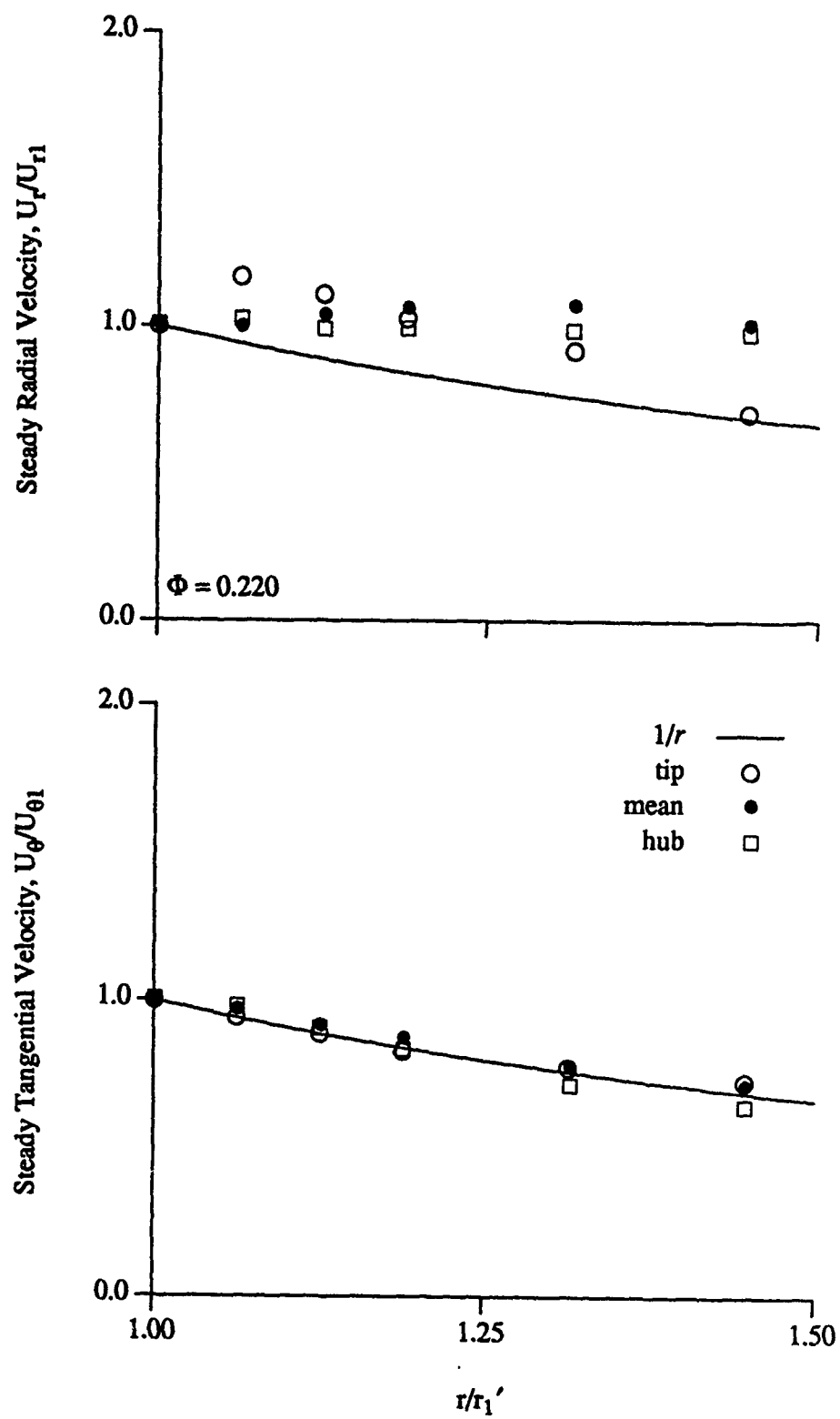
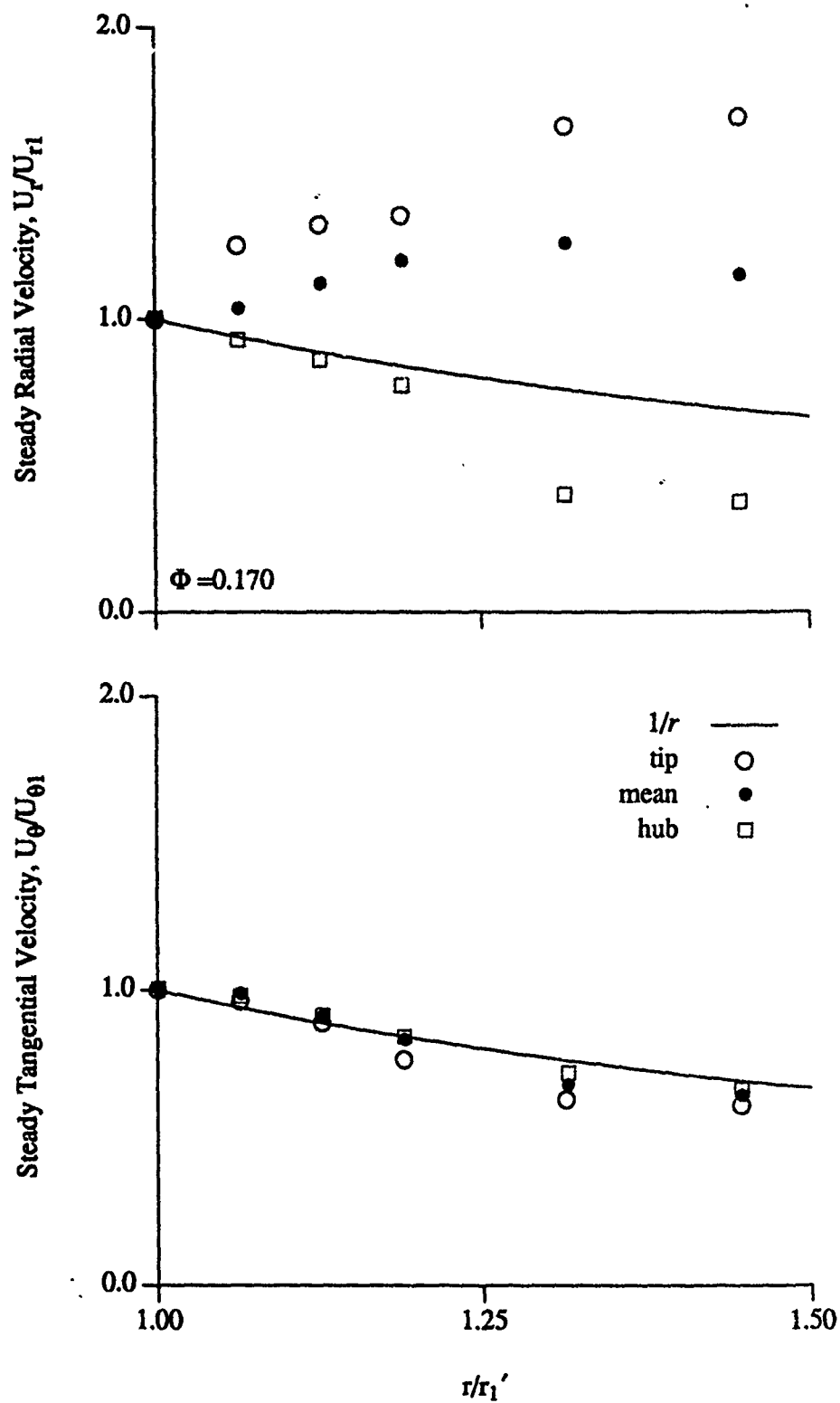


Figure 6.24 Vaneless Diffuser Time-Averaged Velocity ( $\Phi = 0.22$ )

Figure 6.25 Vaneless Diffuser Time-Averaged Velocity ( $\Phi = 0.17$ )

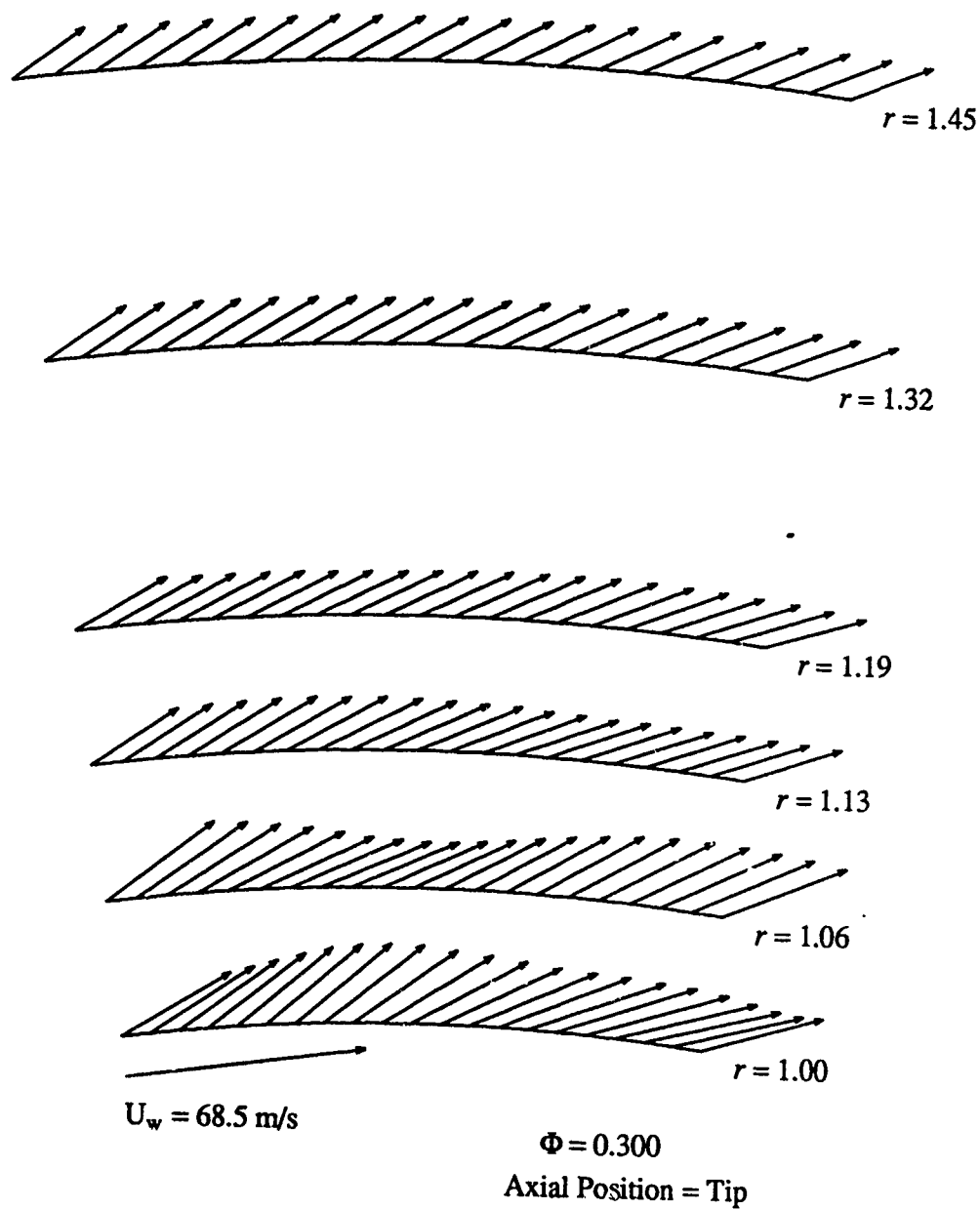


Figure 6.26 Vaneless Diffuser Total Velocity (Tip Position,  $\Phi = 0.30$ )

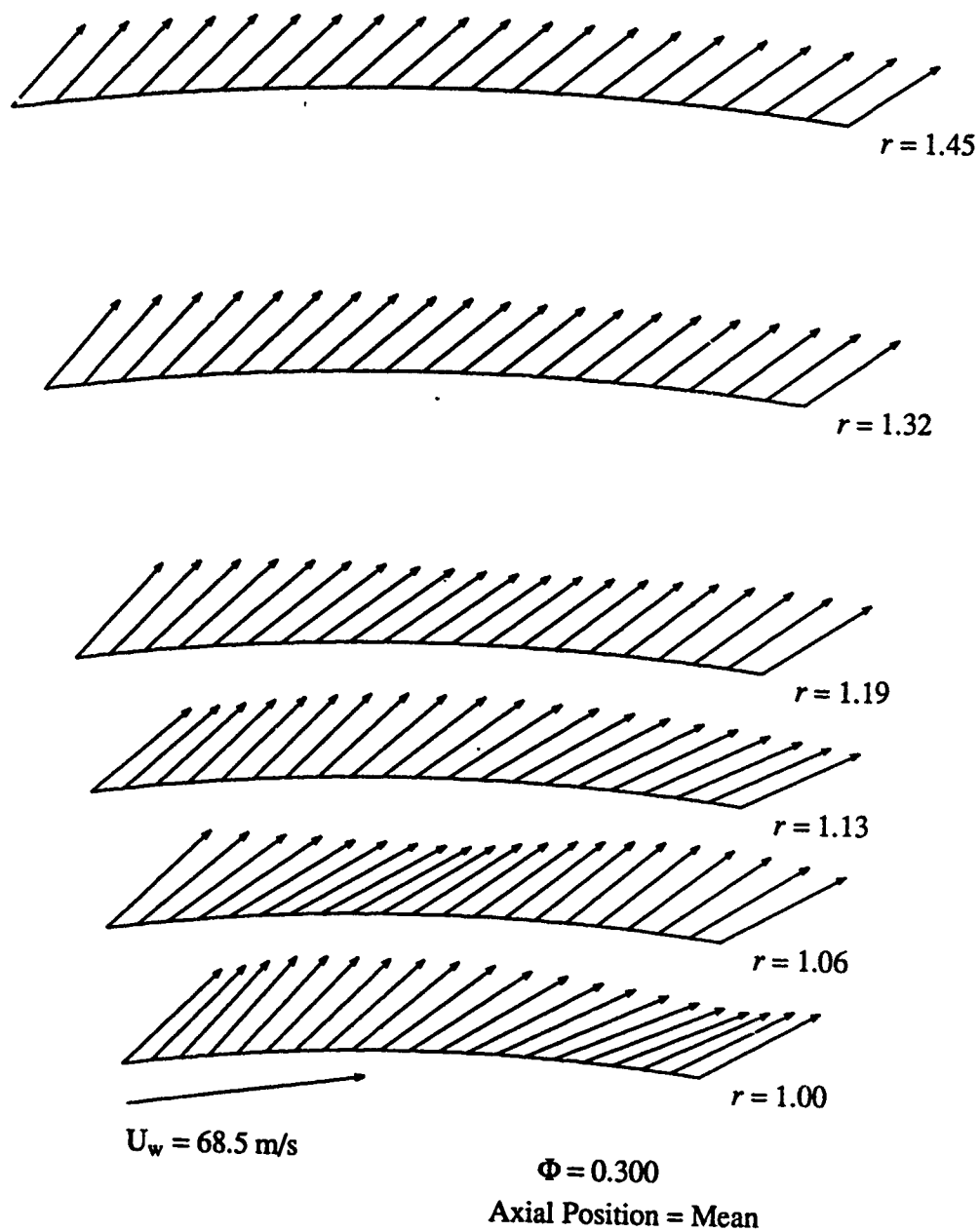


Figure 6.27 Vaneless Diffuser Total Velocity (Mean Position,  $\Phi = 0.30$ )

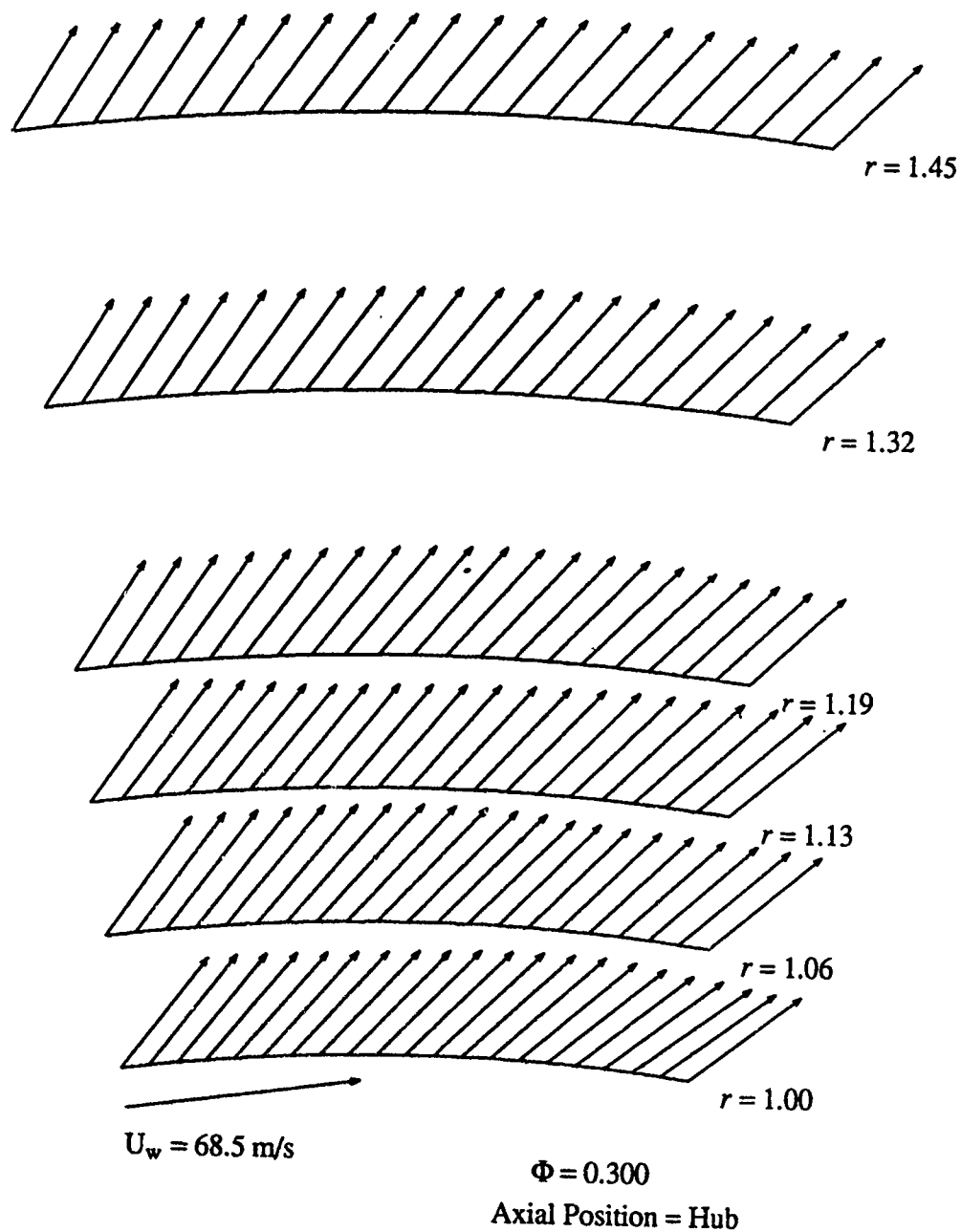


Figure 6.28 Vaneless Diffuser Total Velocity (Hub Position,  $\Phi = 0.30$ )

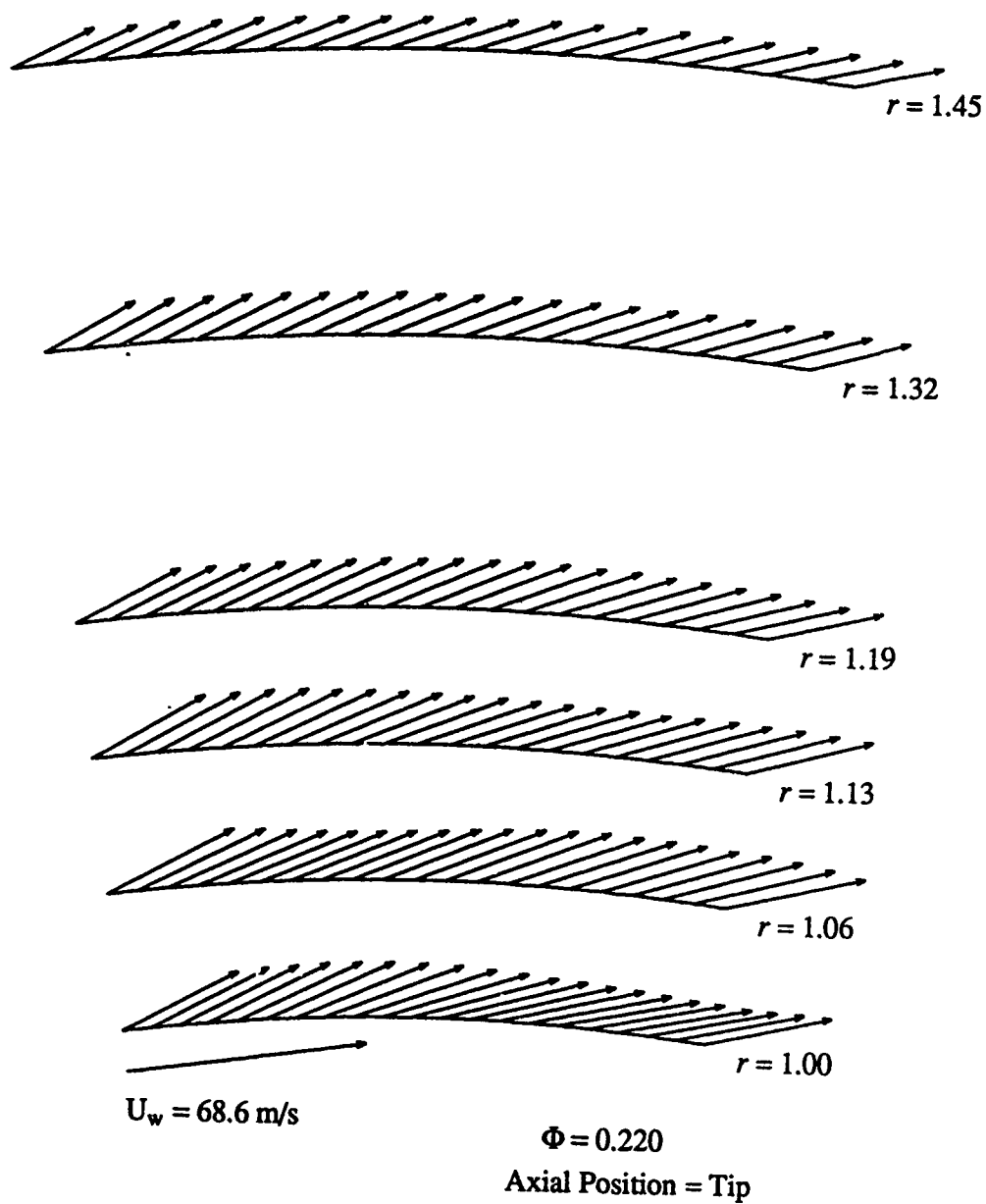


Figure 6.29 Vaneless Diffuser Total Velocity (Tip Position,  $\Phi = 0.22$ )

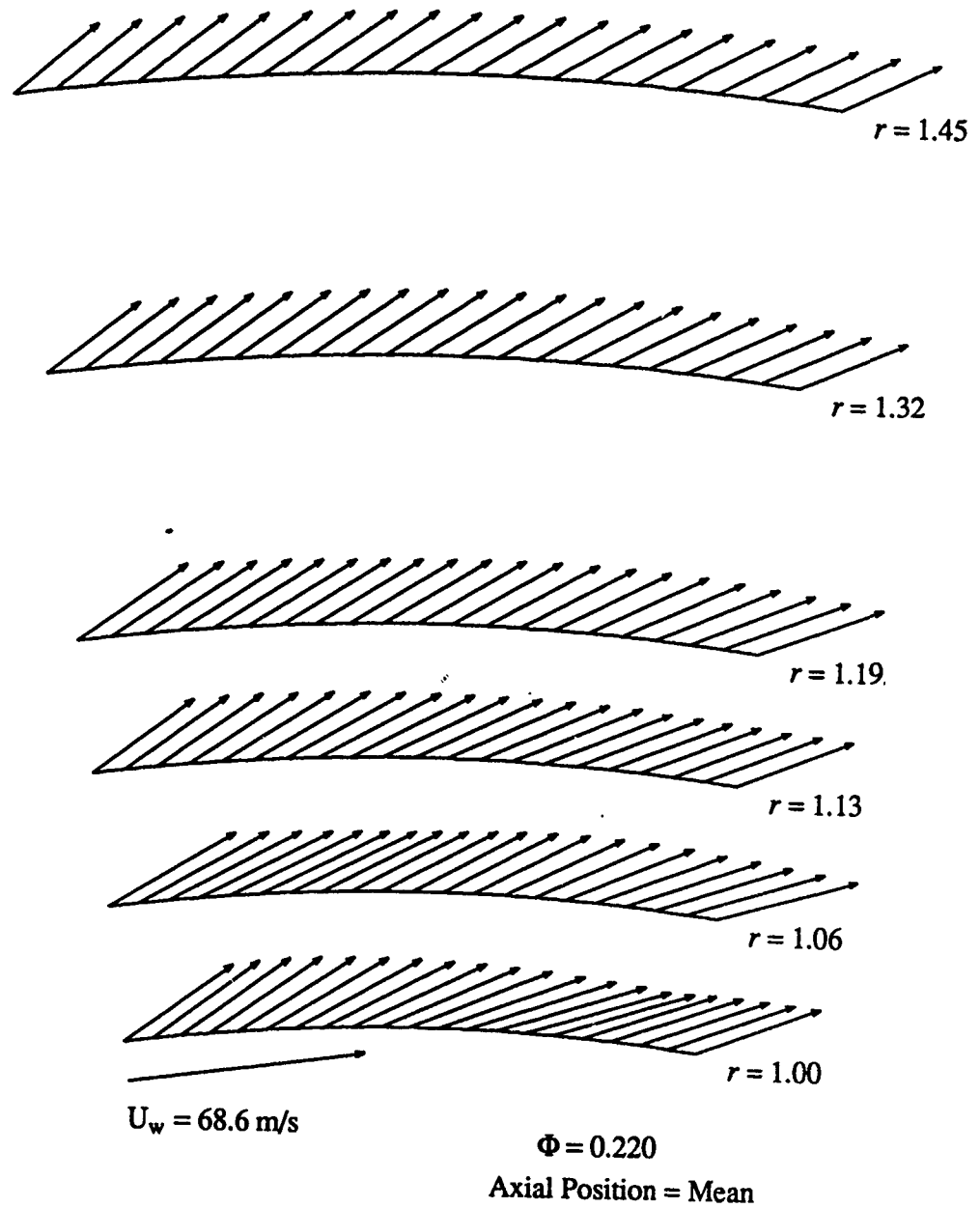


Figure 6.30 Vaneless Diffuser Total Velocity (Mean Position,  $\Phi = 0.22$ )



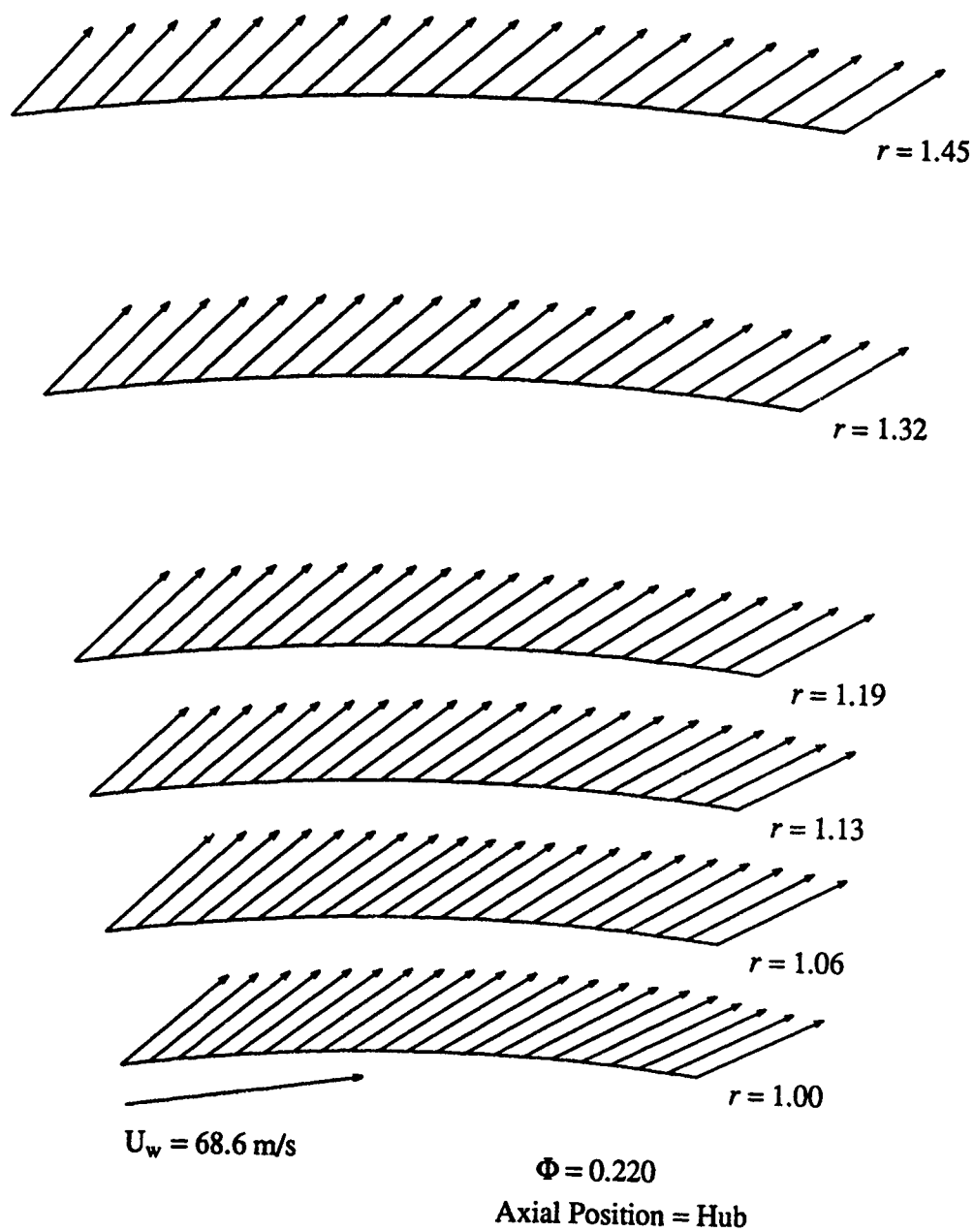


Figure 6.31 Vaneless Diffuser Total Velocity (Hub Position,  $\Phi = 0.22$ )

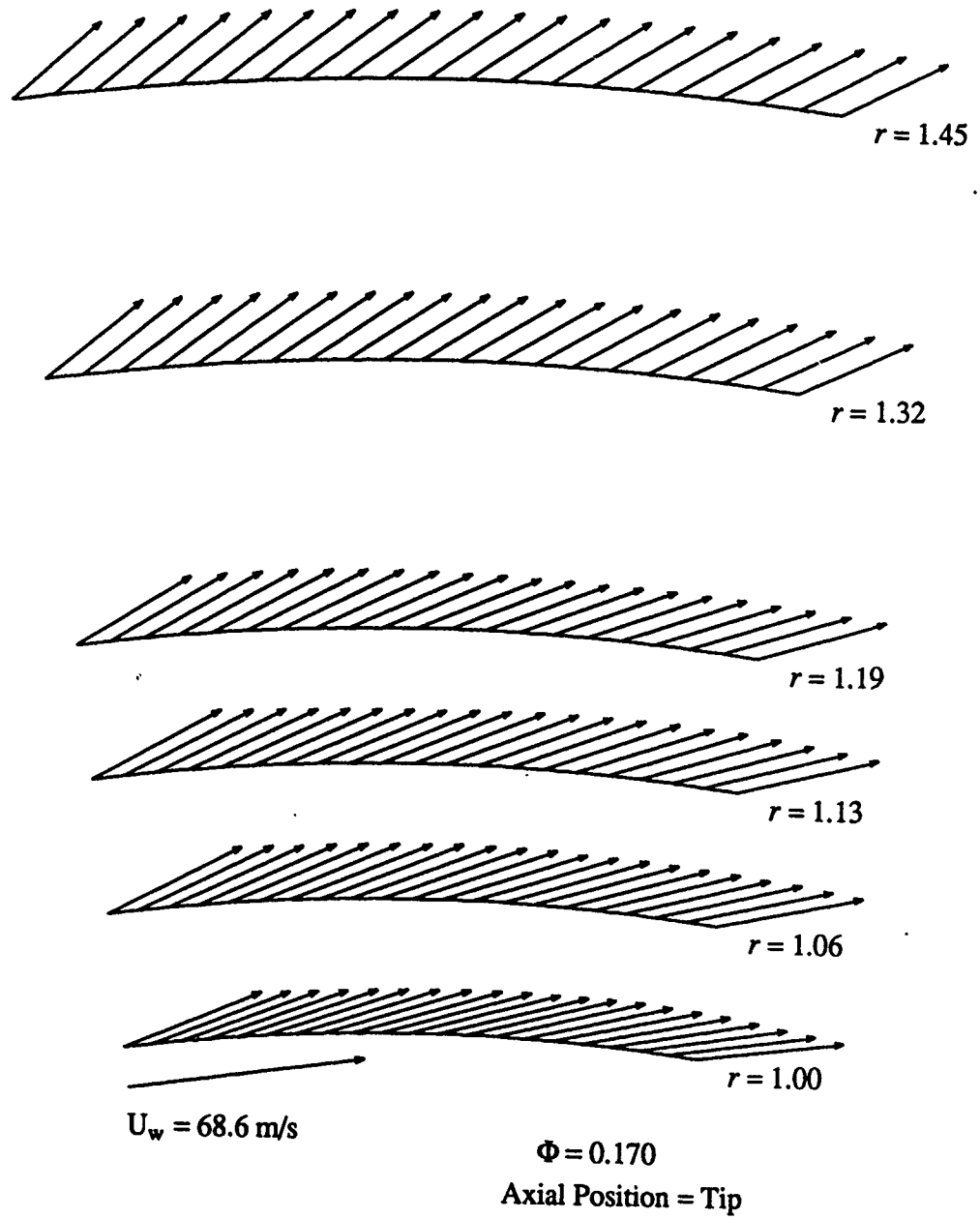


Figure 6.32 Vaneless Diffuser Total Velocity (Tip Position;  $\Phi = 0.17$ )

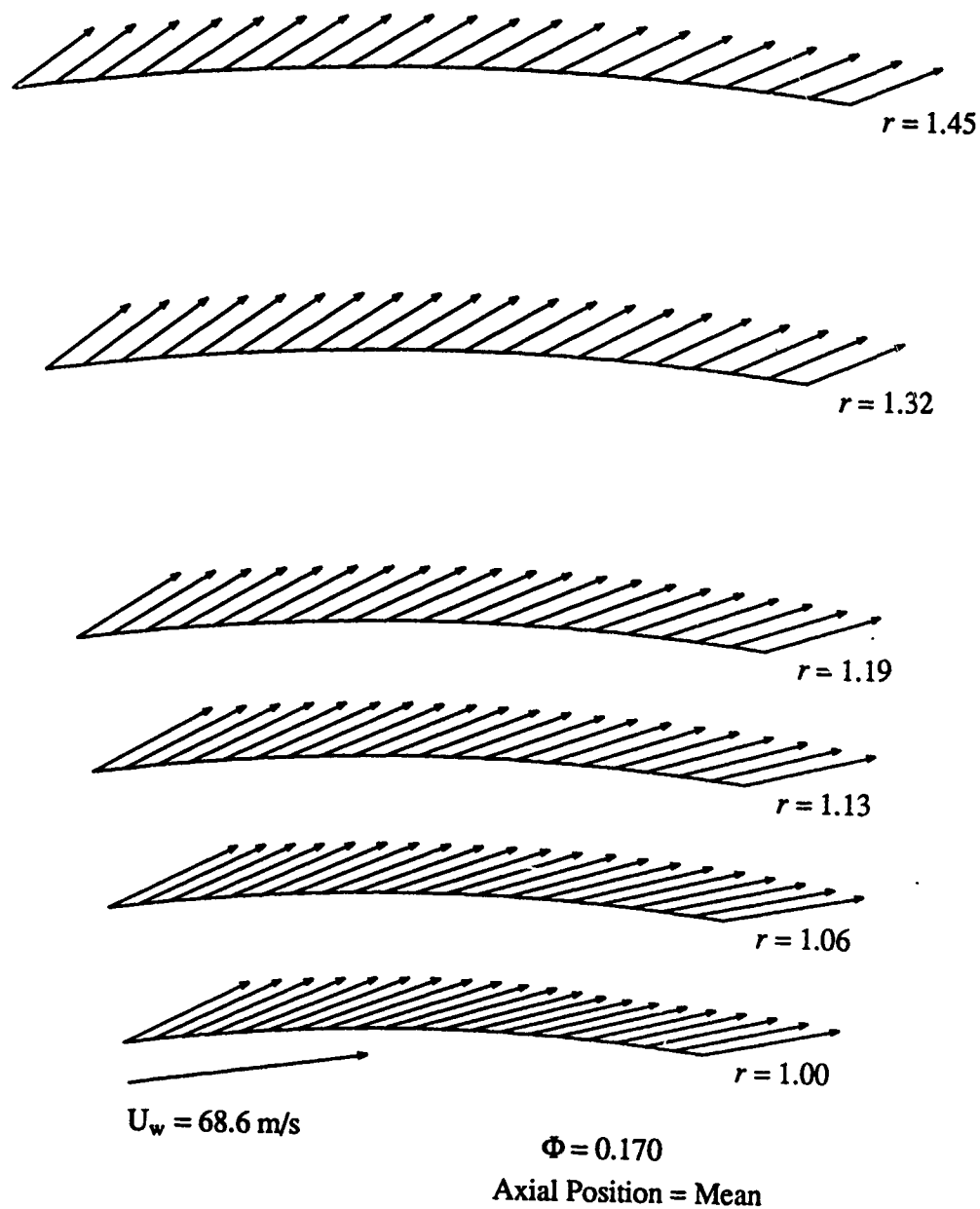


Figure 6.33 Vaneless Diffuser Total Velocity (Mean Position,  $\Phi = 0.17$ )

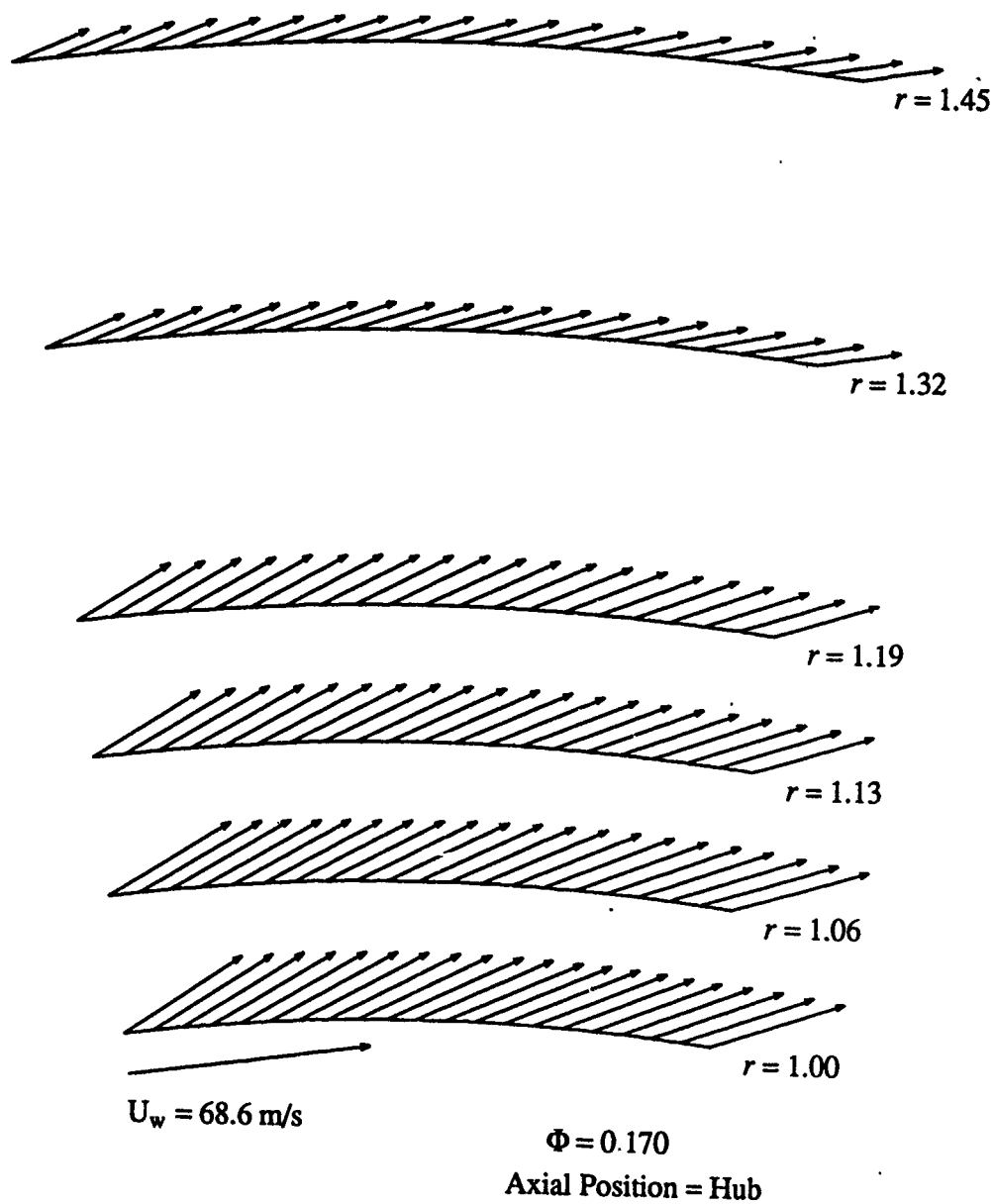


Figure 6.34 Vaneless Diffuser Total Velocity (Hub Position,  $\Phi = 0.17$ )

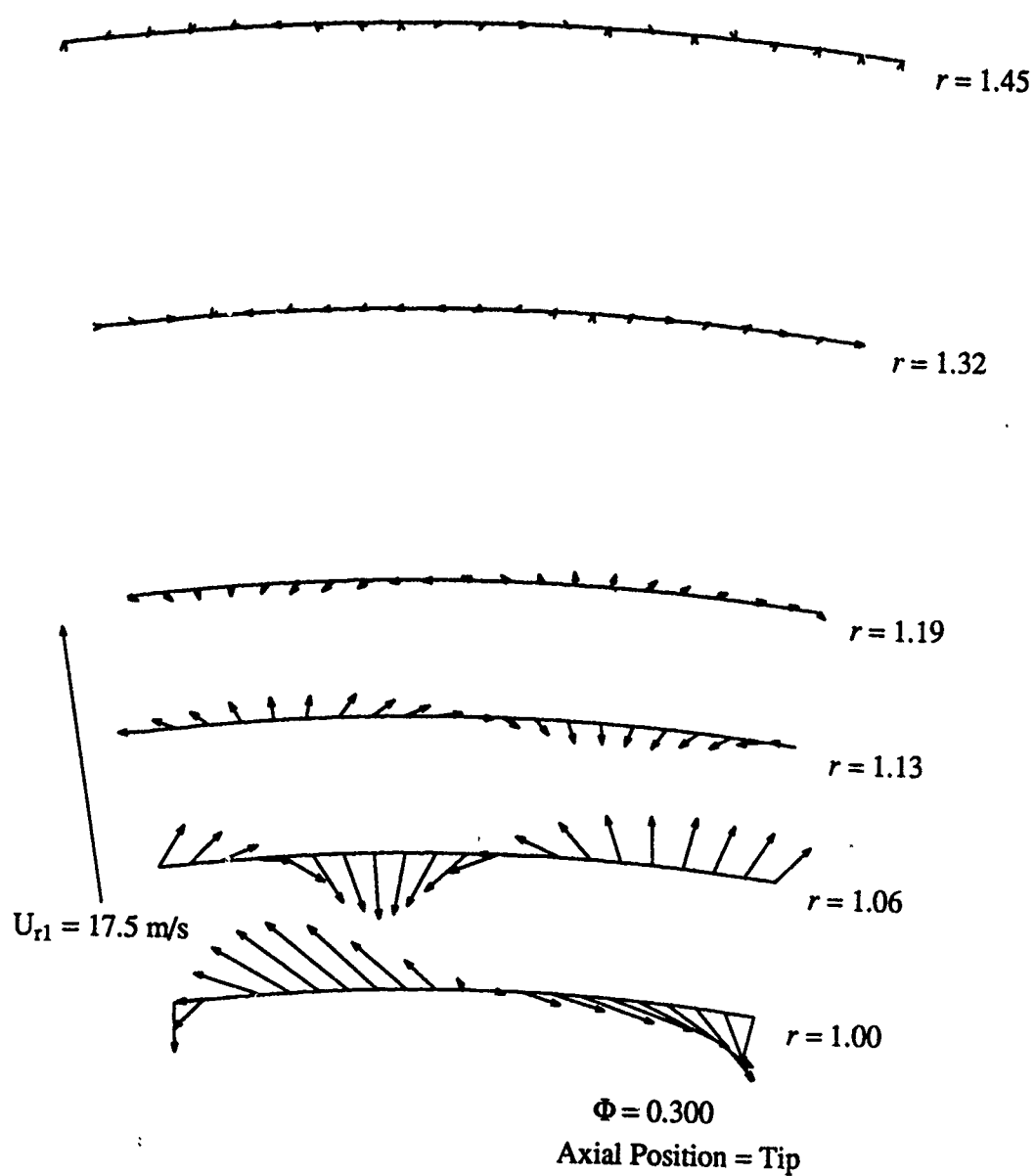


Figure 6.35 Vaneless Diffuser Unsteady Velocity (Tip Position,  $\Phi = 0.30$ )

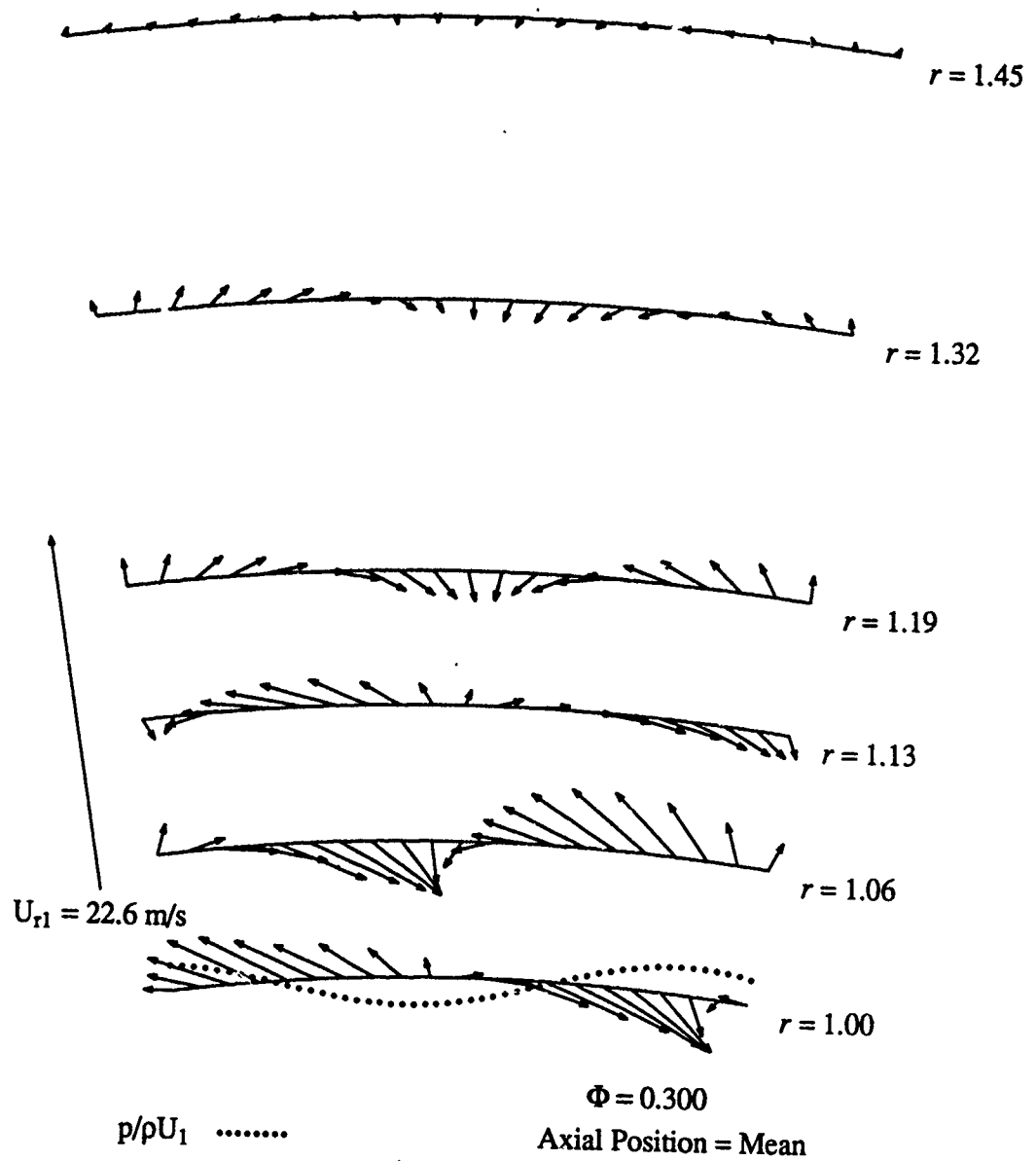


Figure 6.36 Vaneless Diffuser Unsteady Velocity (Mean Position,  $\Phi = 0.30$ )

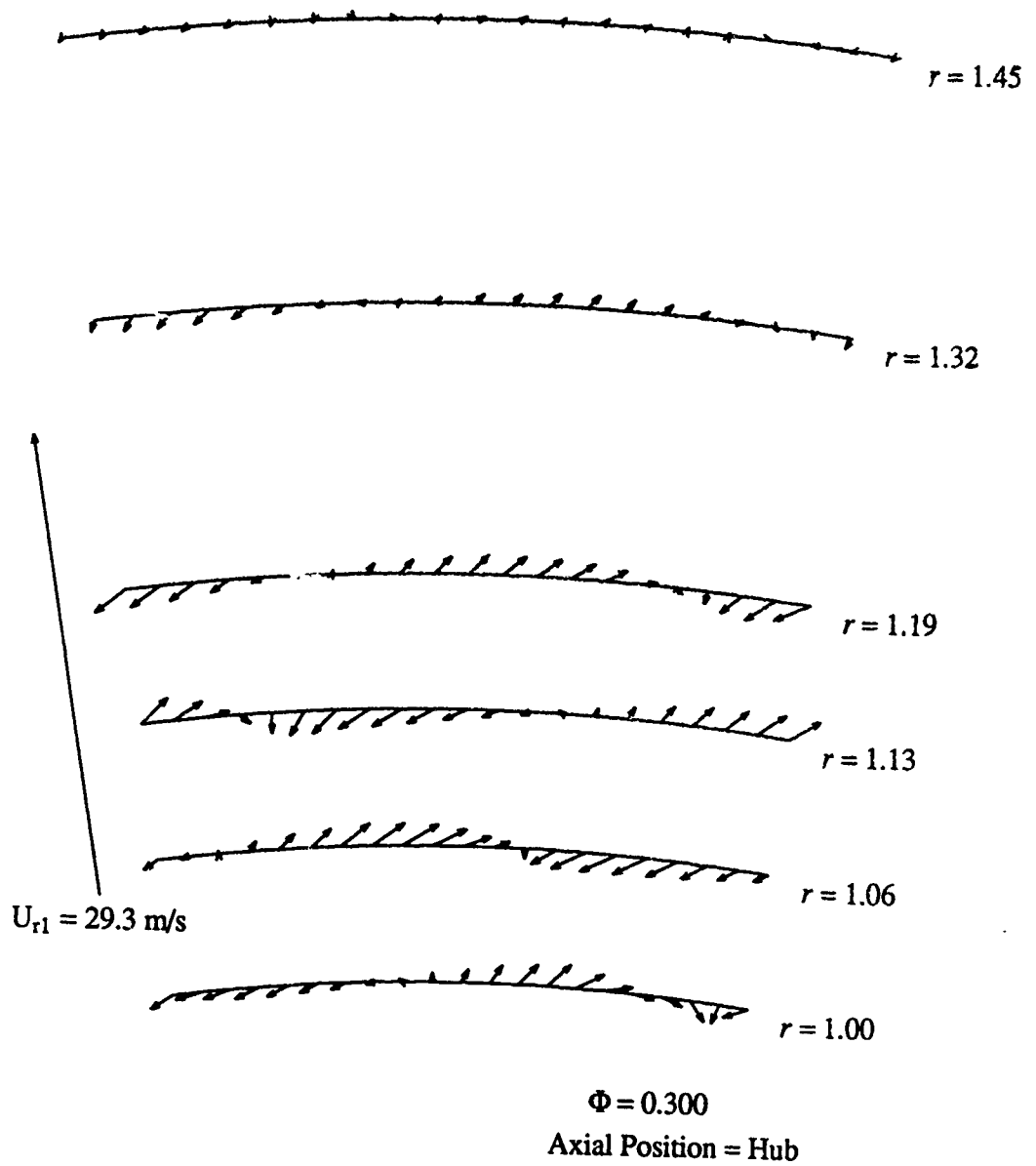


Figure 6.37 Vaneless Diffuser Unsteady Velocity (Hub Position,  $\Phi = 0.30$ )

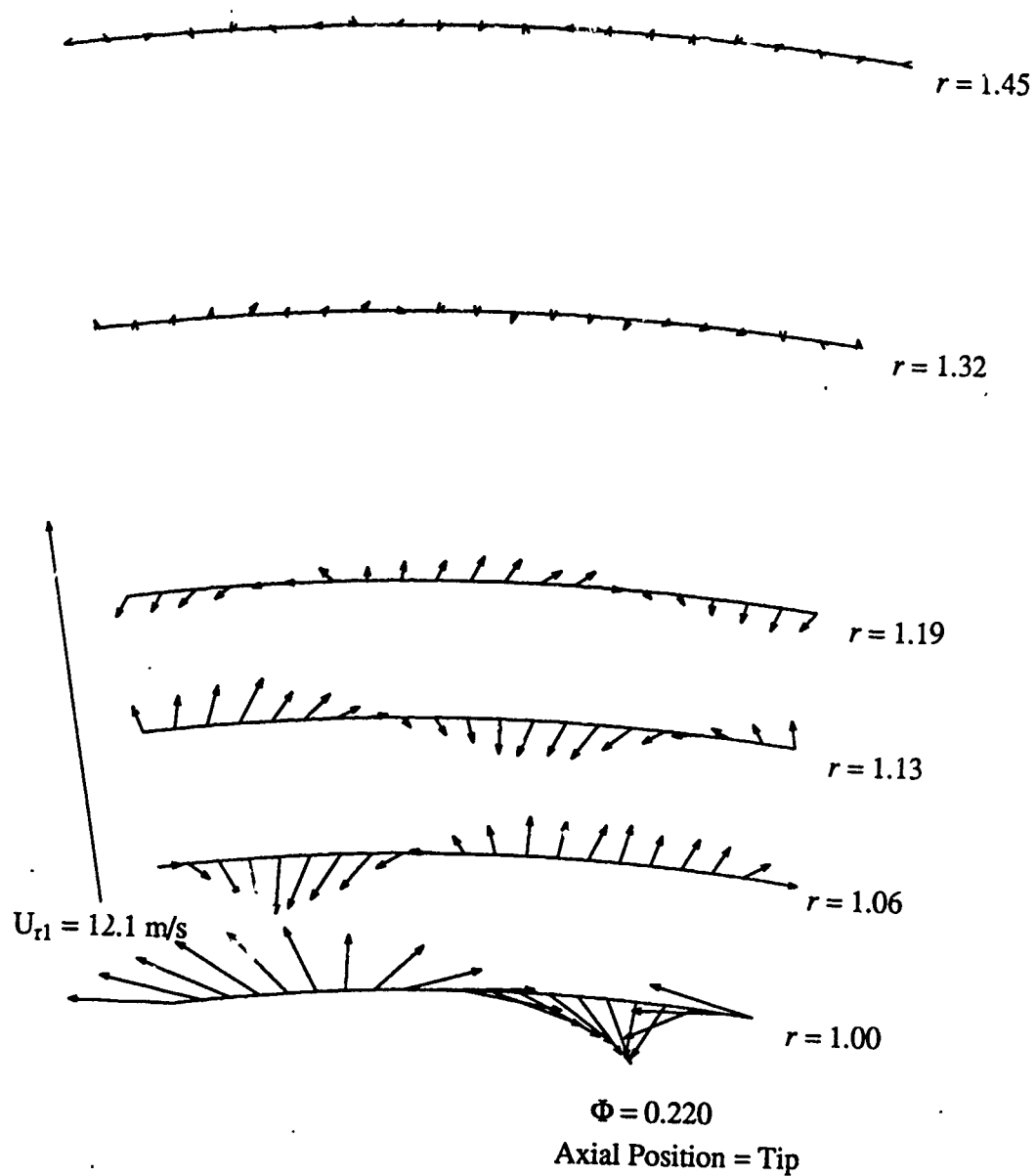


Figure 6.38 Vaneless Diffuser Unsteady Velocity (Tip Position,  $\Phi = 0.22$ )



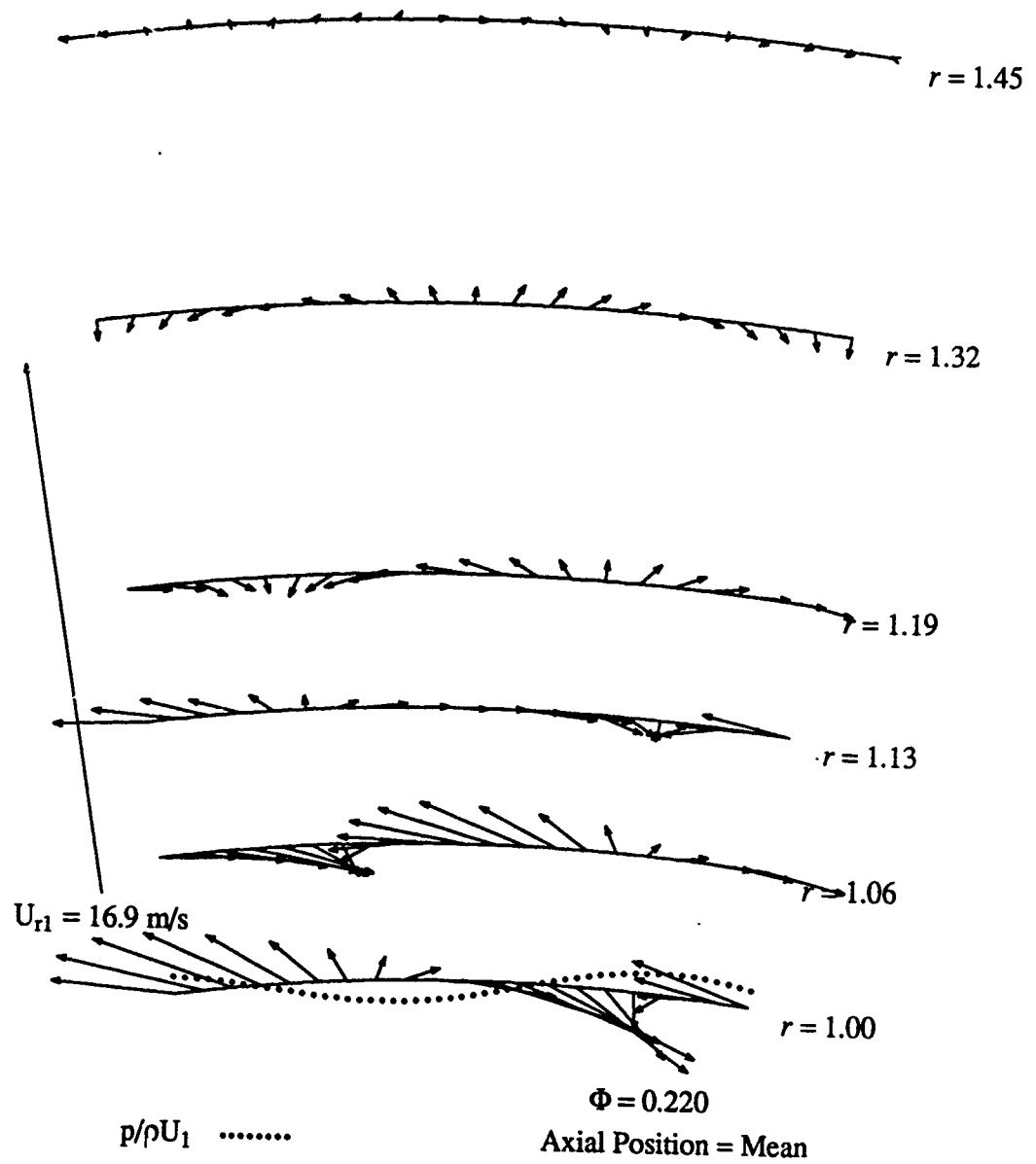


Figure 6.39 Vaneless Diffuser Unsteady Velocity (Mean Position,  $\Phi = 0.22$ )

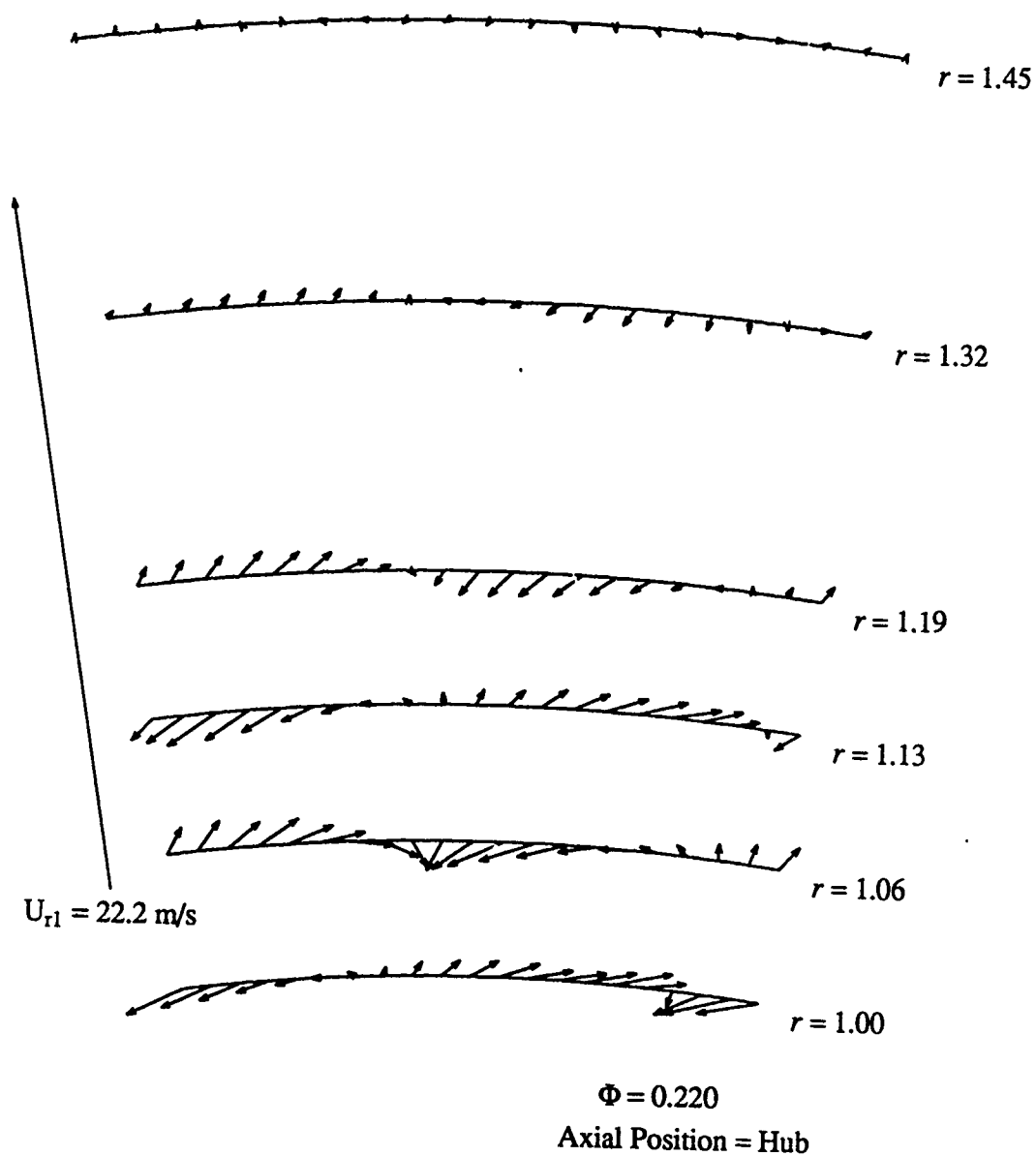


Figure 6.40 Vaneless Diffuser Unsteady Velocity (Hub Position,  $\Phi = 0.22$ )

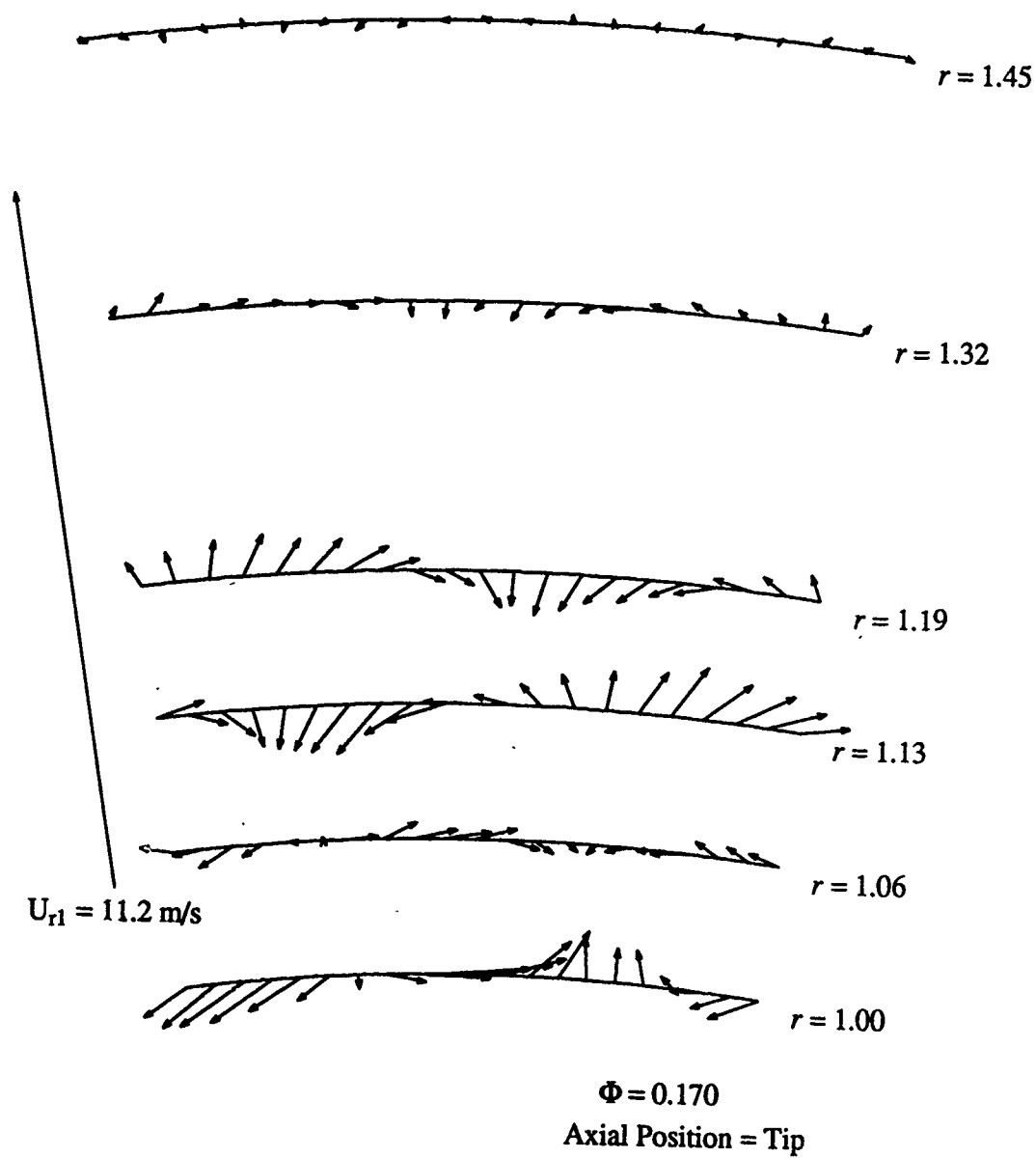


Figure 6.41 Vaneless Diffuser Unsteady Velocity (Tip Position,  $\Phi = 0.17$ )

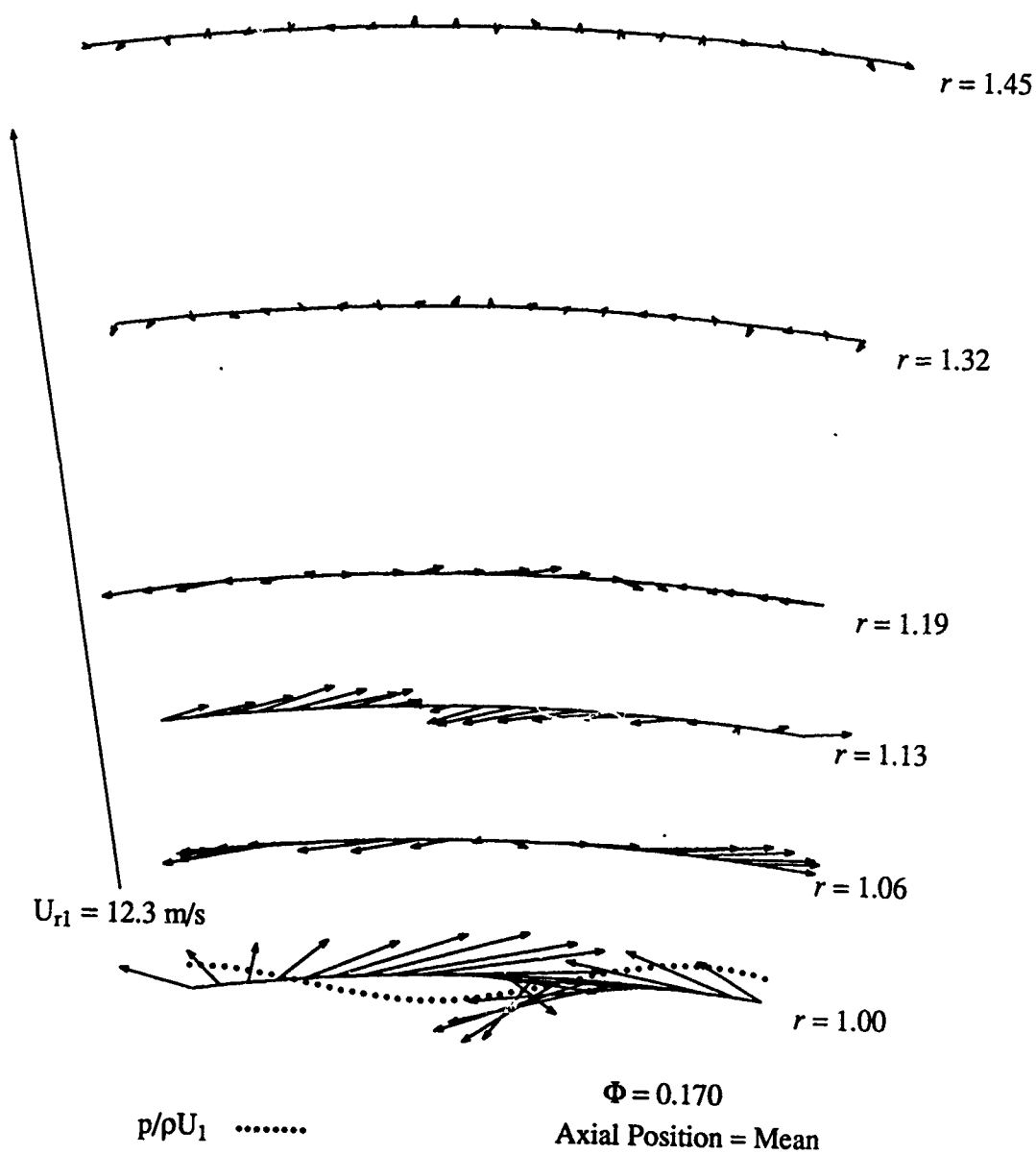


Figure 6.42 Vaneless Diffuser Unsteady Velocity (Mean Position,  $\Phi = 0.17$ )

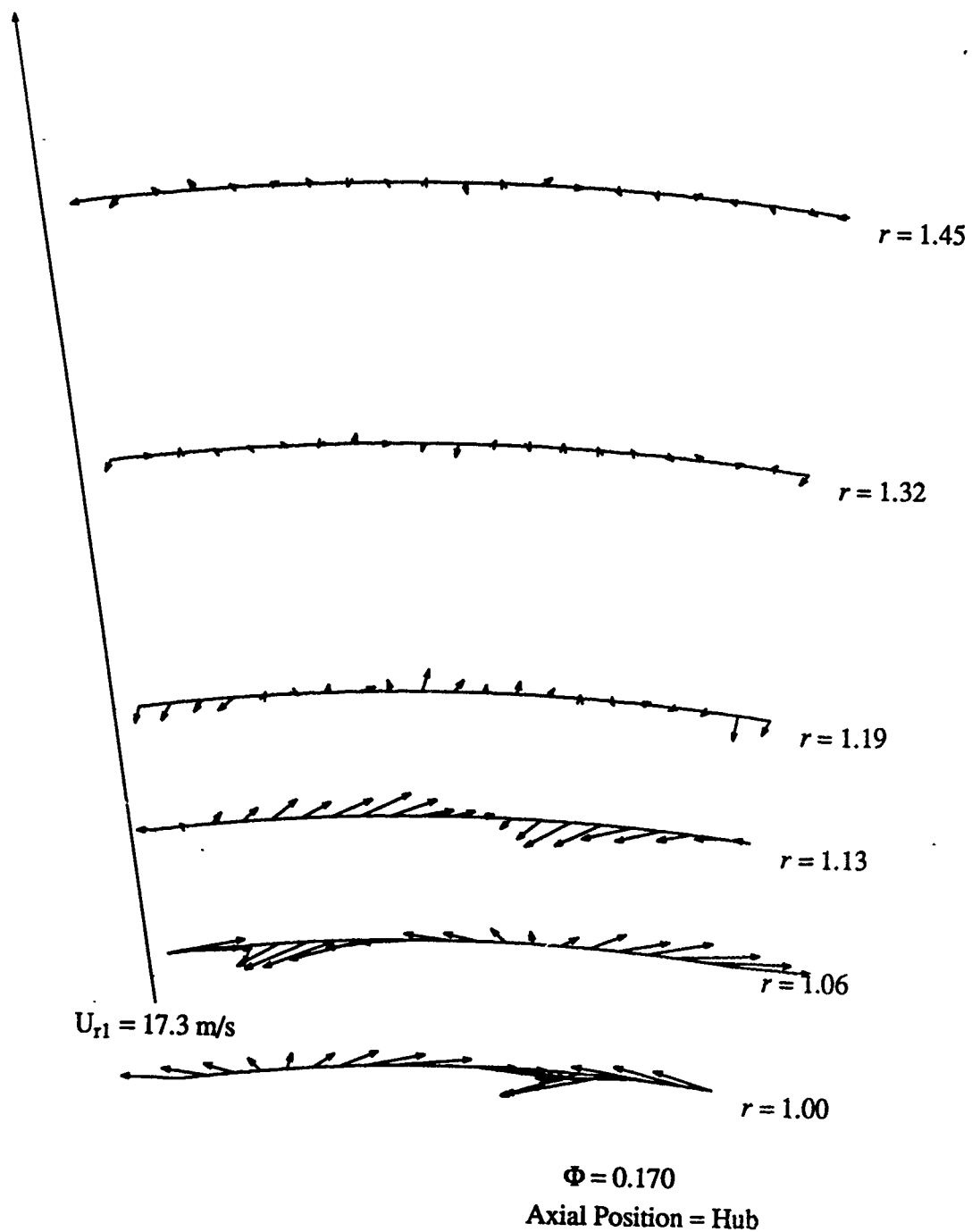


Figure 6.43 Vaneless Diffuser Unsteady Velocity (Hub Position,  $\Phi = 0.17$ )

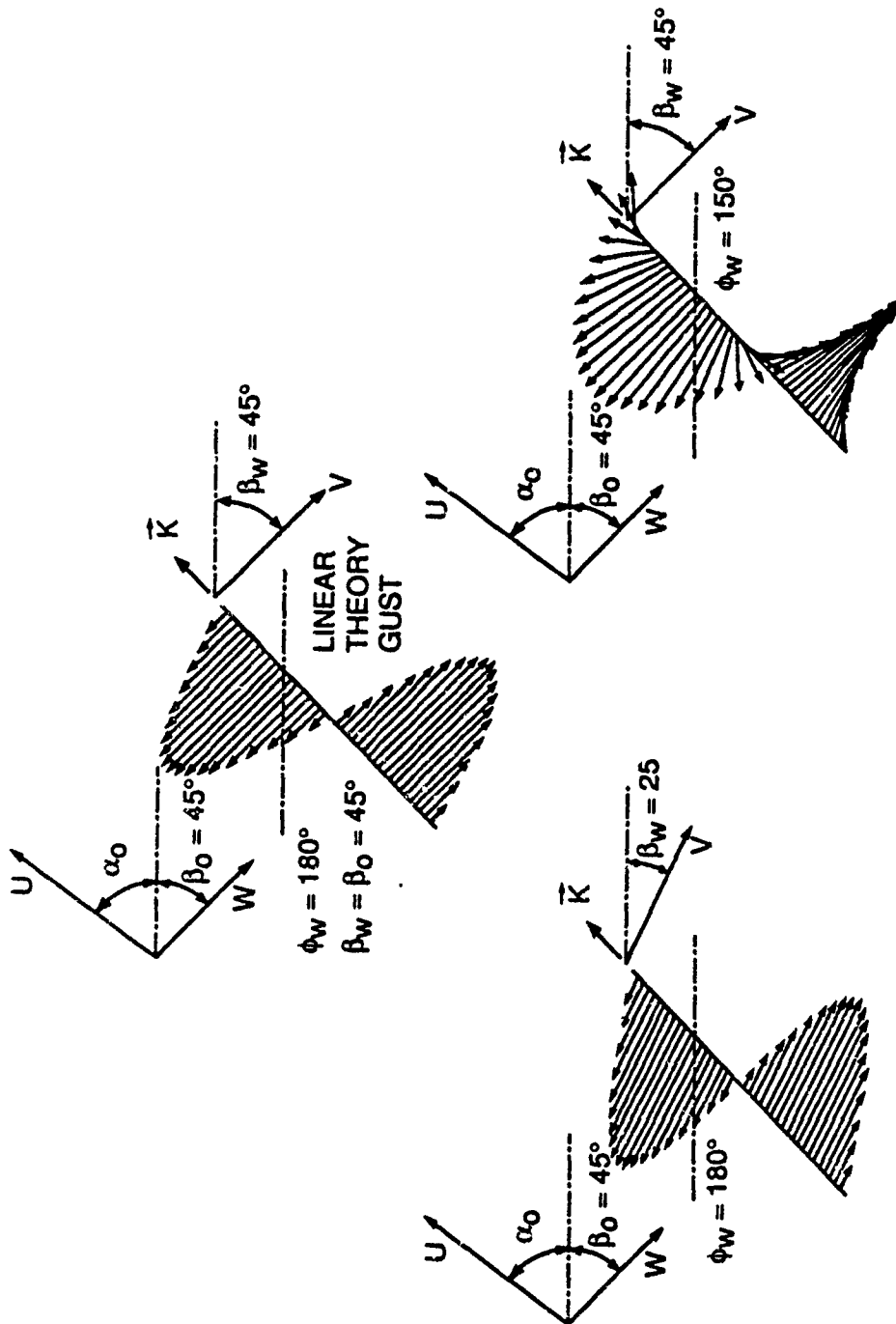


Figure 6.44 Linear Theory Aerodynamic Gusts

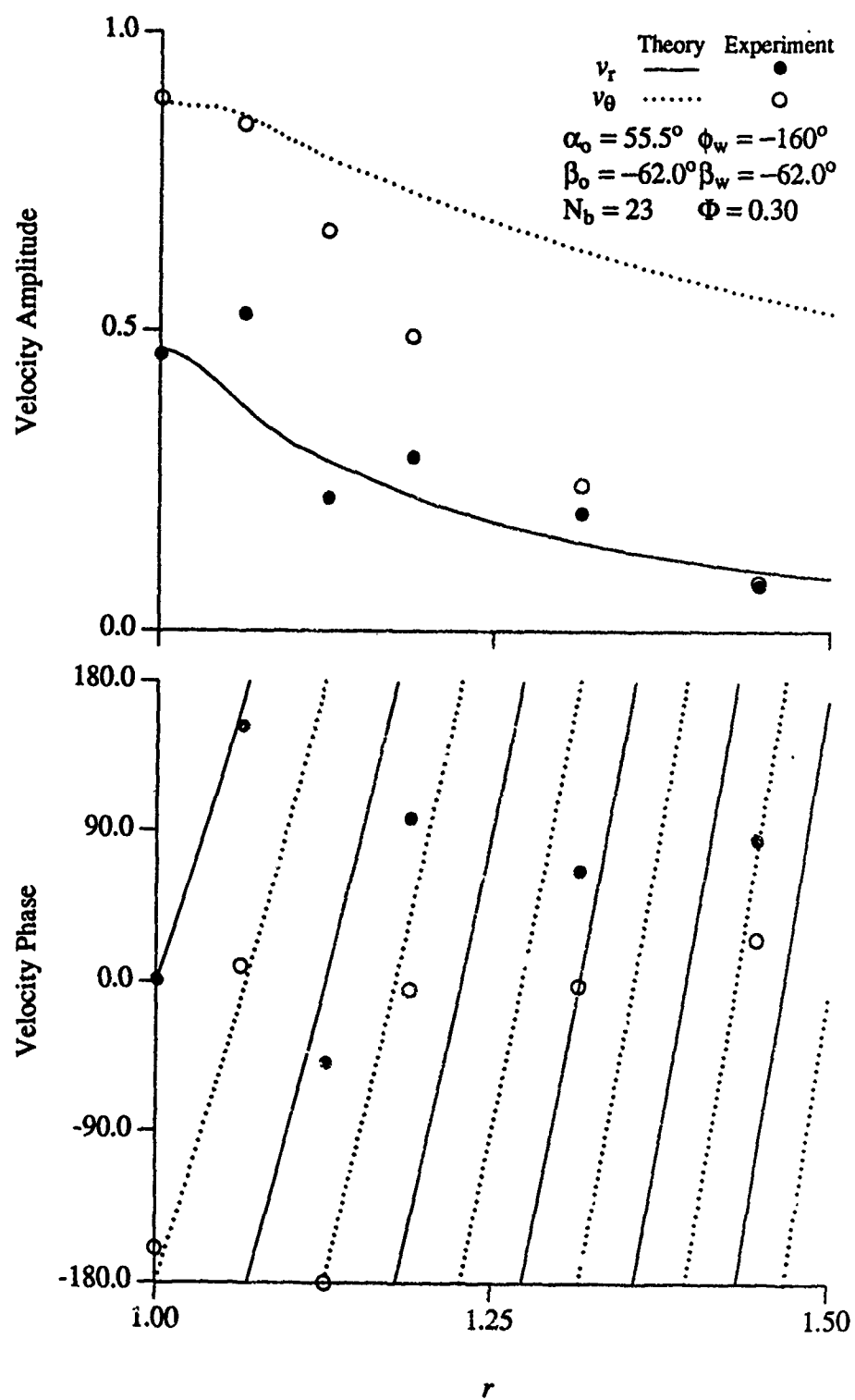


Figure 6.45 Vaneless Diffuser First Harmonic Unsteady Velocity and Theory ( $\Phi = 0.30$ )

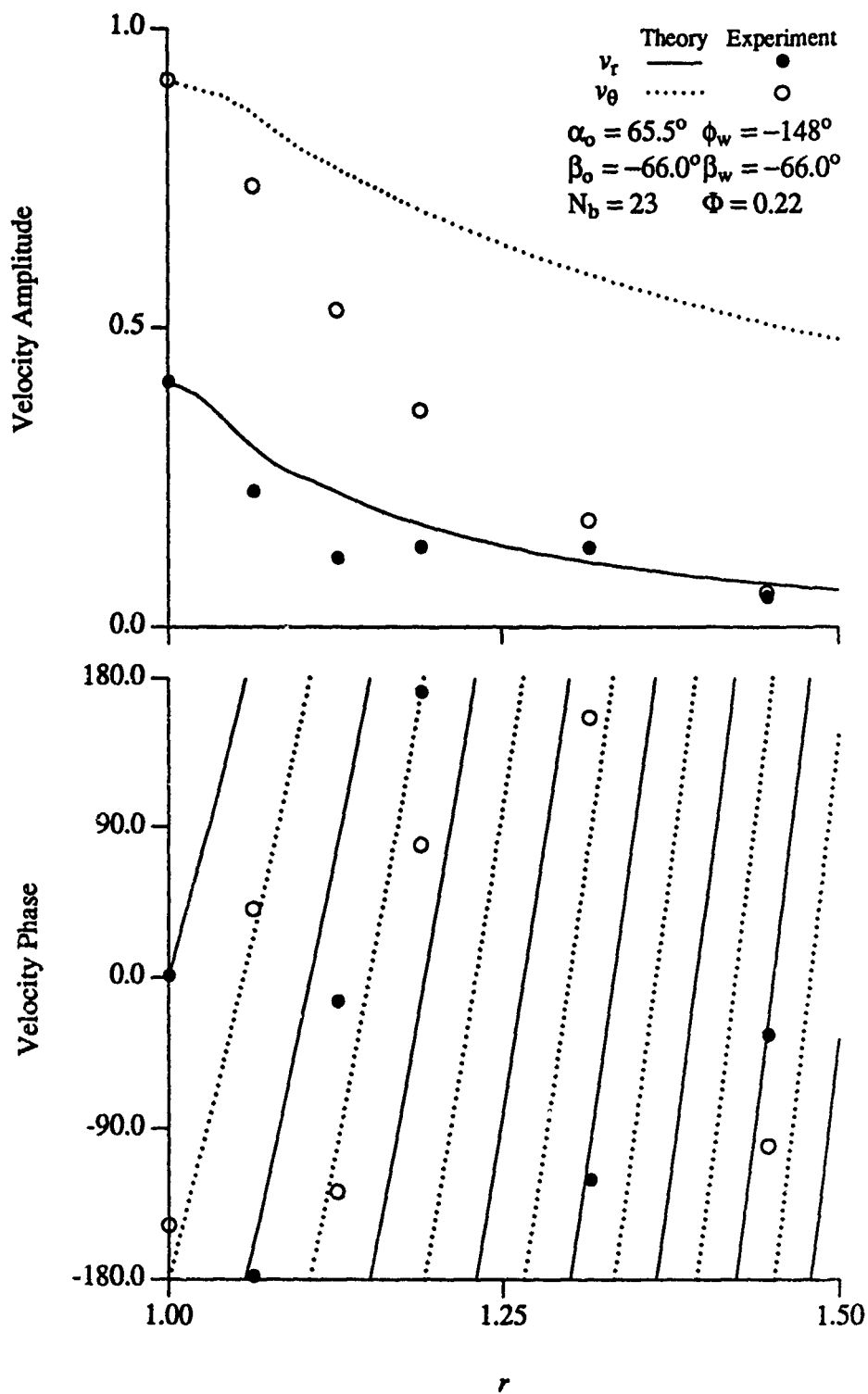


Figure 6.46 Vaneless Diffuser First Harmonic Unsteady Velocity and Theory ( $\Phi = 0.22$ )



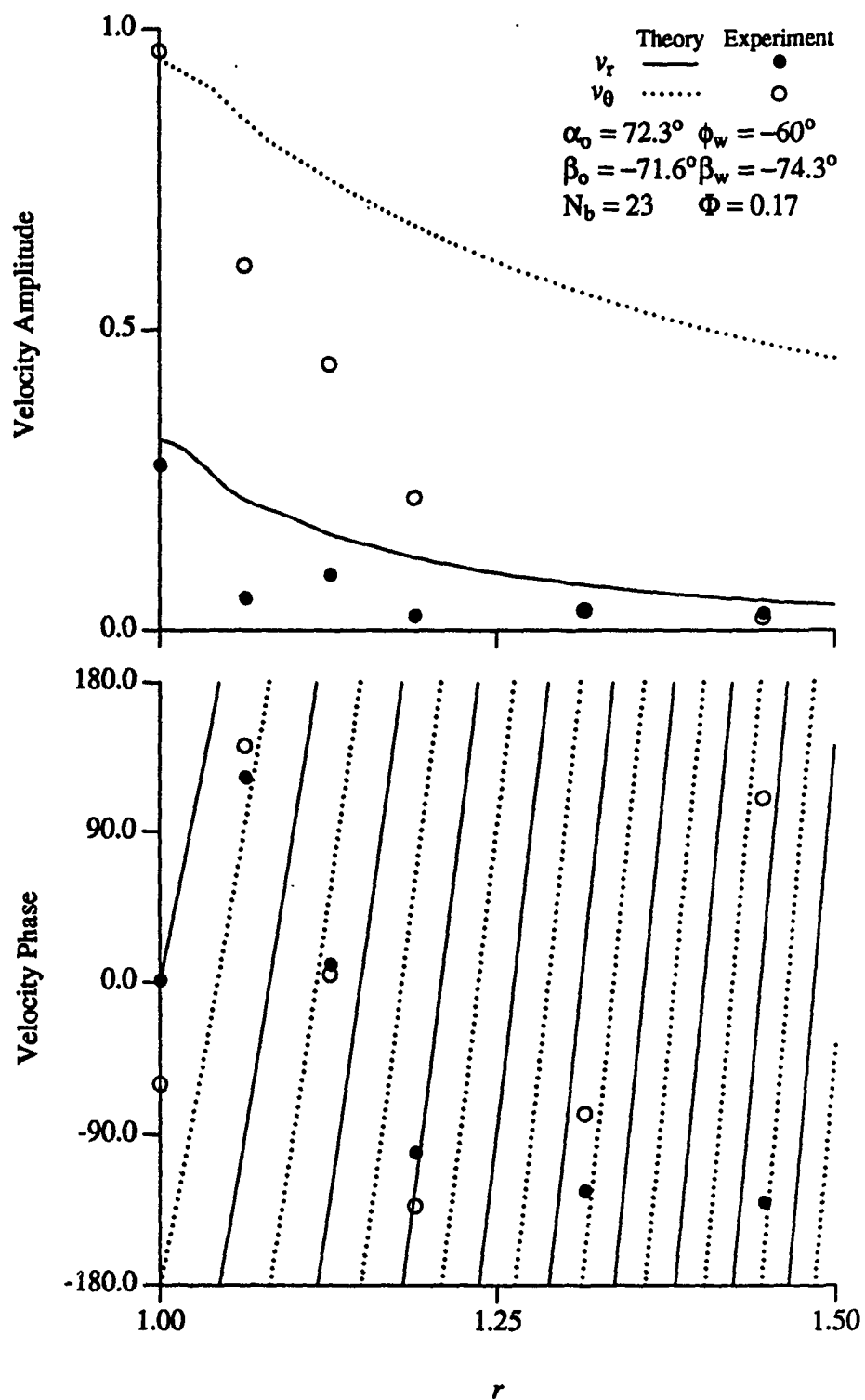


Figure 6.47 Vaneless Diffuser First Harmonic Unsteady Velocity and Theory ( $\Phi = 0.17$ )

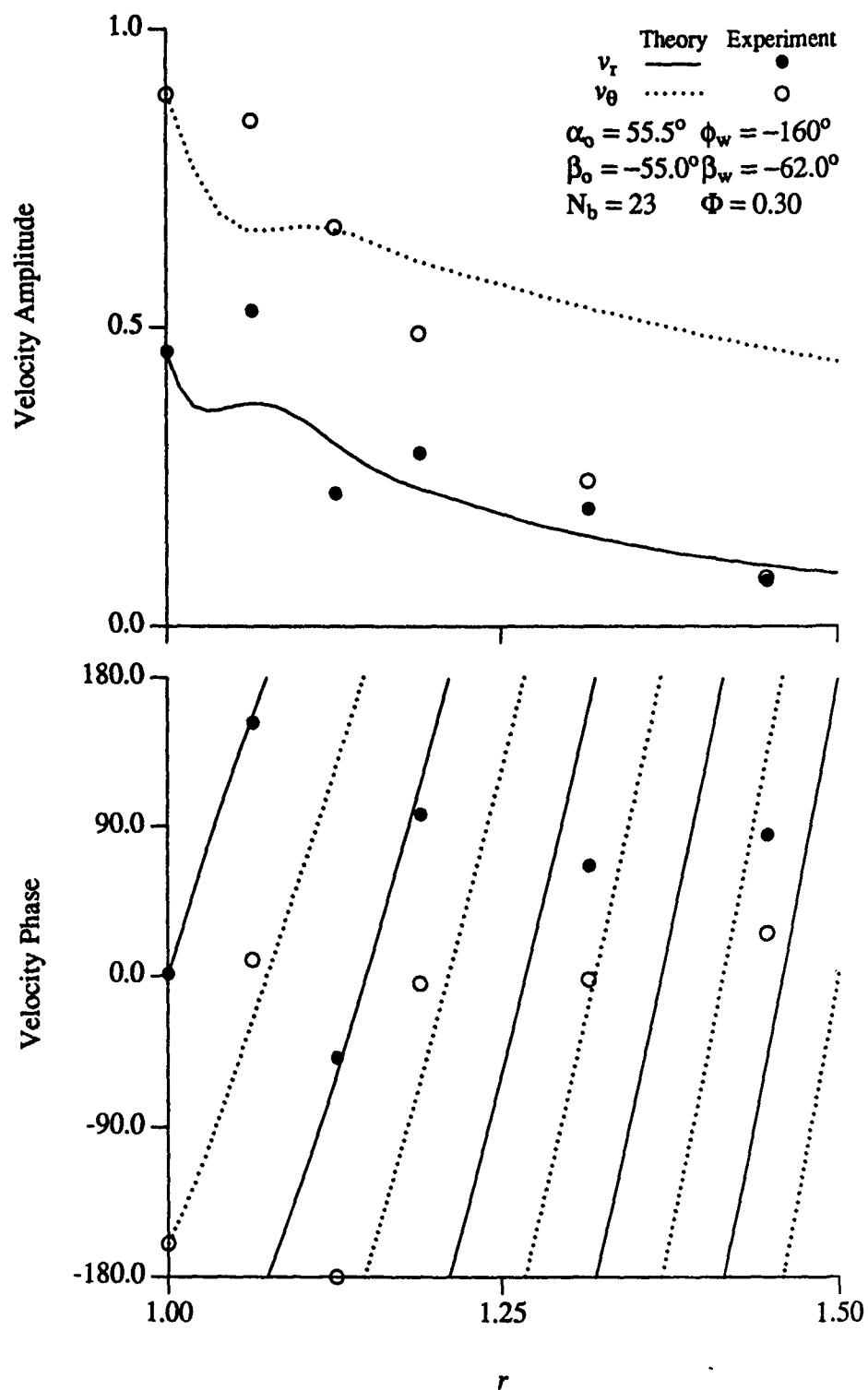


Figure 6.48 Vaneless Diffuser First Harmonic Unsteady Velocity and Theory  
(Theory  $\phi_w = -160^\circ, \Phi = 0.30$ )

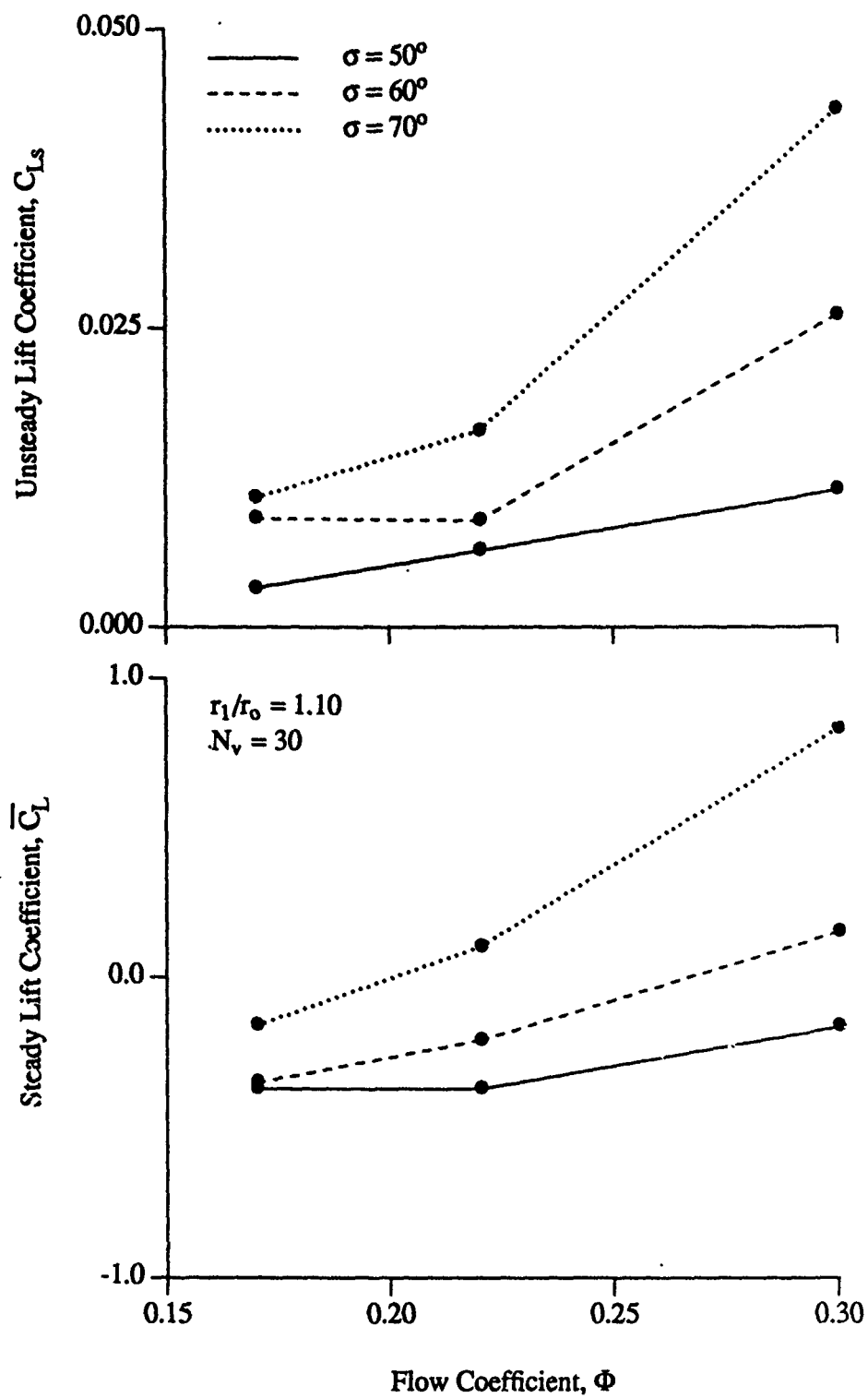


Figure 6.49 Diffuser Vane First Harmonic Unsteady Lift ( $r_1/r_0 = 1.10$ ,  $N_v = 30$ )

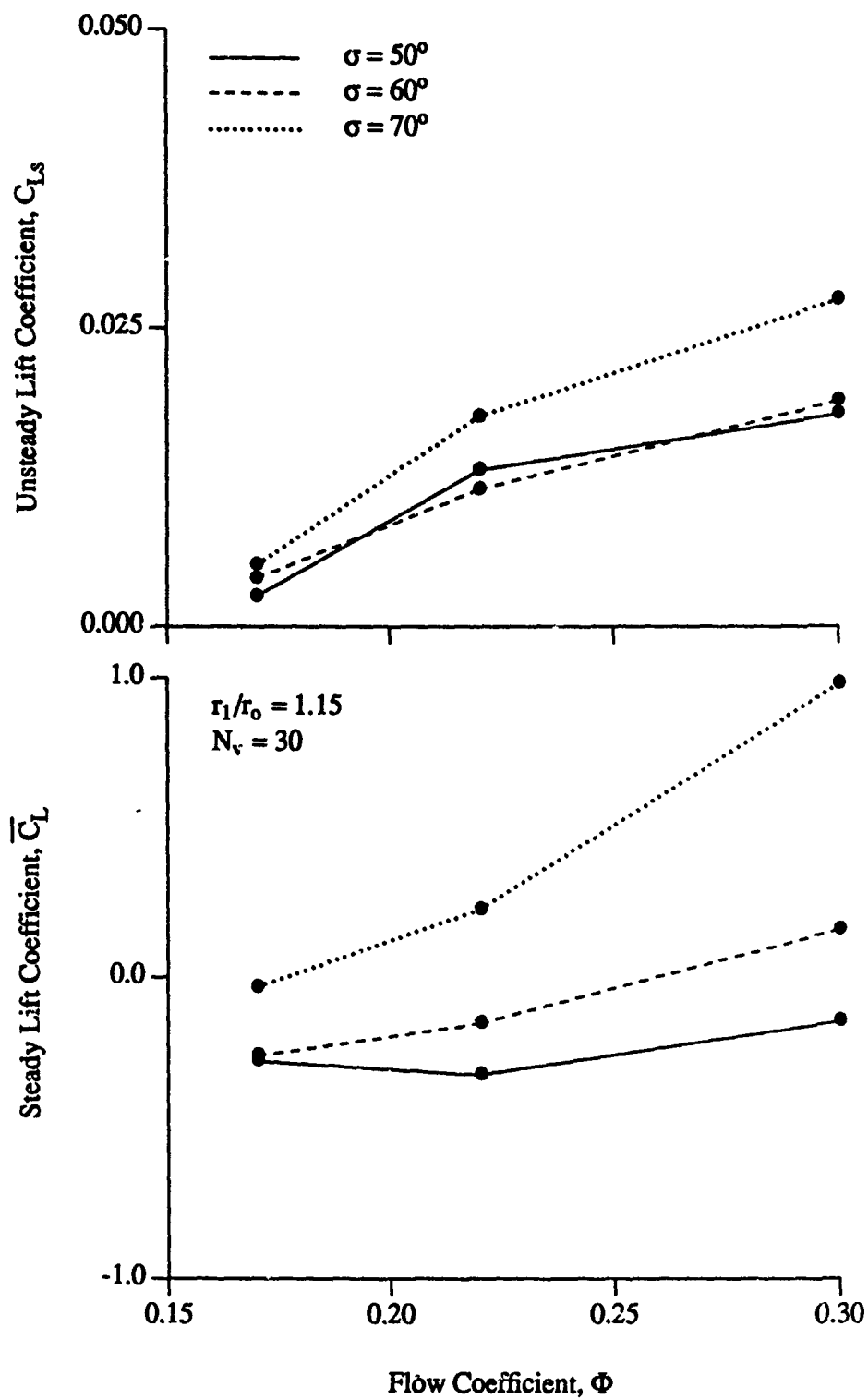


Figure 6.50 Diffuser Vane First Harmonic Unsteady Lift ( $r_1/r_0 = 1.15$ ,  $N_v = 30$ )

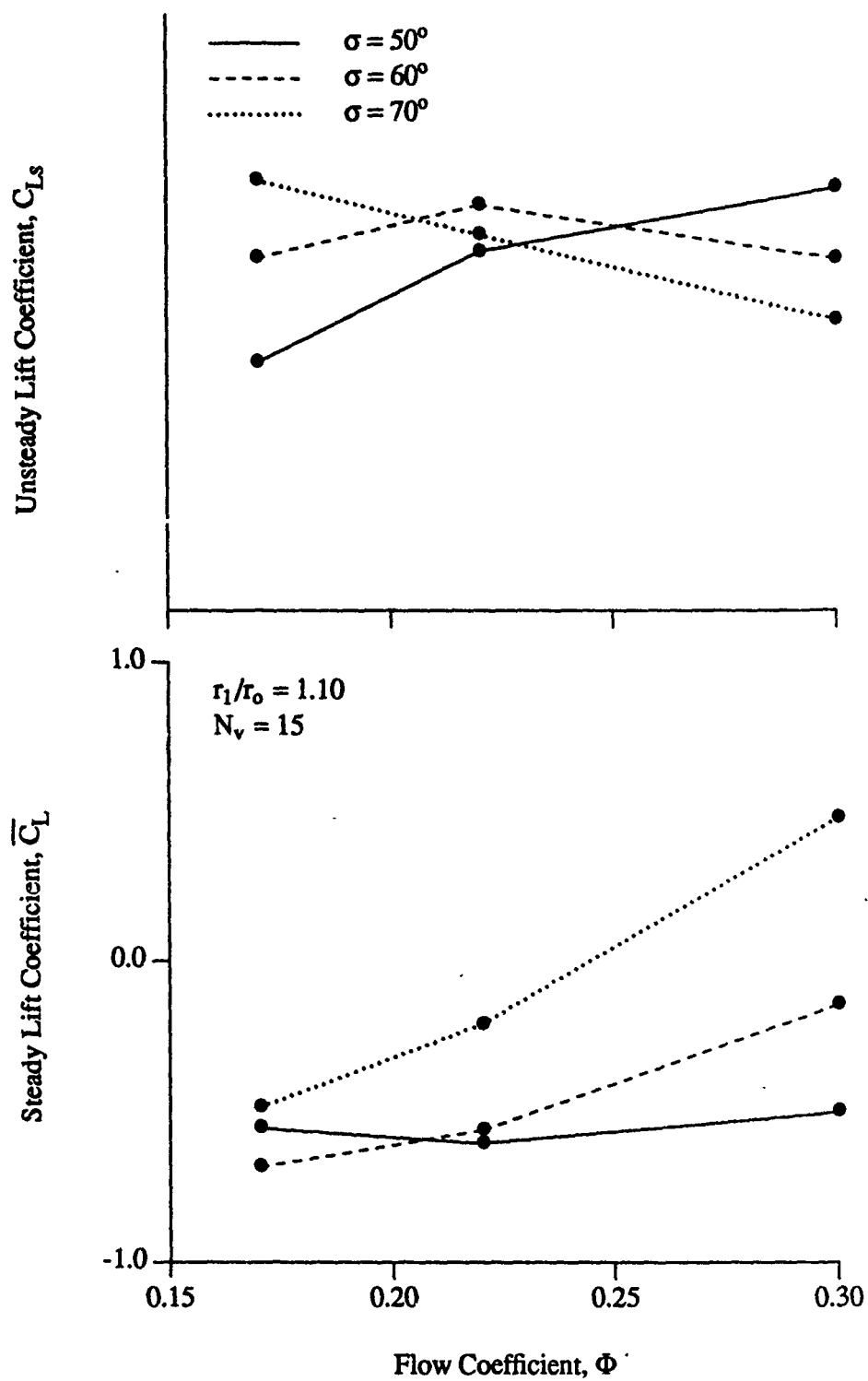


Figure 6.51 Diffuser Vane First Harmonic Unsteady Lift ( $r_1/r_0 = 1.10$ ,  $N_v = 15$ )

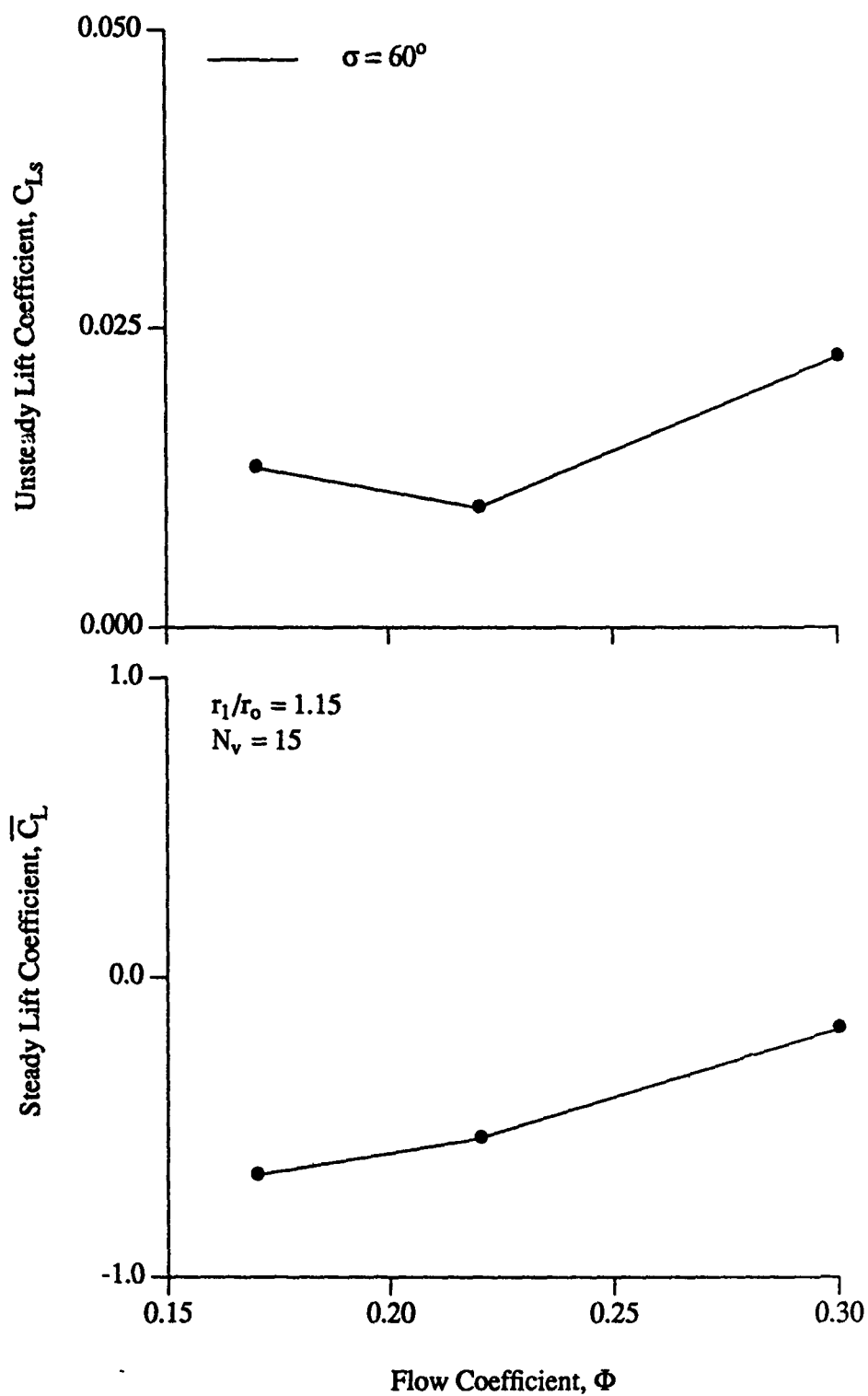


Figure 6.52 Diffuser Vane First Harmonic Unsteady Lift ( $r_1/r_0 = 1.15$ ,  $N_v = 15$ )

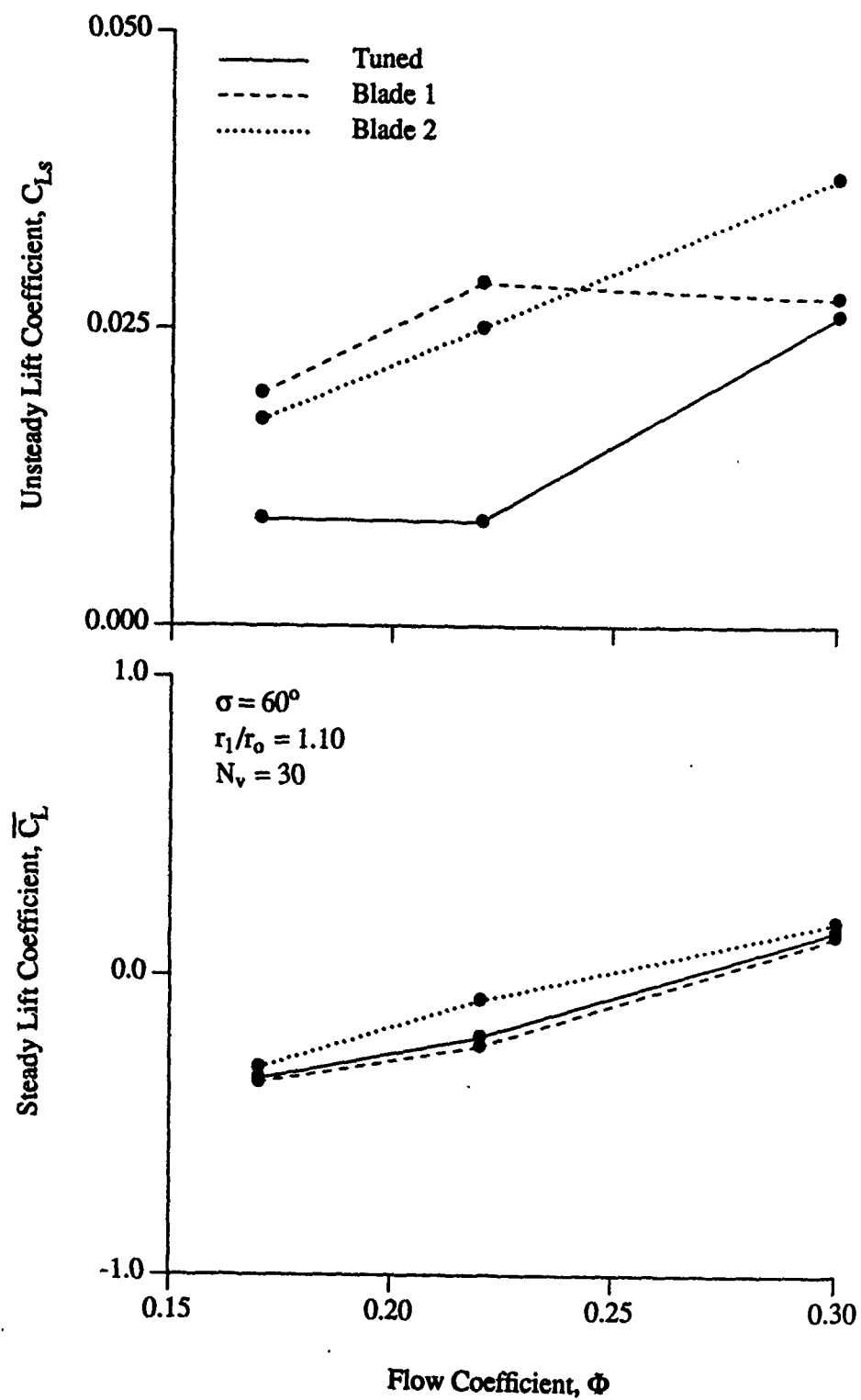


Figure 6.53 Detuned Diffuser Vane First Harmonic Unsteady Lift ( $r_1/r_0 = 1.10$ ,  $N_v = 30$ )

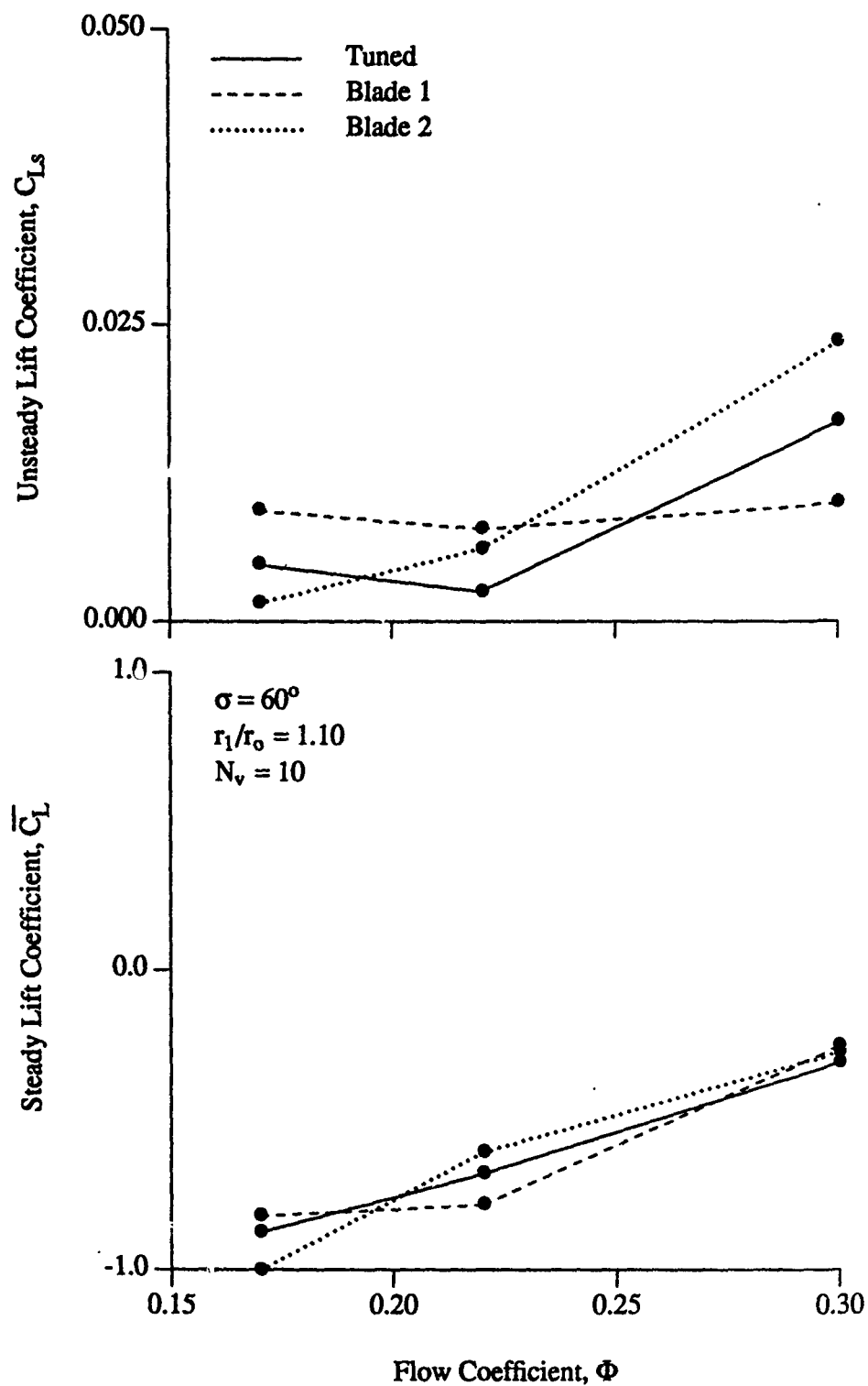
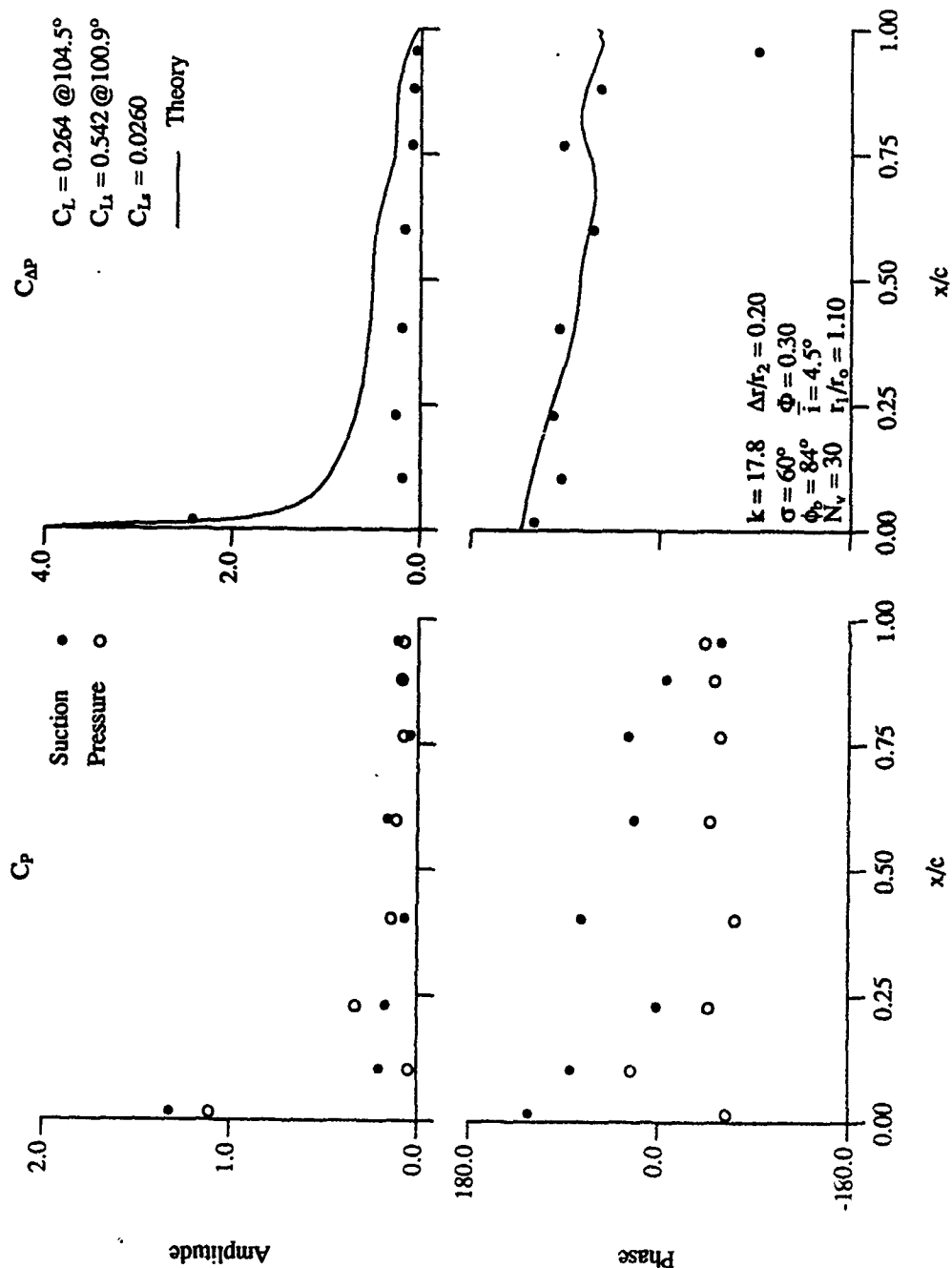
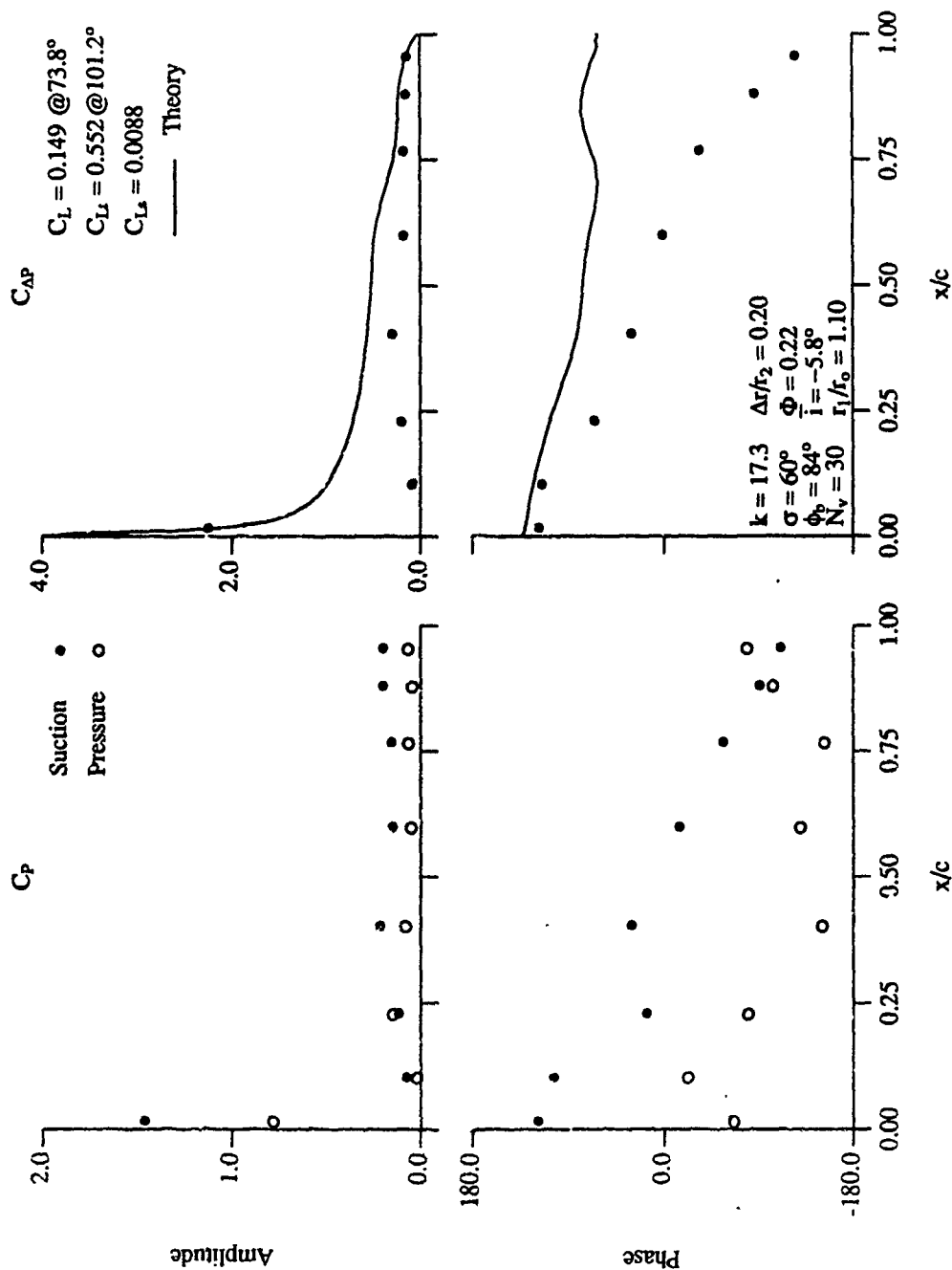
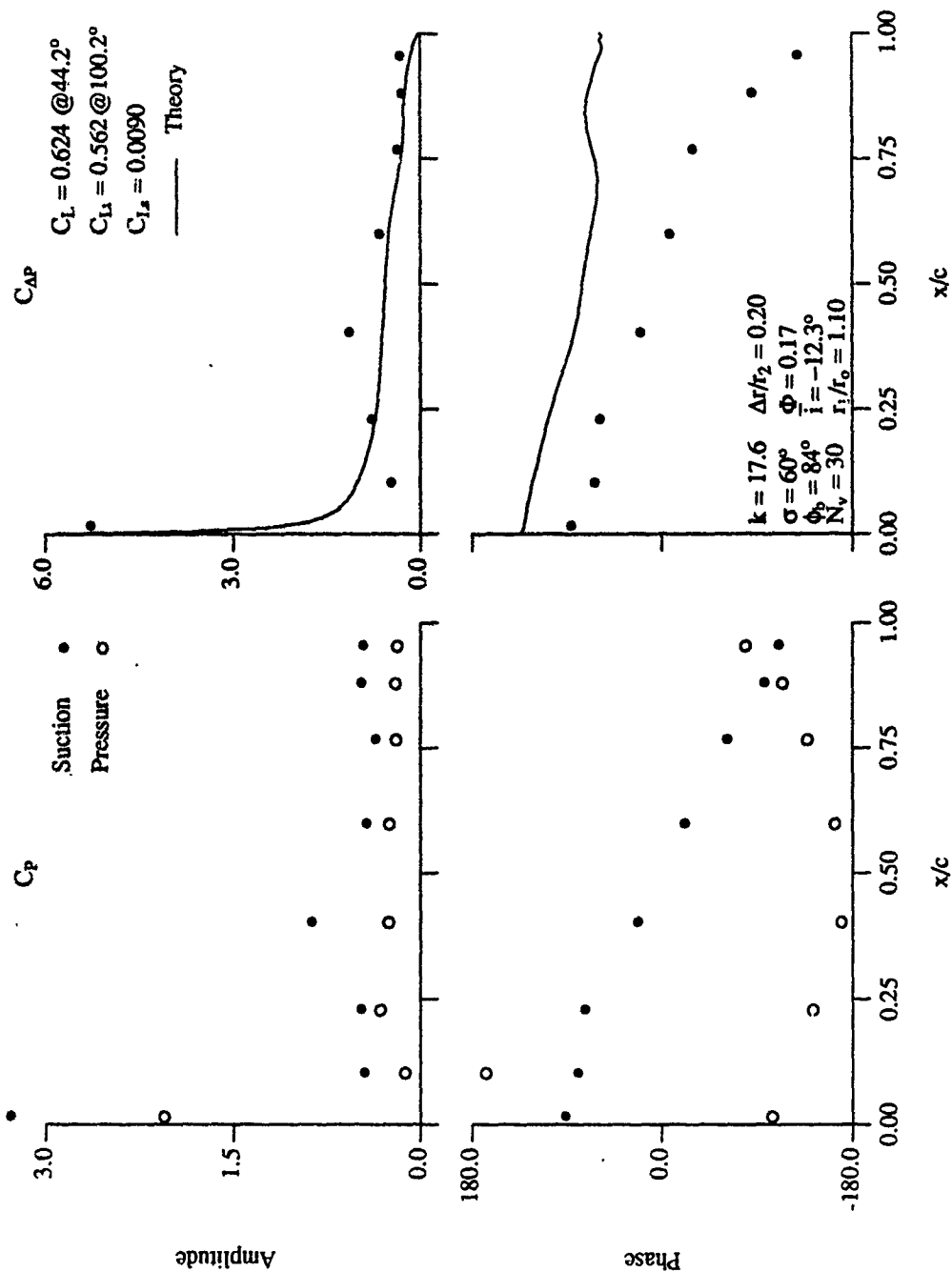


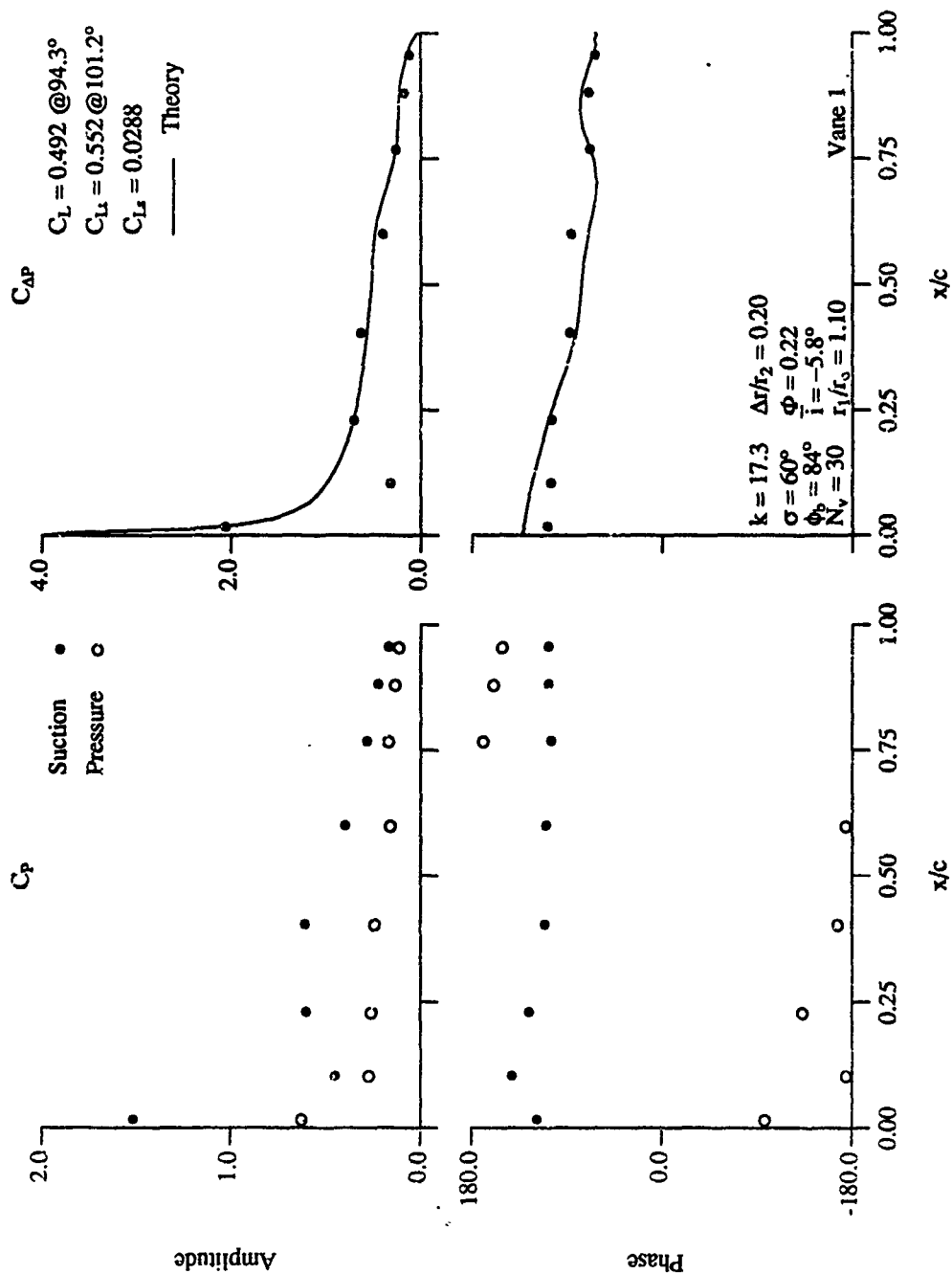
Figure 6.54 Detuned Diffuser Vane First Harmonic Unsteady Lift ( $r_1/r_0 = 1.10$ ,  $N_v = 10$ )

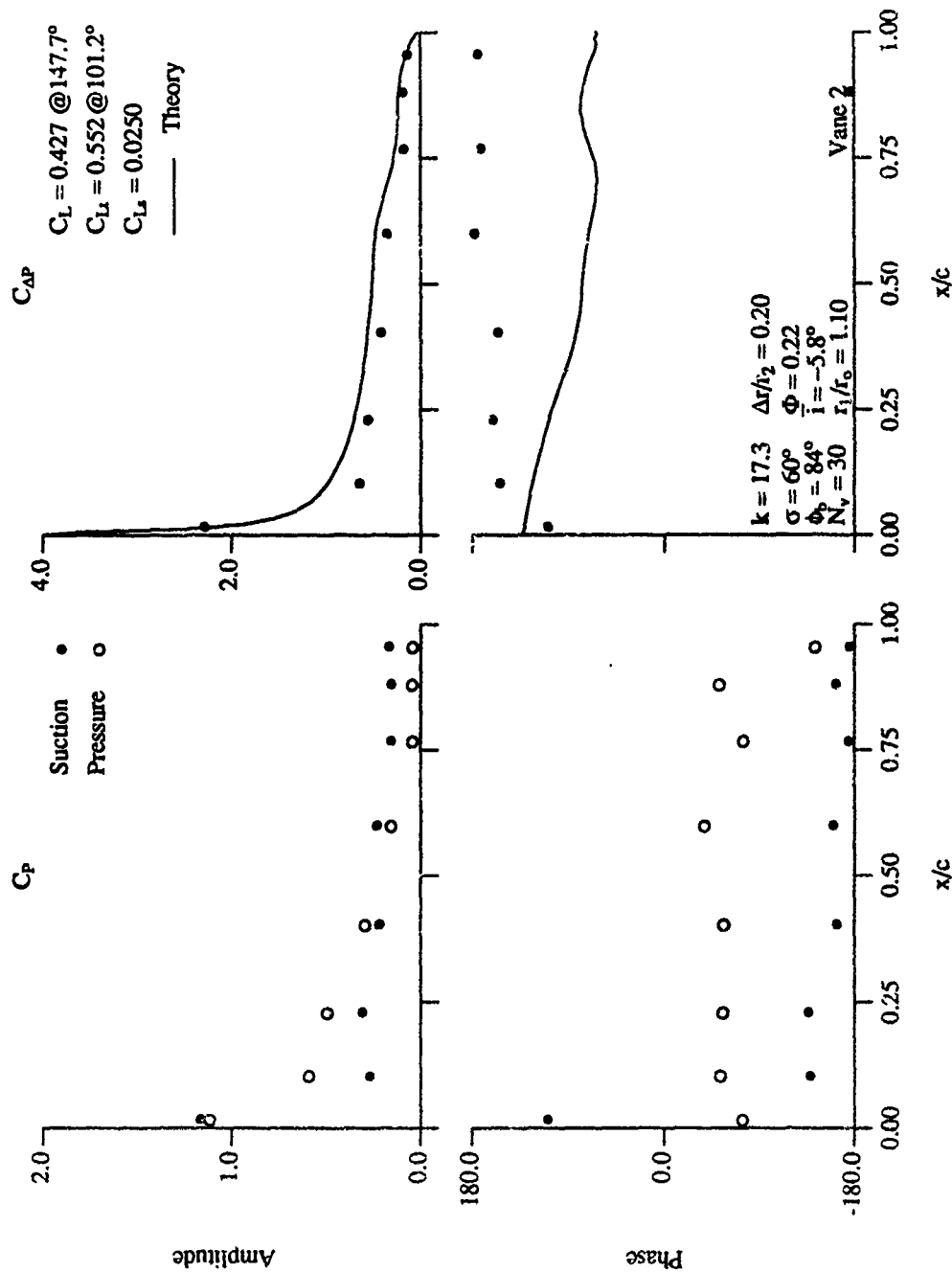


Figure 6.55 Diffuser Vane First Harmonic Unsteady Static Pressure ( $r_1/r_0 = 1.10$ ,  $N_v = 30$ ,  $\sigma = 60^\circ$ ,  $\Phi = 0.30$ )


 Figure 6.56 Diffuser Vane First Harmonic Unsteady Static Pressure ( $r_1/r_0 = 1.10$ ,  $N_v = 30$ ,  $\sigma = 60^\circ$ ,  $\Phi = 0.22$ )


 Figure 6.57 Diffuser Vane First Harmonic Unsteady Static Pressure ( $r_1/r_0 = 1.10$ ,  $N_v = 30$ ,  $\sigma = 60^\circ$ ,  $\Phi = 0.17$ )

Figure 6.58 Diffuser Vane First Harmonic Unsteady Static Pressure (Vane 1, 40% det.,  $r_1/r_0 = 1.10$ ,  $N_v = 30$ ,  $\sigma = 60^\circ$ ,  $\Phi = 0.22$ )


 Figure 6.59 Diffuser Vane First Harmonic Unsteady Static Pressure (Vane 2, 40% det.,  $r_1/r_0 = 1.10$ ,  $N_v = 30$ ,  $\sigma = 60^\circ$ ,  $\Phi = 0.22$ )

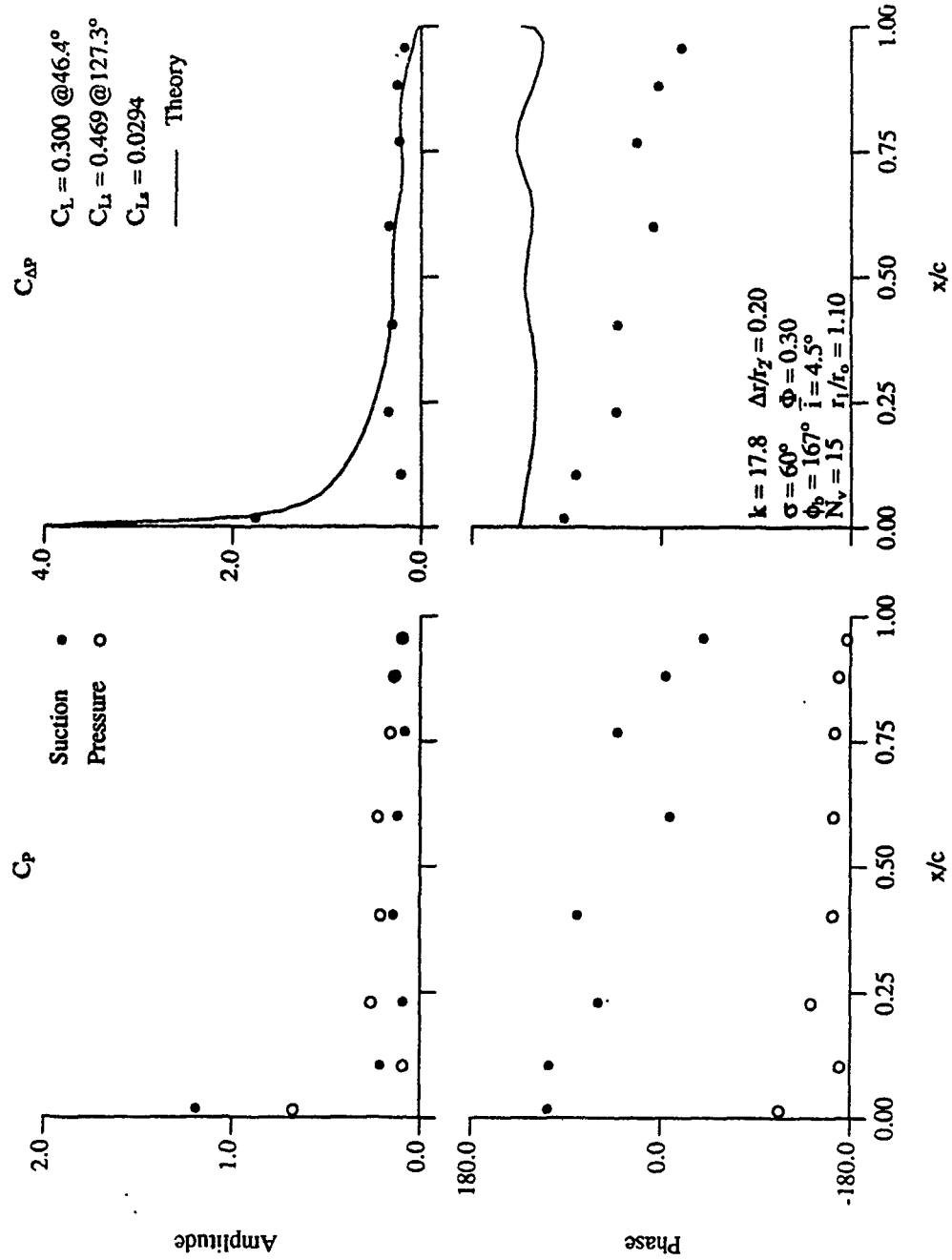
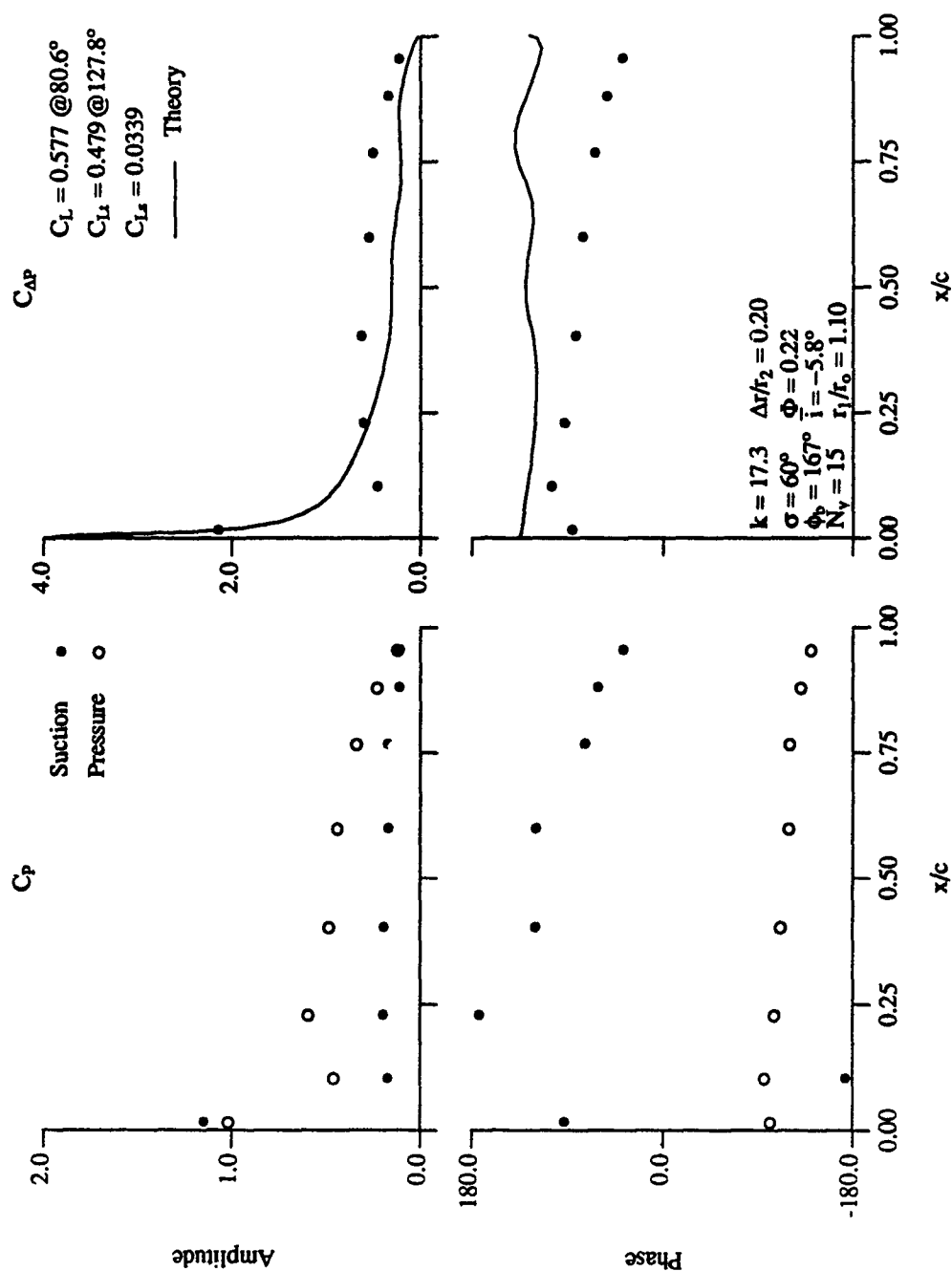
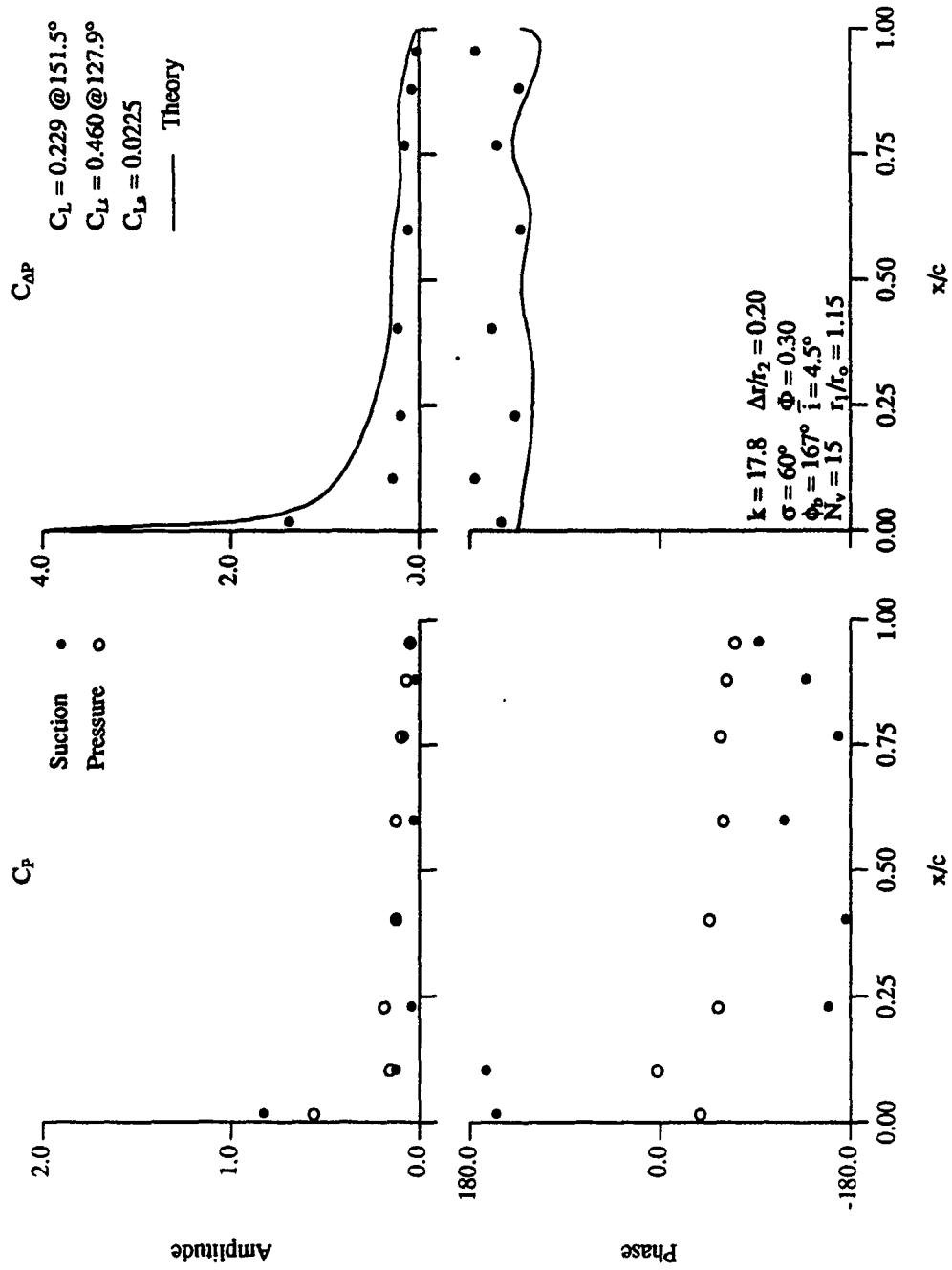


Figure 6.60 Diffuser Vane First Harmonic Unsteady Static Pressure ( $r_1/r_0 = 1.10$ ,  $N_v = 15$ ,  $\sigma = 60^\circ$ ,  $\Phi = 0.30$ )

Figure 6.61 Diffuser Vane First Harmonic Unsteady Static Pressure ( $r_1/r_0 = 1.10$ ,  $N_v = 15$ ,  $\sigma = 60^\circ$ ,  $\Phi = 0.22$ )

Figure 6.62 Diffuser Vane First Harmonic Unsteady Static Pressure ( $r_1/r_0 = 1.15$ ,  $N_v = 15$ ,  $\sigma = 60^\circ$ ,  $\Phi = 0.30$ )



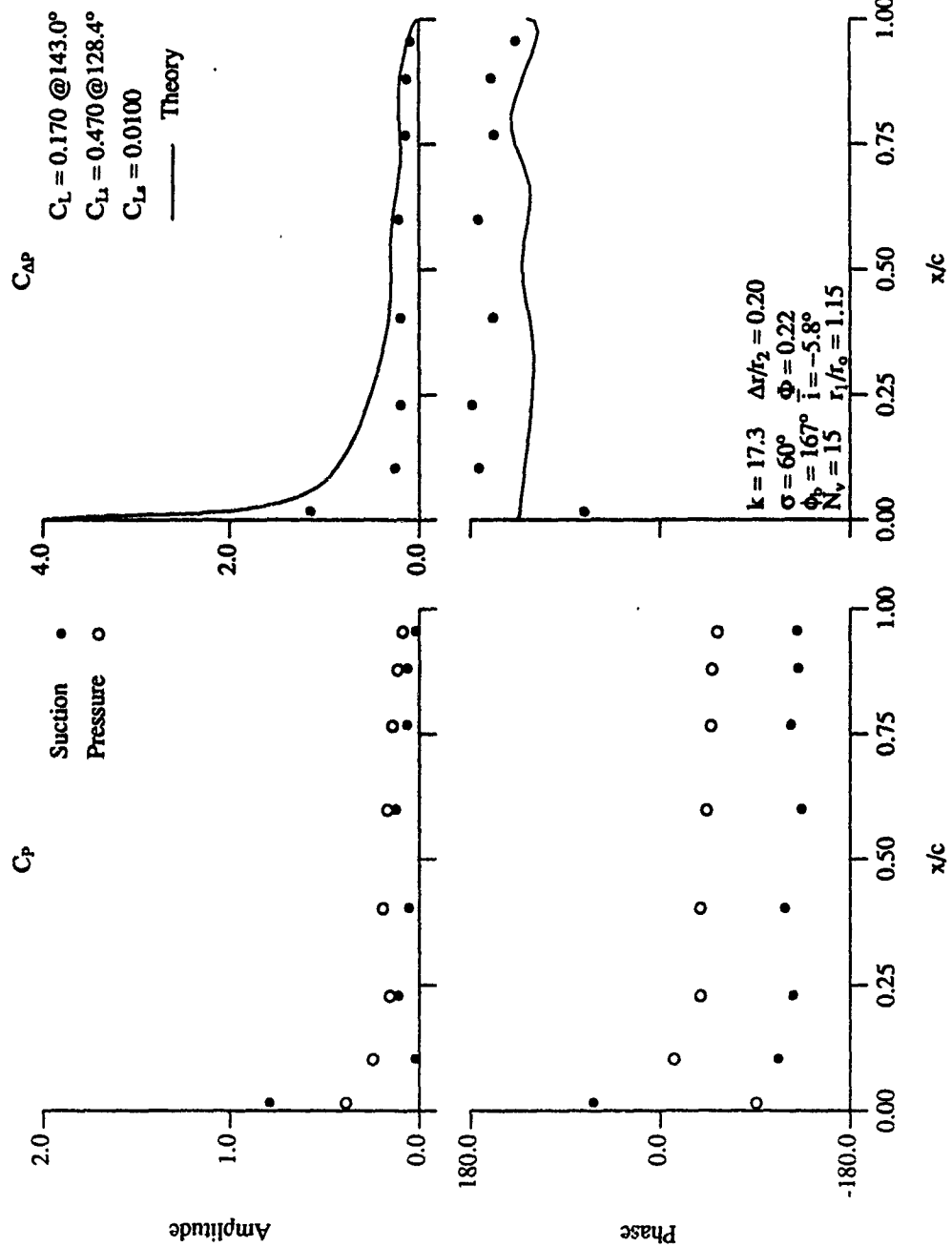
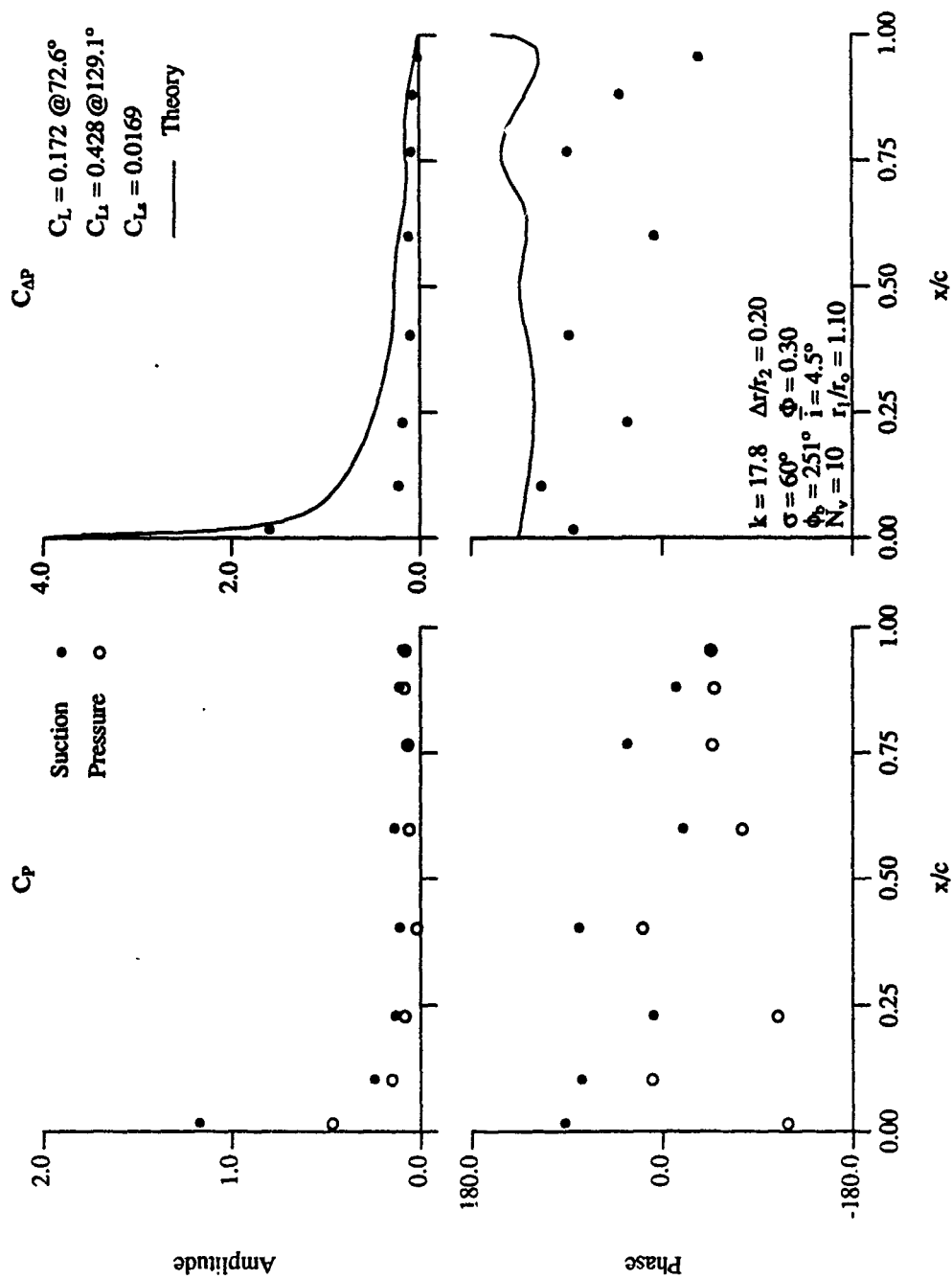
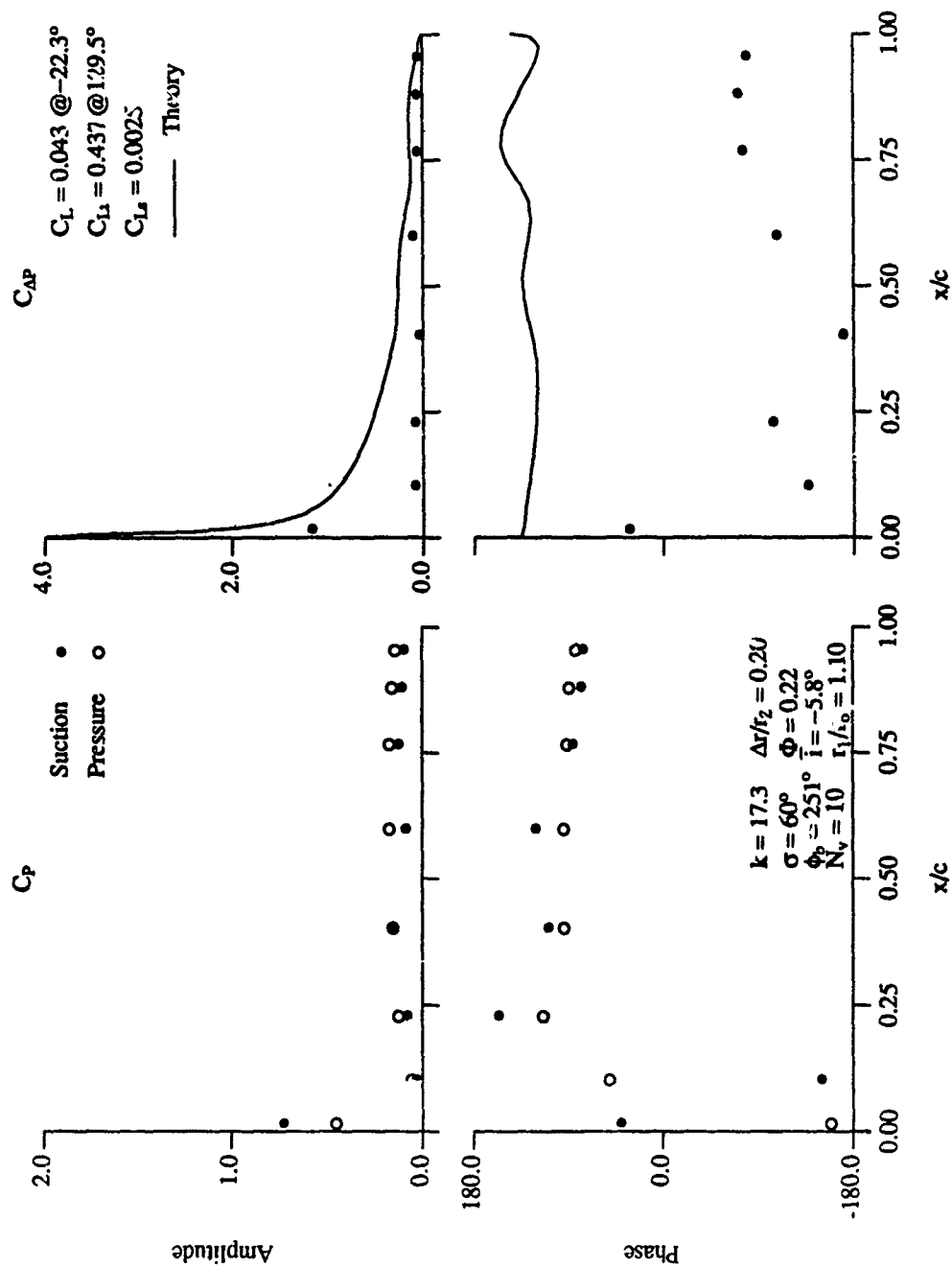


Figure 6.63 Diffuser Vane First Harmonic Unsteady Static Pressure ( $r_1/r_0 = 1.15$ ,  $N_v = 15$ ,  $\sigma = 60^\circ$ ,  $\Phi = 0.22$ )

Figure 6.64 Diffuser Vane First Harmonic Unsteady Static Pressure ( $r_1/r_0 = 1.10$ ,  $N_v = 10$ ,  $\sigma = 60^\circ$ ,  $\Phi = 0.30$ )

Figure 6.65 Diffuser Vane First Harmonic Unsteady Static Pressure ( $r_1/r_0 = 1.10$ ,  $N_v = 10$ ,  $\sigma = 60^\circ$ ,  $\Phi = 0.22$ )

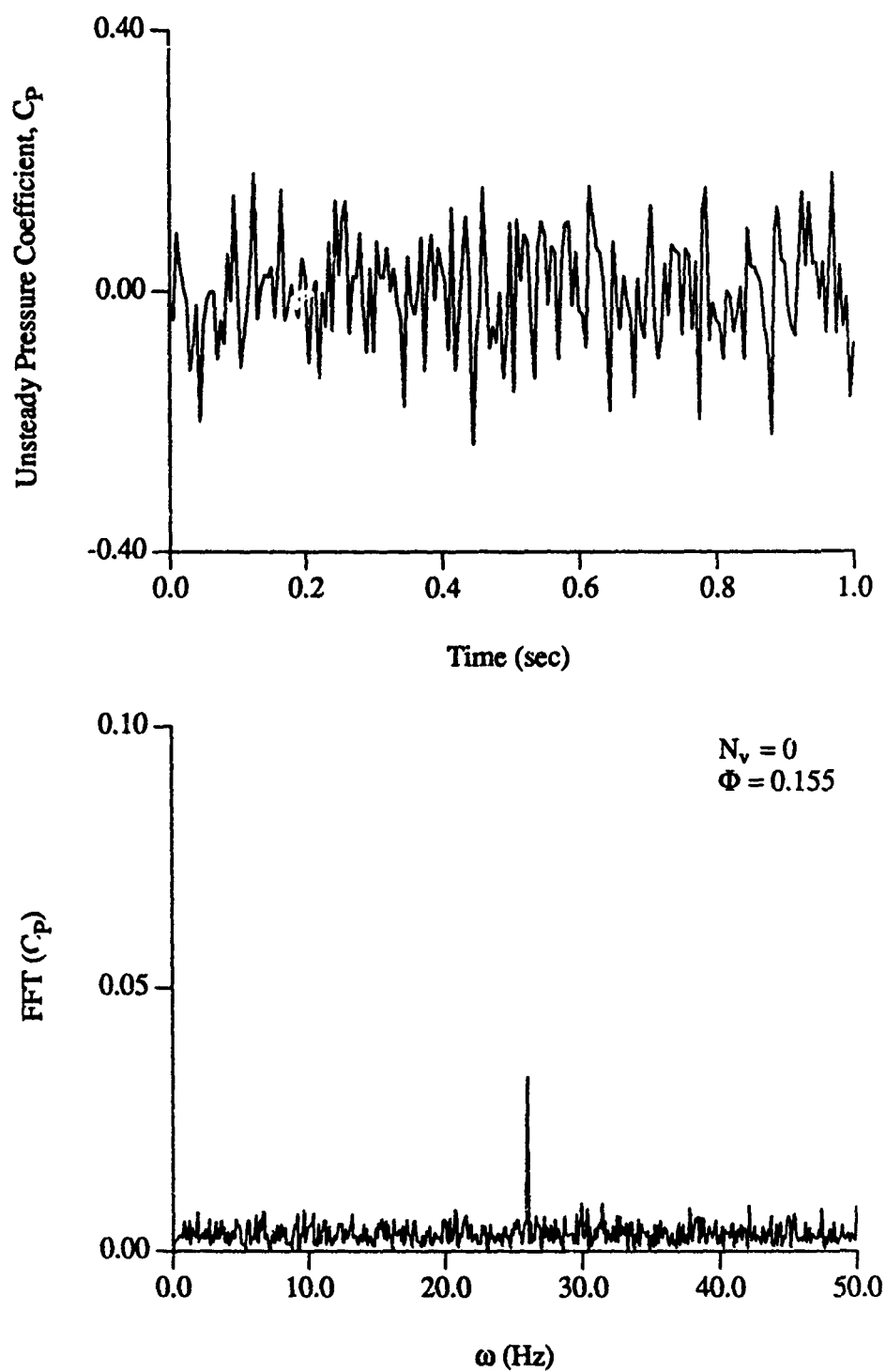


Figure 6.66 Rotating Stall Unsteady Static Pressure ( $N_v = 0$ ,  $\Phi = 0.155$ )

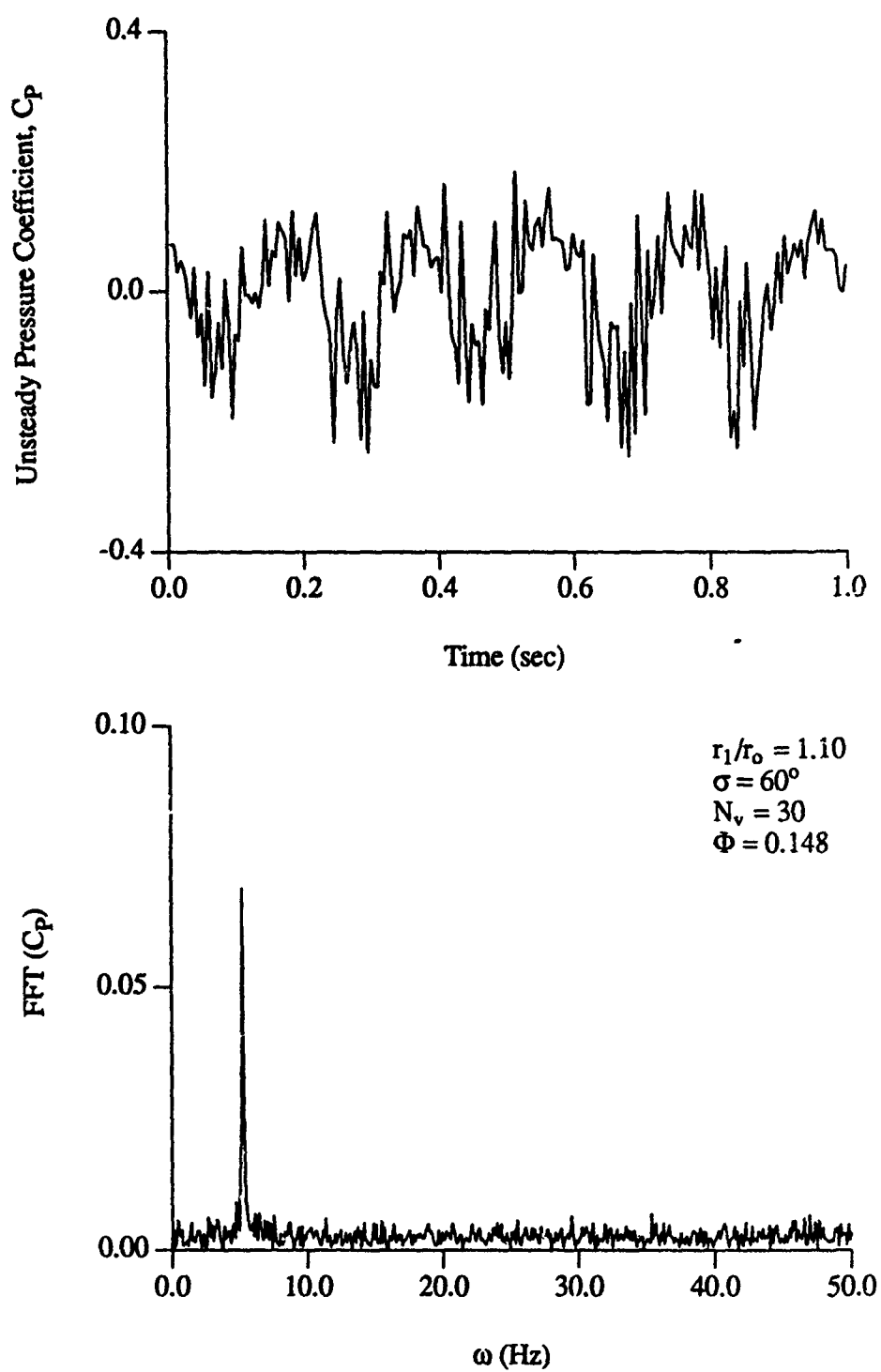


Figure 6.67 Rotating Stall Unsteady Static Pressure  
( $r_1/r_0 = 1.10$ ,  $N_v = 30$ ,  $\sigma = 60^\circ$ ,  $\Phi = 0.148$ )

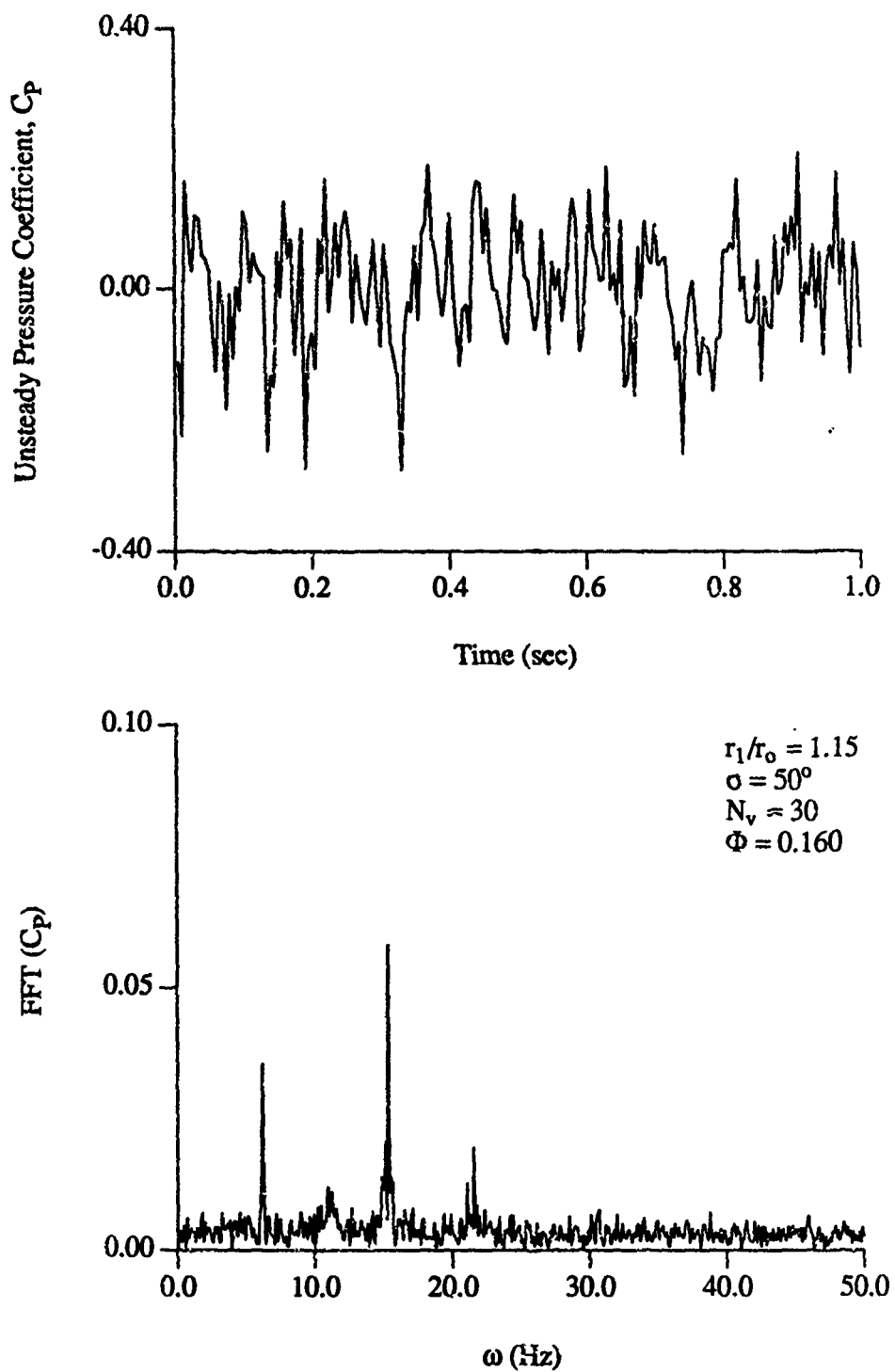


Figure 6.68 Rotating Stall Unsteady Static Pressure  
( $r_1/r_0 = 1.15$ ,  $N_v = 30$ ,  $\sigma = 50^\circ$ ,  $\Phi = 0.160$ )

## CHAPTER 7

### SUMMARY, CONCLUSIONS AND RECOMMENDATIONS

An investigation of some of the unsteady phenomena occurring in centrifugal compressors has been performed, with the diffuser vane unsteady pressure generated by impeller wakes of particular interest. It was found that little attention has been devoted in the literature to the effect of the vaned diffuser on the unsteady aerodynamics inherent in centrifugal compressors. Therefore, analyses were developed to predict the wake behavior and diffuser vane unsteady loading. In conjunction with these, a series of experiments was performed to evaluate this unsteady behavior. The effect of vaned diffuser geometry on the compressor steady performance and loading as well as surge and rotating stall was experimentally determined.

The performance of the Purdue Research Centrifugal Compressor was measured for various diffuser geometries. It was found that the vaned diffuser increases efficiency and overall pressure rise with proper geometry selection. The diffuser stagger angle and number of diffuser vanes were seen to be particularly important, with a smaller number of diffuser vanes generally preferable. The mechanism of this performance improvement was investigated by considering the rotating impeller blade and diffuser vane static loading. The vaned diffuser was determined to affect the impeller loading only at higher flow rates with small vane loading. The diffuser loading increased with steady incidence and with a decreasing number of vanes. It was concluded that the vaned diffuser affects the aft impeller and vaneless space flowfields, reducing mixing and inhibiting secondary flows, thereby improving performance. Performance improvements were only realized when the diffuser vanes were lightly loaded, with no performance advantage from a loaded diffuser.

The wake velocities in the vaneless radial diffuser were experimentally determined using laser anemometry. The radial and tangential unsteady wake velocities decreased rapidly with increasing radius, with a greater decrease at lower flow rates. A theoretical model to predict this behavior was developed by obtaining a solution to the linearized Euler Equations in a radial vaneless diffuser for convected rotational wakes. At higher flow rates, the theory matched the data for the radial velocity in a general sense.

However, the measured tangential velocity decreased more rapidly with increasing radius than predicted by the theory. The amplitude ratio and phase angle between the wake radial and tangential velocities was concluded to affect the correlation with theory, as well as an unsteady circumferential static pressure generated by the rotating impeller.

Unsteady surface static pressure measurements were made on the diffuser vanes to determine unsteady loading. The unsteady lift increased with flow rate using 30 diffuser vanes, especially at higher vane stagger. Increasing the diffuser leading edge/impeller exit radial spacing decreased the lift at higher flow rates and stagger angles, although at lower flow rates, the effect was less pronounced. With 15 diffuser vanes, the unsteady lift was generally greater, with less variation due to flow rate. Increasing the diffuser leading edge/impeller exit radial spacing decreased the unsteady lift significantly. Nonuniform circumferential spacing detuning increased the lift on one or both of the vanes in all cases.

A theory to predict the unsteady diffuser vane loading was developed by applying conformal mapping to existing axial cascade unsteady aerodynamic theory and incorporating the wake model as a boundary condition. Poor correlation of the data with the theory was seen with 30 diffuser vanes, which was attributed to the very close vane spacing. Reasonable correlation between data and theory was seen with 15 diffuser vanes at points of low vane steady loading. An unexplainable poor correlation with theory was seen using 10 diffuser vanes. Mismatch of data with theory is believed to be due to mismatch of the wake model and steady loading on the diffuser vanes, which the theory does not consider.

Finally, flow instabilities in the compressor were experimentally investigated. A one-lobed impeller stall existed at low flow coefficient for the vaneless diffuser. For the vaned diffuser, several instabilities were observed. With 30 diffuser vanes, diffuser stall and surge were the only instabilities occurring. For 60° vane stagger, surge typically occurred at a flow coefficient of approximately 0.155, with rotating stall not observed. At the higher diffuser vane leading edge/impeller exit ratio for 60° vane stagger, the compressor was operated at very low flow coefficient without surge or rotating stall. With 15 diffuser vanes, the impeller stalled before the diffuser, with surge again occurring at 60° vane stagger without rotating stall occurrence. It was seen that localized vane stalling was not a sufficient condition for rotating stall to occur. Also, significant improvement in stall margin was realized by proper adjustment of the vaned diffuser.

The recommendations for further study are basically twofold. First, further experimental investigation is needed to more accurately determine the parameters that affect the impeller/radial diffuser unsteady wake behavior. The determination of how the



amplitude ratio and phase angle between the wake velocities affect the wake behavior and how these vary with impeller geometry, operating point and rotational speed would be useful. More data on unsteady diffuser vane loading would also be beneficial to more accurately determine the effects of diffuser vane row geometry on the unsteady response. More evidence on the effect of diffuser geometry on rotating stall would also be a significant experimental contribution. Since the current investigation was performed at low speed, it is important to establish the correlation between measurements made at low speed and behavior of high speed machines.

The second recommendation concerns the theoretical prediction of unsteady behavior. A more accurate model for radial diffuser wake behavior would certainly be useful. It is likely a model that considers the circumferential pressure variation as a boundary condition will be necessary. Once this is accomplished, incorporating this model into unsteady vane loading prediction is of primary importance. The effects of vane loading and gust distortion should be considered in the unsteady loading analysis. Since the unsteady diffuser vane loading analysis is only valid for incompressible flow, prediction of unsteady loading in high speed machines will require consideration of compressibility effects.

In conclusion, a more significant data base along with more general analyses will be necessary before accurate prediction of unsteady aerodynamics in centrifugal compressors is realized.

## LIST OF REFERENCES

## LIST OF REFERENCES

- Arndt, N.; Acosta, A.J.; Brennen, C.E. and Caughey, T.K. "Rotor-Stator Interaction in a Diffuser Pump," ASME Paper 88-GT-55, 1988.
- Bammert, K.; Jansen, M. and Rautenberg, M. "On the Influence of the Diffuser Inlet Shape on the Performance of a Centrifugal Compressor Stage," ASME Paper 83-GT-9, 1983.
- Bryan, W. B. and Fleeter, S. "The Effect of Prewirl on the Internal Aerodynamics and Performance of a Mixed Flow Research Centrifugal Compressor," Thermal Sciences and Propulsion Center Technical Report, ME-TSPC-TR-87-12, Purdue University, August 1987.
- Bryan, W.B. and Fleeter, S. "Flow Induced Forced Response of an Incompressible Radial Cascade Including Profile and Incidence Effects," AIAA Paper 90-2352, July, 1990.
- Bryer, D. W. and Pankhurst, R. C. *Pressure Probe Methods for Determining Wind Speed and Flow Direction*, London: Her Majesty's Stationery Office, 1971.
- Capece, V. R. and Fleeter, S. "Forced Response Unsteady Aerodynamics in a Multistage Compressor," Thermal Sciences and Propulsion Center Report, ME-TSPC-TR-87-12, Purdue University, August, 1987.
- Caruthers, J. E. and Kurosaka, M. "Flow Induced Vibration of Diffuser Excited Radial Compressors," Final Report NAG 3-86, September 1982.
- Cebeci, T. and Bradshaw, P. *Momentum Transfer in Boundary Layers*, McGraw Hill, New York, 1977.
- Chiang, H. W. D. "Aerodynamic Detuning of a Loaded Airfoil in an Incompressible Flow by a Locally Analytical Method," PhD Thesis, Purdue University, August 1988.
- Churchill, R.V. and Brown, J.W. *Complex Variables and Applications*, McGraw Hill, New York, 1984.
- Clements, W. W. and Artt, D. W. "The Influence of Diffuser Channel Geometry on the Flow Range and Efficiency of a Centrifugal Compressor," Proceedings of the Institution of Mechanical Engineers, Vol 201, No. A2, 1986, pp. 145 -152.

- Dean, R. C. "On the Necessity of Unsteady Flow in Fluid Machines," ASME Journal of Basic Engineering, Vol. 87, March, 1959, pp. 24-28.
- Dean, R. C. and Senoo, Y. "Rotating Wakes in Vaneless Diffusers," ASME Journal of Basic Engineering, Vol. 88, January 1960, pp. 49-60.
- Dixon, S. L. *Thermodynamics of Turbomachinery*, Pergamon Press, Oxford, 1978.
- Eckardt, D. "Instantaneous Measurements in the Jet-Wake Discharge Flow of a Centrifugal Compressor Impeller," ASME Journal of Engineering for Power, July 1975, pp. 337-345.
- Emmons, H. W.; Pearson, C. F. and Grant, H. P. "Compressor Surge and Stall Propagation," Transactions of the ASME, Vol. 79, 1955.
- Fagan, J. R. "An Investigation of the Three-Dimensional Flow Field in a Centrifugal Compressor," Ph.D. Thesis, Purdue University, June, 1989.
- Faulders, C.R. "Aerodynamic Design of Vaned Diffusers for Centrifugal Compressors," ASME Technical Paper 56-A-213, 1956.
- Fisher, E. H. and Inoue, M. "A Study of Diffuser/Rotor Interaction in a Centrifugal Compressor," Journal of Mechanical Engineering Science, Vol. 23, No. 3, 1981.
- Goldstein, M. E. and Atassi, H. "A Complete Second-Order Theory for the Unsteady Flow about an Airfoil due to a Periodic Gust," Journal of Fluid Mechanics, Vol. 74, Part 4, 1976, pp 741-765.
- Gostelow, J. P. *Cascade Aerodynamics*, Pergamon Press, Oxford, 1984.
- Grietz, E. M. "The Stability of Pumping Systems-The 1980 Freeman Scholar Lecture," ASME Journal of Fluids Engineering, Vol. 103, pp 193-242, June 1981.
- Henderson, G. "Forcing Function and Steady Loading Effects on Unsteady Aerodynamic Gust Response," PhD Thesis, Purdue University, August 1991.
- Hoyniak, D. and Fleeter, S. "Prediction of Aerodynamically Induced Vibrations in Turbomachinery Blading," ASME Journal of Fluids Engineering, Vol. 105, pp 375-381, December 1983.
- Inoue, M. and Cumpsty, N.A. "Experimental Study of Centrifugal Impeller Discharge Flow in Vaneless and Vaned Diffusers," ASME Journal of Engineering for Gas Turbines and Power, April, 1984, Vol. 106, pp. 455 -467.

- Krain, H. "Swirling Impeller Flow," ASME Paper 87-GT-19, June 1987.
- Panton, R. L. *Incompressible Flow*, Wiley-Interscience, New York, 1984.
- Rodgers, C. "The Performane of Centrifugal Compressor Channel Diffusers," ASME Paper 82-GT-10, 1982.
- Ross, S.H. *Introduction to Ordinary Differential Equations*, John Wiley and Sons, 1980.
- Scheaffer, Richard L. and McClave, James T. *Statistics for Engineers*, Duxbury Press, Boston, 1982. .
- Senoo, Y. and Ishida, M. "Behavior of Severely Asymmetric Flow in a Vaneless Diffuser," ASME Journal of Engineering for Power, Vol. 97, 1975, pp. 375-387.
- Smith, V. J. "A Review of the Design Practice and Technology of Radial Compressor Diffusers," ASME Technical Paper 70-GT-116, 1970.
- Van den Braembussche, R. "Surge and Stall in Centrifugal Compressors," von Karman Institute for Fluid Dynamics Lecture Series 1984-07, May 28-30, 1984.
- Vavra, M. H. and Gawain, T. H. "Compressor Test Rig For Investigation of Flow Phenomena in Turbo-Machines," Technical Report No. 12 on Project No. NR 061-058, February, 1955.
- Verdon, Joseph M. "The Unsteady Flow in the Far Field of an Isolated Blade Row," United Technologies Research Center Report R87-957333-1, April, 1987.
- Whitehead, D.S., "Force and Moment Coefficients for Vibrating Aerofoils in Cascade," Aeronautical Research Council Reports and Memoranda No. 3254, February, 1960.
- Whitehead, D.S. "Classical Two-Dimensional Methods," AGARDograph No. 298, AGARD Manual on Aeroelasticity in Axial Flow Turbomachines, Volume 1: Unsteady Turbomachinery Aerodynamics, 1984, pp. 3.1-3.30.
- Wood, J.R.; Adam, P.W. and Buggele, A.E. "NASA Low-Speed Centrifugal Compressor For Fundamental Research," NASA Technical Memorandum 83398, 1983.
- Yoshinaga, Y.; Gyobu, I.; Mishina, H.; Koseki, F. and Nishida, H. "Aerodynamic Performance of a Centrifugal Compressor with Vaned Diffusers," ASME Journal of Fluids Engineering, Vol. 102, December 1980.

Zachmanoglou, E.C. and Thoe, D.W. *Introduction to Partial Differential Equations with Applications*, Dover Publications, Inc., New York, 1986.